



Fakultät für Chemie

Fachgebiet Synthese und Charakterisierung innovativer Materialien

Contribution to the synthesis and morphology control of LiCoPO_4 -*Pnma* using polyol method

Carlos Eduardo Alarcón Suesca

Vollständiger Abdruck der von der Fakultät für Chemie der Technischen Universität München zur Erlangung des akademischen Grades eines *Doktors der Naturwissenschaften (Dr. rer. nat.)* genehmigten Dissertation.

Vorsitzender:

Univ.-Prof. Dr. Thomas Brück

Prüfer der Dissertation:

1. Univ.-Prof. Dr. Tom Nilges

2. Univ.-Prof. Dr. Shigeyoshi Inoue

Die Dissertation wurde am 06.06.2017 bei der Technischen Universität München eingereicht und durch die Fakultät für Chemie am 29.06.2017 angenommen.

The experimental part of this work was in the period from August 2012 to Juli 2016 in the Fachgebiet Synthese und Charakterisierung innovativer Materialien at the Technical University of Munich under the supervision of Prof. Dr. Tom Nilges

I would like to thank my Ph.D. supervisor Professor Dr. Tom Nilges for the interesting topic of this work, his commitment, scientific support, and the many valuable suggestions during its execution.

I would also like to thank BMW, DAAD and Colciencias, who have funded this dissertation and a large part of the equipment used.

I hereby declare that I have produced the present work without the unacceptable assistance of third parties and without the use of any means other than those indicated. The data and concepts taken directly or indirectly from other sources are marked with the bibliography.

Acknowledgments

I would like to express my sincere gratitude to the following persons who support this work:

Prof. Dr. Tom Nilges for his valuable guidance, professional advice and the big opportunity he gave me to be part of his work group.

Prof. Dr. T. F. Fässler and Prof. Dr. F. Kraus for his academic suggestions. Prof. Dr. H. Gasteiger and Dr. Christoph Stinner for the valuable discussions and kind-co-operation in the project. Dr. Cyril Marino and Dr. Dominik Haering for the electrochemical and BET measurements. The members of the Phospholocat project for the good cooperation and help. Dr. Michael Hörmannsdorfer for his support and guidance with the laboratory organization. Ms. Katia Rodewald for the HR-SEM measurements.

Dr. Viktor Hlukhyy and Dr. Wilhelm Klein for the support in the magnetic measurements and in-situ XRD characterization. The members of the Synthese und Charakterisierung innovativer Materialien and the Anorganische Chemie mit Schwerpunkt Neue Materialien group for their help along those years and discussion in the seminars. Ms Katia Rodewald for the HR-SEM measurements. Dr. Inés Puente-Orech for the neutron diffraction measurements at ILL laboratory. Ms Lucia Weissenborn for her patience in the solve of different organizational issues, without her I will be lost in the “German bureaucrazy”.

To my practical laboratory and bachelor students Thomas Braun, Jan Schwämmlein, Havva Atay-Ergin, Florian Munziger, Alex Engebart, and Matthias Keller. To Daniel Wahrmann, M.Sc Sofia Romero, Екатерина Баскакова and Таня Голнева for the proofreading, english corrections and support in the design of the images.

Dr. Oksana Storcheva and Dr. Gabriele Raudaschl-Sieber for all nice suggestions and cheering and friendly conversations. To “Hola amigo” Daniel Lemma at the Zentralbereiche of the Chemical Department for his help with the chemicals.

To my “ANFOL-guys” (Karl, Benno, Marius and Sandro), thanks for the time and fun making music, definitely, one of my personal highlights.

To all my friends in Germany and Colombia for their unceasing encouragement and help over the distance. Especially thanks to the people from the Mision Católica the Lengua Española, your prayers were listened. To Rev. Mr. José Ayllon for the spiritual guidance. To my Dad, Mom, Bro and family for their love and prayers.

To God, thanks for guiding me and give me force to follow your path.

Abstract

Since the commercialization of lithium ion batteries (LIB's) in the 90's, its development has been growing in parallel with the electronic market, making a remarkable synergistic link between their applications range and their energy requirements. Therefore, in recent years, intense research has been performed and intense studies around the battery components (cathode, anode, and electrolyte), in order to enhance their electrochemical performance. In the case of cathode materials, the phospho-olivines type materials, with formula LiMPO_4 ($M = \text{Ni, Co, Fe, Mn}$) have received particular attention due to their excellent theoretical capacity, good thermal stability and low cost. This work focuses on the synthesis and characterization of LiCoPO_4 (LCP) by mean polyol synthesis. LCP offers a high redox potential (~ 4.8 V) and reduced cobalt weight fraction per formula unit compared to the commercial LiCoO_2 . The synthesis procedure is based on a kinetically controlled approach, useful to control the morphology and shape of the synthesized material, as well as the grain size; two parameters that are crucial for the electrochemical performance in any LIB system. Since only few reports on LCP synthesis by polyol method were published prior to this work, a systematic methodology based on the synthesis of other transition-metal olivines have been adapted and tested for the first time, resulting in the successful synthesis of phase pure LCP-*Pnma*. In addition, the use of surfactants to control the nucleation and growth of particles have been implemented by the variation of experimental parameters, like temperature and molar ratio. Using this methodology, a well-defined control of the particle size can be achieved. Moreover, the synthesis of other modifications of LCP (*Pn2₁a* and *Cmcm*) and LFP-*Cmcm* is reported for the first time, by the use of polyol synthesis method.

Kurzzusammenfassung

Seit der Kommerzialisierung von Lithium-Ionen-Batterien (LIB's) in den 90er Jahren wächst die Entwicklung parallel zum elektronischen Markt und führt zu einer bemerkenswerten synergistischen Verbindung zwischen ihrem Anwendungsbereich und ihrem Energiebedarf. Daher wurden in den letzten Jahren intensive Forschung und tiefgreifende Studien im Bereich der Batteriekomponenten (Kathode, Anode und Elektrolyt) durchgeführt, um ihre elektrochemischen Eigenschaften zu verbessern. Im Falle von Kathodenmaterialien haben die Materialien des Phospho-Olivin-Typs mit der Formel LiMPO_4 ($M = \text{Ni, Co, Fe, Mn}$) aufgrund ihrer hervorragenden theoretischen Kapazität, guter thermischer Stabilität und niedrigen Kosten besondere Aufmerksamkeit erhalten. Die vorliegende Arbeit konzentriert sich auf die Synthese und Charakterisierung von LiCoPO_4 (LCP) durch kinetisch kontrollierte Polyolsynthese. LCP bietet ein hohes Redoxpotential ($\sim 4,8\text{V}$) und eine reduzierte Kobaltgewichtsfraktion pro Formeleinheit gegenüber dem kommerziellen LiCoO_2 . Das Syntheseverfahren basiert auf einem kinetisch kontrollierten Ansatz, der aufgrund der Kontrolle der Morphologie und Form des synthetisierten Materials sowie der Korngröße nützlich ist; zwei Parameter, die für eine Verbesserung der elektrochemischen Leistung in jedem LIB-System entscheidend sind. Da bisher nur wenige Berichte über die LCP-Synthese durch die Polyol-Methode veröffentlicht wurden, sind in dieser Studie erstmals systematische Untersuchungen basierend auf der Synthese anderer Übergangsmetall-Olivine angepasst und getestet worden. Dies führte zur Synthese von phasenreinem LCP- $Pnma$. Darüber hinaus wurde die Anwendung von Tensiden zur Kontrolle der Keimbildung und des Wachstums von Partikeln angewendet und durch die Variation von experimentellen Parametern wie Zeit, Temperatur und Molverhältnis optimiert. Mit dieser Methodologie kann eine wohldefinierte Kontrolle der Partikelgröße erreicht werden. Darüber hinaus wird erstmals über die Synthese anderer Polymorphe des LCP ($Pn2_1a$ und $Cmcm$) und LFP- $Cmcm$ unter Verwendung der Polyol-Methode berichtet.

Index

1. Introduction and background.....	25
1.1 Energy storage problem.....	25
1.2 Environmental contamination and human health.....	26
1.3 Battery research: Why lithium-ion?.....	27
1.4 LIB components. Cathode: The Holy Grail?.....	28
1.5 Phospho-olivines: The LiCoPO ₄ option.....	37
1.6 Kinetically controlled routes of synthesis: Polyol assisted.....	40
1.7 Design of cathode materials: trends and remarks.....	44
1.8 Motivation: scope and objectives of this thesis.....	46
1.9 Methodology.....	47
2. Experimental procedures.....	48
2.1 Summary of LCP- <i>Pnma</i> synthesized using polyol method.....	48
2.2 Educts used.....	50
2.3 Polyol synthesis of LCP- <i>Pnma</i>	51
2.3.1 Synthesis using the CoAc ₂ , ADP and LiAc system ¹²⁴ – standard procedure.....	51
2.3.2 Synthesis using the CoAc ₂ and LDP system (adapted from LiMnPO ₄ polyol synthesis) ⁹⁸ – standard procedure.....	52
2.3.2.1 Synthesis using CoAc ₂ and LDP system combined with PVP ^{98, 128}	53
2.3.3 Synthesis using the CoAc ₂ , H ₃ PO ₄ and LiAc system (adapted from LiFePO ₄ polyol synthesis) ¹²⁹ – standard procedure.....	54
2.4 MW-assisted polyol synthesis of LCP- <i>Pnma</i>	55
2.4.1 MW-assisted synthesis using the CoX and LDP system (X = Ac ₂ , SO ₄ , CO ₃).....	55
2.4.2 MW-assisted polyol synthesis using the CoAc ₂ , H ₃ PO ₄ and LiOH system ¹³⁰	56
2.5 Acetate-assisted antisolvent precipitation (AAAP) synthesis (adapted from LiMnPO ₄ antisolvent synthesis ¹³¹).....	57
2.6 Polyol synthesis of LiFePO ₄ - <i>Pnma</i>	59

2.7	Further equipment used for synthesis and characterization	60
2.7.1	Furnaces and tube ovens	60
2.7.2	X-ray diffraction analysis - XRD	60
2.7.3	Scanning electron microscopy - SEM.....	61
2.7.4	Electrochemical characterization.....	61
2.7.5	Brunauer-Emmett-Teller (BET) Analysis	62
2.7.6	Measurements of electrical conductivity	62
2.7.7	CHNS-Elemental analysis.....	63
2.7.8	Ball milling.....	63
3.	Results and discussion	64
3.1	Polyol synthesis of LCP- <i>Pnma</i> phase.....	64
3.1.1	Synthesis using the CoAc ₂ , ADP and LiAc system (synthesis reproduction ¹²⁴).....	64
3.1.2	Synthesis using the CoAc ₂ and LDP system (adapted from LiMnPO ₄ polyol synthesis ⁹⁸)	66
3.1.2.1	Influence of the reflux temperature and reaction time	67
3.1.2.2	Influence of the surfactants on the morphology	75
3.1.2.3	Influence of the annealing process program	83
3.1.2.4	Influence of the water content on pre-dissolution of CoAc ₂	85
3.1.2.5	Influence of additional synthesis parameters on the crystal structure and morphology using the CoAc ₂ and LDP system.....	90
3.1.3	Synthesis using the CoAc ₂ , H ₃ PO ₄ , LiAc system (adapted from LiFePO ₄) – standard procedure	100
3.2	Microwave assisted-polyol synthesis route of LCP- <i>Pnma</i>	105
3.2.1	MW-assisted synthesis using the CoX and LDP system (X = Ac ₂ , SO ₄ , CO ₃).....	105
3.2.2	MW-assisted polyol synthesis using the CoAc ₂ , H ₃ PO ₄ and LiOH system	109
3.3	Acetate-assisted antisolvent precipitation (AAAP) synthesis of LCP- <i>Pnma</i>	112
3.3.1	Standard procedure.....	112
3.3.2	Discussion about the influence of cobalt source and dropping rate	117
3.4	Synthesis of LCP- <i>Cmcm</i> phase and Li _{0.5} CoPO ₄ - <i>Cmcm</i>	122
3.5	Synthesis of LFP- <i>Pnma</i> by polyol method.....	129
3.5.1	First step: reproduction of the synthesis reported in literature	129
3.5.2	Second step: variation of the synthesis parameters	131
3.5.3	Third step: tuning the Li:Fe:P molar ratio	132
3.5.4	Fourth step: variation of the mixing method of educts.....	133

3.5.5	Fifth step: variation of the polyalcohol.....	135
3.6	Synthesis of LFP- <i>Cmcm</i> phase.....	138
4.	Conclusions and outlook	141
4.1	Conclusions.....	141
4.2	Outlook.....	143
5.	Appendix.....	144
5.1	Parameters tested using the CoAc ₂ , ADP and LiAc polyol synthesis	144
5.2	Table of parameters tested using the CoAc ₂ and LDP system (Adapted from LiMnPO ₄ polyol synthesis ⁹⁸)	146
5.3	Table of parameters tested using the CoAc ₂ , H ₃ PO ₄ , LiAc system (adapted from LiFePO ₄) 148	
5.4	Other systems tested in the polyol synthesis of LCP- <i>Pnma</i>	149
5.5	Tables of experimental parameters tested during the polyol synthesis of LFP- <i>Pnma</i>	150
6.	Publications and participation in conferences	152
7.	References.....	178

Figure list

- Figure 1-1: Energy density (Wh/kg) vs specific density (Wh/L) for a series of batteries. A battery directed to the consumer electronics market, especially to the electric vehicle market, should be as light (high energy density) and as small (high specific energy) as possible that is, the ideal battery should lay in the upper right corner of the diagram..... 28
- Figure 1-2: Schematic representation of rechargeable LIB's. There are two systems according the nature of the negative electrode either Li metal (a) or Li insertion compound (b) In both cases, the positive electrode is constituted by an insertion compound, in which the redox reaction occurs at high potential versus Li^0/Li^+ (c) The types of insertion compounds as a function of the dimensionality. Red circles are intercalated ions across the host channels..... 29
- Figure 1-3: Schematic illustration of a typical lithium-ion battery with a cathode material of LiFePO_4 and anode material of graphite 30
- Figure 1-4: Electrode materials and corresponding electrochemical performances in the current LIB technologies 32
- Figure 1-5: Crystal structures and electrochemical reactions of various cathodes: (A) Layered LiMO_2 , (B) spinel LiM_2O_4 , (C) olivine LiMPO_4 , (D) Li_2MSiO_4 , (E) LiMBO_3 , (F) LiV_3O_8 , (G) V_2O_5 , (H) FeF_3 33
- Figure 1-6: Cathode materials for LIB's. Background colours reflect characteristics of bulk materials. Green denotes relative strength, red relative weakness, yellow intermediate characteristics and white no data. Absence of circle (o) indicates no data for the material. The grey background denotes the 'baseline' material use for comparison. NCA: lithium nickel cobalt aluminium oxide; NMC: lithium nickel manganese cobalt oxide; LCO: lithium cobalt oxide; LMR: lithium/manganese rich transition metal oxide; LFP: lithium iron phosphate; LVP: lithium vanadyl phosphate; LMO: lithium manganese oxide 35
- Figure 1-7: Schematic energy diagram of a lithium cell at open circuit. HOMO and LUMO refer, respectively, to the highest occupied molecular orbital and lowest unoccupied molecular orbital in the electrolyte. 37
- Figure 1-8: Crystal structure of LiMPO_4 (LMP) $Pnma$: $[\text{MO}_6]$ with $M=\text{Co}$. a) Projection along a -axis b) Projection along b -axis c) Projection along c -axis. d) Alternative projection to see the corner shared

octahedral between $[\text{CoO}_6]$ and $[\text{PO}_4]$ units. Octahedra are drawn in blue, $[\text{PO}_4]$ tetrahedra in yellow, Li^+ ions in green and O^{2-} ions in red.....	39
Figure 1-9: Typical routes for producing LMPO_4 powders using solid state methods. Adapted from ⁶⁹	41
Figure 1-10: Typical routes for producing LiMPO_4 powders using solution based methods. Adapted from ⁶⁹	41
Figure 1-11: General strategies for performance enhancement and their rationale: 1 reducing dimensions of active materials, 2 formation of composites, 3 doping and functionalization, 4 tuning particle morphology, 5 formation of coatings or shells around active materials, 6 modification of electrolyte.....	45
Figure 1-12: Flowchart of the methodology implemented for the synthesis of LCP. The blocks in blue represent part of the scope of the project.	47
Figure 2-1: Flowchart of polyol synthesis using the CoAc_2 , ADP and LiAc system. The middle column present the synthesis parameters. Pictures of dissolution in EG, centrifugation, appearance of the final product (before and after annealing) and reflux system.....	52
Figure 2-2: Flowchart of polyol synthesis using the CoAc_2 and LDP system ⁹⁸	53
Figure 2-3: Flowchart of polyol synthesis using the CoAc_2 and LDP system combined with PVP.....	54
Figure 2-4: Flowchart of polyol synthesis using the CoAc_2 , H_3PO_4 and LiAc system.....	55
Figure 2-5: Flowchart of microwave-assisted polyol synthesis using the CoX and LDP system ($X = \text{Ac}_2, \text{SO}_4, \text{CO}_3$).....	56
Figure 2-6: Flowchart of microwave-assisted polyol synthesis using CoAc_2 , H_3PO_4 and LiOH system.....	57
Figure 2-7: Flowchart of acetate-assisted antisolvent precipitation synthesis of LCP- <i>Pnma</i>	58
Figure 2-8: Experimental setup for the acetate-assisted antisolvent synthesis. Left side: the Syringe driver adapted to the round flask. The syringe tip cross trough rubber septa. The reflux cooler is use to avoid the evaporation of the solvent.....	59
Figure 2-9: Flowchart of polyol synthesis of LFP- <i>Pnma</i>	60
Figure 2-10: Tool used for the determination of the electric conductivity.....	63
Figure 2-11: Ball mill procedure for the C-coating in the AAAP method.....	63
Figure 3-1: PXRD pattern of samples after annealing. The red pattern corresponds to the synthesis uses a EG:Water ratio of 100:0 (mL). The black pattern corresponds to the synthesis using a EG:Water ratio of 70:30 (mL). The negative intensity corresponds to the reported LCP- <i>Pnma</i> (black), $\text{Co}_3\text{PO}_4\text{-Fd-3ms}$ (\diamond blue), $\text{Co}_3(\text{PO}_4)_2\text{-P1121/b}$ (\circ green) and $\text{Li}_3\text{PO}_4\text{-Pcmn}$ (\square orange). The measuring time is 1 hour.	66
Figure 3-2: <i>Effect of reflux time</i> . PXRD of samples refluxed at 135 °C. Pattern recorded after the drying process. The black pattern corresponds to the synthesis for 4 hours at 135 °C and the red to the	

synthesis for 14 hours at 135 °C. The negative intensity corresponds to the reported phases of LCP- <i>Pn2₁a</i> (◇ black) and Co ₃ (HPO ₄) ₂ (OH) ₂ (○ blue). The measuring time is 20 minutes.....	68
Figure 3-3: <i>Effect of the reflux time</i> . PXRD of samples refluxed at 190 °C. Pattern recorded after the drying process. The negative intensity corresponds to the reported phases of LCP- <i>Pnma</i> (black), LCP- <i>Pn2₁a</i> (◇ Green) and Co ₃ (HPO ₄) ₂ (OH) ₂ (○ blue). The measuring time is 20 minutes.....	68
Figure 3-4: <i>Effect of reflux temperature</i> . PXRD pattern of the samples refluxed at 135 °C for 14 h. Pattern recorded after annealing at different temperatures. The negative intensity corresponds to the reported phases of LCP- <i>Pnma</i> ¹³³ (gray). The measuring time is 20 min.....	70
Figure 3-5: <i>Effect of reflux temperature</i> . PXRD pattern of the samples refluxed at 190 °C for 14 h. Pattern recorded after the annealing at different temperatures. The negative intensity corresponds to the reported phases of LCP- <i>Pnma</i> . ¹³³ (gray). The measuring time is 30 min.	71
Figure 3-6: <i>Effect of reflux temperature and time</i> . PXRD pattern after last annealing at 750 °C. The negative intensity corresponds to the reported LCP- <i>Pnma</i> (gray). The measuring time is 1 hour.	71
Figure 3-7: SEM images of the samples produced using the CoAc ₂ and LDP system. The left side shows the samples after drying process. On the right side, the particles after the last annealing step at 750 °C. Microscope B. Magnification: a) 2000X, b) 5000X, c) 2000X, d) 2000X, e) 1000X, f) 1000X, g) 2000X and h) 2000X.....	74
Figure 3-8: <i>Influence of PVP surfactant</i> . PXRD patterns of the samples synthesized using PVP after drying process. The negative intensity corresponds to the reported LCP- <i>Pn2₁a</i> (◇ gray) and Co ₃ (HPO ₄) ₂ (OH) ₂ (○ blue). The measuring time is 30 min.	76
Figure 3-9: Schematic representation of the bonding between LCP and PVP. Discrete metal collide on PVP backbone.....	77
Figure 3-10: <i>Influence of PVP surfactant</i> PXRD patterns of the samples synthesized using PVP. The negative intensity corresponds to the reported LCP- <i>Pnma</i> (gray). The measuring time is 1 hour.....	77
Figure 3-11: Schematic illustration of the growth mechanism of LCP microspheres with PVP.....	78
Figure 3-12: Schematic diagram of the annealing processes: a) Partial recrystallization b) Full recrystallization c) Grain growth d) Abnormal grain growth. PVP functionality and issues: e) Protective layer against grain growth d) Inhomogeneous C-coating e) Highly thick C-coating.....	80
Figure 3-13: SEM images of the samples produced using the CoAc ₂ and LDP system with PVP. The left side shows the samples after drying process. On the right side, the particles after the last annealing step at 750 °C. a) - b): PVP dissolved half on EG and half on CoAc ₂ solution at 100 °C; c) – h) PVP dissolved on CoAc ₂ solution. Microscope B. Magnification: a) 5000X, b) 5000X, c) 2000X, d) 2000X, e) 1000X, f) 1000X, g) 2000X and h) 2000X.....	81
Figure 3-14: SEM images of LCP- <i>Pnma</i> synthesized using PVP. a) Sample after drying process. Detailed view of the spheres. Micro-spheres are formed by primary nano-sheets b) Sample after	

- annealing. The porosity collapses after the successive annealing in order to complete the formation of LCP-*Pnma*. c) Detailed view of the primary nano-sheets d) Additional to the spheres, big blocks of around 6 μm are also present. Microscope B. Magnification: a) 25000X, b) 10000X c) 50000X and d) 8000X..... 82
- Figure 3-15: PXRD pattern of samples after annealing for 10 h under air atmosphere at 550 °C. In red the synthesis uses a precursor using PVP as surfactant. In black the synthesis uses a EG:Water ratio of 70:30 (mL). The negative intensity corresponds to the reported LCP-*Pnma* (black), $\text{Co}_3(\text{PO}_4)_2\text{-P12}_1/\text{c1}$ (o blue) and $\text{CoO-I4}/\text{mmm}$ (□ green) The measuring time is 1 hour..... 83
- Figure 3-16: SEM images of LCP-*Pnma* synthesized using the CoAc_2 , LDP system. a – b: Samples produced without PVP c – d: Samples produced with PVP. Microscope B. Magnification: a) 9500X, b) 30000X c) 5000X and d) 10000X. 84
- Figure 3-17: Influence of the water content in the pre-dissolution step. PXRD after drying process. The negative intensity corresponds to the reported LCP-*Pn2_{1a}*¹³⁹(black). LCP-*Pnma* (o red) and an unidentified phase (■ Lila). The measuring time is 20 mins. 86
- Figure 3-18: Influence of the water content in the pre-dissolution step. PXRD after annealing process at 400 °C for 1 hour. The negative intensity corresponds to the reported LCP-*Pnma* (Black). The measuring time is 1 hour. 87
- Figure 3-19: SEM images of the samples produced using the CoAc_2 and LDP with different amounts of water. Left side: shows the samples after drying process. Right side: the particles after annealing at 400 °C. a) - b) 10 mL; c) – d) 20 mL; e) – f) 30 mL. Microscope A. Magnification: left column 1000X, right column 4000X 89
- Figure 3-20: Influence of the polyalcohol media. PXRD of samples refluxed using DEG, TEG and TTEG with their respective b. p. reached. Pattern recorded after the drying process. The negative intensity corresponds to the reported phase of LCP-*Pn2_{1a}* (grey). The measuring time is 20 min. 91
- Figure 3-21: Influence of the polyalcohol media. Solvents: DEG, TEG and TTEG with their respective b. p. reached. Pattern recorded after annealing at 400 °C for 5 hours under air. The negative intensity corresponds to the reported phases of LCP-*Pnma* (grey), LCP-*Pn2_{1a}* (◇ red), $\text{LiPO}_3\text{-P12n1}$ (o blue), $\text{Co}_3(\text{PO}_4)_2\text{-P12}_1/\text{c1}$ (▲ orange) and a unidentified phase (■ lila). The measuring time is 20 min. 92
- Figure 3-22: SEM images of the samples produced using the CoAc_2 and LDP system with different polyalcohols. The pictures correspond to the samples after drying/annealing process. a) DEG; b) TEG; c) TTEG. Microscope B. Magnification: left column 10000X, right column 20000X..... 93
- Figure 3-23: Influence of the predissolution of CoAc_2 and polyalcohol media. PXRD patter of the samples after drying. The negative intensity corresponds to the reported phases of LCP-*Pn2_{1a}* (◇ black) and an unidentified phase (■ lila). The measuring time is 20 min. 94

- Figure 3-24: *Influence of the predissolution of CoAc_2 and polyalcohol media.* PXRD of the samples after drying at 400 °C for 1 hour under air. The negative intensity corresponds to the reported phases of LCP-*Pnma* (black), LCP-*Pn2_{1a}* (○ red), $\text{LiP}_3\text{-P6}_3/\text{mmc}$ (◇ blue), and an unidentified phase (▪ lila). The measuring time is 20 min. 95
- Figure 3-25: SEM images of the samples produced using the CoAc_2 and LDP system with pre-dissolution of CoAc_2 in 10 mL water. The pictures correspond to the samples after drying/annealing process. a) DEG; b) TEG; c) TTEG. Microscope A. Magnification: left column 1000X, right column 6000X..... 96
- Figure 3-26 *Influence of the cobalt source on the synthesis of LCP by polyol method.* PXRD of the samples synthesized using CoCO_3 and CoSO_4 as cobalt precursor and their temperature under refluxing conditions. Pattern recorded after the drying process. The negative intensity corresponds to the reported phases of $\text{SO}_2\text{-Aba2}$ (▼ blue), $\text{CoSO}_4\text{-Cmcm}$ (black ◇), LCP-*Cmcm* (○ red) and an unidentified phase (▪ lila). The measuring time is 20 min. 98
- Figure 3-27 *Influence of the cobalt source on the synthesis of LCP by polyol method.* PXRD of the samples synthesized using CoCO_3 and CoSO_4 as cobalt precursor and their temperature under refluxing conditions after annealing at 400 °C for 1 hour under air. The negative intensity corresponds to the reported phases of $\text{CoSO}_4\text{-Cmcm}$ (◇ black) and LCP-*Cmcm* (○ red). The measure time is 20 min. 98
- Figure 3-28: *Influence of the cobalt source on the morphology of LCP produced by mean polyol synthesis.* SEM pictures of the samples using CoCO_3 and CoSO_4 as cobalt precursor after drying and annealing respectively. Microscope B. Magnification: a) 10000X, b) 10000X c) 10000X and d) 30000X..... 99
- Figure 3-29: PXRD pattern of samples after drying process using CoAc_2 , H_3PO_4 and LiAc as starting precursors. The red pattern corresponds to the synthesis with PVP. The black pattern corresponds to the standard synthesis as described in experimental section. The negative intensity corresponds to LCP-*Cmcm* (○ black) and LCP- *Pn2_{1a}* (◇ red). The measuring time is 20 min. 100
- Figure 3-30: PXRD pattern of samples after annealing process using CoAc_2 , H_3PO_4 and LiAc as starting precursors. The red pattern corresponds to the synthesis with PVP. The black corresponds to the standard synthesis as described in experimental section. The negative intensity corresponds to LCP-*Pnma*. The measure time is 1 hour. 101
- Figure 3-31: SEM images of the samples produced by using the CoAc_2 and LiAc and H_3PO_4 system with PVP and without PVP. The left side shows the samples after drying process. On the right side, the morphology of the particles after the last annealing step at 800 °C for 6 hours a) - b): with PVP; c) – h) without PVP. Microscope B. Magnification: left column 1000X, right column 20000X 102
- Figure 3-32: Schematic illustration of the growth mechanism of LCP sticks with PVP..... 103
- Figure 3-33: Influence of the cobalt source in the MW synthesis of LCP. PXRD pattern of the samples using CoCO_3 , CoSO_4 and CoAc_2 as cobalt precursor, after drying process. The negative intensity

- corresponds to the reported phases of LCP-*Pnma* (◇ black) and LCP-*Pn2₁a* (○ red) and $\text{Co}_3(\text{PO}_4)_2\text{-P12}_1/\text{c1}$ (▲ blue). The measuring time is 20 min. 106
- Figure 3-34: Influence of the cobalt source in MW-assisted polyol synthesis. SEM pictures of the samples using CoAc_2 (LCP-*Pn2₁a*), CoCO_3 (LCP-*Pnma*) and CoSO_4 (LCP-*Pnma*) as cobalt precursor after drying. Microscope A. Magnification: left column 2000X, right column 10000X..... 108
- Figure 3-35: PXRD pattern of sample produced by MW-assisted polyol synthesis. The blue pattern sample synthesized in EG. Black pattern is the sample synthesized in TTEG (Manthiram *et. al.* reproduction ¹³⁰). The negative intensity corresponds to the reported phases of LCP-*Pnma* ¹³³ (black), $\text{Li}_3\text{PO}_4\text{-Pcmm}$ (○ red) and $\text{Co}_3\text{O}_4\text{-Fd-3m}$ (◇ green). The measuring time is 1 hour 109
- Figure 3-36: SEM images of the LCP samples produced using the MW-assisted polyol route using the CoAc_2 , H_3PO_4 and LiOH system. Samples after drying process are shown. Figures a - b: synthesis in EG. Figures c - d: Synthesis in TTEG. Microscope B. Magnification: a) X1000, b) 55000X, c) 10000X and d) 30000X..... 110
- Figure 3-37: Schematic of particle precipitation process 113
- Figure 3-38: Schematic illustration of the acetate-assisted antisolvent precipitation process 113
- Figure 3-39: AAAP synthesis of LCP-*Pnma*. PXRD pattern of the precursor material prior carbon coating and annealing. Pattern recorded after the drying process. The negative intensity corresponds to the reported phases of $\text{Co}_2\text{P}_2\text{O}_7\text{-P2}_1/\text{c1}$ (◇ black) and $(\text{H}_3\text{O})(\text{Co}_2(\text{OH})_2(\text{HPO}_4)(\text{H}_2\text{PO}_4)\text{-Pcab}$ (○ red). The measuring time is 20 min. 114
- Figure 3-40: AAAP synthesis of LCP. PXRD pattern of the C-composite. The red pattern corresponds to the sample annealed under Ar atmosphere. The sample annealed under air atmosphere is shown in black. Peaks marked with symbols correspond to the secondary phases of $\text{Co}_3\text{O}_4\text{-Fd-3m}$ (▼ orange), $\text{LiP}_7\text{-I4}_1/\text{acd}$ (○ blue), $\text{Li}_6\text{CoO}_4\text{-P4}_2/\text{mmc}$ (◇ green) and an unidentified phase (■ lila). The measure time is 1 hour. 115
- Figure 3-41: SEM images of the samples produced using the AAAP method. Samples after drying process: figures a – c, corresponding to the precursor after drying process. Figures b - d: sample after C-coating and annealing. Microscope A. Magnification: a) 1000X b) 2000X, c) 3000X and d) 7000X 116
- Figure 3-42: AAAP synthesis of LCP. Influence of cobalt source. XRD pattern recorded after annealing process under air. The patterns correspond to: CoSO_4 (green), CoCl_2 (blue) and CoCO_3 (black). Negative intensity corresponds to reported LCP-*Pnma* (black) Peaks marked with symbols are the main secondary phases: $\text{CoSO}_4\text{-Cmcm}$ (▼ orange), $\text{Co}_3(\text{PO}_4)_2\text{-P12}_1/\text{c1}$ (○ red), $\text{Co}_2\text{O}_3\text{-R-3}/\text{cb}$ (◇ gray), $\text{Co}_2\text{P}_2\text{O}_7\text{-P12}_1/\text{c1}$ (▲ pink) and $\text{LiSO}_4\text{-P12}_1/\text{a1}$ (■ lila). The measuring time is 20 min. 117
- Figure 3-43: AAAP synthesis of LCP. Influence of dropping rate. XRD pattern recorded after annealing process under air. The patterns corresponds to a rate of: 1.0 mL/min (green), 0.6 mL/min (blue) and

- 0.1 mL/min (black). Negative intensity correspond to reported LCP-*Pnma* (black). Peaks marked with symbols are the main secondary phases: $\text{Co}_2\text{P}_2\text{O}_7\text{-P}12_1/c1$ (○ red), $\text{Co}_3\text{O}_4\text{-Fd-}3mS$ (◇ gray). The measuring time is 1 hour..... 120
- Figure 3-44: SEM images of the LCP samples produced using the AAAP method at different dropping rates. Samples after annealing at 550 °C for 10 hours. Microscope A. Magnification: left column 1000X, right column 5000X..... 121
- Figure 3-45: PXRD pattern of LCP-*Cmcm* synthesized using polyol synthesis. Pattern recorder after drying process. The measuring time is 1 hour..... 122
- Figure 3-46: LCP-*Cmcm* samples using the standard and modified polyol route. a) and b) samples obtained using the standard method. c) and d) samples obtained using a variation in the educts mixture. Microscope B. Magnification: left column 10000X, right column 20000X..... 123
- Figure 3-47: Change of the color of solution during polyol synthesis of LCP-*Cmcm*..... 124
- Figure 3-48: PXRD pattern of LCP-*Cmcm* synthesized using polyol synthesis. Black pattern corresponds to the synthesis using 3 hours of reflux. The red, green and blue patterns correspond to the synthesis using 3 hours of reflux and use of SDBS and PVP (M.W. 58000 and 360000) surfactants. Pattern recorder after drying process. The measuring time is 20 minutes. 125
- Figure 3-49: SEM pictures of LCP-*Cmcm*. a) and b): Synthesis using 3 hours of reflux time. c) to h) synthesis using 14 hours with different surfactants. Microscope A. Magnification: left column 5000X, right column 10000X..... 126
- Figure 3-50: PXRD pattern of $\text{Li}_{0.5}\text{CoPO}_4\text{-}Cmcm$ synthesized using polyol synthesis. Blue pattern corresponds to full lithiated LCP-*Cmcm*. Negative intensity corresponds to $\text{Li}_{0.5}\text{CoPO}_4\text{-}Cmcm$. Pattern recorder after drying process. The measure time is 1 hour..... 127
- Figure 3-51: LCP-*Cmcm* samples using the standard and modified polyol route. Microscope B. Magnification: left column 10000X, right column 20000X 127
- Figure 3-52: Schematic view parallel to (010) surface, showing the sinusoidal Li^+ -migration path (dotted line) to a Li^+ vacancy (open square for *Pnma*). The tilting of the PO_4 tetrahedron near the Li^+ vacancy is also shown. Li^+ : green; Co^{2+} : blue spheres; PO_4^{3-} : yellow tetrahedra..... 128
- Figure 3-53: Influence of the molar ratio on the synthesis of LFP-*Pnma*. PXRD pattern of samples refluxed after the drying process. The patterns corresponds to samples with Li:Fe:P molar ratios of 3:1:1 (black) and 1:1:1 (blue) respectively. The negative intensity corresponds to the reported phases of LFP-*Pnma* (black), $\text{Li}_2\text{SO}_4\text{-P}12_1/a1$ (○ Green), $\text{FeSO}_4\text{-}Cmcm$ (◇ blue), $\text{Li}_4\text{P}_2\text{O}_7\text{-P}12_1n1$ (▲ red) and unidentified phase (■ lila). The measuring time is 30 min. 132
- Figure 3-54: Influence of the Li:Fe:P molar ratio on the synthesis of LFP-*Pnma*. PXRD pattern of the samples after drying process. The PXRD pattern in black corresponds to the Li:Fe:P ratio 2:1:1. Negative intensity corresponds to LFP-*Pnma*. The measuring time is 20 minutes. 133

Figure 3-55: Mixing methods tested in the polyol synthesis of LFP- <i>Pnma</i> . Additional experimental details are described in experimental section 2.6.....	134
Figure 3-56: Influence of the mixing method on the synthesis of LFP- <i>Pnma</i> . PXRD pattern of the samples after drying process. The mixing details are specified in figure 3-55. Negative intensity corresponds to LFP- <i>Pnma</i> . Secondary phases corresponds to (○ red) $\text{Li}_2\text{SO}_4\text{-}F\text{-}4_3m$ and (◇ yellow) $\text{Li}_3\text{PO}_4\text{-}Pcmm$. The measuring time is 1 hour.	135
Figure 3-57: Influence of the polyalcohol on the synthesis of LFP- <i>Pnma</i> . PXRD pattern of the samples after drying process. Black pattern: EG; blue: DEG and green: TEG. The reflux temperature is also included. Negative intensity corresponds to LFP- <i>Pnma</i> . The measure time is 1 hour.....	136
Figure 3-58: Influence of the polyalcohol. SEM images of LFP- <i>Pnma</i> produced using EG, DEG and TEG. Microscope B. Magnification: left column 50000X, right column 100000X	137
Figure 3-59: PXRD pattern of the LFP precursor sample using LiAc, iron oxalate and H_3PO_4 in molar ratio 2:1:1. Sample synthesized in TTEG. The negative intensity corresponds to the reported phases of LFP- <i>Cmcm</i> (black), LFP- <i>Pnma</i> (blue ○), $\text{Li}_3\text{PO}_4\text{-}Pcmm$ (green ▼), $\text{LiFeO-I}4_1\text{/amd}$ (orange ◇) and an unidentified phase (■ lila). The measuring time is 30 min.....	139
Figure 3-60: PXRD pattern of the sample using LiAc, iron oxalate and H_3PO_4 in molar ratio 1:1:1. Sample synthesized in TTEG. The negative intensity corresponds to the reported phases of LFP- <i>Cmcm</i> (black), LFP- <i>Pnma</i> (blue ◇). The measuring time is 1 h.....	139
Figure 3-61: SEM images of LFP- <i>Cmcm</i> produced using TTEG. Microscope A. Magnification: left 1000X, right 5000X.....	140

Table List

	Page
Table 1-1: The voltage of common electrodes, relative to Li metal ³¹	34
Table 1-2: Properties of the LFP, LMP, LCP and LNP olivine compounds compared with other cathode materials currently used in LIB's ⁶⁷	40
Table 1-3: Lattice constants reported for LiCoPO ₄ ⁶⁶ by different synthesis routes	42
Table 1-4: Summary of the shapes and methods for synthesis of Ag nanoparticles using polyol synthesis ¹¹⁴	44
Table 2-1: Summary of polyol synthesis published for LCP- <i>Pnma</i> (up to June 2012).....	49
Table 2-2: List of the chemicals used.....	50
Table 3-1: Summary of two polyol syntheses with differences in solvent composition, reaction time and annealing program.....	65
Table 3-2: Temperature and reaction time parameters using the CoAc ₂ - LDP system.....	67
Table 3-3: Lattice parameter of LCP- <i>Pnma</i> synthesized under different temperatures and reaction times. Reported lattice parameters are presented at bottom of the table to comparison	72
Table 3-4: Capacity values of LCP- <i>Pnma</i> obtained by polyol synthesis (CoAc ₂ and LDP system) after annealed at 750 °C. The measurements were made under different C-rates.	75
Table 3-5: Highlighted experiments for the synthesis of LCP- <i>Pnma</i> using the CoAc ₂ and LDP system with PVP	75
Table 3-6: Lattice parameters and crystallite size of LCP- <i>Pnma</i> synthesized under different temperatures and reaction times with PVP. Reported lattice parameters are presented at bottom of the table.....	77
Table 3-7: Morphology, average grain size of LCP- <i>Pnma</i> of figure 3-13 and capacity values after annealed at 750 °C. The measurements were made under different C-rates.	82
Table 3-8: Capacity values and BET areas of LCP- <i>Pnma</i> using a single-long annealing procedure	84
Table 3-9: Lattice parameter of LCP- <i>Pnma</i> synthesized using different water volumes in the pre-dissolution step. Reported lattice parameters are presented at bottom of the table.....	87
Table 3-10: Capacity values and BET areas of LCP- <i>Pnma</i> produced using different amounts of water.....	88
Table 3-11: Morphology and average grain size of particles of LCP- <i>Pnma</i> synthesized using the CoAc ₂ and LDP system in various solvents.....	95
Table 3-12: Lattice parameter and crystallite size of LCP- <i>Pnma</i> synthesized with and without PVP. Reported lattice parameters are presented at the top of the table	101
Table 3-13: Capacity values and BET areas of LCP- <i>Pnma</i> using a the using the CoAc ₂ and LiAc and H ₃ PO ₄ system.....	102

Table 3-14: Summary of phases formed after polyol and microwave synthesis using the CoX and LDP systems ($X = \text{Ac}_2, \text{SO}_4, \text{CO}_3$) system.....	107
Table 3-15: Capacity values and BET areas of LCP- <i>Pnma</i> using the using the CoAc ₂ , LiOH and H ₃ PO ₄ system.....	110
Table 3-16: Mechanism and energies of Li ⁺ migration in LMP- <i>Pnma</i> ($M = \text{Mn, Fe, Co and Ni}$) ¹⁷⁷ ...	111
Table 3-17: Capacity values and BET area of LCP- <i>Pnma</i> produced by AAAP method.....	116
Table 3-18: Phase analysis of the product mixture after drying process and annealing process for AAAP method using different cobalt sources.....	118
Table 3-19: Lattice parameter and mean domain size of LCP- <i>Cmcm</i> synthesized with surfactants. Reported lattice parameters are presented at the bottom of the table ¹⁵⁵	125
Table 3-20: Summary of polyol synthesis published for LFP- <i>Pnma</i> (up to June 2012)	130
Table 3-21: Phase analysis after reproduction of synthesis based on table 3-20.....	131
Table 3-22: Lattice parameter and crystallite size of LFP- <i>Pnma</i> synthesized in EG, DEG and TTEG. Reported lattice parameters are presented at the top of the table.....	135
Table 3-23: Summary of the variations in molar ratio and solvent in the polyol synthesis of LFP- <i>Cmcm</i>	138
Table 3-24: Lattice parameters and crystallite size of LFP- <i>Cmcm</i> synthesized in TTEG. Reported lattice parameters are presented at the top of the table.	140

Abbreviators

Abbreviator	Term
2-D	Two dimensional
3-D	Three dimensional
AAAP	acetate-assisted antisolvent precipitation
ADP	Ammonium dihydrogen phosphate
BEV's	Battery electric vehicles
b.p.	Boiling points
DAHP	Di-Ammonium hydrogen phosphate
DEC	Diethyl carbonate
DEG	Diethylene glycol
DFT	Density functional theory
DMC	Dimethyl carbonate
EAH	Energy above the hull
EC	Ethylene carbonate
EtOH	Ethanol
EV's	Electric vehicles
hcp	Hexagonal closed-packed
LCO	LiCoO_2
LCP	LiCoPO_4
LFP	LiFePO_4
LIB's	Lithium ion batteries
LiAc	Lithium acetate
Li_xMyX_z	Lithium insertion compound
LMP	LiMnPO_4
LMO	LiMnO_2
LMP	LiMPO_4 ($M = \text{Co, Fe, Ni, Mn}$)
LMR	$\text{LiCo}_{1-x}\text{Mn}_x\text{O}_2$
LNP	LiNiPO_4
Abbreviator	Term
LMV	LiMVO_4 ($M = \text{Co, Fe, Ni, Mn}$)

MW	Microwave
NCA	LiNiCoAlO ₂
NMC	LiNiMnCoO ₂
NO_x	Nitrogen dioxide
PAH's	Polycyclic aromatic hydrocarbons
PM	Particulate matter
PVP	Poly vinylpyrrolidone
PXRD	Powder X-ray diffraction
RES	Renovable Energy Sources
RGO	Reduced graphene oxide
SDBS	Sodium dodecylbenzene sulfonate
TEG	Triethylene glycol
TMO	Transition-metal oxide
TTEG	Tetraethylene glycol
$\sigma_{Li(a)}$	Lithium chemical potential cathode
$\sigma_{Li(c)}$	Lithium chemical potential cathode
V	Cell potential/cell voltage
V_{oc}	Open-circuit voltage
VOC's	Volatile organic compounds
VWR	VWR Chemicals
ZEV's	Zero-emission vehicles
σ_e	electronic conductivity
σ_{Li^+}	Li ⁺ conductivity

1. Introduction and background

This chapter starts with an overview and brief description of the energy storage and its connection with energy sources; followed by a description of the environmental pollution problem due to vehicle emissions and their depletion based on the application of solutions oriented in the electromobility technologies. Then, an explanations of the importance of battery research; as well as, the fundamentals of lithium ion batteries (LIB's) are discussed. The connotation of the cathode materials focused on phospho-olivines, especially LiCoPO_4 (LCP) as candidate for LIB's is described. Finally, the principal synthesis routes of LCP, motivation and methodology of this work are explained in detail.

1.1 Energy storage problem

“Renewable energy is not a viable option unless energy can be stored on a large scale”

Of all developments in the area of materials science in the last decades of the XX and XXI centuries, the progress in the field of energy storage devices is perhaps one of the most remarkable advances. In fact, energy production and energy storage play an important role in the development of the modern society. However, the increase in hydrocarbon fuel demands, environmental pollution and global warming², exert pressure on an already stretched energetic infrastructure. Those factors make it essential to find new ways of energy production and efficient energy storage methods. Although some renewable energy sources (RES) have been developed in recent years, such as solar, nuclear and geothermal ones, they have not reached widespread use due to problems in the propagation in time and space, radioactive wastes and geographical limitations respectively^{3,4}. As a specific case, during the sudden cold snap in February of 2008 in west Texas, thousands of turbines fell silent producing a cut in the energy service until winds picked up again. This would not have been an event if the companies had a few hundred megawatt of energy stored¹.

In this sense, *the most appropriate method of energy storage is portable chemical energy and batteries* that have the advantage to store chemical energy and deliver it as electric energy. Moreover, they show long cycle life, wide range of operating temperatures, high energy density, low cost and they are safe ⁵. Batteries are the modern electricity-based trend-topics, due to their wide usage in electronic devices and transportation systems; they also solve load-leveling issues and provide extra advantages in different uses as portability and conversion efficiency ⁶.

1.2 Environmental contamination and human health

“Low birth weight rate and preterm birth are associated with outdoor air pollution. This problem has a substantial public health impact and economic burden of \$26.2 billion”

On the other hand, one of the main goals concerning the scientific research is to find a way to minimize the effects of air-pollution. United Nations studies determined that in urban areas over 6 million people are continuously exposed to risky levels of traffic generated by air pollutants ⁷. In fact, air pollution is associated with many diseases related to respiratory, immunologic, gastrointestinal and central nervous systems, pregnancy problems; as well as, late effects on behavioral, hearing, motor, cognitive, visual systems and increased mortality risks ⁸⁻¹². Rates of hospital admissions and emergency department visits are increased and have critical implications for social and environmental policies. As example, in 2005, the economic burden in the United States associated with preterm birth reached US \$26.2 billion dollars ¹³; furthermore, air pollution has an important impact on economy, tourism and deterioration of ecological environment.

Common air pollutants include lead (Pb), nitrogen dioxide (NO_x), volatile organic compounds (VOC's), Carbon monoxide (CO), ozone (O₃), particulate matter (PM), sulfur dioxide (SO₂) and polycyclic aromatic hydrocarbons (PAH's), meanwhile, PM, VOC's and NO_x are caused by the large number of fossil-fuel driven vehicles ¹⁴. In order to preserve the environment and to decrease the air pollution, a worldwide effort to promote the development of alternative transportation is an urgent requirement, maintaining the economic growth and diminishing the dependence on traditional vehicles. In this sense, implementation of electric vehicles (EV's), zero-emission vehicles (ZEV's) or battery electric vehicles (BEV's) can contribute to air pollution mitigation if coupled with decarbonized electricity, but only if the vehicle range matches travelers' needs ¹⁵.

1.3 Battery research: Why lithium-ion?

“Cheap energy storage will break the constraint that power must be generated at the same rate that it is used”¹⁶

As presented before, the RES integration and electrification of automotive transportation constitute two imperative ways to help to decrease global warming and gas emission. These ways incur challenges in terms of energy storage technologies, for which batteries emerge as a versatile and efficient option.

Among all battery alternatives, LIB's show a considerable higher performance compared with other storage battery systems. The unparalleled superiority of LIB's over other commercial rechargeable batteries is illustrated in the figure 1-1¹⁷. Here, the **energy density (Wh/kg) and the specific density (Wh/L) corresponds to the amount of electrical energy**, expressed either per unit of weight or per unit of volume, respectively; **they are function of the cell potential (V) and capacity (Ah/kg)**, both of which are linked directly to the chemistry of the system¹⁸.

In addition, LIB systems exhibits an improved, longer cycle of life, negligible self-discharge, less toxicity, stability, and low maintenance cost¹⁹. For these reasons, since their commercialization in the early 1990's by Sony®, Asahi Kasei and Toshiba®²⁰, LIB's have been dominated the market and prompted the progress of electronic devices commercialization; such as, mobile phones, laptops, wearable electronics and digital cameras.

On the other hand, the LIB knowledge is rooted in the studies of intercalation of guest ions into inorganic host materials (developed ca. 40 years ago)²¹. This technology (which will soon blow its 26th candle) experiments a critical moment where a deep understanding of the limits of electrochemical energy storage and developments of advanced materials are still necessary, in order to achieve better performances and to satisfy the requirements in the newly generated markets.

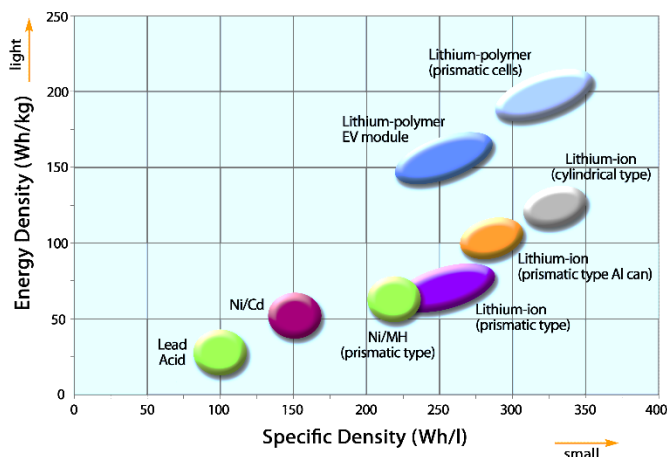


Figure 1-1: Energy density (Wh/kg) vs specific density (Wh/L) for a series of batteries. A battery directed to the consumer electronics market, especially to the electric vehicle market, should be as light (high energy density) and as small (high specific energy) as possible that is, the ideal battery should lay in the upper right corner of the diagram. The figure was modified on basis of reference ¹⁷

The new trends, applications and the battery features/performances relation is an essential subject. Depending on the application field (i.e. portable electronic devices, transportation systems or electrical power storage) factors such as, the energy density, fast charging, safety, cost, power, cycle life and cost play different levels of importance ⁴. Indeed, in the case of mobile devices, it predicts an increase of the power requirement of 20% per year but the real situation is a power advancement of 10% per year ⁴. The request for high performance of LIB's generates strong motivations for the raise of first-rate studies in materials sciences, electrochemistry, crystallography, surface science, microscopy and spectroscopy. New challenges in the fabrication of the LIB's components are critical in order to increase the power capacity, energy density and life cycle.

1.4 LIB components. Cathode: The Holy Grail?

“Electrodes with higher rate capability, higher charge capacity, and (for cathodes) sufficiently high voltage can improve the energy and power densities of Li batteries and make them smaller and cheaper ²²”

As commented in the previous section, the idea of using materials that implement insertion reactions as electrochemically active components began around the 70's. This concept is used for the design of for LIB's, that are classified in two systems. **The first system uses an insertion/intercalation compound** as a positive material and a Li-metal foils as negative electrode (counter-electrode), as depicted in figure

1-2 a). This system is called “*lithium-metal battery*”. *The second system uses two open-structured materials* as electrodes, in which Li^+ ions can be shuttled from one *intercalation compound* (source) to another which receives Li^+ ions and vice versa. This one is called “*lithium-ion battery*”, (see figure 1-2 b). In other words, LIB is based on an intercalation process (reversible process) of introduction-extraction of species, ions or molecules into a layered host structure. On the other hand, the term “*insertion*” refers to the inclusion in tunnel-like frameworks structures. *Insertion compounds* have been classified in various ways, like dimensionality according to the passageway of the guest ions into the host as shown in the figure 1.2-c.

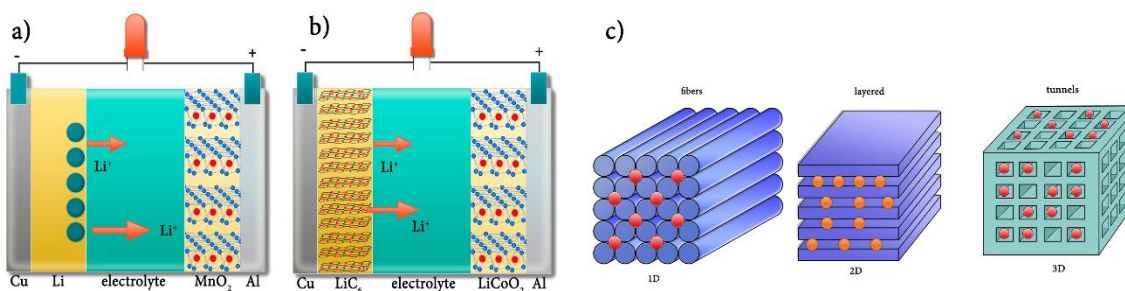


Figure 1-2: Schematic representation of rechargeable LIB's. There are two systems according to the nature of the negative electrode either Li metal (a) or Li insertion compound (b) In both cases, the positive electrode is constituted by an insertion compound, in which the redox reaction occurs at high potential versus Li^0/Li^+ (c) The types of insertion compounds as a function of the dimensionality. Red circles are intercalated ions across the host channels

A *typical LIB is composed by a negative electrode* (anode) which is a material capable of intercalating Li^+ ions or alloying them with metallic Li, most of the times graphite. *The positive electrode (cathode) is a transition-metal oxide (TMO)*. The cathode and the anode are electronically isolated from each other by a porous polyethylene or a thin polypropylene film separator and filled with a *Li ion-conducting organic liquid electrolyte*, as depicted in figure 1.5²³. LIB's are dual intercalation systems, in which both the cathode and the anode have structures that allow reversible insertion and extraction of Li^+ cations. In principle, numerous materials undergo reversible intercalation and can serve as electrode materials. Hence, the chemistry of the LIB is not fixed, unlike the great majority of battery systems²⁴. Finally, the typical electrolyte is a solution of LiPF_6 dissolved in an alkyl carbonate solvent mixture, usually ethylene carbonate (EC), dimethyl carbonate (DMC) or diethyl carbonate (DEC)²⁵. The electrolyte solvents used commonly are in fact unstable below ca. 0.8 V vs Li^+/Li and above ca. 4.5 V vs Li^+/Li in the presence of electrode materials. Depending on their state of charge/discharge, they can be strongly oxidize/reduce²¹.

The operating principle consist of a *swing of Li^+ ions from one electrode to another throughout the electrolyte* that is a good ionic conductor and an electronic insulator. The representation of the

chemical-cell chain of the figure 1-3 is written in the form $\text{Li}_x\text{FePO}_4 \mid \text{LiPF}_6\text{-EC-DMC} \mid \text{Li}_x\text{C}_6$. A fresh cell will be in a discharge state, i.e., at low potential. Thus, in the initial state, the positive electrode framework is full of Li^+ ions (Li_1FePO_4), while the anode is empty (carbon, C-graphite). The electrochemical process implies the transportation of ions and electrons and at the same time, a redox process is carried out. During the charge process, Li^+ ions are released by the positive electrode (anode at this time), migrate across the electrolyte and penetrate the negative electrode (cathode at this time); at the same time, the electrons circulate through an external circuit. The positive electrode is oxidized losing an amount x of electrons ($\text{Li}_{1-x}\text{FePO}_4$) and the negative electrode is reduced capturing x electrons (Li_xC_6). The vice versa reaction occurs for the discharge process.

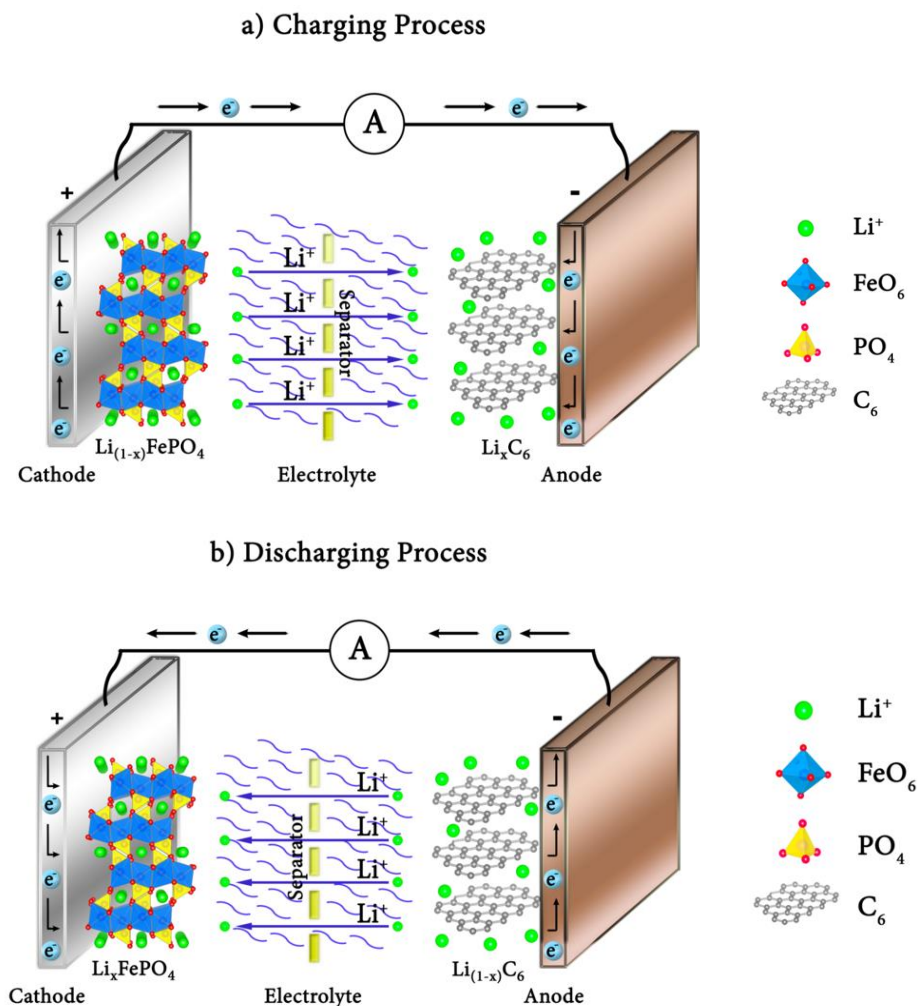
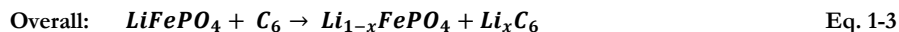
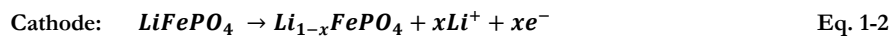
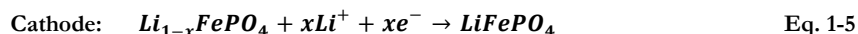
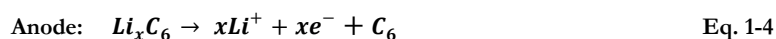


Figure 1-3: Schematic illustration of a typical lithium-ion battery with a cathode material of LiFePO_4 and anode material of graphite

The chemical reactions during the charge processes are expressed as following ²⁶:



During the discharge cycle, de-intercalation of the lithiated graphite (LiC_6) initiates the transfer of Li^+ ions from anode to cathode. The electrons flowing through the external circuit performs the work. The reactions involved during the discharge cycle are presented in Eqs. 1.4 - 1.6.



In other words, in a discharging battery, the cathode is the positive electrode, at which electrochemical reduction takes place. On the other side, the oxidation occurs at the anode. As current flows, electrons from the circuit and cations from the electrolytic solution in the device move toward the cathode. Although these processes are reversed during cell charge in secondary batteries, the positive electrode in these systems is still commonly (if somewhat inaccurately) denoted to as the cathode, and the negative as the anode. Because this terminology is well known throughout the LIB literature, this usage is adopted for most of the publications.

The *open-circuit voltage* V_{oc} is given by the *difference in the lithium chemical potential between the cathode* ($\mu_{Li(c)}$) *and the anode* ($\mu_{Li(a)}$) as follows:

$$V_{oc} = \frac{\mu_{Li(c)} - \mu_{Li(a)}}{F} \quad \text{Eq. 1-7}$$

where F is the Faraday constant. *The cell voltage V_{oc} is determined by the energies involved in both the electron transfer and the Li^+ -ion transfer.* While the energy involved in electron transfer is related to the work functions of the cathode and the anode, the energy involved in Li^+ -ion transfer is determined by the crystal structure and the coordination geometry of the site into/from which Li^+ ions are inserted/extracted ²⁷.

On the other hand, the choice of cathode material significantly affects the performance and cost of a LIB. For example, it is a major determinant of energy density, since it typically has a lower specific capacity than the most common anode material, graphite (372 mAh/g), to which it must be matched ²⁴.

Dillon *et.al*²⁸ reports that a significant fraction in the volume, cost and mass production of LIB's are related to the cathode material and one of the reasons of their importance is due to constitution the sink for the lithium ions. This is considered a fundamental statement for the production and commercialization of LIB's.

On the other hand, cathode materials can be categorized by their crystal structure, voltage versus lithium metal or simple as intercalation/insertion or conversion compounds.

Typically, **2-Volt cathode materials are:** TiS_2 and MoS_2 with 2-D layered structure; **3-Volt cathode materials are:** MnO_2 and V_2O_5 ; **4-Volt cathode materials are:** LiCoO_2 , LiNiO_2 with 2-D layered structure and 3-D spinel LiMn_2O_4 and olivine LiFePO_4 ; **5-Volt cathode materials are:** olivine LiMnPO_4 , LiCoPO_4 , and $\text{Li}_2\text{M}_x\text{Mn}_{4-x}\text{O}_8$ ($\text{M} = \text{Fe}, \text{Co}$) with spinel 3-D structure. **Generally, high cathode voltage is desirable, as stored energy is proportional to the cell operating voltage.** However, electrolyte stability has to be taken into consideration in selecting high voltage cathode materials. The common existing electrode materials ordered by their Li^+ intercalation potentials and crystal structure are summarized in Table 1.1²⁹. In addition, the figure 1-4 shows a suggested road map for the research and development of LIB electrode materials in terms of the achievable voltage and capacity and some of their structures are shown in figure 1-5. Finally, figure 1-6³⁰ present a comparative material life-cycle attributes of some cathode materials, including an important aspect related to the environmental intensity, the subject that is less discussed in the literature.

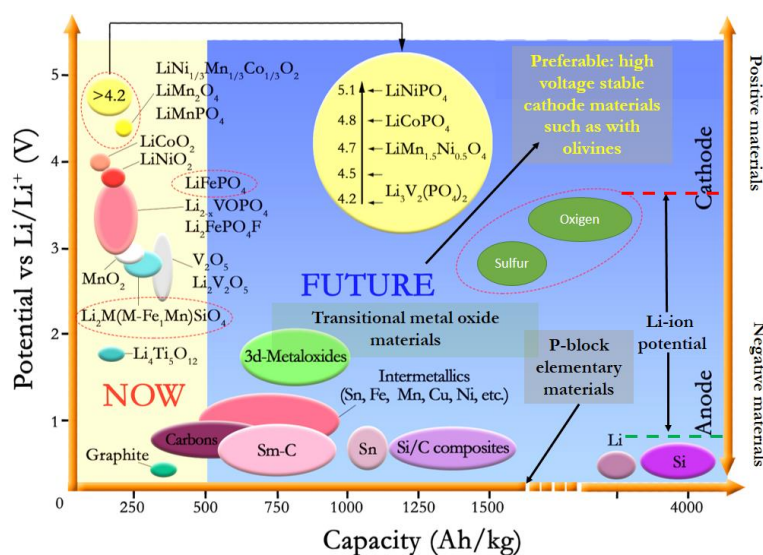


Figure 1-4: Electrode materials and corresponding electrochemical performances in the current LIB technologies. The figure was modified on basis of references^{17 31}

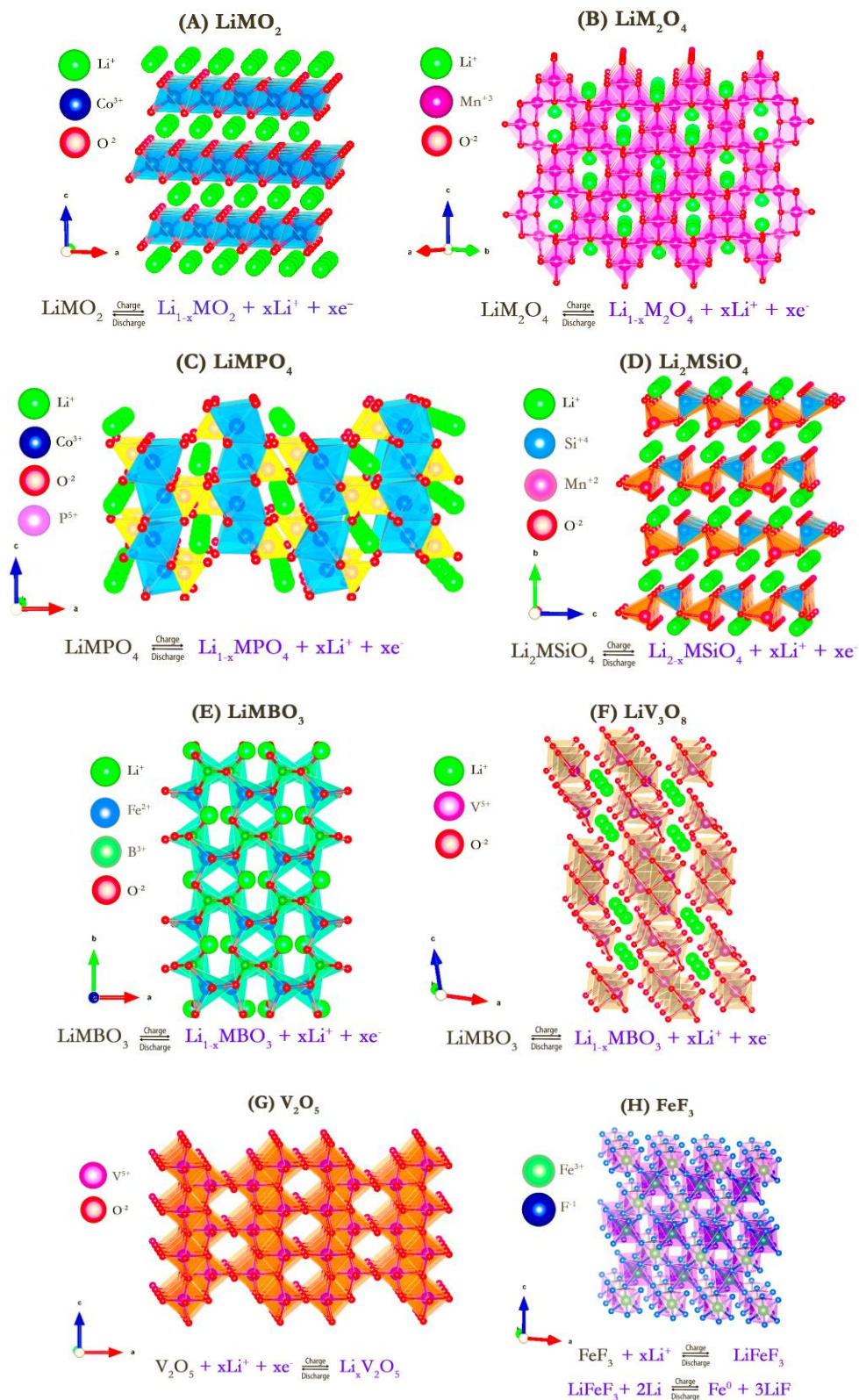


Figure 1-5: Crystal structures and electrochemical reactions of various cathodes: (A) Layered LiMO_2 , (B) spinel LiM_2O_4 , (C) olivine LiMPO_4 , (D) Li_2MSiO_4 , (E) LiMBO_3 , (F) LiV_3O_8 , (G) V_2O_5 , (H) FeF_3

Table 1-1: The voltage of common electrodes, relative to Li metal ³²

	~ 0V	0-1 V	1-2 V	2-3 V	3-4 V	4-4.5 V	> 4.5 V
Alloys	Li	Li alloys, graphite/carbon, Si/SiO ₂ , Sn/son, TCO-1, Si-C, 3M L-20772	Sn-C				
Phosphides		FeP, NiP ₂ , NiP ₃ , Cu ₃ P					
Sulfides		MoS ₂ , MnS, CrS	Co ₉ S ₈ , FeS, Ni ₃ S ₂ , FeS ₂ , NiS, NiS ₂ , Cu ₂ S, CuS, TiS ₂				
Oxides		MnO ₂ , MoO ₃ , NiO, FeO, CoO	Co ₃ O ₄ , CuO, Cu ₂ O		MnO ₂ , V ₂ O ₅ , LiV ₃ O ₈		
Layered oxides					Li ₄ Mn _{1-y} M _y O ₂ [M = Cr, Co, ...], Li _{1-x} Ni _{1+y} Co _y M ₂ O ₄ [M = Mg, Al, ...]		
Spinel oxides			Li ₄ Ti ₃ O ₁₂		LiMn ₂ O ₄		LiMn _{1.5} Ni _{0.5} ° ₄ , LiMn _{1.45} Ni _{0.55} Cr _{0.1} ° ₄ , LiMn _{1.5} Cr _{0.5} ° ₄ , LiMn _{1.5} Cu _{0.5} ° ₄ , LiCrMnO ₄ , LiCoMnO ₄ , LiFeMnO ₄
Fluorides		VF ₃ , TiF ₃	CrF ₃ , NiF ₂ FeF ₃	CoF ₂	CuF ₂		
Borates				LiFeBO ₃			
NASICON phosphates			Li ₃ TiNb(PO ₄) ₃ Li ₃ V ₂ (PO ₄) ₃	Li ₃ TiNb(PO ₄) ₃ Li ₃ Ti ₂ (PO ₄) ₃ Li ₄ FeTi(PO ₄) ₃ , Li ₃ FeTi(PO ₄) ₃ Li ₃ Fe ₂ (PO ₄) ₃	Li ₃ V ₂ (PO ₄) ₃	LiV ₂ (PO ₄) ₃	
Olivine phosphates					LiFePO ₄ , Li _{1-x} Fe _{2x/3} PO ₄	LiMnPO ₄	LiCoPO ₄ , LiNiPO ₄ , LiNVO ₄
Hydrated phosphates				P-LiFePO ₄ ·2H ₂ O, S-LiFePO ₄ ·2H ₂ O, M-LiFePO ₄ ·2H ₂ O			
Diphosphates and diarsenates			Li ₂ VP ₂ O ₇	Li ₂ FeP ₂ O ₇ Li ₂ FeAs ₂ O ₇	Li ₄ Fe ₄ (P ₂ O ₇) ₃ ·4H ₂ O, Li ₄ Fe ₄ (P ₂ O ₇) ₃	Li ₃ V ₃ (P ₂ O ₇) ₃ (PO ₄) ₂	LiCrP ₂ O ₇ , LiMn ₂ O ₇ , LiFeP ₂ O ₇ , LiCoP ₂ O ₇
NASICON sulfates				Li ₂ V ₂ (SO ₄) ₃	Li ₂ Fe ₂ (SO ₄) ₃		
Marinite					Li ₂ Fe(SO ₄) ₂		
Other NASICON					Li ₂ Fe ₂ (MoO ₄) ₃ Li ₂ Fe ₂ (WO ₄) ₃ , Li ₃ Fe ₂ (SO ₄) ₂ PO ₄		
Anti-NASICON				Li ₃ Fe ₂ (PO ₄) ₃ , Li ₃ Fe ₂ (AsO ₄) ₃	Li ₂ Fe ₂ (PO ₄) ₃		
Fluoro-			Li ₂ VPO ₄ F	Li ₂ FePO ₄ F	LiZn _{0.1} Fe _{0.9} SOF LiFeSO ₄ F, Li ₃ V(PO ₄) ₂ F ₂	LiVPO ₄ F	LiCoPO ₄ F, LiCrPO ₄ F, LiMnPO ₄ F, LiFePO ₄ F
Hydroxy-				Li ₂ FePO ₄ (OH)		LiFeSO ₄ (OH)	LiCoPO ₄ OH, LiCrPO ₄ OH, LiFePO ₄ OH
Oxy-				Li ₂ VPO ₄ O	LiVPO ₄ O, e-LiVPO ₄ O, LiVPO ₄ O·H ₂ O, LiVPO ₄ O·2H ₂ O	Li ₃ VO(PO ₄) ₂ , Li ₂ VO(HPO ₄) ₂ , LiVO(H ₂ PO ₄) ₂ , Li ₂ VOP ₂ O ₇ , LiVOAsO ₄	

Material Type			Intercalation					Conversion			
			Layered		Olivine		Spinel	Chalcogenide			
Material			NCA	NMC	LCO	LMR	LFP	LVP	LMO	Sulfur	Lithium Sulfide
Environmental intensity of material	Intrinsic	Exposure risks and hazards	Red	Red	Yellow	Red	Green	Red	Yellow	Green	Red
		Scarcity	Yellow	Yellow	Red	Yellow	Green	Yellow	Green	Green	Yellow
	Value chain	Damages to human health	Yellow	Yellow	Yellow	Yellow	Green	Yellow	Green	Green	Yellow
		Damages to ecosystems	Yellow	Yellow	Yellow	Yellow	Green	Yellow	Green	Green	Yellow
Material and weight efficiency	Intrinsic	Energy density	Yellow	Green	Yellow	Green	Red	Yellow	Yellow	Green	Green
		Power density	Green	Green	Green	Green	Yellow	Red	Green	Green	Green
		Lifetime and Stability	Green	Red	Red	Red	Green	Yellow	Green	Red	Yellow
		Recyclability	Green	Green	Green	Green	Green	Green	Green	N/A	Yellow
	Value chain	Synthesis material Losses	N/A	Red	Yellow	White	Green	Green	Green	Red	Red
Energy efficiency	Intrinsic	Device efficiency	Green	Red	Yellow	Red	Yellow	Red	Green	Red	Yellow
	Value chain	Energy of nanosynthesis	N/A	Red	Yellow	Red	Yellow	Yellow	Yellow	Green	Yellow

Figure 1-6: Cathode materials for LIB's. Background colours reflect characteristics of bulk materials. Green denotes relative strength, red relative weakness, yellow intermediate characteristics and white no data. Absence of circle (○) indicates no data for the material. The grey background denotes the 'baseline' material use for comparison. **NCA:** lithium nickel cobalt aluminium oxide; **NMC:** lithium nickel manganese cobalt oxide; **LCO:** lithium cobalt oxide; **LMR:** lithium/manganese rich transition metal oxide; **LFP:** lithium iron phosphate; **LVP:** lithium vanadyl phosphate; **LMO:** lithium manganese oxide.

Altogether, several criteria must be satisfied by the *lithium insertion compound* - " $\text{Li}_x\text{M}_y\text{X}_z$ " (or intercalation material) to be successful as a cathode material in a rechargeable LIB. Some of the most important conditions^{33,34} are:

- Easy and reversible reduction/oxidation of transition metal ion presented in the cathode material.

-
- The cathode should have a low-lithium chemical potential ($\mu_{Li(c)}$) and the anode should have a high-lithium chemical potential ($\mu_{Li(a)}$) to maximize the cell voltage (V) and hence energy density. This implies that the transition metal ion M^{n+} in the Li_xMyX_z should have a high oxidation state to serve as a cathode and a low oxidation state to serve as an anode.
 - The Li_xMyX_z should allow an insertion/extraction of a large amount of lithium per unit weight or per unit volume to maximize the cell capacity (Ah/L or A h/kg). This depends on the number of lithium sites which are available in the lithium insertion/extraction host. A combination of the high capacity and the cell voltage can maximize the energy density (Wh/L or Wh/kg), which is given by the product of the cell capacity and cell voltage.
 - The lithium insertion compound should support both high-electronic conductivity (σ_e) and high- Li^+ conductivity (σ_{Li^+}) to facilitate fast charge/discharge (rate capability) and offer high-power capability, i.e., it should support mixed ionic–electronic conduction. This depends on the crystal structure, arrangement of the $M-X$ polyhedra, geometry, interconnection of the lithium sites, nature, and electronic configuration of the M^{n+} ion, and the relative positions of the M^{n+} and X^{n-} energies.
 - High structural stability of the cathode material to enhance cycle life, without breaking any $M-X$ bonds. The Li_xMyX_z should support a reversible insertion/extraction of lithium with no or minimal changes in the host structure over the entire range of lithium insertion/extraction in order to provide good cycle life for the cell.
 - The Li_xMyX_z must be thermally and chemically stable without undergoing any reaction with the electrolyte over the entire range of lithium insertion/extraction process.
 - The redox energies of the cathode and anode in the entire range of lithium insertion/extraction process should lie within the bandgap of the electrolyte, as shown in Fig. 1-7 to prevent any unwanted oxidation or reduction of the electrolyte.
 - The Li_xMyX_z should be cheap, must be environmentally friendliness and be lightweight from a commercial point of view. This implies that the M^{n+} ion should preferably be from the 3d transition series.

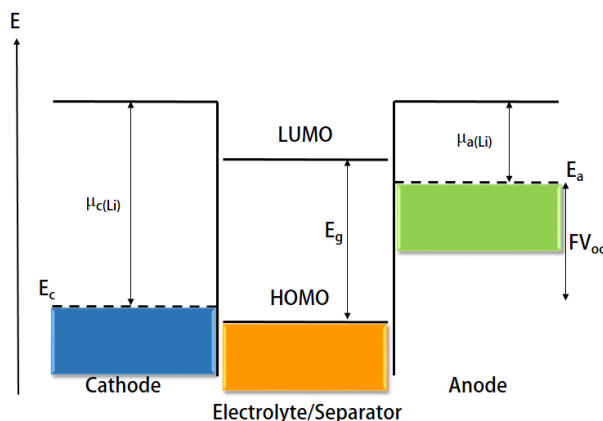


Figure 1-7: Schematic energy diagram of a lithium cell at open circuit. HOMO and LUMO refer, respectively, to the highest occupied molecular orbital and lowest unoccupied molecular orbital in the electrolyte.

1.5 Phospho-olivines: The LiCoPO_4 option

“The use of lithiated frameworks has revolutionized the concept of lithium rechargeable batteries for high-power sources applied to hybrid electric vehicles (HEVs) and plug-in hybrid electric vehicles (PHEVs)”³⁵

Among all materials presented in the last section, the most widely used in commercial LIB are the 3.5–4 V (versus Li metal) LiCoO_2 (layered), LiMn_2O_4 (spinel) and LiFePO_4 (olivine). These active materials have experimental capacities of 150, 120 and 160 mAh/g, respectively³⁶.

In the case of the **LiCoO_2 (layered)** their main problems are related with to its structural stability. LiCoO_2 presents two different structures depending of on the synthesis temperature: around 350 °C the structure is a cubic spinel and around 750 °C a layered trigonal³⁷. The layered structure shows better electrochemical performance compared with the cubic spinel lattice. In fully lithiated state, the layer structure of LiCoO_2 is retained. During charging, Li^+ is removed from the layered crystal lattice, nonstoichiometric $\text{Li}_{1-x}\text{CoO}_2$ compounds are formed and the oxidation from Co^{2+} changes to Co^{3+} for charge compensation. Indeed, after 50 % of the lithium has been extracted from the parent structure, the structural transformation from hexagonal to monoclinic phase is observed. This intrinsic structural instability reduces the electrochemical capacity from a theoretical value of 280 mAh/g to 140 mAh/g. On the other hand, the iso-structural LiNiO_2 was proposed³⁸; however, during synthesis, it is very

difficult to restrict the migration of Li⁺ ions to the transition metal layers and vice versa (called the Li/Ni disorder), which pulls down the electrochemical performance³⁹. Furthermore, its poor thermal stability in contact with organic solvents at the charged state prohibits its practical use⁴⁰. In addition, the working potential of LiNiO₂ is slightly lower (≈ 3.8 V) than LiCoO₂ but its lithium diffusion coefficient is higher (6×10^{-6} cm² s⁻¹)³⁴.

The **LiMn₂O₄ (spinel)** has low cost, is environmentally friendly and safer alternative compared with to LiCoO₂⁴¹. In this case, the unique MnO₂ framework in the structure provides a three-dimensional (3D) diffusion pathway for Li⁺ ions without collapsing the M₂O₄ spinel framework⁴². The ionic and electronic conductivities are of the order of 10⁻⁶ and 10⁻⁴ S cm⁻¹⁴³. Despite this good features, the experimental capacity only reaches 100-120 mAh/g. The reasons of this capacity fade are: **first**, the dissolution of Mn²⁺ due to a disproportionation ($2\text{Mn}^{3+} \rightarrow \text{Mn}^{2+} + \text{Mn}^{4+}$) in the electrolyte²¹; **second**, the irreversible structural transformation from a spinel (cubic) to tetragonal structure due to the presence of Jahn-Teller active Mn³⁺ ions leading to a asymmetric lattice distortion during lithiation/delithiation process⁴⁴. In order to stabilize and improve the capacity of LiMn₂O₄, partial cationic or anionic substitutions^{45,46} (Ni, Al, F, etc) or surface modification have been done using coating procedures with inert materials such as Al₂O₃, AlPO₄, AlF₃, ZrO₂ have been done⁴⁷⁻⁴⁹. However, only limited success was achieved since the amount of impurities or secondary phases are difficult to be controlled during synthesis.

The **olivine LiFePO₄** has been considered as *promise cathode material* due to its low cost, abundant availability, low toxicity, low volume expansion, relatively high specific capacity, low capacity fade, and high safety⁵⁰. Since the work of Padhi *et al.*⁵¹ where he reported that Li⁺ ions can be extracted reversibly from olivine LiFePO₄ at ca. 3.5 V vs Li⁺/Li, this positive electrode has received considerable attention from the scientific community. This cathode material has led to the commercialization, and it is widely described in several reviews⁵²⁻⁵⁴ and patents⁵⁵⁻⁵⁷. LiFePO₄ belongs to the family of the lithium transition-metal orthophosphates with the sum formula LiMPO₄ ($M = \text{Fe, Mn, Co, Ni}$) or simply LMP (LFP, LMP, LCP, LNP). The olivine-type LMP crystallizes rhombohedral and it is represent by the space group *Pnma* (No 62). The Li, *M* and P atoms occupying octahedral 4*a*, octahedral 4*c*, and tetrahedral 4*d* sites respectively and the oxygen atoms are localized in a slightly distorted, hexagonal closed-packed (*hcp*) arrangement⁵⁸. Layers of MO₆ octahedra are corner-shared in the *bc* plane and linear chains of LiO₆ octahedra are edge-shared in a direction parallel to *b*-axis. These chains are bridged by edge and corner shared PO₄ tetrahedra, creating a stable three-dimensional structure. In this material, the frameworks made of PO₄ units provide a highly stable three dimensional network owing to the strong covalent nature of the P-O bonds⁵¹. This eliminates the possibility of oxygen liberation and hence improves the operational safety of batteries⁵⁹. However, the separation of the MO₆ octahedra by PO₄ polyanions

significantly reduces the electronic conductivity ($\sim 10^{-9}$ S/cm at room temperature)⁶⁰. A representation of the olivine structure is shown in the figure 1.8. On the other hand, one of the main drawbacks is the low electrical conductivity also results from the slow 1D migration of Li^+ ions limited by the *hcp* oxygen atoms⁴¹.

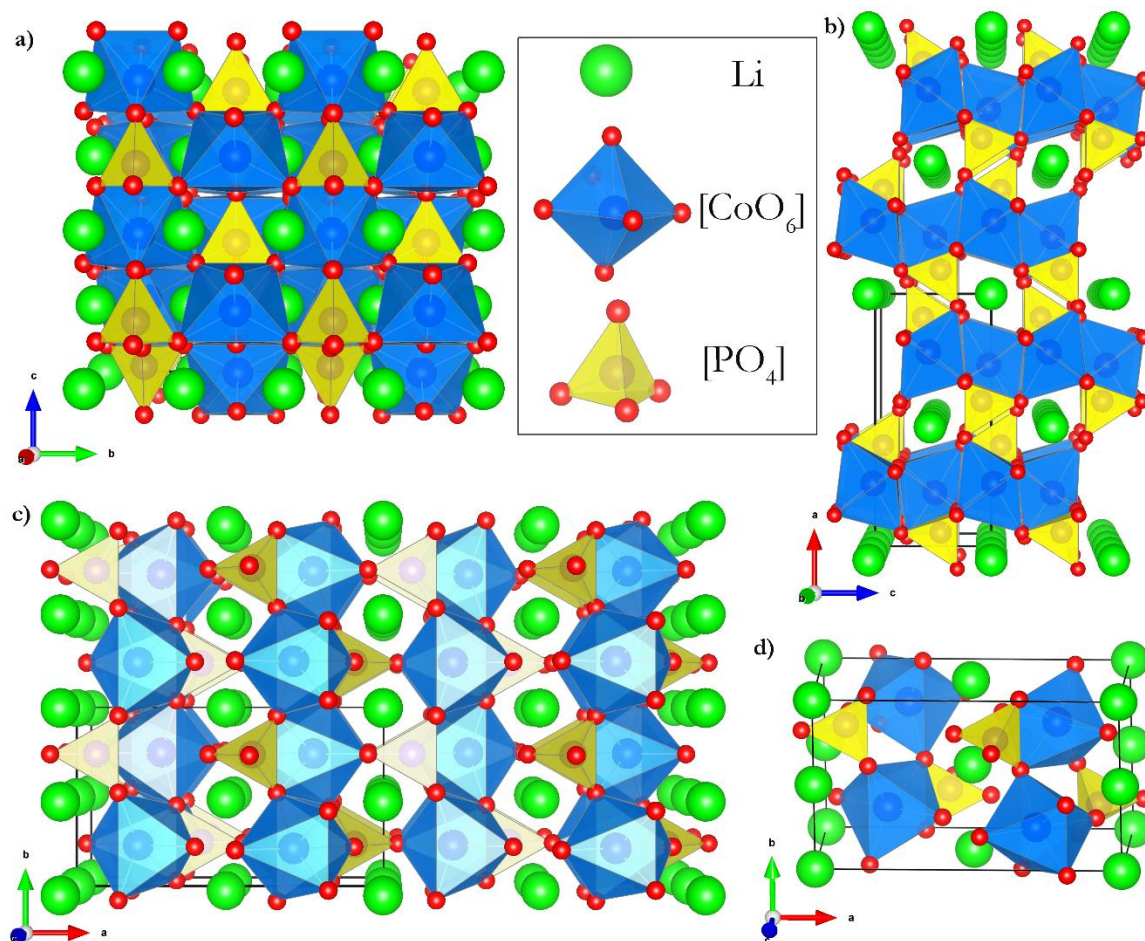


Figure 1-8: Crystal structure of LiMPO_4 (LMP) $Pnma$: $[\text{MO}_6]$ with $M = \text{Co}$. **a)** Projection along a -axis **b)** Projection along b -axis **c)** Projection along c -axis. **d)** Alternative projection to see the corner shared octahedral between $[\text{CoO}_6]$ and $[\text{PO}_4]$ units. Octahedra are drawn in blue, $[\text{PO}_4]$ tetrahedra in yellow, Li^+ ions in green and O^{2-} ions in red

In order to overcome the issues regarding of low conductivity in the case of LFP, three main methods have been adopted: reduction of particle/grain size, apply of conductive layer (coating) and doping with other polyvalent cations. Synthesis of nano-sized LFP particles resulted in the improvement of lithium and electron diffusion due to shorter path length⁶¹⁻⁶³. Equally important, carbon coating is the most efficient method to increase the electronic conductivity of LFP⁶⁴. This can be improved from 10^{-9} S/cm to 10^{-2} S/cm⁶⁵, allowing LFP to deliver excellent rate capability at room temperature⁶⁶. Finally, several

metal ions such as Mg^{2+} , Ni^{2+} , Co^{2+} , Al^{3+} , Ti^{4+} , Zr^{4+} , Nb^{5+} and W^{6+} , improving the electrical conductivity by a factor of $\approx 10^8$ ⁶⁰.

Similarly, **LiCoPO₄ (LCP)** could potentially impart gains in performance because the tailoring system chemistry is comparable to LFP; in fact, *it incorporates the advantage of work at higher potential, with larger theoretical performance and reduced cobalt weight fraction per formula unit compared to the commercial LiCoO₂* ⁶⁷. As a consequence, if compared with LFP and LNMO, larger raw material costs are counterbalanced and the resulting energy cost is greatly reduced ^{68, 69}. Indeed, the cost/performance ratio is comparable with the spinel $\text{LiNi}_{0.5}\text{Mn}_{0.5}\text{O}_4$ (see table 1.2 ⁶⁸).

Table 1-2: Properties of the LFP, LMP, LCP and LNP olivine compounds compared with other cathode materials currently used in LIB's ⁶⁸

Cathode materials	Discharge voltage vs. Li (V)	Theoretical capacity (mAhg ⁻¹)	Density (g cm ⁻³)	Energy cost US\$ kWh ⁻¹ US\$ 18650 cell vs. graphite (LP30 electrolyte) ^a
LiFePO ₄	3.4	160	3.6	158
LiCoO ₂	3.6	137	5.1	198
LiAl _{0.05} Co _{0.15} Ni _{0.8} O ₂	3.6	265	4.7	158
LiMn ₂ O ₄	3.9	117	4.2	168
LiMnPO ₄	4.1	171	3.4	150
LiNi _{0.5} Mn _{1.5} O ₄	4.7	146	4.4	141
LiCoPO ₄	4.8	167	3.7	142
LiNiPO ₄	5.1	167	3.9	123

^a LP30 electrolyte: 1 M LiPF₆ in 1:1 w/w ethylene carbonate/dimethyl carbonate

1.6 Kinetically controlled routes of synthesis: Polyol assisted

Considering the features mentioned above, LCP olivine is *technically able to improve*, or, in other words, the material allows a broad range of exploration in order to improve its electrochemical performance. Now, the discussion is focused on the importance of the synthesis routes of olivine materials. Briefly, the methods can be classified in two groups: **solid state** methods and **solution-based** methods. Solid state synthesis, mechano-chemical activation, carbothermal reduction and microwave heating are based on solid state chemistry and are the most common **solid state methods** for preparing LiMPO₄ powders. Fig. 1.9 ⁷⁰ presents the basic steps involved in these routes. They are important in terms of obtaining ordered crystal structure in a simple way at elevated temperatures, high reproducibility and relative easiness of control of secondary phases. However, as expected of solid state routes, the particles are strongly agglomerated, inhomogeneous in shape, size and typically are highly time and energy consuming ⁶⁷. Equally important, **solution-based or wet chemical methods** group

hydrothermal/solvothermal synthesis, sol-gel synthesis, spray pyrolysis, coprecipitation, microemulsion drying, microwave-assisted method and polyol. General synthesis steps are shown schematically in Fig. 1.10⁷⁰. In general, wet chemical methods often result in smaller and uniform particle size, more possibilities for morphology control and decrease in annealing times and temperatures.

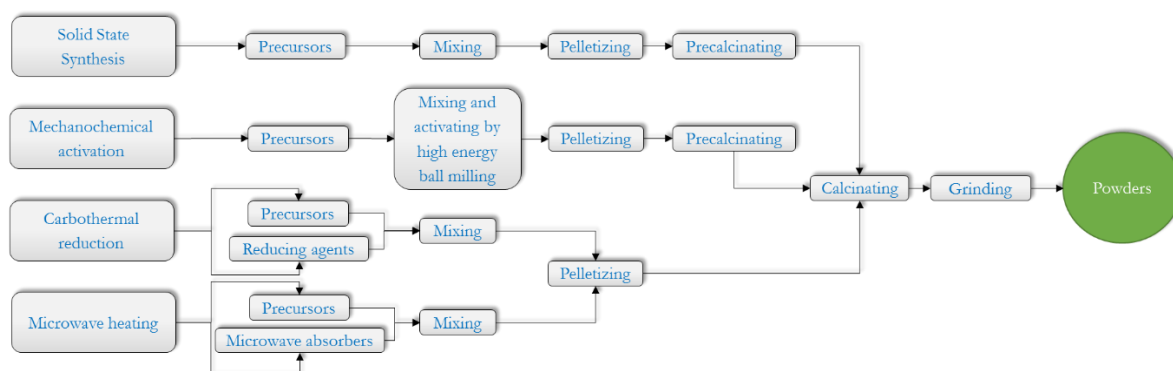


Figure 1-9: Typical routes for producing LMPO₄ powders using solid state methods. Adapted from⁷⁰

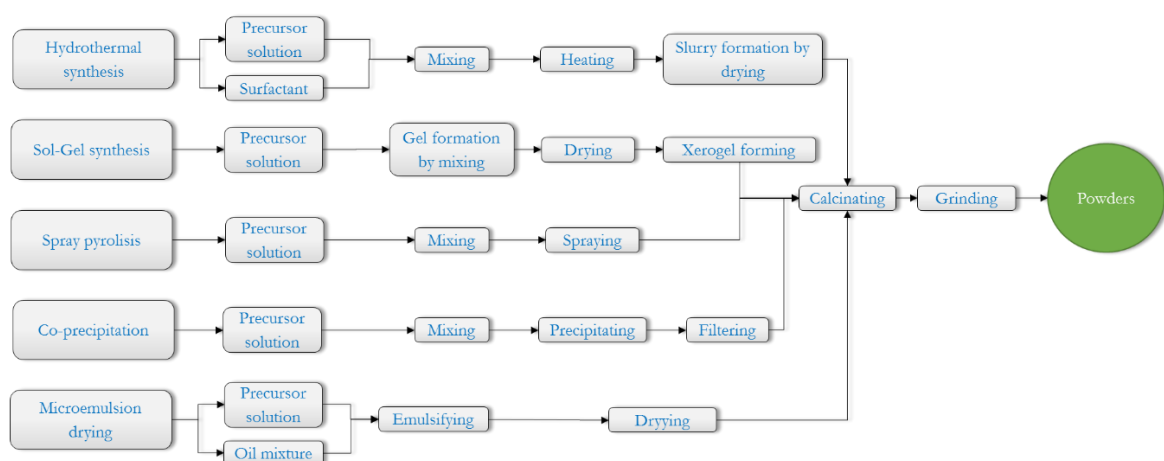


Figure 1-10: Typical routes for producing LiMPO₄ powders using solution based methods. Adapted from⁷⁰

In case of LCP, different synthesis routes have been implemented. A resume of them with reported lattice parameters and temperatures used for annealing process are presented in the table 1-3. In this table, *the first point to remark* is the fact that *cell constants show slight variation depending on the synthesis route* and synthesis conditions; such as, chemical nature of the precursors, duration of the annealing, annealing atmosphere, heating rates, dynamic or static annealing flow and chemical characteristics of the intermediates. Although, the change in lattice parameters does not represent a

strong difference with reported single crystal, the synthesis parameters can also be responsible for the chemical, morphological and electrochemical features.

Table 1-3: Lattice constants reported for LiCoPO₄⁶⁷ by different synthesis routes

Synthesis	Annealing conditions		Lattice constants (Å)			Ref	
	Gas	Temperature (°C)	<i>a</i>	<i>b</i>	<i>c</i>		
Solid State	Air	750	10.202	5.922	4.699	71	
			10.206	5.926	4.706	72	
			10.188	5.904	4.701	73	
	Air	850	10.24	5.97	4.72	74	
		Microwave heating	10.205	5.925	4.702	75	
		Ar	600	10.196	5.919	4.697	76
		650	10.209	5.923	4.716	77	
		N ₂	750	10.192	5.917	4.695	78
		800	10.195	5.920	4.698	79	
		450	10.203	5.921	4.699	80	
Wet Chemistry	Air	500	10.193	5.913	4.687	81	
		10.205	5.921	4.700	80		
		600	10.206	5.923	4.701	80	
		400	10.187	5.918	4.696	82	
		10.201	5.923	4.700	83		
Sol-Gel	Air	600	10.195	5.918	4.692	84	
		10.194	5.925	4.698	85		
		700	10.195	5.914	4.699	85	
		800	10.2	5.91	4.73	86	
		10.180	5.901	4.703	85		
		850	10.286	5.927	4.726	85	
		Ar	700	10.202	5.921	4.700	86
		200	10.206	5.923	4.701	87	
Spray-Pyrolysis	N ₂ /3% H ₂	300	10.21	5.95	4.7	88	
		10.206	5.922	4.700	87		
		400	10.203	5.921	4.701	87	
		500	10.202	5.924	4.700	87	
		N ₂ /5% H ₂	700	10.199	5.921	4.700	89
Molten salt ^a	Ar	900	10.150	5.90	4.70	90	

^a Single crystal

The second point is the fact that all synthesis reported in the table (solid state and solution-based) **request the use of an annealing procedure or final thermal treatment** that allows to obtain the final olivine structure. Since the use of this annealing temperatures induces process of particle growth and particle inhomogeneity, a direct methodology where the olivine phase could be achieved after the mixing of the precursor will be ideal. The answer to this statement is give by the **polyol synthesis route**; this procedure has been widely used for synthesis of lithium metal phosphates, such as LFP⁹¹⁻⁹⁷, LMP⁹⁸⁻¹⁰¹ and LNP¹⁰², resulting in nano-particles, with discrete particle size distribution and values with the capacity of over 120 mAhg⁻¹. The polyol process involves the reduction of inorganic compounds in liquid polyols. Polyols were either polyhydric alcohols like α -diols; such as, 1,2-ethanediol (ethylene

glycol), 1,2-propanediol (propylene glycol) or ether glycol namely di(ethylene) or tri(ethylene glycol). The solid precursor (nitrate, carbonate, phosphate, chloride, acetate, oxide, hydroxide) is dissolved in the polyol and further stirred and heated to a given temperature. Polyols are interesting among non-aqueous solvents because like water and monoalcohols, because they are hydrogen-bonded liquids with a high value of relative permittivity; therefore, they are able to dissolve ionic inorganic compounds. Equally important, owing to their chelating properties, they are coordinating solvents which can form complexes with many metal cations. Consequently, they can form reactive intermediate species on the one hand, and on the other hand they can adsorb onto the surface of the growing particles preventing aggregation¹⁰³.

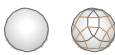
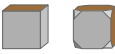
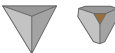
Briefly, the main advantages of this technique are:

- The electrode material can be synthesized at a low temperature without performing an additional heat treatment annealing process¹⁰⁴.
- Synthesis of a high crystalline material with uniform particle size from micrometers until to nanometers size⁵⁶.
- Since alcohols are ineffective protecting agents, polyols are used because they contain a larger number of hydroxyl groups per molecule, which effectively chelate (multiply coordinate) the metal ions. This allows metal ions to remain in their reduced form¹⁰⁵.
- Polyol-mediated methods are of great importance as they allow large scale synthesis, and most importantly the shape and size of the particles are easy to control by adjusting the ratio of reactants¹⁰⁶.
- Since the additional heat treatment process is not necessary, the production process is simplified, the manufacturing cost of the electrode material is decreased and the environmental pollution generated during the process is reduced¹⁰⁷.

An important remark is the fact that this technique is frequently use to modify the morphology of several materials. The table 1-4 shows some examples of the morphology obtained in the synthesis of silver nanoparticles using a polyol process. On the other hand, the final morphology also depends on the ***hydrolysis ratio h***, defined as the ratio between the amount of water added in the polyol and the amount

of metal involved as exemplified for cobalt in the publication of Poul *et. al.* ¹⁰⁸. Finally, the morphological characteristics of the final particles, i.e., size, shape and degree of aggregation depend upon the kinetic of two steps: growth and nucleation. In such a case, the precipitation of particles and tune of morphologic characteristics are controlled by experimental parameters, such as nature of reactants, concentration of the solid precursor, nature of the polyol, continue injection of it, temperature ramping and duration of the reaction. As polyols are able to control the growth of the particles, in order to extend their agglomeration it may be useful to use surfactants or polymeric protective agents such as poly (vinylpyrrolidone) (PVP) ¹⁰⁹, citric ¹¹⁰ or lauric ¹¹¹ acid or SDBS ¹¹⁰. This promotes heterogeneous nucleation, providing an efficient tool to steer the average size of spherical particles in a large size range and in other particular cases, obtaining another shapes such as nanorods¹¹², nanoplates¹¹³ and nanowires¹¹⁴.

Table 1-4: Summary of the shapes and methods for synthesis of Ag nanoparticles using polyol synthesis ¹¹⁵

Shape	Illustration	Method of synthesis
Sphere and quasisphere		Polyol process (single-crystal); Citrate reduction (quasisphere)
Cube and truncated cube		Polyol process; seed-mediated growth
Tetrahedron and truncated tetrahedron		Polyol process. light-mediated growth
Octahedron and truncated octahedron		Polyol process; seed-mediated growth; light-mediated growth
Bar		Polyol process
Spheroid		Polyol process
Right bipyramid		Polyol process
Beam		Polyol process
Polygonal plates and disc		Light-mediated growth; polyol process

1.7 Design of cathode materials: trends and remarks

In order to enhance the electrochemical performance of electrode materials, various strategies have been used which are resumed in the figure 1.11. They are common among all kind of cathode materials

investigated and often similar regardless of type of material, crystal structure, or operating mechanism. The figure presents the broadly categorized strategies and the advantages of their implementation.

In case of dimension reduction the use of nano-sized or nano-structured materials may shorten the pathways for the electrons and Li^+ transport to electrochemical reaction sites which can ameliorate the naturally low electronic and ionic conductivities and thus increase their power performance, improve their energy efficiency and reduce voltage hysteresis ¹¹⁶.

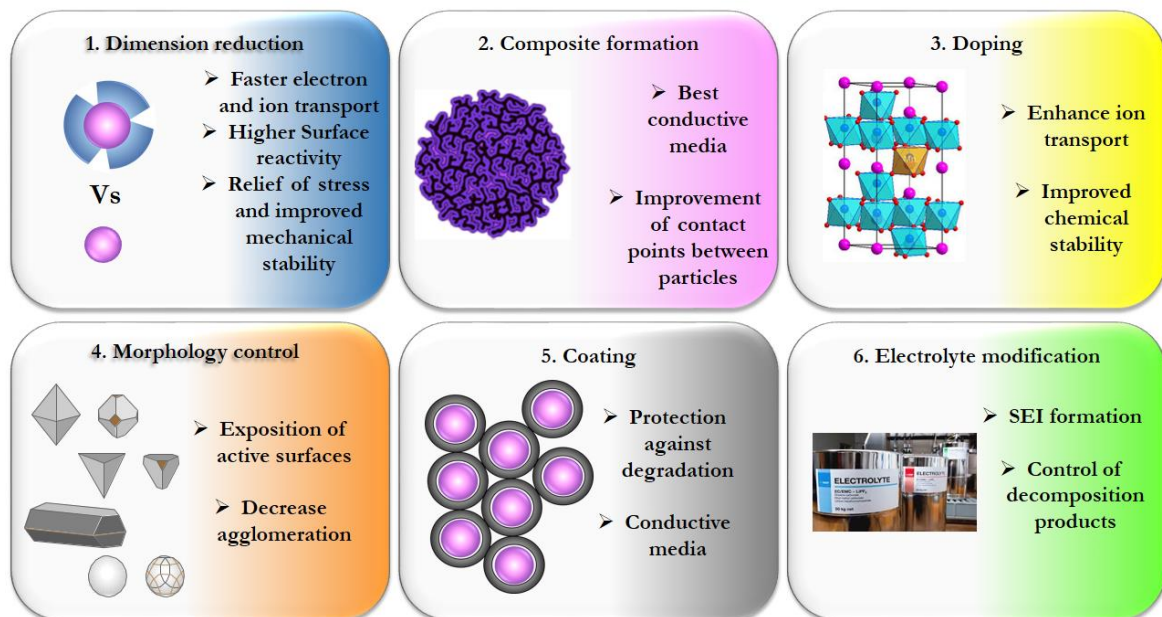


Figure 1-11: General strategies for performance enhancement and their rationale: 1 reducing dimensions of active materials, 2 formation of composites, 3 doping and functionalization, 4 tuning particle morphology, 5 formation of coatings or shells around active materials, 6 modification of electrolyte

Besides, the formation of hybrid nano-composites in combination with functional media that enhance electrical conductivity, mechanical stability and other performance metrics (e.g., reduced dissolution) has been done using conductive carbons, including, carbon blacks, graphene, carbon nanotubes (CNT's), carbon fibers, micro and mesoporus carbons which showed visible electrochemical improvements ^{3, 63, 117-121}.

A factor to be considered while designing new electrodes is the **architecture or arrangement** of the active material. Most of currently available commercial LIB electrodes are formed as thin films in the order of hundreds of microns thick. These films often consist of polymer-based binders, active-material powder and additives that allow to increase electric conductivity of the electrode. The geometric considerations of the electrode design are important in the light of inherent limitations of the charge

transport characteristics. This is a consequence of the formation of bottlenecks during the lithium diffusion from the surface of the active material that impedes additional ion transport.

In this sense, the structure of the electrodes, their thickness and the length of diffusion pathways play an important role in the ionic mobility and limit the batteries to slower rates than could otherwise be possible. For these reasons, 3-dimensional (3D) porous electrode architectures have attracted a lot of attention particularly because battery size and mass are expected to be reduced in next generation power systems without reduction in energy density ¹²². Another way to improve the electrochemical performance is the doping procedure by aliovalent substitutions using ions such as Mg^{2+} , Cu^{2+} , Zr^{4+} and Cr^{2+} . In case of LFP, aliovalent solutes from 2+ through to 5+ valences are readily accommodated in the olivine lattice, especially when the overall composition is formulated to allow the simultaneous introduction of cation vacancies for charge compensation ^{123, 124}.

1.8 Motivation: scope and objectives of this thesis

As presented in the section 1.5, due to the high energy density and high theoretical capacity of LCP, it is considered as potential cathode material for LIB's. Thus, the motivation and goals of this work are:

- a. The ***principal objective*** of this work ***is the synthesis of LCP-Pnma by polyol synthesis*** attempting to obtain a material with good electrochemical performance (cycle stability and high capacity at high rates).
- b. ***Synthesize LCP-Pnma with high crystallinity, small particle size (nm range) and a discrete range of particle distribution.*** This is important in order to obtain high capacity at high C-rates. To achieve this, the ideal polyol process should be performed in a single-step procedure to avoid the use of any further annealing procedures or thermal treatments.
- c. Use a systematic approach in order to ***explore the influence of synthesis conditions*** (time (reflux time), temperature, educts source) to analyze their influence ***in crystalline and morphologic characteristics of the material obtained*** as well as in the control of secondary phases.
- d. ***Complement the study with additional synthesis methods*** that can be found along the research process and support the synthesis of LCP-Pnma by the ***adaption of synthesis methods reported for other metal orthophosphates (LMPO₄).***

1.9 Methodology

The methodology of the synthesis is described in the chart presented in figure 1.12. As defined in the motivation, the work is focused on the synthesis of the LCP. This was made at laboratories of Prof. Dr. Tom Nilges and Prof. Dr. Bernhard Rieger.

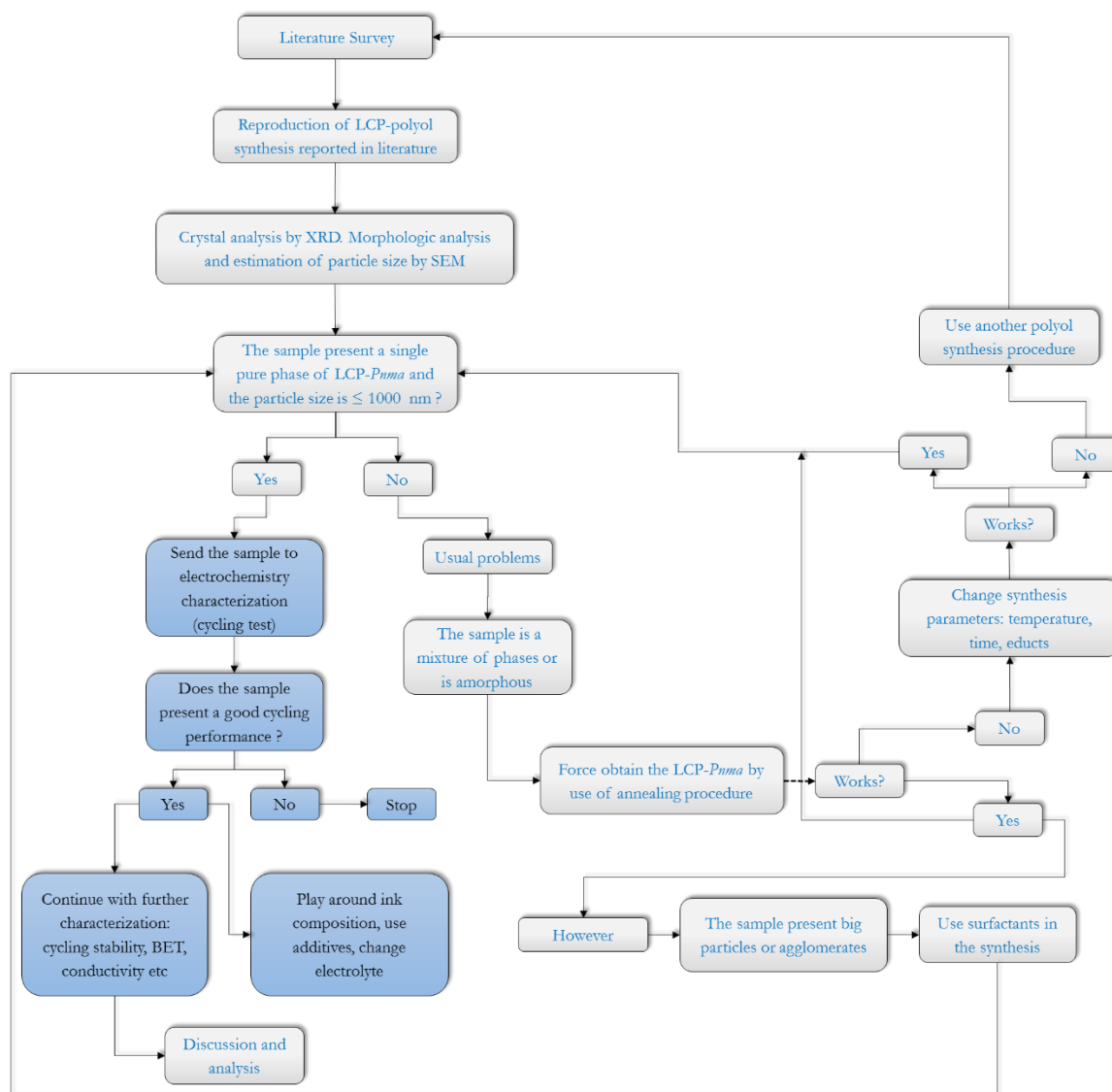


Figure 1-12: Flowchart of the methodology implemented for the synthesis of LCP. The blocks in blue represent part of the scope of the project.

2. Experimental procedures

This section begins with the literature survey regarding the synthesis of LCP-*Pnma* by polyol synthesis. Then, the list of the educts used is depicted. Next, the detailed explanation of the different polyol synthesis used for the obtaining of LCP-*Pnma* is described in detail. Complementary synthesis routes of LCP-*Pnma* such as microwave-assisted polyol and acetate-assisted antisolvent precipitation (AAAP) method are explained. Finally, the polyol synthesis of LFP polymorphs is also included.

2.1 Summary of LCP-*Pnma* synthesized using polyol method

Up to 2012 few reports about the synthesis of LCP using polyol method have been published. The Table 2-1 presents a review of the literature found in the beginning of the project for LCP-*Pnma* using polyol synthesis. The starting point of this research was the selection and reproduction of one of the methods described in the table 2-1. It can be observed, that based on the combination of starting materials only two systems are reported. Furthermore, an important aspect to underline is the ***lack of information about the complete synthesis details***. In general, experimental information is not deeply specified; namely purity of the educts, order of mixing, pre-dissolution of educts, solutions with pre-determined molar concentration, mixing order of the educts, educts mixing rate (one-shot or dropwise after dissolution step), pH control, volume of the reactor, molar ratio, stirring rate, temperature rate and annealing process. In this sense, the synthesis that offers more experimental information was reported by Satyanayana *et. al.*¹²⁵ and his procedure: synthesis using the CoAc₂, (Cobalt acetate) ADP (Ammonium dihydrogen phosphate) and LiAc (Lithium acetate) system, was selected as the starting point for the production of LCP-*Pnma*.

Table 2-1: Summary of polyol synthesis published for LCP-*Pnma* (up to June 2012)

System No	Starting Materials	Reflux time (h)	Reflux temperature (°C)	Molar ratio Li:M:P	Solvent	Special conditions	Annealing time and temperature	Capacity (mAh/g)	Year	Ref.
1	LiAc (99.99% Aldrich) Co(Ac) ₂ .4H ₂ O (98% Alfa Aesar) H ₃ PO ₄ (85% wt% H ₂ O Fisher)	20	320	1:1:1	TTEG	Reflux under nitrogen atmosphere	650 °C for 0.5 h or longer in Ar	Not reported	2009	Wang <i>et. al.</i> ¹²⁶
	LiAc.2H ₂ O CoAc ₂ .4H ₂ O (NH ₄)H ₂ PO ₄	4	180	1:1:1	DEG	No	350 °C in air	Not reported	2009	Exnar <i>et. al.</i> ¹²⁷
2	LiAc (Qualigens) CoAc ₂ .4H ₂ O (Qualigens) (NH ₄)H ₂ PO ₄ (Qualigens) PVP(C ₆ H ₉ NO) _n , Mw: 10 ⁶	2	190	Not mentioned	EG	Use of PVP as surfactant	Intervals between 350 °C – 600 °C for 3 h in air	Not reported	2011	Satyanayana <i>et. al.</i> ¹²⁵
	LiAc (Merck 99.999%) CoAc ₂ .4H ₂ O (Merck 99.999%) (NH ₄)H ₂ PO ₄ (Sisco 99.99%)	35	250	1:1:1	PEG	No	800 °C for 2 and 4 h	6.08	2008	Renganathan <i>et. al.</i> ¹²⁸

2.2 Educts used

The chemical substances used in this work are listed in Table 2-2. They have been used without any further purification process.

Table 2-2: List of the chemicals used

Compound and purity grade	Formula	Supplier*	Abbreviation	Form
Acetone techn.	CH ₃ COCH ₃	MV	Ac	Liquid
L-(+)-Ascorbic acid 99+%	C ₆ H ₈ O ₆	AA	AsAc	Powder
Ammonia water 25%	NH ₄ OH	MV	NH ₃ /H ₂ O	Liquid
Ammonium dihydrogen phosphate 99,995%	NH ₄ H ₂ PO ₄	AA	ADP	Powder
Di-Ammonium hydrogen phosphate 99%+	(NH ₄) ₂ HPO ₄	M	DAHP	Powder
Argon 5.0 99.999%	Ar	Wf	Ar	Gas
Citric Acid ≥ 99,5%	HOC(COOH)(CH ₂ COOH) ₂	SA	CA	Powder
Cobalt(II) acetate tetrahydrate 99.98%	(CH ₃ COO) ₂ Co.4H ₂ O	AA	CoAc ₂	Powder
Cobalt(II) chloride hexahydrate 99.95%	CoCl ₂ .6H ₂ O	AA	CoCl ₂	Powder
Cobalt(II) sulfate heptahydrate 99.95%	CoSO ₄ .7H ₂ O	Ch	CoSO ₄	Powder
Cobalt(II) carbonate heptahydrate 99.95%	CoCO ₃ .7H ₂ O	AA	CoCO ₃	Powder
Diethylene glycol ≥ 99,0%	(HOCH ₂ CH ₂) ₂ O	VWR	DEG	Liquid
Ethanol techn.	CH ₃ CH ₂ OH	MV	EtOH	Liquid
Ethylene glycol normapur ≥ 99,0%	HOCH ₂ CH ₂ OH	VWR	EG	Liquid
D-Glucose · H ₂ O 99%	C ₆ H ₁₂ O ₆	AA	Glu	Powder
Iron(II) acetylacetonate 99.95%	[CH ₃ COCHC(O)CH ₃] ₂ Fe	SA	Fe(AcAc) ₂	Powder
Iron acetate 99.999%	Fe(CH ₃ COO)	SA	FeAc	Powder
Iron sulfate heptahydrate 99.999%	FeSO ₄ .7H ₂ O	AA	FeSO ₄	Powder
Iron oxalate dehydrate 99.999%	FeC ₂ O ₄ .2 H ₂ O	AA	FeOx	Powder
Lithium acetate dihydrate 99%+	CH ₃ COOLi.2H ₂ O	Ch	LiAc	Powder
Lithium hydroxide monohydrate	LiOH.H ₂ O	SA	LiOH	Powder
Lithium phosphate monobasic 99%	LiH ₂ PO ₄	SA	LDP	Powder
Phosphoric acid 98 %	H ₃ PO ₄	Ap	H ₃ PO ₄	Liquid
Polyvinyl pyrrolidone (M.W. 56000, 360000, 1300000)	(C ₆ H ₉ NO) _n	AA	PVP	Powder
Sodium dodecyl sulfate ≥ 99,0%	CH ₃ (CH ₂) ₁₁ OSO ₃ Na	SA	SDS	Powder
Sodium dodecylbenzenesulfonate ≥ 99,0%	CH ₃ (CH ₂) ₁₁ C ₆ H ₄ SO ₃ Na	SA	SDBS	Powder
Tetraethylene glycol ≥ 99,0%	HO(CH ₂ CH ₂ O) ₃ CH ₂ CH ₂ OH	Ch	TTEG	Liquid
Tetraethylene glycol dimethylether ≥ 99,0%	CH ₃ O(CH ₂ CH ₂ O) ₄ CH ₃	Ch	TTEG-DME	Liquid
Triethylene glycol ≥ 99,0%	HO(CH ₂ CH ₂ O) ₂ CH ₂ CH ₂ OH	VWR	TEG	Liquid
Water Millipore	H ₂ O	TEC	H ₂ O	Liquid

* Ap = Applichem, AA = Alfa Aesar, Wf = Westfalen, SA = Sigma-Adrich, Ch = Chempur, M = Merck, VWR = VWR Chemicals, MV = faculty's supply, TEC = Chair of technical electrochemistry.

2.3 Polyol synthesis of LCP-*Pnma*

This section groups the different polyol systems used for the synthesis of LCP-*Pnma*. The chemical reaction is possible due to the mixture of chemical reagents based on cobalt, phosphorous and lithium in a polyalcohol. The influence of synthesis parameters such as solvent (polyalcohols type), educts, temperatures and reaction times is discussed. The formation of crystalline structures and morphology is also analyzed.

2.3.1 Synthesis using the CoAc₂, ADP and LiAc system¹²⁵ – standard procedure

The solid educts CoAc₂, ADP and LiAc were weighed using a Sartorius TE124-s balance. Each substance (8.76 mmol) was dissolved using EG (25 mL). The molar ratio of Li:Co:P was 1:1:1. The dissolutions of ADP and LiAc were mixed together in a 250 mL three-neck round flask and stirred for 10 minutes. Later, the dissolution of CoAc₂ was added into a round flask and temperature was increased up to 190 °C (the temperature value is fixed in a magnetic stirrer). The heating process was conducted using a heat-on attachment in a MR Hei-Standard heating plate form Heidolph and adapted to an EKT Hei-Con temperature sensor. This mixture was refluxed for 3 hours. The stirring rate was fixed at 1000 rpm using a 20 x 6 mm magnetic stirrer. After that, the solution was slowly cooled. In order to separate the final product from the rest of the organic components and the rest of the EG, the mixture was centrifuged in a Hettich-Rottanta centrifuge at 1500 rpm. Subsequently, the solvent was disposed, the sediment re-dissolved in pure ethanol and centrifuged again. This procedure was repeated until the filtrate became colorless. At last, the product was washed with a rinse of acetone. The product was filtered under vacuum and dried in a furnace at 100 °C overnight. Finally, the precursor was annealed at 300 °C and 650 °C for 3 hours. Figure 2-1 presents a flux chart of the synthesis procedure, overall synthesis parameters that can be varied, and the pictures of the dissolution, reflux, filtration and samples after annealing.

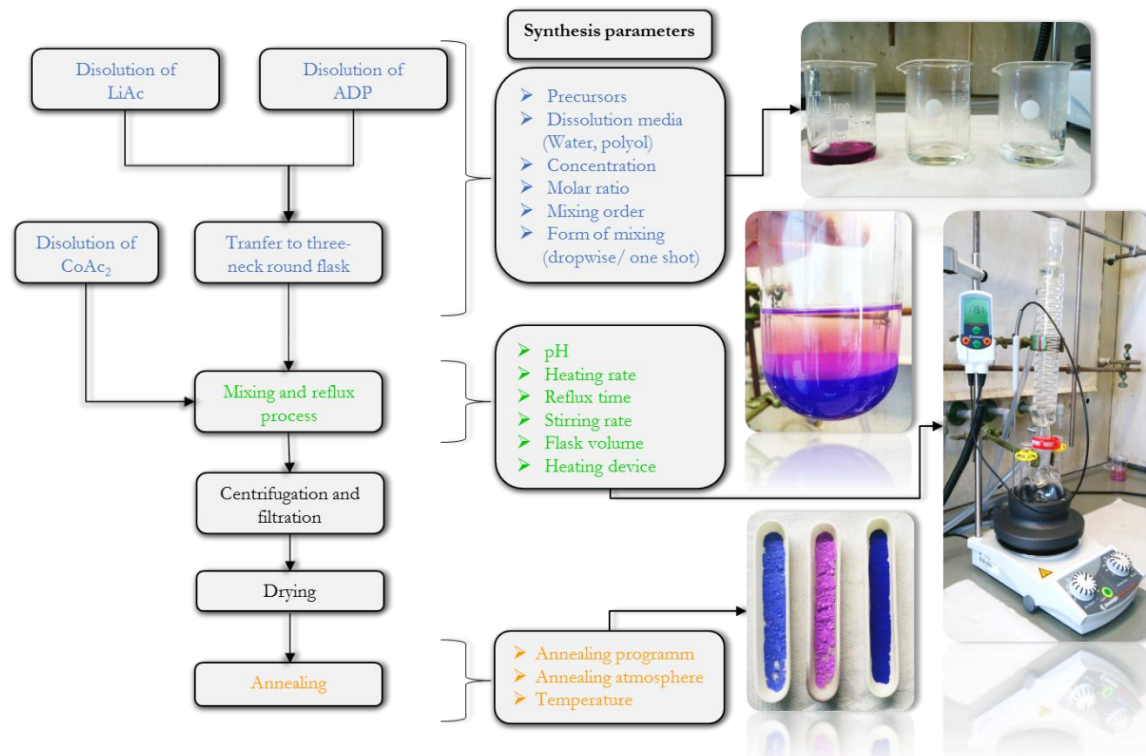


Figure 2-1: Flowchart of polyol synthesis using the CoAc₂, ADP and LiAc system. The middle column present the synthesis parameters. Pictures of dissolution in EG, centrifugation, appearance of the final product (before and after annealing) and reflux system.

2.3.2 Synthesis using the CoAc₂ and LDP system (adapted from LiMnPO₄ polyol synthesis)⁹⁹ – standard procedure

For the adapted synthesis, 150 mL of EG were added into a 250 mL 3-neck round bottom flask with a condenser and 20 x 6 mm magnetic stir-bar. The EG was heated up to 100 °C and stirred at 1000 rpm. Then, 3 mmol of CoAc₂·4H₂O were added on EG and, after complete dissolution, 3 mmol of LiH₂PO₄ (1.0 M solution) were added dropwise (at less than 1 mL/min rate) using a graduate drip funnel. The temperature was increased up to 135 °C (nominal value fixed in the magnetic stirrer). The heating process was conducted by a heat-on attachment in a MR Hei-Standard heating plate from Heidolph adapted to an EKT Hei-Con temperature sensor. This mixture was refluxed for 4 hours. After that the solution was slowly cooled. The following steps of centrifugation, filtration and drying are the same as described in the synthesis using the CoAc₂, ADP and LiAc system. The annealing procedure was done under air. The flowchart of the synthesis procedure is presented in figure 2-2.

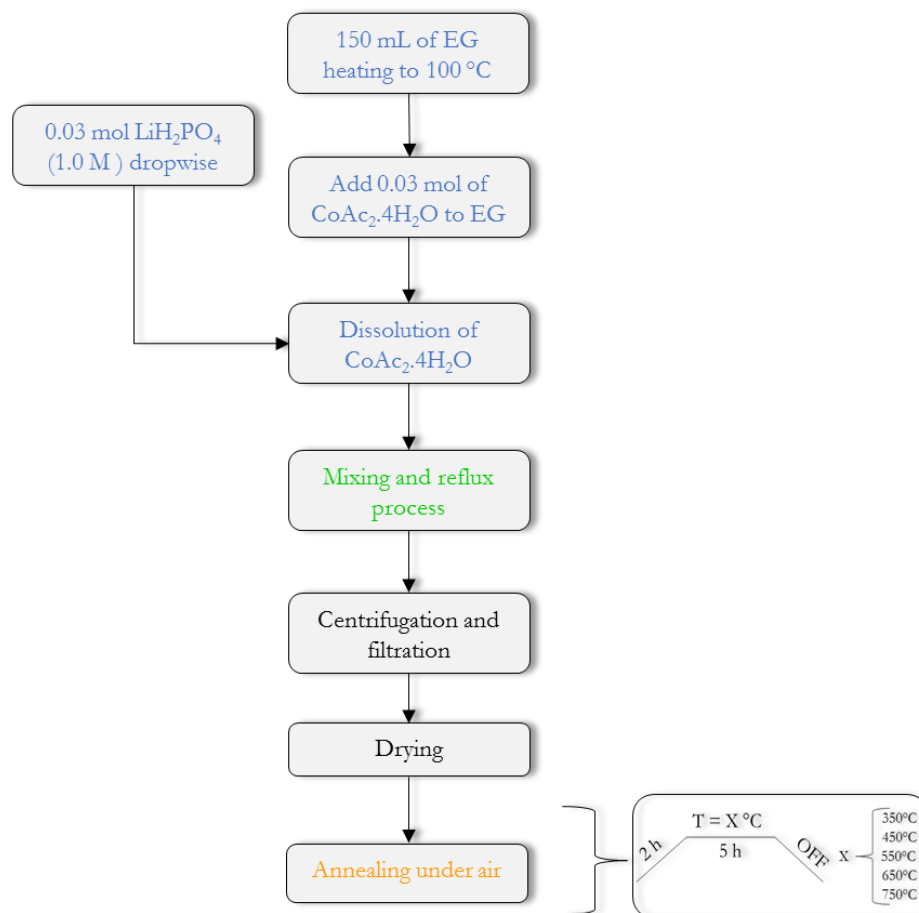


Figure 2-2: Flowchart of polyol synthesis using the CoAc₂ and LDP system ⁹⁹

2.3.2.1 Synthesis using CoAc₂ and LDP system combined with PVP ^{99, 129}

PVP (Polyvinylpyrrolidone; m.w. 56000) was used as a surfactant to address the control of the particle size and morphology of LCP. The procedure was based on the synthesis using the CoAc₂ and LDP system. The PVP was added on CoAc₂ during its dissolution (see figure 2-3). In another procedure, PVP was dissolved separately in 50 mL of EG and heated up to 100 °C. Afterwards this dissolution was mixed with the dissolution of CoAc₂ and finally LDP was added dropwise. The amount of PVP used was 1:4 molar ratio LCP:PVP.

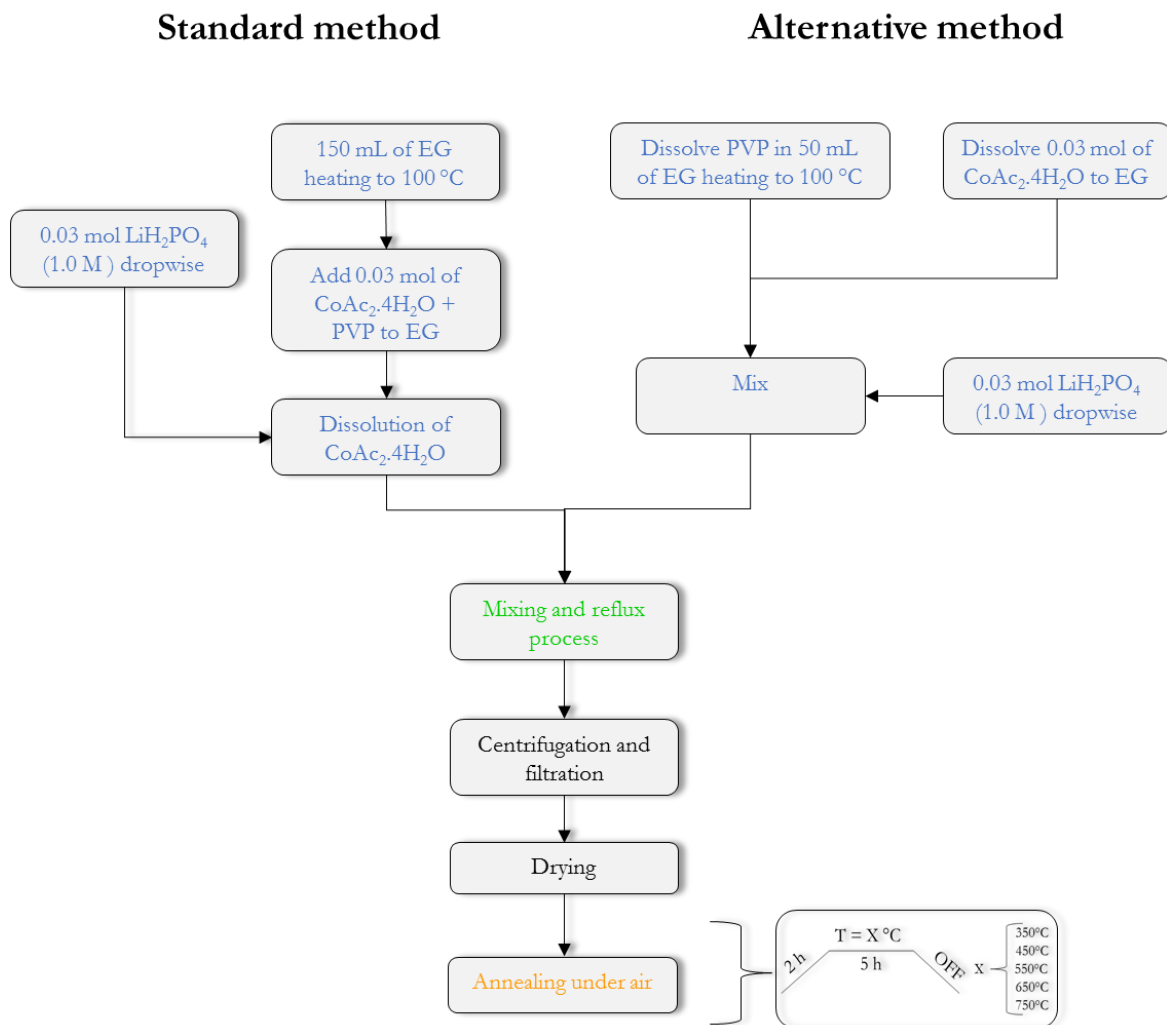


Figure 2-3: Flowchart of polyol synthesis using the CoAc₂ and LDP system combined with PVP

2.3.3 Synthesis using the CoAc₂, H₃PO₄ and LiAc system (adapted from LiFePO₄ polyol synthesis)¹³⁰ – standard procedure

For the synthesis 125 mL of TTEG were added into a 250 mL 3-neck round bottom flask with a condenser and a 20 x 6 mm magnetic stir-bar. Then 7.41 mmol of LiAc were added on TTEG solution at room temperature and the dissolution was heat up to 100 °C. Apart, CoAc₂ were added on 75 mL of TTEG and heated up to 100 °C. When LiAc is totally dissolved, 0.5 mL of H₃PO₄ (98%) were added dropwise. Here the solution in maintained for 1 hour under stirring. Then CoAc₂ solution is added on previous mixture. The Li:Co:P molar ratio is 1:1:1. Then the mixture was heated until refluxing conditions were reached. The heating process was assisted by the use of a heating mantle (Horst three-stages) with the stage selector placed in position 2 in order to try to reach temperatures above 250 °C. This mixture was refluxed for 14 hours. After that, the solution was slowly cooled. The posterior steps

of centrifugation, filtration and drying are the same as described before. A flowchart of the synthesis procedure is presented in the figure 2-4.

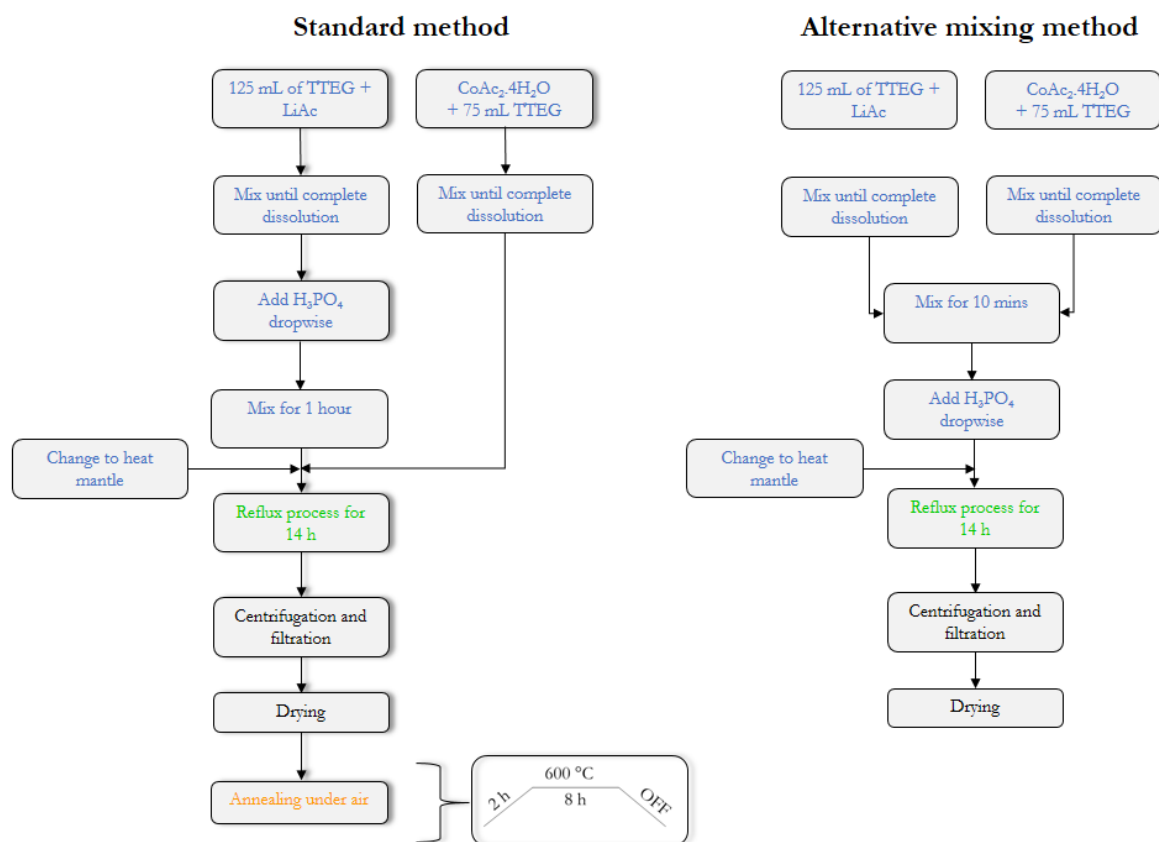


Figure 2-4: Flowchart of polyol synthesis using the CoAc_2 , H_3PO_4 and LiAc system

2.4 MW-assisted polyol synthesis of LCP-*Pnma*

2.4.1 MW-assisted synthesis using the CoX and LDP system ($X = \text{Ac}_2$, SO_4 , CO_3)

For the microwave-assisted polyol synthesis, CoAc_2 , CoSO_4 , CoCl_2 and LDP (1.0 M) were used as starting materials. The Li/P molar ratio was 1:1. First, CoAc_2 was dissolved in 150 mL of EG and after complete dissolution 3 mmol of LDP (1.0 M solution) were added dropwise (at less than 1 mL/min rate) using a graduate drip funnel, to form a precursor solution. Afterwards 50 mL of the precursor solution were transferred into Teflon® vessels and sealed to form a high-pressure closed system. The vessels were covered by a housed thermowell and located in a rotor placed on a turntable for uniform heating in an Ethos One microwave system (MLS GmbH, MR- 8 HT high-temperature rotor). The desired time and temperature were programmed with the easyCONTROL-640 software. The automatic

temperature control system allowed for continuous monitoring and control of the internal temperature. Preset profile (desired time, temperature, and pressure) was followed automatically by continuously adjusting applied power. The system was operated at a frequency of 2.45 GHz and power of 600 W. The sample temperature was ramped up to 300 °C and kept at 300 °C for 15 min under the solvothermal conditions. After cooling the mixture is collected, centrifuged, filtered and dried as described in the polyol synthesis method. A diagram of the synthesis procedure is shown in the figure 2-5.

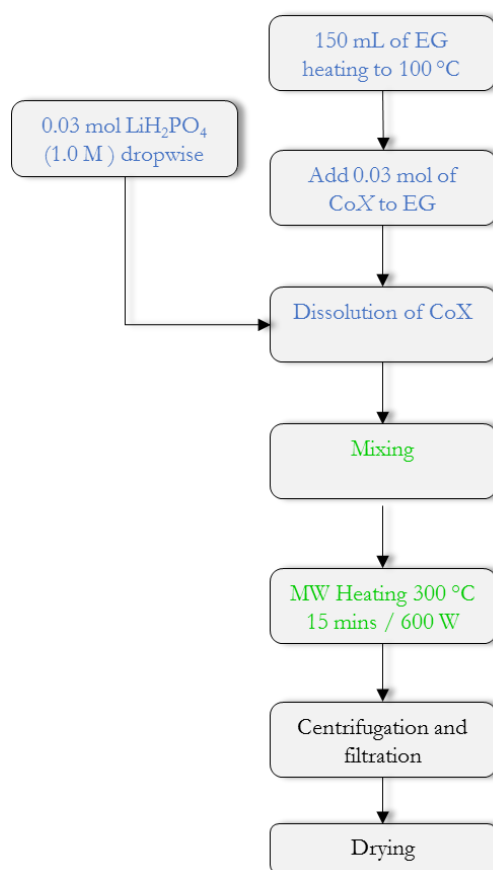


Figure 2-5: Flowchart of microwave-assisted polyol synthesis using the CoX and LDP system ($X = \text{Ac}_2, \text{SO}_4, \text{CO}_3$)

2.4.2 MW-assisted polyol synthesis using the CoAc_2 , H_3PO_4 and LiOH system ¹³¹

The synthesis is based on the procedure reported by Manthiram *et. al* ¹³¹. For the microwave-assisted polyol synthesis, LiOH, CoAc_2 and H_3PO_4 were used as starting materials. The Li:Co:P proportion was 1:1:1 and the amount of substance used was 3 mmol. Firstly, CoAc_2 and LiOH were dissolved separately in 10 mL of water each. CoAc_2 solution was mixed with 50 mL of the polyalcohol and stirred for 10 minutes. Then the LiOH solution was added on CoAc_2 dissolution and mixed for another 10 minutes. Finally, the H_3PO_4 was added dropwise and pH of the reaction mixture was adjusted to around 9.0 with

ammonia. The mixture was transferred into Teflon® vessels and sealed to form a high-pressure closed system. The following steps of microwave set-up, centrifugation, filtration and drying were the same as described before. A diagram of the synthesis procedure is shown in the Figure 2-6.

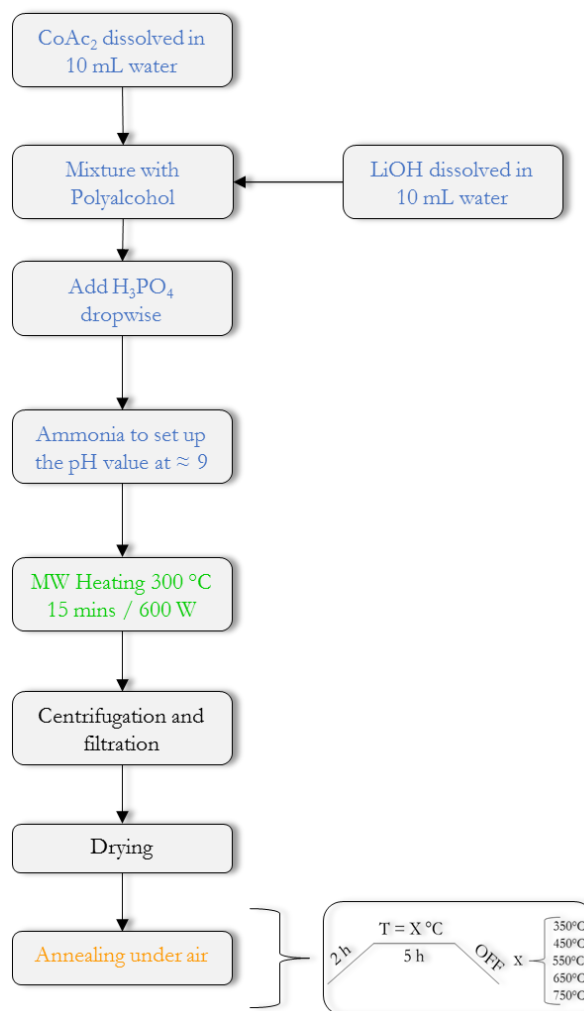


Figure 2-6: Flowchart of microwave-assisted polyol synthesis using CoAc_2 , H_3PO_4 and LiOH system

2.5 Acetate-assisted antisolvent precipitation (AAAP) synthesis (adapted from LiMnPO_4 antisolvent synthesis¹³²)

This method involves the preparation of an aqueous solution and an antisolvent solution. For the aqueous solution, 20 mmol of CoAc_2 were dissolved in 16,5 ml of deionized water; afterwards, 20 mmol (1.35 mL) of H_3PO_4 and 2 mL of HCl (37 % wt) were added dropwise. The solution was mixed for 20 minutes until the obtainment of a homogeneous mixture. For the antisolvent solution, 20 mmol of LiAc

were solved in 65 mL of EtOH (Absolute) and the solution was heated up 70 °C using a stirring rate of 400 rpm with a 20x2 magnetic stirrer.

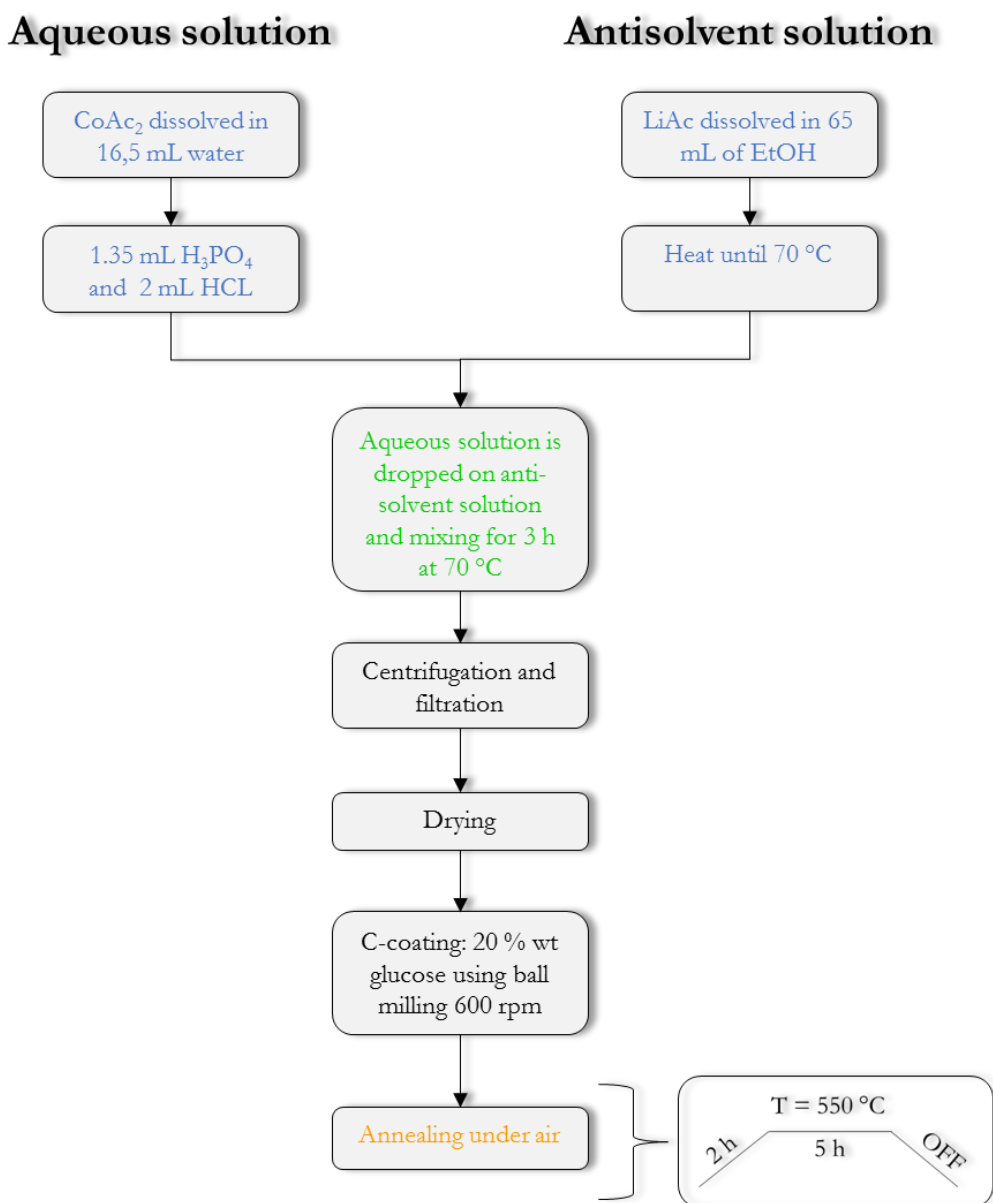


Figure 2-7: Flowchart of acetate-assisted antisolvent precipitation synthesis of LCP-*Pnma*

The antisolvent solution was transferred into a round 250 mL flask connected to a reflux system. In order to avoid loss of solvent due to evaporation of alcohol and to control the flux rate, aqueous solution was being dropped into antisolvent solution using a KDS 200 LEGACY syringe pump at 0.8 mL/min. A formation of a blue/violet viscous solution was noted (see figure 2-8). The solution was maintained for 3 h at 70 °C until a precipitate formed. The stirring rate was fixed at 1000 rpm using a 20 x 6 mm magnetic stirrer. The formed precipitate was separated from the rest of the solution by vacuum filtration.

The product was collected and dried in an oven at 75 °C overnight. Subsequently, the precipitate was ball-milled with glucose for 6 h using a program composed of 72 steps of 5 minutes of mixing with 20 minutes pauses between them. For the ball milling 1 cm in diameter ZrO₂ balls in a 45 mL jar were used. The annealing of the sample was conducted under air and argon at 550 °C for 5 hours. The flowchart of the process, as well as the graphical description of the montage, is shown in the figures 2-7 and 2-8.

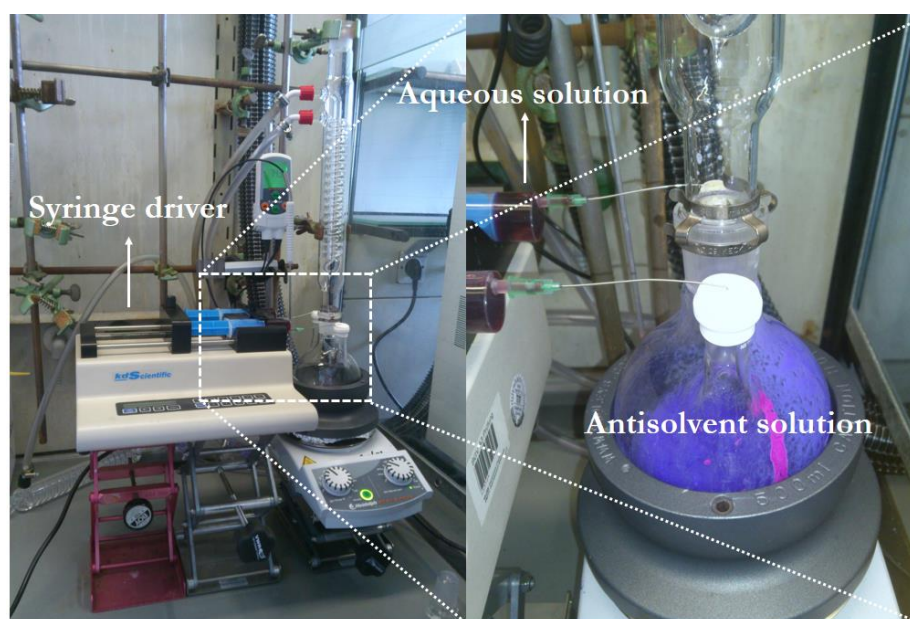


Figure 2-8: Experimental setup for the acetate-assisted antisolvent synthesis. Left side: the Syringe driver adapted to the round flask. The syringe tip cross through rubber septa. The reflux cooler is use to avoid the evaporation of the solvent.

2.6 Polyol synthesis of LiFePO₄-*Pnma*

For the synthesis LFP-*Pnma*, 125 mL of TTEG were added into a 250 mL 3-neck round bottom flask with a condenser and a 20 x 6 mm magnetic stir-bar. Then 14.8 mmol mol of LiAc were added on the TTEG at room temperature, the mixture was stirred for 10 minutes at 1000 rpm and the temperature increased up to 100 °C. After total dissolution of the LiAc, 7.41 mmol of H₃PO₄ (98%) were added dropwise on the LiAc/TTEG mixture and stirred for another 30 minutes. Apart, 7.41 mmol of FeSO₄·7H₂O are added into 75 mL of TTEG, the mixture is heated up to 100 °C. After complete dissolution of FeSO₄·7H₂O this solution is added into the LiAc/H₃PO₄/TTEG mixture. The Li:Co:P molar ratio is 2:1:1. Then the mixture was heated until refluxing conditions were reached. The heating process was assisted by the use of a heating mantle. This mixture was refluxed for 16 hours. After that, the solution was slowly cooled. The posterior steps of centrifugation, filtration and drying are the same as described before. A flowchart of the synthesis procedure is presented in the figure 2-9.

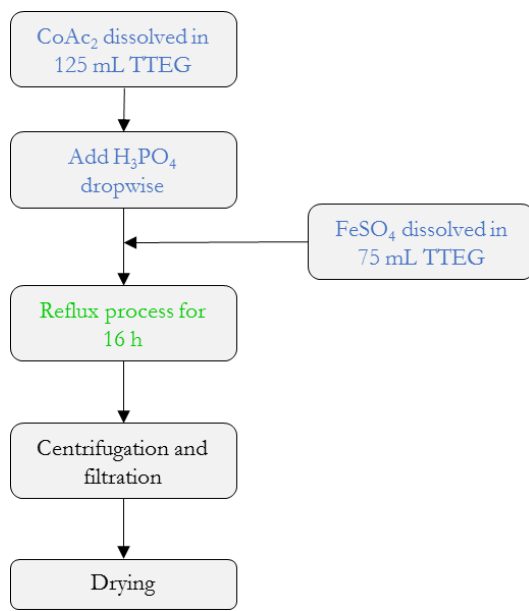


Figure 2-9: Flowchart of polyol synthesis of LFP-Pnma

2.7 Further equipment used for synthesis and characterization

2.7.1 Furnaces and tube ovens

Dry and anneal processes of the samples were done in a Nabertherm oven (30 - 3000°C). In this oven, a heating rate, a target temperature and a holding time can be set. Subsequently, the furnace cools to room temperature on its own. The annealing process under argon atmosphere was done in a tube furnace controlled by an external flux regulator.

2.7.2 X-ray diffraction analysis - XRD

The qualitative crystal analysis was done at room temperature on a Stoe STADI P diffractometer using Mo K α radiation (Ge(111) monochromator, $\lambda = 0.70930 \text{ \AA}$) equipped with a Dectris Mythen DCS 1K silicon solid-state detector. The sample is grounded and fine homogenized in an agate mortar and the powder put between two gluing tape stripes (Scotch® Magic TM Tape 810, 3M). The tape is fixed in a sample holder. The sample holder is clamped in the diffractometer and spin during measurement. The measure is done using transmission geometry in a 2θ range of $2^\circ - 60^\circ$ in two ranges of measurement with a step size of 0.015 in 2θ and measure time per step of 2.0, 1.0 and 0.5 seconds (20 minutes, 30 minutes and 1 hour measure time). The generator is operated with 50 kV and 40 mA.

For the analysis of the obtained diffractograms, crystallographic information files (.cif files) from the Inorganic Crystal Structure Database (ICSD-FIZ Karlsruhe) were used. The phase analysis was performed using the X'pert Highscore Plus software from PANalytical¹³³. The graphic interface of the software WinXpow was used. The .cif files were converted in negative intensity in order to compare the PXRD patterns. The .cif file reported by Kubel *et. al*¹³⁴ for LCP-*Pnma* was used as literature reference. The calculation of the crystallite size was done by the use of Scherrer equation¹³⁵:

$$\Delta(2\theta) = \frac{K \cdot \lambda}{L \cdot \cos \theta} \quad \text{Eq. 2-1}$$

where $\Delta(2\theta)$ is the full width at half maximum corresponding to the main signal in the PXRD pattern, K is the Scherrer form factor, λ is the wavelength, L the crystallite size and θ is the incidence angle. The Scherrer form factor used was 0.94.

2.7.3 Scanning electron microscopy - SEM

Examination of the dry material regarding the shape and size of the particles was performed using scanning electron microscopy (SEM). Two different microscopes were used:

A: For examination of morphology and approximately estimation of grain size and agglomerates size: JCM-6000 NeoScope from JEOL. Acceleration voltage of 15 kV.

B: For approximately estimation of grain size, agglomerates size and high resolution images: High-resolution scanning electron microscopy (HR-SEM) was performed on a JEOL JSM-7500F instrument at an accelerating voltage of 1 kV.

The powders were prepared on carbon tape, which was attached to an aluminum stub. Both microscopes were operated at high vacuum.

2.7.4 Electrochemical characterization

Electrochemical characterization was carried out in cooperation with the Electrochemical Chair of Prof. Dr. H. Gasteiger. M.Sc. D. Haering developed the measurements and calculations. First, the active material is homogenized in an agate mortar. Then, the active material, binder (PVdF) and carbon black were mixed in a planetary centrifugal mixer (Thinky ARV-310). The composition of cathode ink was 80:10:10 (active material:binder:carbon black). The LCP inks were cast on the rough side of an aluminum foil (MTI, thickness: 18 μm , 4.7 g/cm^3) using a doctor blade coater. The wet film thickness is of around

250 μm . The resulting coatings were dried at 50 $^{\circ}\text{C}$ in a convection oven for 3 hours. The electrodes are punched with a 10 mm diameter and pressed 2 times for 1 minute at 3 tons of pressure. As electrolyte 1 M LiPF_6 in a solution of EC:DMC was used. Two glass fiber separators were used with 8 μL of electrolyte solution. The measures were done in two cells, each using three cycles at different C-rates (C/10, C/5, C/2, 1C and 2C). The potential range was between 3.5 – 5.2 against Li/Li^+ .

2.7.5 Brunauer-Emmett-Teller (BET) Analysis

The specific surface area of the samples was determined by a multipoint (11) BET measurement, using an N_2 adsorption isotherm on a gas adsorption device (QUANTACHROM, autosorbe® iQ). The samples were placed in a glass tube with spherical tip (diameter = 9 mm), dried for 1 h at 90 $^{\circ}\text{C}$ and heated for 16 h at 150 $^{\circ}\text{C}$. The measurements were carried out to reduce the dead volume with a filling rod while cooling with liquid nitrogen (-196 $^{\circ}\text{C}$). M.Sc. D. Haering developed the measurements and calculations.

2.7.6 Measurements of electrical conductivity

The electrical conductivity was measured using a tool designed at the Electrochemical Chair of Prof. Dr. H. Gasteiger. The tool (see figure 2-10) was manufactured at the mechanics workshop of the Chemistry department of TUM. The powder was homogenized in an agate mortar and then introduced inside the tool. The sample inside is pressed and the height of the pellet is determined using a micrometer scale. The pellet is located between two electrodes and across the compressed powder a defined voltage is applied and the current is measured. The voltage is controlled by a BIOLOGIC, VMP3 device. The electrical conductivity is calculated using the following formula:

$$\sigma = \frac{I \cdot L}{u \cdot A} \quad \text{Eq. 2-2}$$

Where σ is the electrical conductivity, I is the value of the current, L is the height of the pellet, u is the voltage applied and A is the surface of the pellet. M.Sc. D. Haering performed the measurements and calculations.



Figure 2-10: Tool used for the determination of the electric conductivity

2.7.7 CHNS-Elemental analysis

This technique was implemented to determine the carbon content in coated samples. Approximately 2.0 mg of the sample were transferred into an elemental analysis device (ELEMENTAR, vario MICRO cube) and burned at 1150 °C. Nitrogen oxide and sulfur oxide were reduced into N₂ and SO₂ at 850 °C. The detection system uses a thermal conductivity detector (WLD). The reference gas used is argon 5.0. The data collection is controlled using the EAS vario CHNS software. M.Sc. Stephanie Bretzke developed the measurements and calculations.

2.7.8 Ball milling

For the AAAP synthesis the C-coating procedure was made using a FRITTSCH, Pulverisette 6 classic line ball mill, using 45 mL jars with 10 mm balls both made of ZrO₂. The carbon source was glucose (20% wt). The program used was for 30 minutes at 600 rpm with pauses of 10 minutes. Figure 2-11 shows the diagram of the ball milling procedure.

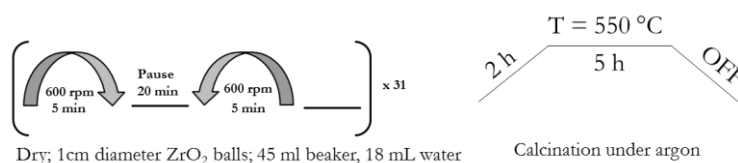


Figure 2-11: Ball mill procedure for the C-coating in the AAAP method

3. Results and discussion

This chapter presents the highlighted results of the different polyol routes tested. Since the variation of the different synthesis parameters can produce a big matrix of experiments, only the most outstanding results are shown according to the objectives and scope of the project. Moreover, in order to give an overview of the additional parameters tested and attempts conducted, a compilation of tables resuming the synthesis variations (e.g. time, temperature, pH, etc.) are presented in the appendix. This chapter discusses the polyol synthesis of LCP-*Pnma*, followed by additional information regarding microwave, acetate anti-solvent and solid state synthesis of LCP-*Pnma*. Finally, a section describing the application of the polyol synthesis to LiFePO₄ olivine is shown.

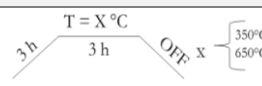
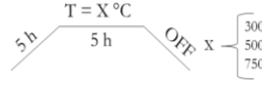
3.1 Polyol synthesis of LCP-*Pnma* phase

This section describes the polyol syntheses reproduced from literature, adapted from other LMP materials or tested as first time for LCP. The first part corresponds to a reproduction of a polyol synthesis reported in a publication as well as a patent. Then, the adaptation of a polyol route used for LMP-*Pnma* is explained and the use of PVP as surfactant in order to control the particle size and morphology. Afterwards, the influence of annealing temperatures, cobalt educts and water:polyalcohol ratio on the crystal structure and morphology of the samples are analyzed. Finally, a system used for the synthesis of LFP-*Pnma* is adapted and implemented to produce LCP-*Pnma*.

3.1.1 Synthesis using the CoAc₂, ADP and LiAc system (synthesis reproduction ¹²⁵)

Table 3-1 summarizes two polyol syntheses (*a* and *b*) with differences in the solvent composition, reaction time and the annealing program. These procedures allow to obtain a main phase of LCP-*Pnma*; however, some remarks regarding the crystallinity, solvent and annealing are necessary in order to analyze the preliminary results.

Table 3-1: Summary of two polyol syntheses with differences in solvent composition, reaction time and annealing program

Synthesis	Li:M:P Ratio	Batch size (mmol)	Solvent vol. (ml)	Set T (°C)	Time (h)	Annealing program (Air)
<i>a</i>	1:1:1	0.876	EG : 100	190	18	
	The educts are solved in 20 mL of EG separately; then, mixed together with 40 mL of EG					
<i>b</i>	1:1:1	0.876	H ₂ O : 30 EG : 70	190	3	
	The educts are solved in 10 mL of water separately; then, mixed together with 70 mL of EG					

The first point to discuss is the crystalline characteristic of the product obtained after the drying process. In both cases (procedure *a* and *b*), the PXRD pattern does not show any reflection in the 2-theta range, indicating that both samples are amorphous. No crystallization process occurs. If some crystalline phase exists, it is too small to be reflected in the PXRD pattern; even, after using long XRD measurements of 1 hour. This also occurs when other synthesis parameters are changed: reflux time, reflux temperature, Li:M:P ratio and pH.

The second point to discuss relates to the solvent. Despite the fact that the method proposed by Satyanayana *et. al.*¹²⁵ reported the use of EG as unique solvent, other literature⁵⁷ reports the use of water as a co-solvent for two reasons: ***it increases the solubility of the educts and, water acts as hydrolysis agent.*** However, the use of water causes a reduction of the boiling point compared to the pure polyalcohol used. For instance, the boiling point of pure EG is 197 °C; however, a mixture of EG: water ratio 90:10 presents a boiling point of approximately 130° C (decrease of approximately 34%) . As a consequence of the decrease in the boiling point, the implementation of annealing processes is necessary to complete the formation of the LCP-*Pnma*^{136, 137}.

The third aspect to analyze is the formation of the phase after the thermal treatment. After the annealing procedure at 350 °C over 3 hours (experiment *a* on table 3-1), the PXRD pattern still shows an amorphous phase. The same occurs for experiment *b*, after annealing at 300 °C, over 5 hours. Only after a second annealing, samples show reflections corresponding to LCP-*Pnma*, ***suggesting that the formation of the LCP-*Pnma* phase occurs at temperatures above 350 °C*** . The presence of secondary phases; such as, Co₃O₄, Co₃(PO₄)₂ and Li₃PO₄ is a general trend using this system.

Figure 3-1 presents the PXRD pattern of the samples after the last annealing at 650 °C and 750 °C respectively. The existence of Co₃O₄ is attributed to the effect of successive annealing procedures under

air atmosphere. Furthermore, a thorough comparison between the samples presented can not be done since there are parameters that make them non-equivalent (variation of more than one parameter at the same time). Additional experiments were conducted based on the variation of synthesis parameters; such as, single annealing processes, reflux times (from 3 hours to 44 hours), pH variation and change in the molar ratio of educts. They are summarized in the appendix 5.1. Noticeably, some of them present secondary phases or even do not show reflections corresponding to LCP-*Pnma*, after annealing processes at temperatures over 400 °C.

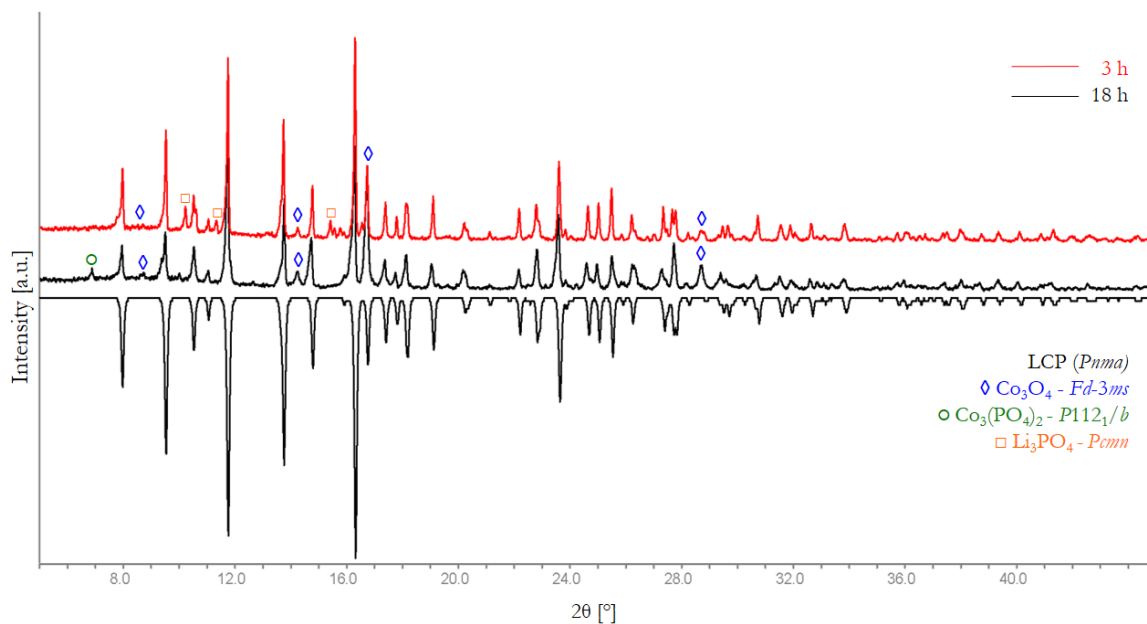


Figure 3-1: PXRD pattern of samples after annealing. The **red** pattern corresponds to the synthesis uses a EG:Water ratio of 100:0 (mL). The **black** pattern corresponds to the synthesis using a EG:Water ratio of 70:30 (mL). The negative intensity corresponds to the reported LCP-*Pnma* (**black**), Co_3PO_4 -*Fd-3ms* (**◇ blue**), $\text{Co}_3(\text{PO}_4)_2$ -*P1121/b* (**○ green**) and Li_3PO_4 -*Pcmn* (**□ orange**). The measuring time is 1 hour.

*As a final remark, the polyol synthesis using the CoAc₂, ADP and LiAc system leads to the formation of LCP-*Pnma* with the presence of secondary phases.* Although the experiments described by Satyanayana *et. al.*¹²⁵, Renganathan *et. al.*¹³⁸ and Exnar *et. al.*⁵⁷ assure the obtaining of pure LCP-*Pnma*, still exist a lack of information on details; such as, mixing order, heating rate and molar ratio. Those topics will be discus in the next sections.

3.1.2 Synthesis using the CoAc₂ and LDP system (adapted from LiMnPO₄ polyol synthesis⁹⁹)

This method was based on the procedure used for the synthesis of LiMnPO₄ (LMP-*Pnma*) reported by Kim *et. al.*⁹⁹, due to the detailed information regarding the concentration of precursor solutions, exact

amount of educts used and exact order of mixing. Similarly, the fact that only two educts are used instead of three can decrease the probability to form undesirable secondary phases. Besides, the influence of time and temperature on the formation of crystalline phases is analyze.

3.1.2.1 Influence of the reflux temperature and reaction time

The experimental procedure reported by Kim *et. al.*⁹⁹ used a reflux time of 4 hours, in EG, at 135 °C, without use of annealing steps to obtain LMP-*Pnma*. Despite the last section demonstrates that short or long reflux times does not influence the crystallization of LCP-*Pnma*, those parameters will be deeply analyzed using this system. For this reason, two sets of experiments were performed, changing only one parameter at the time (see table 3-2). The other synthesis parameters were kept same as it is described in the experimental section 2.3.2.

Table 3-2: Temperature and reaction time parameters using the CoAc₂ - LDP system

Educts	Li:Co:P ratio	Batch size (mmol)	Set T (°C)	Time (h)
LDP (1,0 M), CoAc ₂	1:1:1	3	135	14
LDP (1,0 M), CoAc ₂	1:1:1	3	190	14
LDP (1,0 M), CoAc ₂	1:1:1	3	135	4
LDP (1,0 M), CoAc ₂	1:1:1	3	190	4

The first parameter to analyze is the effect of the reaction time (or reflux time). The samples synthesized at 135 °C are composed by LCP-*Pn2_{1a}* and Co₃(HPO₄)₂(OH)₂ (figure 3-2). In this case, ***the reaction time does not to have a strong influence in the crystallization process, since both samples present the same phase composition.*** The patterns are only differentiated by the background:signal ratio. On the other hand, when temperature was increased up to 190 °C, the sample synthesized during 4 hours presents some reflections corresponding to LCP-*Pnma* (figure 3-3). Surprisingly, with longer times (14 h), a mixture of LCP-*Pn2_{1a}* and Co₃(HPO₄)₂(OH)₂ is found. Based on the PXRD analysis in this case ***the reaction time becomes important when the reaction is performed near the boiling point of the solvent.***

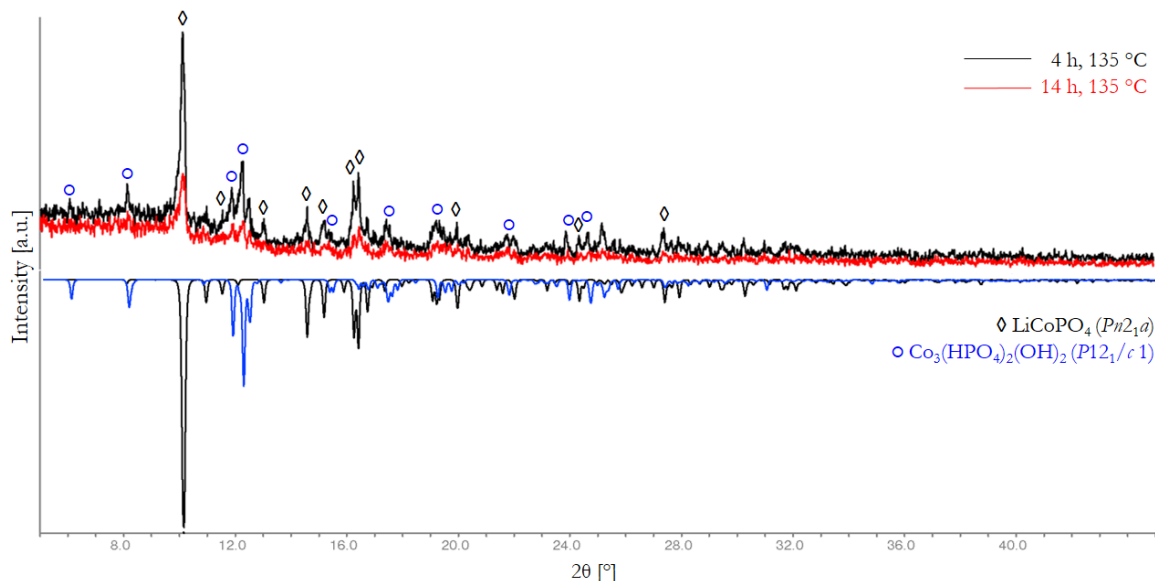


Figure 3-2: Effect of reflux time. PXRD of samples refluxed at 135 °C. Pattern recorded after the drying process. The black pattern corresponds to the synthesis for 4 hours at 135 °C and the red to the synthesis for 14 hours at 135 °C. The negative intensity corresponds to the reported phases of LCP-*Pn21a* (◇ black) and $\text{Co}_3(\text{HPO}_4)_2(\text{OH})_2$ (○ blue). The measuring time is 20 minutes.

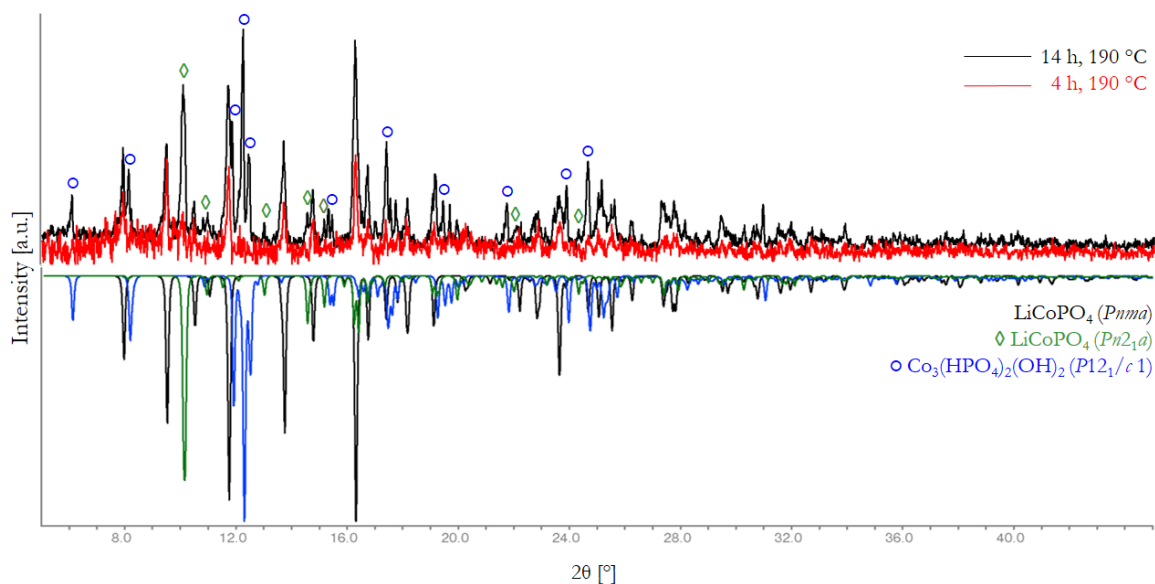


Figure 3-3: Effect of the reflux time. PXRD of samples refluxed at 190 °C. Pattern recorded after the drying process. The negative intensity corresponds to the reported phases of LCP-*Pnma* (black), LCP-*Pn21a* (◇ Green) and $\text{Co}_3(\text{HPO}_4)_2(\text{OH})_2$ (○ blue). The measuring time is 20 minutes.

The second parameter is the effect of temperature. The comparison between the synthesis at 135 °C and 190 °C demonstrates a partial formation of LCP-*Pnma*, suggesting that the synthesis temperature plays a key role in the formation of the desired olivine phase. In the case of the reaction conducted over 4 hours, the figure 3-3 suggested that the sample contains LCP-*Pnma*, however when the reaction time increases to 14 hours, LCP-*Pn21a* as well as $\text{Co}_3(\text{HPO}_4)_2(\text{OH})_2$ are present in

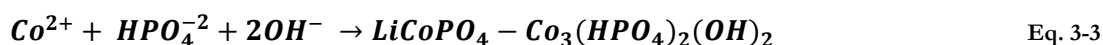
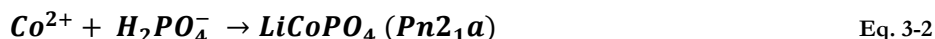
bigger amount. This observation suggest a possibility that LCP-*Pnma* can be formed at really early stages of the synthesis however, over the time, the amount of LCP-*Pn2_{1a}* and $\text{Co}_3(\text{HPO}_4)_2(\text{OH})_2$ formed is higher.

The reaction mechanism proposed during the synthesis is described by the equations 3-1 to 3-3:

First part of the reaction (under 4 hours – small amount of crystalline material):



Second part of the reaction (above 4 hours – high amount of crystalline material):



It is important to remark that after long times reaction, most of the material corresponds to LCP-*Pn2_{1a}* due to its higher stability. This affirmation is based on the computational calculations made by Ceder *et al*¹³⁹. His works predicts the stability of several phosphate cathode materials using *Ab initio* calculations in the framework of the density functional theory (DFT). Additionally, this method allows to predict the electrochemical properties of new potential cathode materials. The stability of the predicted materials was quantified using the **energy above the hull** concept (EAH). When a compound is stable at 0 K (0 K), its EAH is 0 meV/at. The EAH values are always positive, and the magnitude indicates a degree of instability. On the other hand, the local environment is related with the coordination of the transition metals with oxygen atoms that adopt different geometries, such as tetrahedral, octahedral and square planar. For Co^{2+} a LISICON-like structure LCP presents an EAH of 24 meV/ that, compared with the 37 meV/at of LCP-*Pnma*, indicates a more stable state of the tetrahedrally coordinated configuration for Co^{2+} . In figures 3-2 and 3-3 a common secondary phase corresponding to $\text{Co}_3(\text{HPO}_4)_2(\text{OH})_2$ is observed. ***This means that during the addition of the LDP solution, Co^{2+} give priority to form tetrahedrally coordination compounds rather than octahedrally coordinated ones. Only a few amount of material present octahedrally coordination at short times and high temperatures, with low crystallinity.***

As preliminary conclusion: in order to crystallize LCP-*Pnma*, temperatures above 135 °C are required, contrary to the observations reported by Kim et. al.⁹⁹ for LMP-*Pnma*. Additionally, exists a preference from Co^{2+} to form tetrahedral compounds. This process involves different complex chemical equilibria between the chemical-species that should be subject of further analysis.

Finally, it is important to remark that different reflux temperatures induce the formation of different crystalline phases in polyol routes.

In order to complete the formation of the single phase of LCP-*Pnma*, successive annealing procedures were used as described in experimental section 2.3.2. The PXRD patterns of the compounds formed after synthesis at 135 °C/14 h and 190 °C/14 h, are presented in figures 3-4 and 3-5 respectively. For the sample synthesized at 135 °C/14 h, the formation of the main olivine phase begins after annealing at 350 °C (see figure 3-4). At these temperatures, the existence of LCP-*Pn2₁a*, *Pnma* and $\text{Co}_3(\text{HPO}_4)_2(\text{OH})_2$ is observed. In the case of the samples synthesized at 190 °C/14 h, the formation of the main olivine phase begins after annealing at 450 °C (see figure 3-5). After successive thermal treatments, the formation of the pure *Pnma* phase takes place at 750 °C. Finally, figure 3-6 shows the comparison of the final olivine samples obtained in each experiment. Their corresponding lattice parameters are presented in table 3-3.

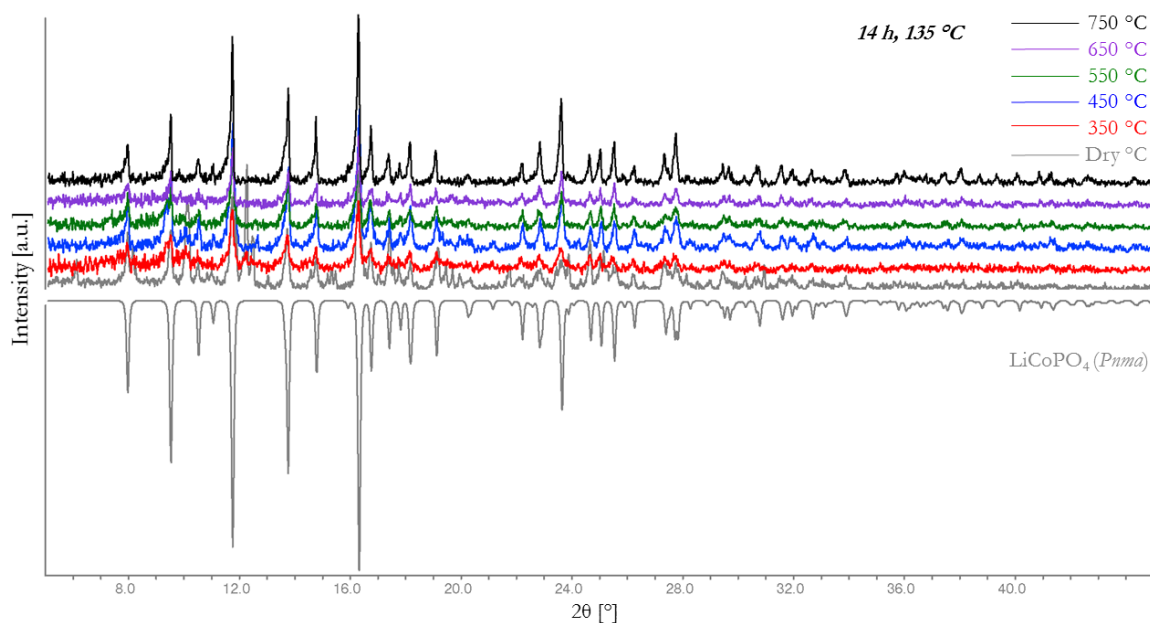


Figure 3-4: Effect of reflux temperature. PXRD pattern of the samples refluxed at 135 °C for 14 h. Pattern recorded after annealing at different temperatures. The negative intensity corresponds to the reported phases of LCP-*Pnma*¹³⁴ (gray). The measuring time is 20 min.

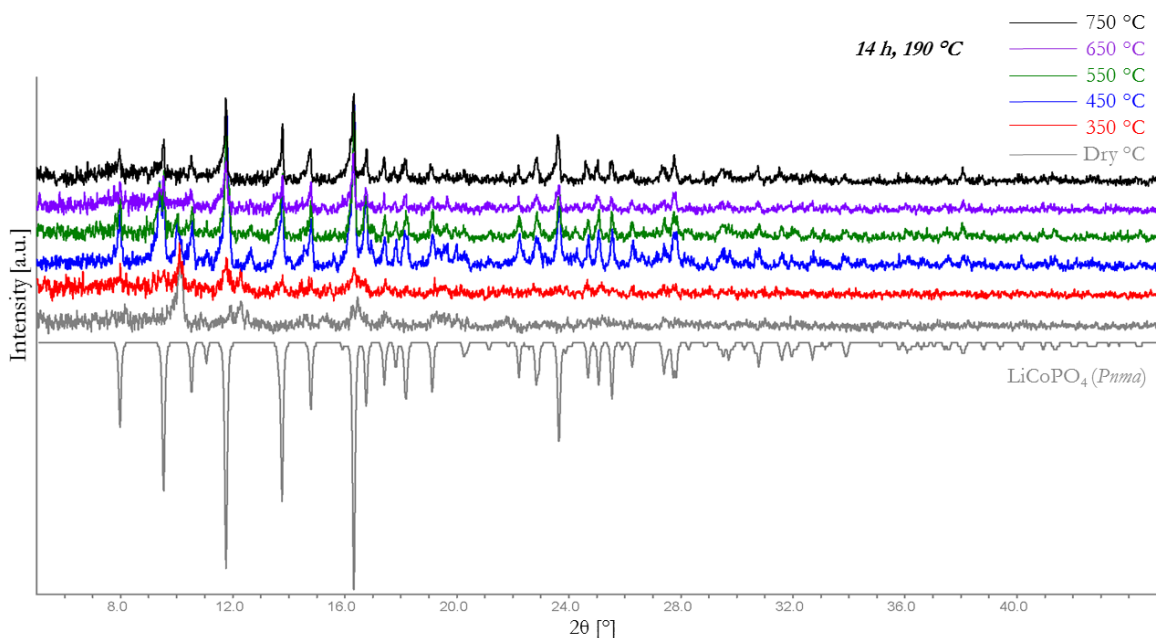


Figure 3-5: Effect of reflux temperature. XRD pattern of the samples refluxed at 190 °C for 14 h. Pattern recorded after the annealing at different temperatures. The negative intensity corresponds to the reported phases of LCP-*Pnma*.¹³⁴ (gray). The measuring time is 30 min.

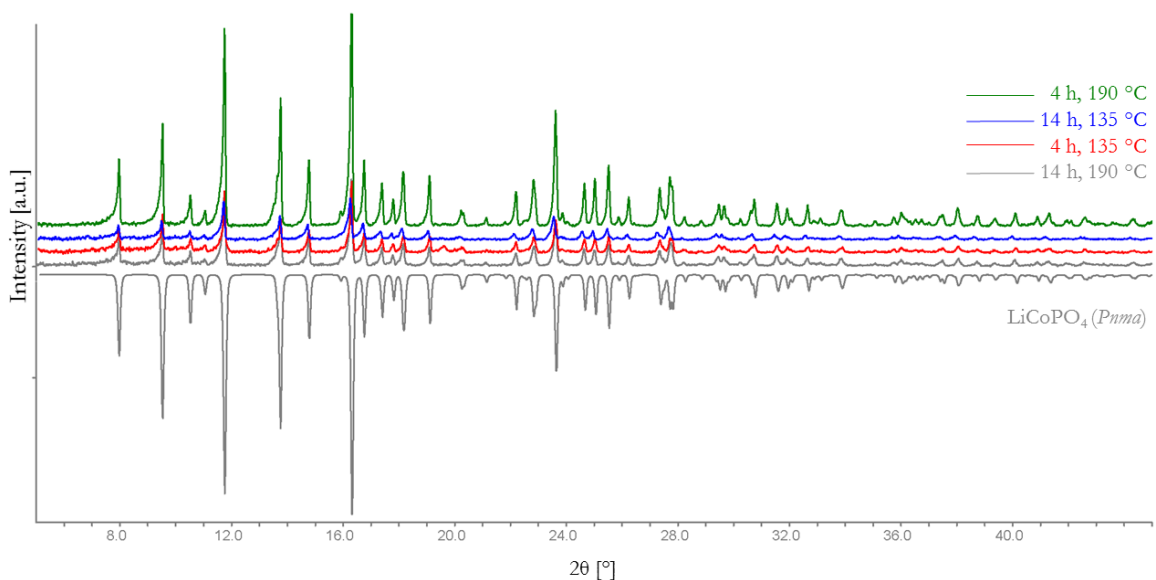


Figure 3-6: Effect of reflux temperature and time. XRD pattern after last annealing at 750 °C. The negative intensity corresponds to the reported LCP-*Pnma* (gray). The measuring time is 1 hour.

Equally important, evidence of the metastable behavior of the LCP-*Pn2₁a* phase is presented by Klingeler *et al.*¹⁴⁰ using a TGA/DSC analysis. The reported data shows an exothermic signal at 221 °C and confirms that the complete transformation to the olivine structure is reached after annealing at 300

°C. The TGA/DSC curve does not present additional exothermic/endothemic signals in the range from 300 °C to 700 °C; concluding that LCP-*Pnma* structure is stable at high temperatures. This information is also corroborated by TGA/DSC measurements in LCP-*Pn21a* samples prepared by mean sol-gel synthesis route ¹⁴¹. Table 3-3 presents the refined lattice parameters of the samples after the last annealing process and their comparison with the data reported for LCP-*Pnma* by ICSD ¹³⁴. The comparison does not represent a significant difference between the experimental lattice parameters and the reported ones.

Table 3-3: Lattice parameter of LCP-*Pnma* synthesized under different temperatures and reaction times. Reported lattice parameters are presented at bottom of the table to comparison

Set T (°C)	Time (h)	<i>a</i> (Å)	<i>b</i> (Å)	<i>c</i> (Å)	<i>V</i> (Å ³)	
135	14	10.2110(6)	5.9170(3)	4.6903(22)	283.4(3)	
190	14	10.2050(8)	5.9220(4)	4.6813(19)	282.9(4)	
135	4	10.2100(4)	5.9155(23)	4.6979(23)	283.7(3)	
190	4	10.2120(7)	5.9165(24)	4.6900(20)	283.4(3)	
Reported LCP-<i>Pnma</i>	-	-	10.2001(6)	5.9199(4)	4.6899(15)	283.2(9)

The morphology of the samples is shown in the figure 3-7. Here, a comparison between the samples after drying process and after the final annealing at 750 °C is sort. In general, after the drying process, the particles agglomerate in clusters of several μm. Particles sizes and shapes are not homogeneous and there is a mixture of several morphologies. Indeed, figure 3-7 c shows mixture of bars, beams and truncated polyhedra.

As consequence of annealing, particles suffer of densification processes and grain growth. This can be observed comparing figures 3-8 c and 3-8 d. After drying process, particles with bar shapes and angular edges are obtained. After annealing process, all of them show rounded borders and bigger agglomerates. Finally, the reflux time and reflux temperature does not affect the morphology of LCP-*Pnma*. The particle shapes after drying process, present in overall same particle shape and morphology: crossing bars, agglomeration of semi-rounded particles and big compact particles with flat surfaces. Even, after the suspension of the particles in ethanol in order to break the agglomerates, particles between 6-8 μm are identified (see figure 3-7 h).

The electrochemical performance is summarized in table 3-4. The best sample corresponds to the one obtained after 4 h of reflux at 135 °C, equivalent to 7.8% of the theoretical capacity. This low capacity value can be explain due to the formation of big particles and their long Li⁺ transport pathway during the intercalation process. The big mean domain size and big distances demands a higher amount of time

and energy to extract the lithium ions from the lattice. Additionally, it is well known, that the chemical reactivity is enhanced when the particle size becomes smaller and the diffusion distance is shortened^{142, 143}.

Finally, it is the first time that LCP-*Pn2₁a* is obtained using a polyol procedure in comparison with the expensive microwave methodology reported by Klingeler *et. al.*¹⁴⁰. Also, a deep analysis and further polyol experiments to obtain $\text{Co}_3(\text{HPO}_4)_2(\text{OH})_2$ as single phase, are relevant, since this compound may have a certain potential as photocatalyst for O_2 evolution; and has been produced only by complex hydrothermal methods^{144, 145}.

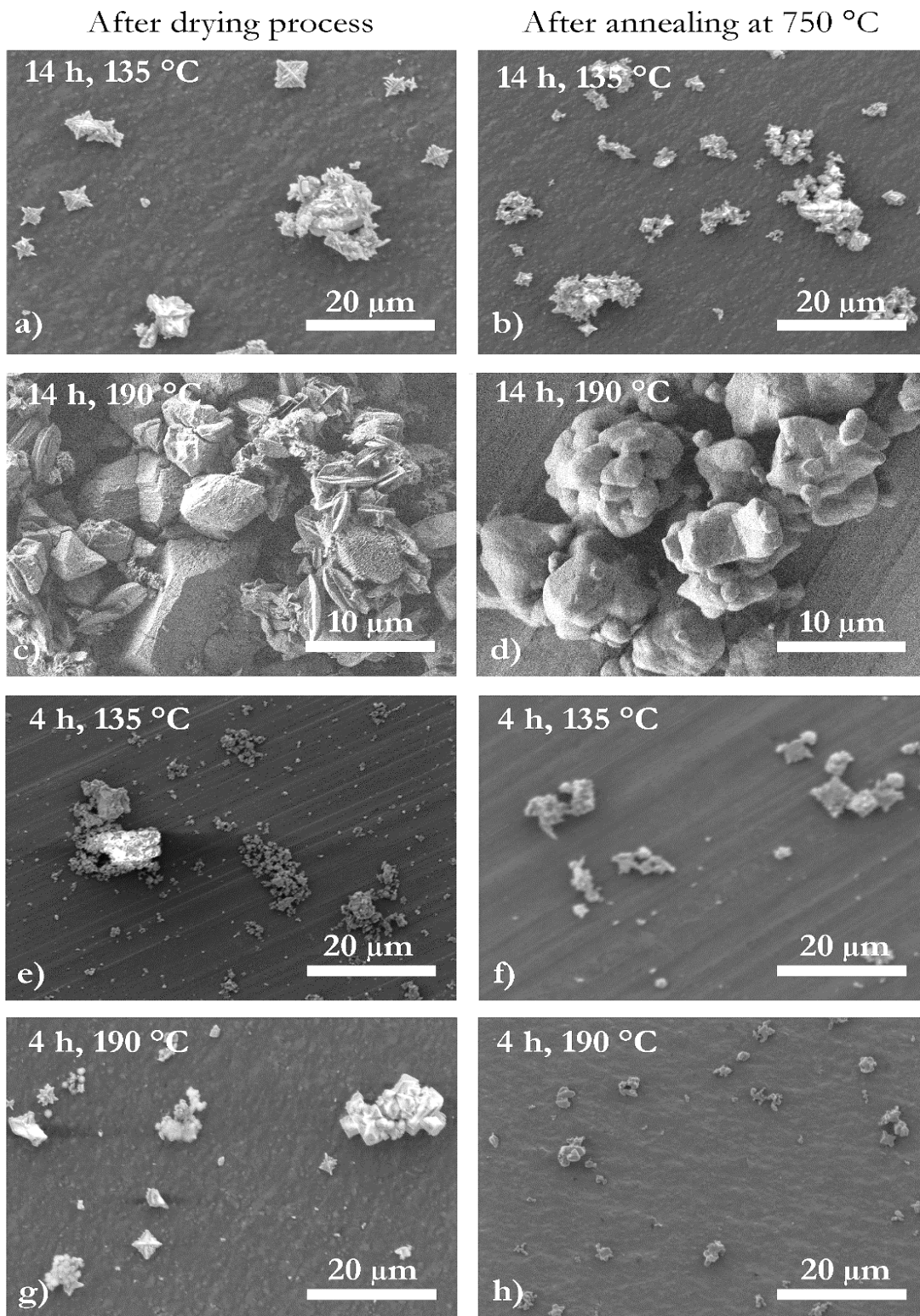


Figure 3-7: SEM images of the samples produced using the CoAc₂ and LDP system. The left side shows the samples after drying process. On the right side, the particles after the last annealing step at 750 °C. Microscope B. Magnification: a) 2000X, b) 5000X, c) 2000X, d) 2000X, e) 1000X, f) 1000X, g) 2000X and h) 2000X

Table 3-4: Capacity values of LCP-*Pnma* obtained by polyol synthesis (CoAc₂ and LDP system) after annealed at 750 °C. The measurements were made under different C-rates.

Set T (°C)	Time (h)	C/10 3 th Cycle	C/5 3 th Cycle	C/2 3 th Cycle	C 3 th Cycle	2C 3 th Cycle
135	14	6	4	3	3	2
190	14	10	8	7	6	5
135	4	13	10	7	5	3
190	4	11	8	6	5	4

As a final remark, this section demonstrates that *the obtained of LCP-Pnma in pure form or without the presence of secondary phases does not assures a good electrochemical performance*. This conclusion permits to focus on the morphology control and grain size as next factors to improve in the polyol synthesis of LCP-*Pnma*. This topic is described in the following section.

3.1.2.2 Influence of the surfactants on the morphology

The last section explains a useful method to synthesize LCP-*Pnma*, however, the electrochemical performance is poor due to the big particle size, wide range in the particle size distribution and the formation of randomly oriented agglomerates above 20 µm. As commented in the introduction section, PVP has been use to control the particle size and particle morphology in the synthesis of cathode materials. Table 3-5 presents the main experiments conducted using PVP as surfactant, based on the synthesis using CoAc₂ and LDP starting materials.

Table 3-5: Highlighted experiments for the synthesis of LCP-*Pnma* using the CoAc₂ and LDP system with PVP

Educts	Li:M:P Ratio	LCP:PVP Ratio	Batch size (mmol)	Set T (°C)	Time (h)
LDP (1,0 M), CoAc ₂	1:1:1	1:4	0.03	135	4
PVP dissolved half in EG and half in CoAc₂ solution at 100 °C					
LDP (1,0 M), CoAc ₂	1:1:1	1:4	0.03	190	14
PVP dissolved in CoAc₂ solution					
LDP (1,0 M), CoAc ₂	1:1:1	1:4	0.03	190	4
PVP dissolved in CoAc₂ solution					
LDP (1,0 M), CoAc ₂	1:1:1	1:4	0.03	135	4
PVP dissolved in CoAc₂ solution					

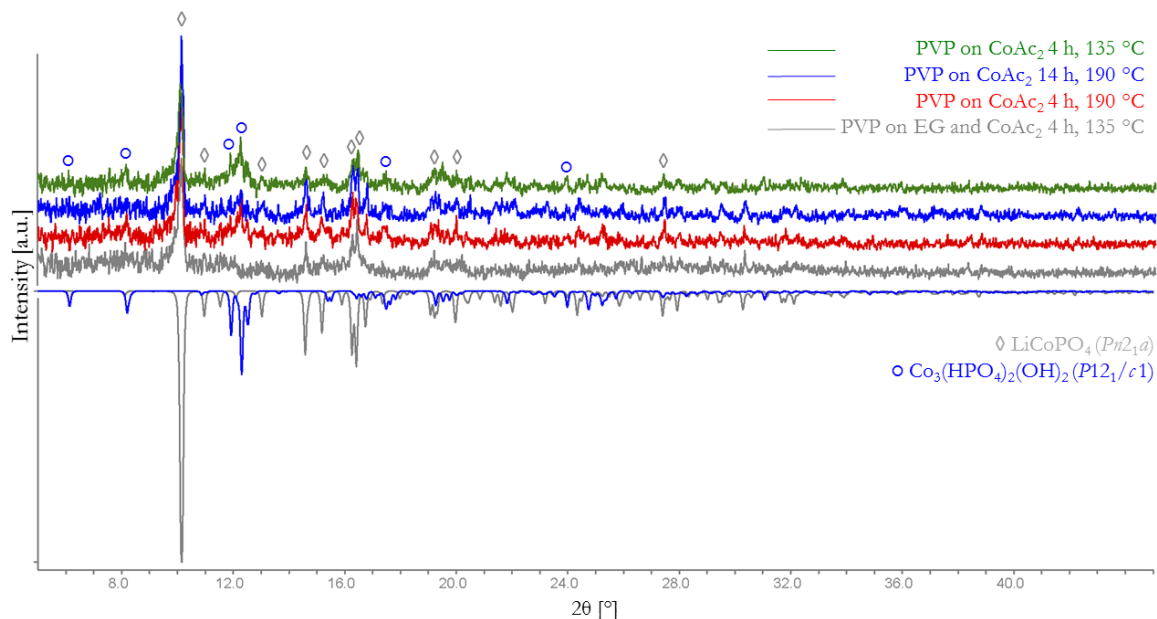


Figure 3-8: Influence of PVP surfactant. PXRD patterns of the samples synthesized using PVP after drying process. The negative intensity corresponds to the reported LCP- $Pn2_1a$ (◊ gray) and $\text{Co}_3(\text{HPO}_4)_2(\text{OH})_2$ (○ blue). The measuring time is 30 min.

Figure 3-8 presents the PXRD pattern of the samples after drying process. Here a mixture between LCP- $Pn2_1a$ and $\text{Co}_3(\text{HPO}_4)_2(\text{OH})_2$ is observed. In comparison to the experiments of the last section conducted at high temperatures (190 °C), no reflections corresponding to LCP- $Pnma$ are found. One of the reasons is the change of the reaction conditions for the chemical species in the solution. When PVP is added to the polyalcohol, its non-ionic surfactant property makes its dissolution easier and, on the other hand, the amide group (N and O atoms) creates strong affinity to a single unit of cobalt-ion¹⁰⁹ (see figure 3-9). This imide-cobalt bond also helps to stabilize the particle growth and increases the probability of nucleus development during the particle formation period. Furthermore, the cobalt-ion particles will be surrounded by the long polymeric chain of PVP, inducing stabilization and formation of tetrahedral coordinated complexes; specifically, the formation of LCP- $Pn2_1a$ ^{146, 147} and $\text{Co}_3(\text{HPO}_4)_2(\text{OH})_2$. The PVP promotes a change in the thermodynamic conditions and kinetics of the polyol synthesis; however, further studies should be done in order to analyze the complete mechanism and equilibrium of chemical species during reaction.

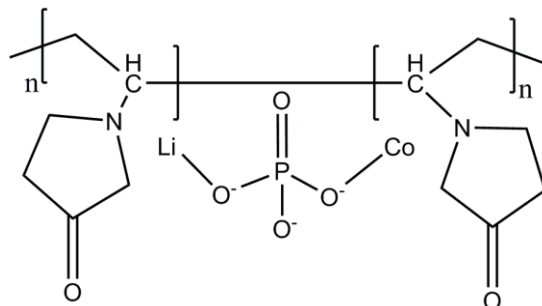


Figure 3-9: Schematic representation of the bonding between LCP and PVP. Discrete metal collide on PVP backbone

After completing the annealing procedures, LCP-*Pnma* is obtained (see figure 3-10). For each experiment the lattice parameters are similar compared to the ones reported in the literature (see table 3-6). This confirms that PVP does not influence the crystallographic parameters of the final samples.

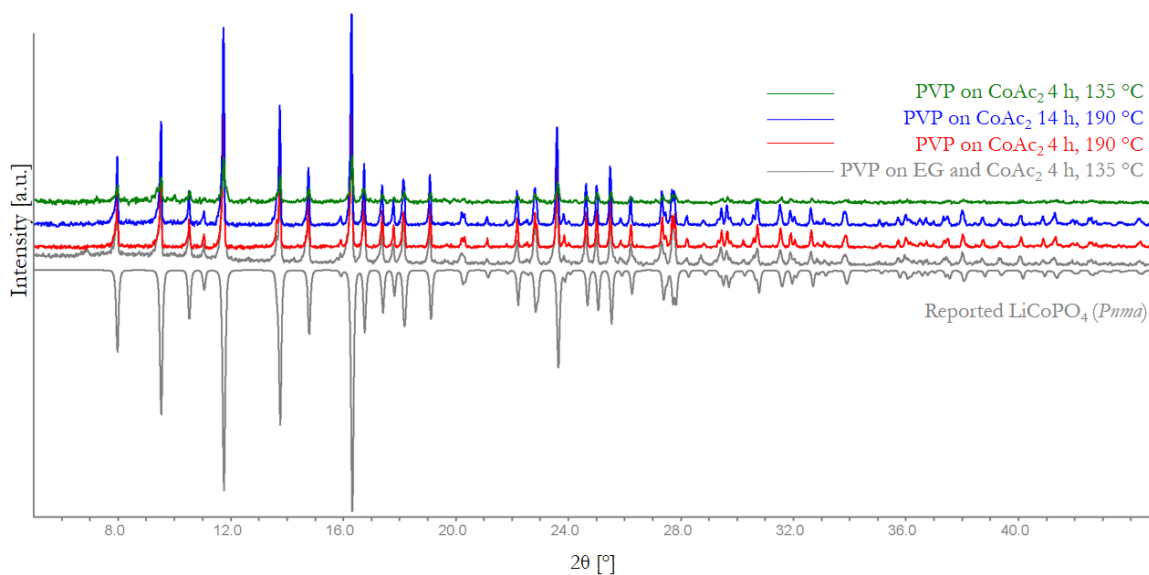


Figure 3-10: Influence of PVP surfactant PXRD patterns of the samples synthesized using PVP. The negative intensity corresponds to the reported LCP-*Pnma* (gray). The measuring time is 1 hour.

Table 3-6: Lattice parameters and crystallite size of LCP-*Pnma* synthesized under different temperatures and reaction times with PVP. Reported lattice parameters are presented at bottom of the table

Set T (°C)	Time (h)	<i>a</i> (Å)	<i>b</i> (Å)	<i>c</i> (Å)	<i>V</i> (Å ³)	Mean domain size (nm)
135	4	10.211(6)	5.914(3)	4.691(22)	283.3(3)	53.7
190	14	10.194(8)	5.918(3)	4.685(22)	282.6(4)	42.9
135	4	10.193(7)	5.919(3)	4.686(23)	282.8(3)	53.7
190	4	10.195(5)	5.913(4)	4.692(20)	282.8(3)	42.9
Reported LCP - <i>Pnma</i>	-	-	-	-	-	-
		10.2001(6)	5.919(4)	4.6899(15)	283.2(9)	

The morphology of the samples is strongly influenced by the use of PVP; specifically, by how it is dissolved and mixed with the CoAc₂ and LDP precursors. As seen in figure 3-13 a and 3-14 a, spheres with average size of 3-5 μm are obtained. These spheres are formed by primary nano-sheet structures and their surface reveals some degree of porosity. Figures 3-13 c to 3-13 h, show that the precursor (powder recovered after drying) and the final product (powder recovered after annealing) present a mixture between irregular blocks, cross-link bars and agglomerates of particles of several μm. In the case of the spheres, the amount of PVP is split in two: one part dissolved with CoAc₂/EG and the other with EG. Thus, the PVP/EG dissolution is added during the dropping of LDP into a CoAc₂ solution improving the surfactant effect during nucleation and growth processes. On the contrary, for the other experiments, the PVP is completely added on the CoAc₂/EG solution and, LDP solution is added dropwise afterwards. A scheme explained the formation of the spheres is depicted in figure 3-11.

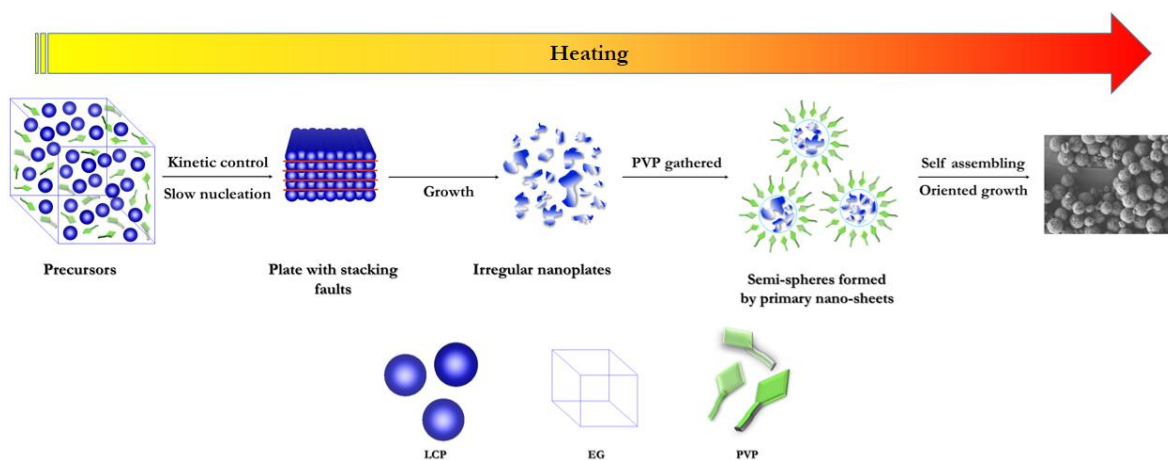


Figure 3-11: Schematic illustration of the growth mechanism of LCP microspheres with PVP

These experimental details are important since, some publications report the advantages of 3D hierarchical nano/micro structures because the electrochemically active planes are preferred exposed and this unique feature can reduce the length of Li⁺/electron diffusion and increase the intercalation kinetics^{32, 148, 149}. However, most of them do not specify the way that surfactants are mixed, dissolved or which molar ratio (surfactant:educts) is used.

In addition, the time and temperature variations do not influence the phase composition this polyol synthesis. The capacity of the samples are shown in the table 3-7. The best capacity mark is presented by the samples with micro-sphere morphology, corresponding to 16.2 % of the theoretical capacity. This value corresponds to the double in comparison to the best sample obtained without PVP, but still too

far from the theoretical capacity. This behavior is explained from the morphology and shape of the particles.

First, the porosity of the samples collapses due to the successive annealing processes. Here, thermally activated processes, such as solid state diffusion, provide mechanisms where the dislocations and interfaces of the material may be removed or arranged in configurations of lower energy. As this process is conducted along long temperatures (350 °C) up to high temperatures (750 °C), recovery processes and recrystallization processes are also involve. The first implicates a partial restoration of the properties because the dislocation structure is not completely removed. The second implicates the formation of new dislocation-free grains within the deformed or recovered structure. Further annealing may result in normal grain growth or a the selective growth of a few large grains (abnormal grain growth or secondary recrystallization)^{150, 151}. A scheme of these processes is shown in figure 3-12 a to 3-12 d.

Second, although the micro-spheres produced with PVP are homogeneous in size, giving a discrete particle size range, the SEM pictures reveal particles bigger than the spheres with cubic forms that can deplete the ionic and electronic transport. The Li⁺ extraction path are extremely big can even work as isolator when they are located above the spheres. This can be confirmed by the SEM images of figures 3-13 a, 3-13 b and 3-14 d.

Third, the surfactants are also considered not only as tool to control the morphology but as source of carbon used for coating. However, even if a carbon coating layer exists, it could be not conductive, not homogenous or it can be highly width. Additionally, inhomogeneous coating difficulty the extraction of Li⁺ ions. This behavior is illustrated in the figures 3-12 e to 3-12 g.

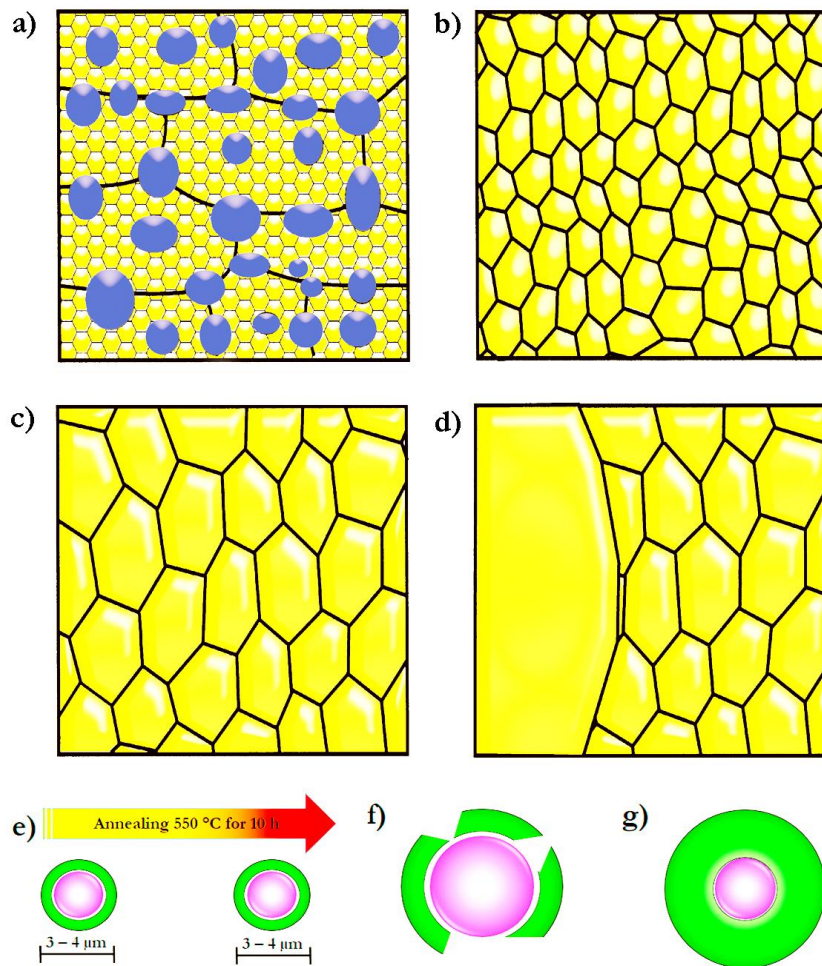


Figure 3-12: Schematic diagram of the annealing processes: a) Partial recrystallization b) Full recrystallization c) Grain growth d) Abnormal grain growth. PVP functionality and issues: e) Protective layer against grain growth d) Inhomogeneous C-coating e) Highly thick C-coating

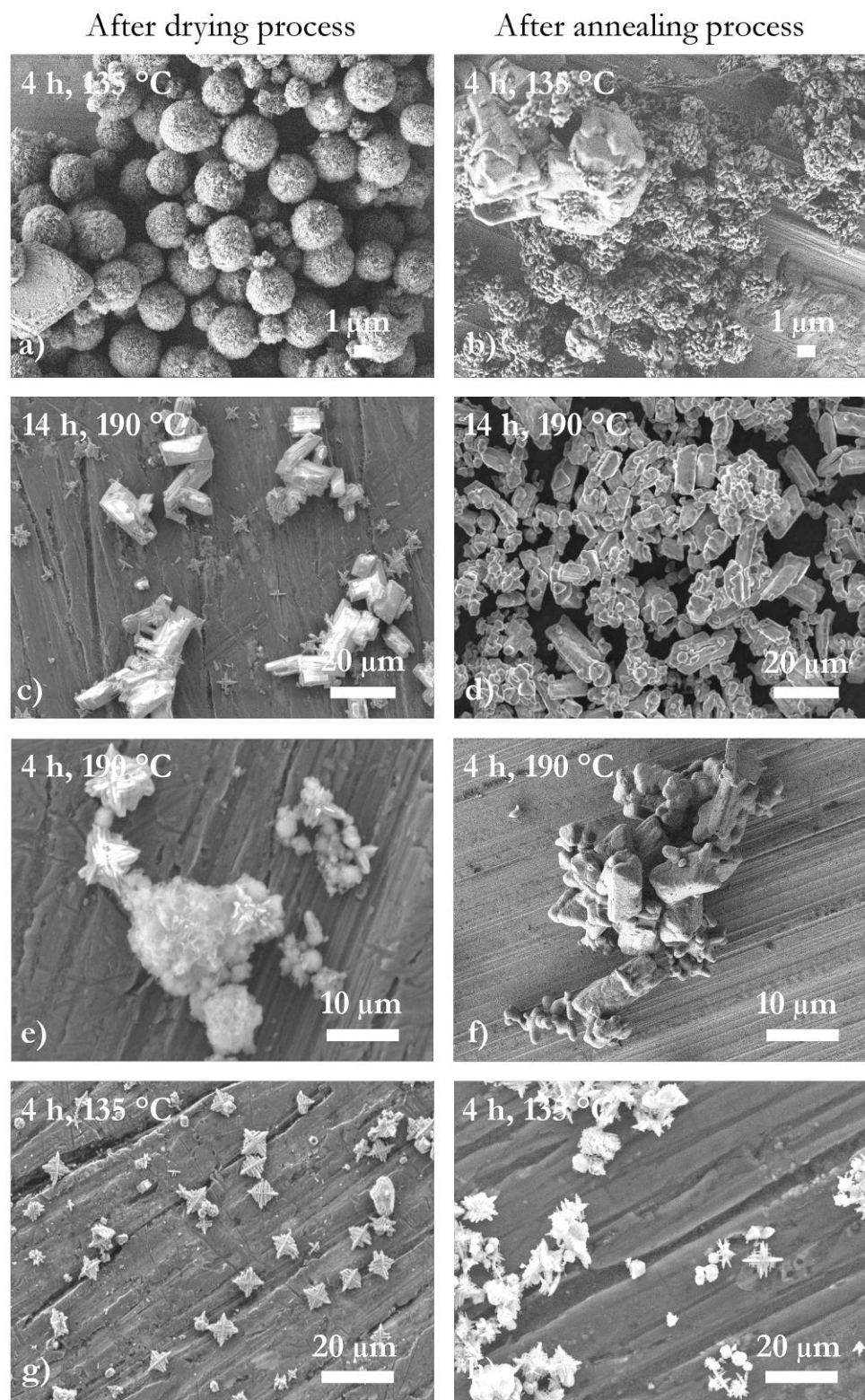


Figure 3-13: SEM images of the samples produced using the CoAc_2 and LDP system with PVP. The left side shows the samples after drying process. On the right side, the particles after the last annealing step at 750 °C. **a) - b)** PVP dissolved half on EG and half on CoAc_2 solution at 100 °C; **c) - h)** PVP dissolved on CoAc_2 solution. Microscope B. Magnification: a) 5000X, b) 5000X, c) 2000X, d) 2000X, e) 1000X, f) 1000X, g) 2000X and h) 2000X

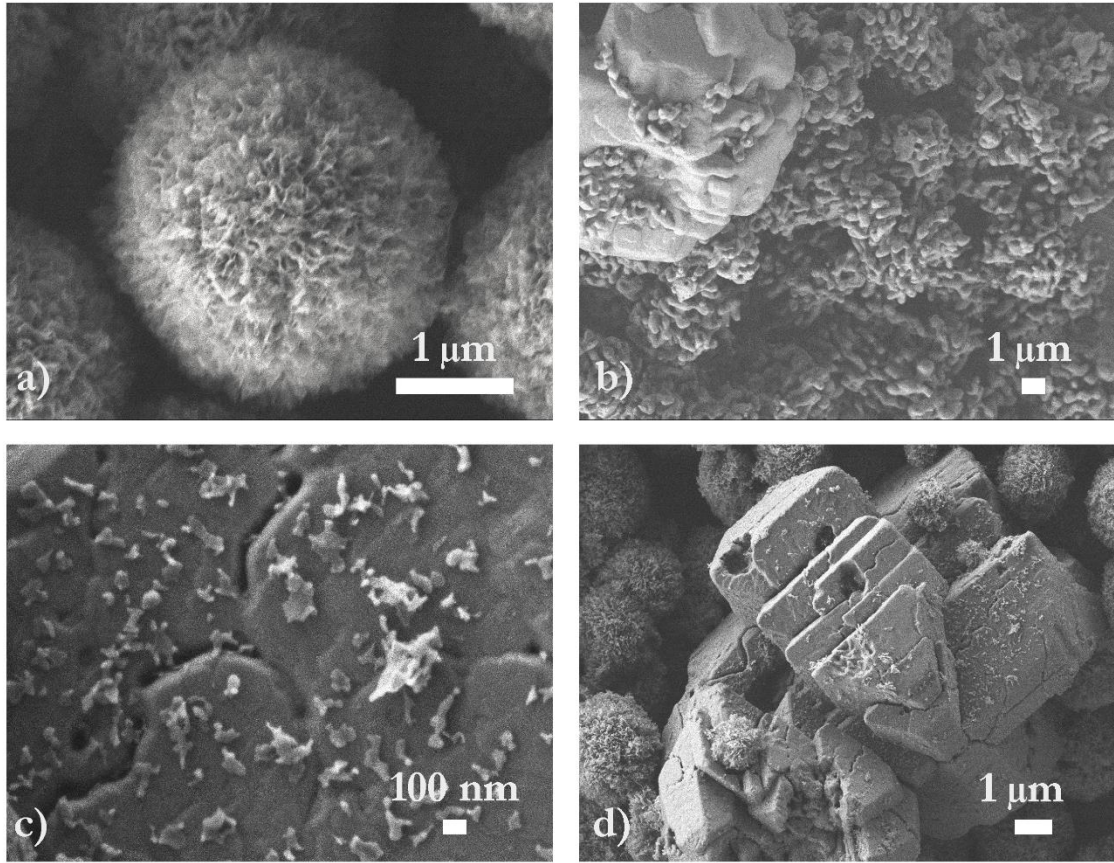


Figure 3-14: SEM images of LCP-*Pnma* synthesized using PVP. **a)** Sample after drying process. Detailed view of the spheres. Micro-spheres are formed by primary nano-sheets **b)** Sample after annealing. The porosity collapses after the successive annealing in order to complete the formation of LCP-*Pnma*. **c)** Detailed view of the primary nano-sheets **d)** Additional to the spheres, big blocks of around 6 μm are also present. Microscope B. Magnification: a) 25000X, b) 10000X c) 50000X and d) 8000X

Table 3-7: Morphology, average grain size of LCP-*Pnma* of figure 3-13 and capacity values after annealed at 750 °C. The measurements were made under different C-rates.

Morphology	Figure	Average grain size	C/10 3 th Cycle	C/5 3 th Cycle	C/2 3 th Cycle	1C 3 th Cycle	2C 3 th Cycle
Agglomerated Spheres	3-13 a - b	Spheres: 3-5 μm Primary layers: <100 nm	27	20	14	9	7
Irregular blocks/spheres	3-13 c -d	\approx 6 μm	14	10	7	6	5
Irregular blocks/spheres	3-13 e - f	\approx 1 – 5 μm	12	9	6	5	3
Cross-link bars agglomerates	3-13 g - h	\approx 4 μm	6	5	4	3	2

3.1.2.3 Influence of the annealing process program

As presented before, an effort to control the particle size and shape is done using PVP; however, the formation of agglomerates, collapse of porosity and possible effects of the carbon coming from the surfactant are the main reasons of the poor electrochemical performance. In this sub-section a single and long annealing at 550 °C for 10 h is tested in order to counteract the negative effects of successive annealings.

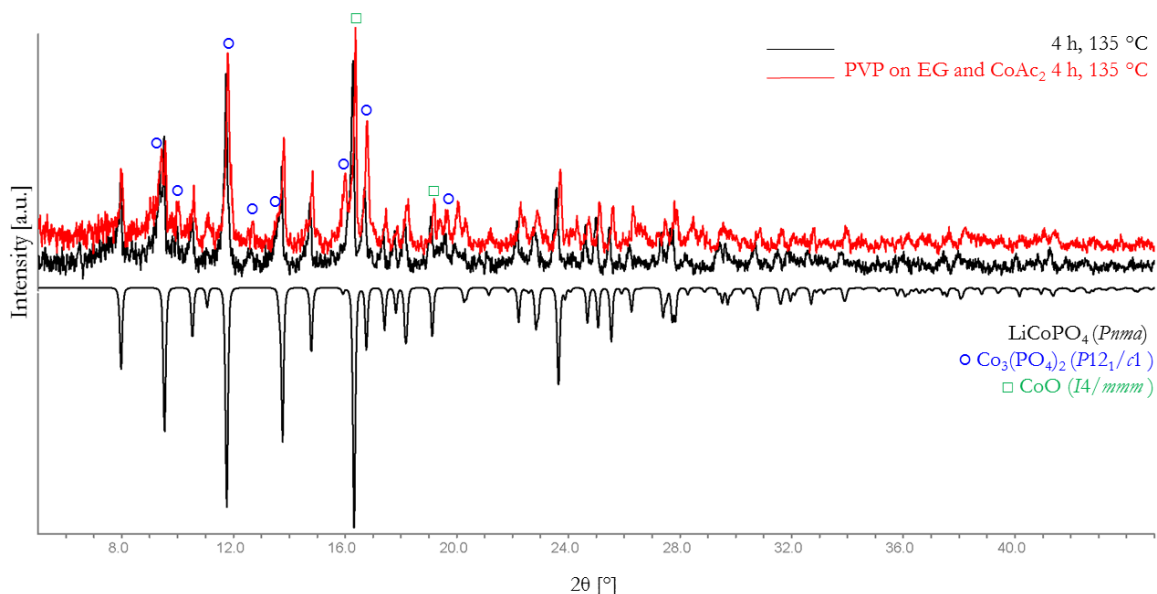


Figure 3-15: PXRD pattern of samples after annealing for 10 h under air atmosphere at 550 °C. In **red** the synthesis uses a precursor using PVP as surfactant. In **black** the synthesis uses a EG:Water ratio of 70:30 (mL). The negative intensity corresponds to the reported LCP-*Pnma* (**black**), $\text{Co}_3(\text{PO}_4)_2$ -*P12₁/c1* (○ **blue**) and CoO -*I4/mmm* (□ **green**). The measuring time is 1 hour.

The precursors used are the same from previous synthesis at 135 °C for 4 hours with and without PVP (samples collected after drying process). The figure 3-15 shows the PXRD pattern of the samples after one single-long annealing. In both cases, the main phase corresponding to LCP-*Pnma* is achieved; however, secondary phases corresponding to $\text{Co}_3(\text{PO}_4)_2$ and CoO are present. Regarding the purity of the phase, it was found that a single and longer annealing step does not achieve the complete formation of the olivine. Regarding the morphology of the samples, figures 3-16 a and 3-16 b present a high degree of agglomeration of particles forming units of several μm . On the other side, the annealing of the sample using PVP shows that the spherical shape of the particles is conserved as well the primary nano-sheets structures. After cycling, the values of capacity decrease for the sample without PVP; in contrast, for the PVP sample, they improve. Only in this case it can be assured that a single thermal treatment is better

for the electrochemical performance in comparison to the successive thermal process until 750 °C (see table 3-8).

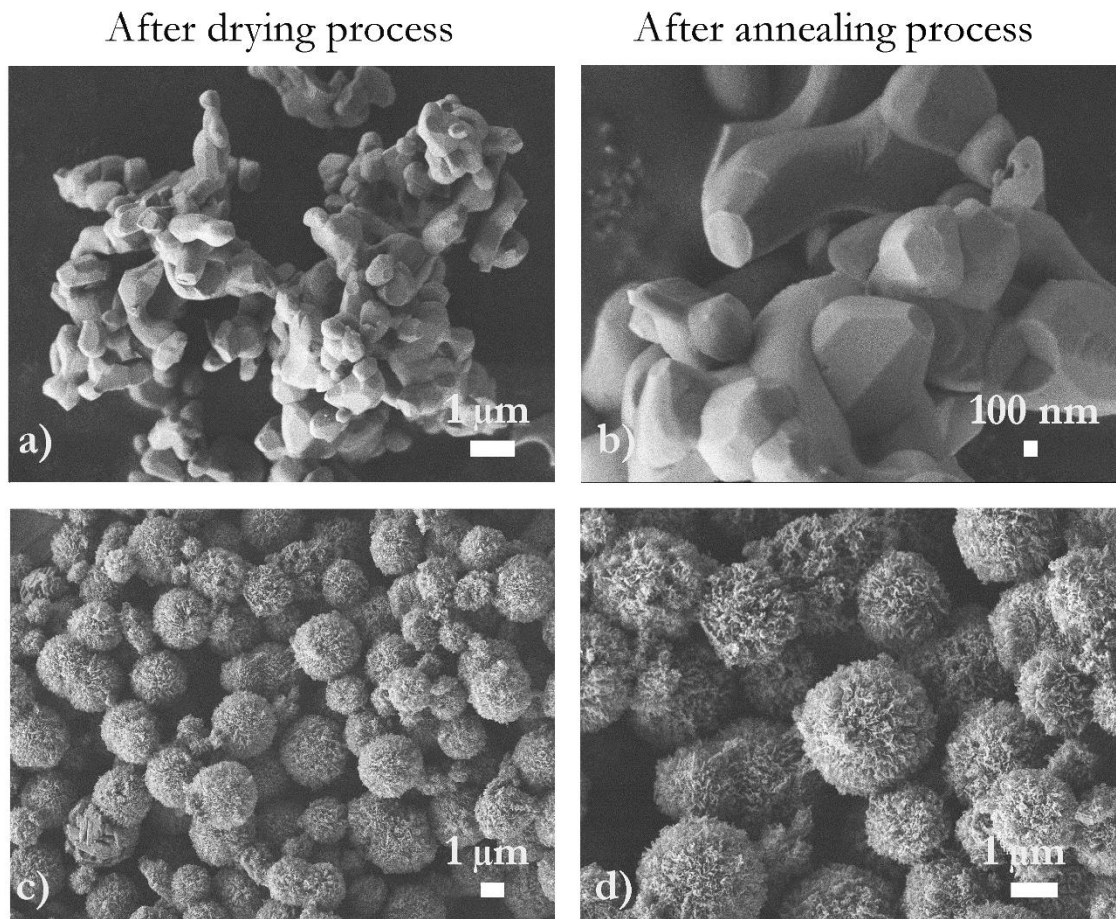


Figure 3-16: SEM images of LCP-*Pnma* synthesized using the CoAc₂, LDP system. **a – b:** Samples produced without PVP **c – d:** Samples produced with PVP. Microscope B. Magnification: a) 9500X, b) 30000X c) 5000X and d) 10000X.

Table 3-8: Capacity values and BET areas of LCP-*Pnma* using a single-long annealing procedure

PVP	Set T (°C)	Time (h)	Mean domain size (nm)	BET m ² g ⁻¹	C/10 3 th Cycle	C/5 3 th Cycle	C/2 3 th Cycle	C 3 th Cycle	2C 3 th Cycle
No	135	4	35.8	2.8	11	8	5	3	2
Yes	135	4	30.7	19.0	34	26	18	13	9

The increase of capacity is due to a rise of the active surface area and smaller crystallite size. The figures 3-14 c and 3.14 d reveal that the micro-spheres are composed by primary nano-sheets with irregular form. Those nano-sheets are coupled leaving spaces between them. These spaces act like pores facilitating the access of the electrolyte to the active material and, as consequence, the electrochemical active area is increased. In order to corroborate this statement, BET measurements were performed. For the sample obtained without PVP the BET value is 2.8 and for the sample obtained with PVP 19.0.

Despite the increase of the surface area, the capacity remains at 20.3% of the theoretical value. It is considered that secondary phases, such as Li_3PO_4 and Co_3O_4 serve as separation media that partly prevents LCP-*Pnma* particles from direct degradation due to contact with the electrolyte¹³⁸. However, in the samples synthesized $\text{Co}_3(\text{PO}_4)_2$ and CoO are no considered intercalation compounds, they are present in a considerable amount, and their possible protective role on LCP can not be verified. Finally, after annealing, the sample with PVP conserves the morphology; this indicates that PVP can create a protective coating-layer that prevents particle growth and particle densification during the long annealing process.

As final remark, this section clarifies the importance of the morphology and particle size in the design and electrochemical performance of cathode materials. It is important to obtain a high crystalline material, with small and homogenous particle size distribution and high electrochemically active areas. Those parameters are strongly correlated and influence the capacity retention and overall electrochemical performance in LIB systems.

3.1.2.4 Influence of the water content on pre-dissolution of CoAc_2

In the section 3.1.1 (Synthesis using CoAc_2 , ADP and LiAc) a pre-dissolution of the educts in water was used; however, this associates a decrease of EG boiling point at refluxing conditions, or in other words, the measured boiling point is lower than the boiling point of pure EG. Now, CoAc_2 was pre-dissolved in water and its influence on the morphology was analyzed. Figure 3.17 shows the PXRD pattern of the samples after the drying process. A main phase corresponding to LCP-*Pn2₁a* and small phase corresponding to LCP-*Pnma* were found. After annealing at 400 °C for 1 hour, a pure LCP-*Pnma* is obtained (see figure 3.18). From the PXRD patterns, the signal/background ratio increases (using approximately the same amount of substance), in comparison to the PXRD pattern of section 3.1.2 (see figure 3-2). The pre-dissolution of CoAc_2 is beneficial in order to increase its solubility; as well as, to decrease the viscosity of the solvent mixture that improves the reaction with de LDP. After one single, short annealing process, the complete formation of LCP-*Pnma* without impurities was obtained. A refinement of the lattice parameters is shown in table 3-9. This is a good achievement, because the short annealing at relatively low temperatures are beneficial against the grain growth and densification of particles. Figure 3-19 shows the SEM images of the samples after drying and annealing. All samples present a common trend based on the formation of agglomerates composed by primary nanoparticles smaller than 500 nm and micro-sized particles under 4 μm . These values and morphology features are summarized in the table 3-12. SEM images also reveal the strong change in the shape of the particles, suggesting that water induces the reduction of the primary particles size; since most of them are under

smaller than one μm (see figure 3-19 b). The previous dissolution of CoAc_2 reveals that the amount of water influences the preliminary steps of grain growth and nucleation. This is a strong tool, as the first experiments have showed sections of particles of several μm (see figure 3-7 c) that increase their size during annealing. Furthermore, the phase transition from LCP- $Pn2_1a$ to LCP- $Pnma$ requires a less of amount of time and energy during the annealing process. In general, the process can be improved, if instead of trying to reach temperatures over $320\text{ }^\circ\text{C}$ with the use of several annealing steps, a fast crystallization of the LCP- $Pn2_1a$ follow by a short annealing is used. This leads an easier formation of the olivine structure.

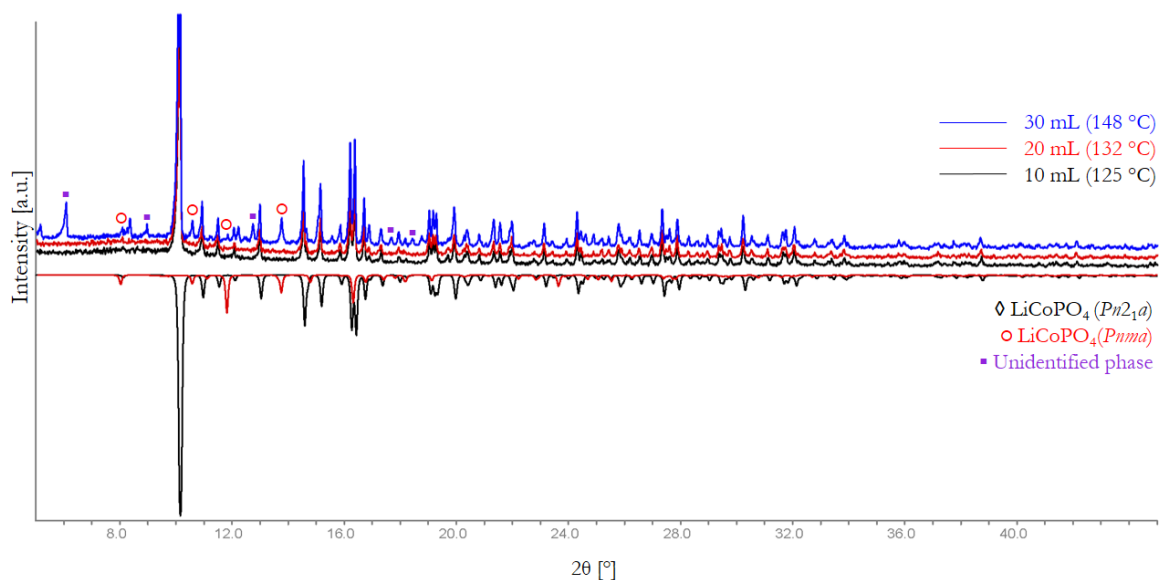


Figure 3-17: Influence of the water content in the pre-dissolution step. PXRD after drying process. The negative intensity corresponds to the reported LCP- $Pn2_1a$ ¹⁴⁰(**black**). LCP- $Pnma$ (**○ red**) and an unidentified phase (**■ Lila**). The measuring time is 20 mins.

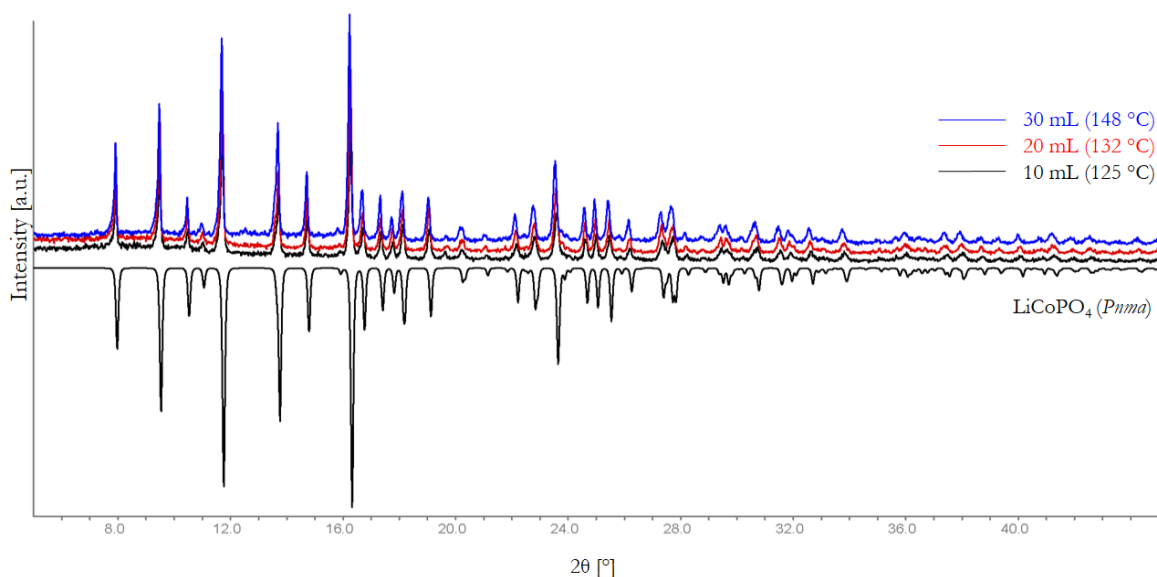


Figure 3-18: Influence of the water content in the pre-dissolution step. PXRD after annealing process at 400 °C for 1 hour. The negative intensity corresponds to the reported LCP-*Pnma* (Black). The measuring time is 1 hour.

Table 3-9: Lattice parameter of LCP-*Pnma* synthesized using different water volumes in the pre-dissolution step. Reported lattice parameters are presented at bottom of the table

Volume water (mL)	<i>a</i> (Å)	<i>b</i> (Å)	<i>c</i> (Å)	<i>V</i> (Å ³)	Mean domain size (nm)	
30	10.178(8)	5.915(3)	4.690(6)	282.4(6)	42	
20	10.177(7)	5.915(3)	4.687(5)	282.2(4)	35	
10	10.193(6)	5.914(3)	4.686(3)	282.5(3)	42	
Reported LCP- <i>Pnma</i>	-	10.2001(6)	5.9199(4)	4.689(15)	283.2(9)	-

The values of the electrochemical capacity are presented in the table 3-10. Compared with the values of the table 3-4, a small improvement of the capacity can be observed. This could be attributed to the small average particles size of LCP-*Pnma*, due to the use of a single-short annealing process. Besides, the comparison of the samples after annealing (figures 3-7 and 3-19) reveals that a single short annealing induces more homogeneity along all samples and, even if some particles in the μm range exist, they will have less impact to the reduction of the capacity. The sample that used a volume of 30 mL of water in the pre-dissolution step presents some particles with plate-like or sheet-like form. This morphology is responsible of the increase in the capacity value due to the preferred oriented form. Some publications report that the plate-like morphology is beneficial in the improvement of Li-ion intercalation rate and diffusivity processes^{152, 153}. This means that the increase of the capacity can be directly related with the morphology of the sample. However, a deeper study of the influence of the water:polyalcohol ratio on the morphology should be addressed in order to find the best water:polyalcohol ratio and the

morphologic changes after the annealing process. The best value in this section corresponds to the 22% of the theoretical capacity. Finally, the active BET area is smaller than the one obtained using PVP as surfactant.

Table 3-10: Capacity values and BET areas of LCP-*Pnma* produced using different amounts of water

Morphology	Average grain size	mL H ₂ O	BET m ² g ⁻¹	C/10 3 th Cycle	C/5 3 th Cycle	C/2 3 th Cycle	C 3 th Cycle	2C 3 th Cycle
Irregular agglomerates	Primary particles: under 100 nm Agglomerates under 5 um	10	6.1	32	24	17	12	8
Truncated bars and beams	Primary particles: under 100 nm Agglomerates under 5 um	20	5.8	31	22	14	9	6
Mixture of plates and bars	Bars: 475 nm x 900 nm Plates 1.5 – 3.5 um	30	5.6	36	25	19	10	7

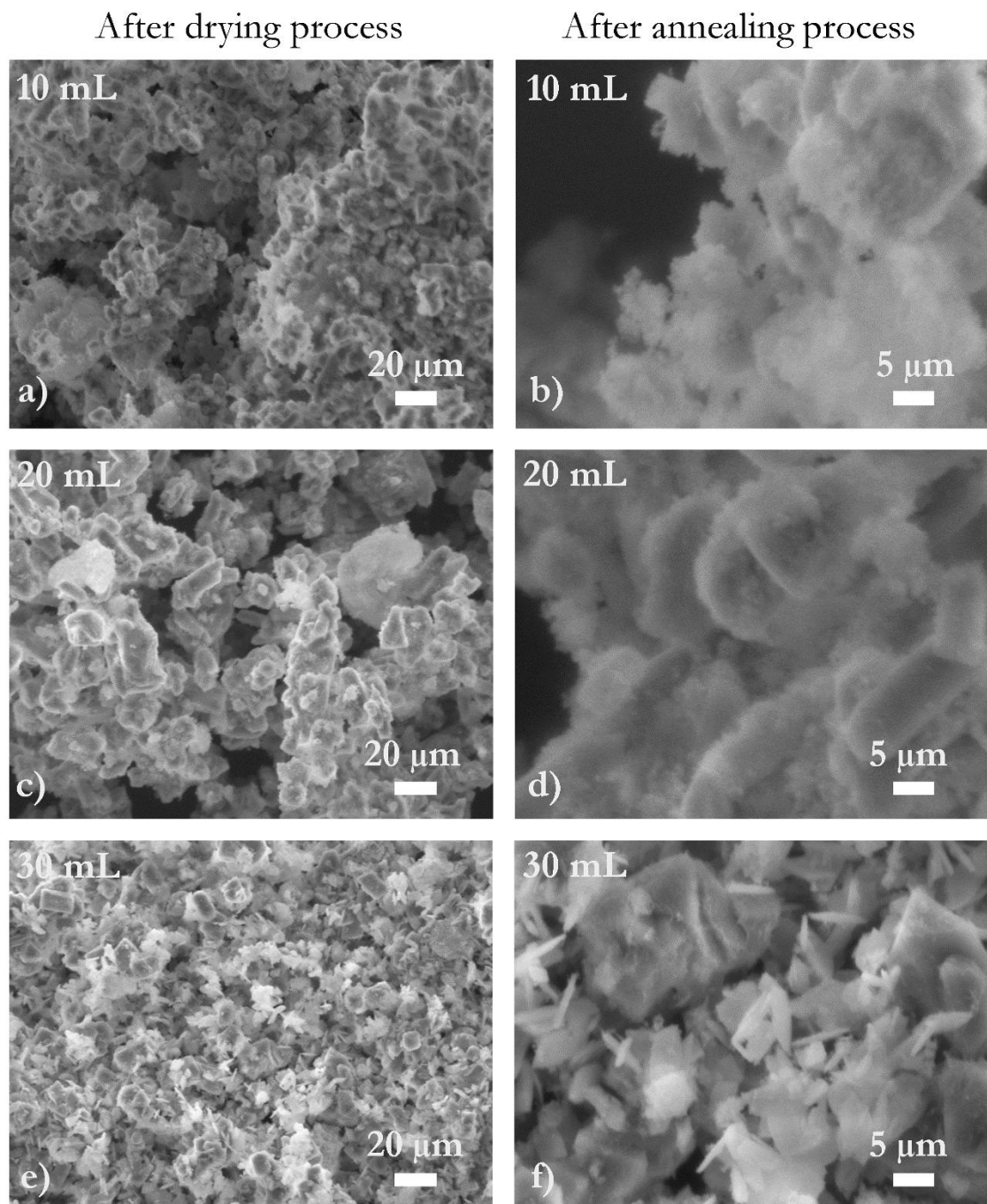


Figure 3-19: SEM images of the samples produced using the CoAc₂ and LDP with different amounts of water. **Left side:** shows the samples after drying process. **Right side:** the particles after annealing at 400 °C. **a) - b)** 10 mL; **c) - d)** 20 mL; **e) - f)** 30 mL. Microscope A. Magnification: left column 1000X, right column 4000X

3.1.2.5 Influence of additional synthesis parameters on the crystal structure and morphology using the CoAc₂ and LDP system

This sub-section describes the influence of the used polyalcohol solvent and cobalt source on the synthesis of LCP-*Pnma*. Despite no electrochemical characterization was performed due to the presence of secondary phases, it is important to discuss briefly the strong impact of those synthesis parameters on the crystal structure and morphology of the samples. The results are present in order to identify experimental conditions that let enhance the morphology control.

3.1.2.5.1 Influence of the polyalcohol media (solvent)

The synthesis of LCP is strongly dependent on the temperature; thus, in the section 3.1.2.1 the effect of the reflux temperature on the formation and equilibrium between LCP-*Pnma* and LCP-*Pn2₁a* phases was subject of discussion. Previously, EG was used with a maximal boiling point of 190 °C; thereafter, a set of different polyalcohols with higher boiling points (b.p.) was tested: DEG, b.p 244 °C; TEG, b.p 285 °C; and TTEG, b.p 314 °C. From these experiments, two main discussion points are derived.

The first point, it is related with the real temperature under refluxing conditions. In the section 3.1.2.1 the temperature of the heating device was set-up at 190 °C and right after the drying process of the samples, a mixture of phases composed by LCP-(*Pn2₁a*/*Pnma*) and Co₃(HPO₄)₂(OH)₂ are obtained. The use of solvents with higher boiling points should increase the temperature, and as consequence, the energy of the system to favor the formation of the LCP-*Pnma* phase. However, in the figure 3-20 it is clear that for all the solvents used (DEG, TEG and TTEG) the phase obtained after drying is LCP-*Pn2₁a*. After complete reproductions of the syntheses using the polyalcohols mentioned above, the measured temperatures under reflux conditions did not exceed a maximum of 230 °C (see figure 3-20).

The difference between the theoretical b.p. and the experimental measured b.p. under refluxing conditions has two main reasons. First, is the water content introduced by the cobalt precursor. In cobalt acetate, the central cobalt orbit is coordinated by four water molecules¹⁵⁴, those water molecules induce the decrease of the boiling point during synthesis. ***Second***, despite cobalt acetate becomes anhydrous at 140 °C and additional experiments were done using the anhydrous form; ***the system does not reach water-free conditions.*** This occurs because the polyalcohol may contain residues of water and there is water coming from the environment. This can happen due to the system is an open one. Other aspect to underline is that the signal/background ratio for the syntheses using TTEG is higher compared to the synthesis using TEG and DEG.

On the other hand, as inquisitiveness point (presented in the section 3.1.2) is the fact that the reaction conducted in EG shows some reflections corresponding to LCP- $Pnma$. Since the temperature does not overcome the value of 190 °C, the reaction in EG solvent has less chances to reach LCP- $Pnma$ compared with the synthesis in DEG, TEG and TTEG solvents; nevertheless, the olivine phase is present in small amount. The reason of this remains unclear, and there are factors that could play a role in the formation of different intermediary species, such as solubility of the precursors as a function of the viscosity, heating rate, and possible formation of Co-O-H-P intermediaries as function of the temperature.

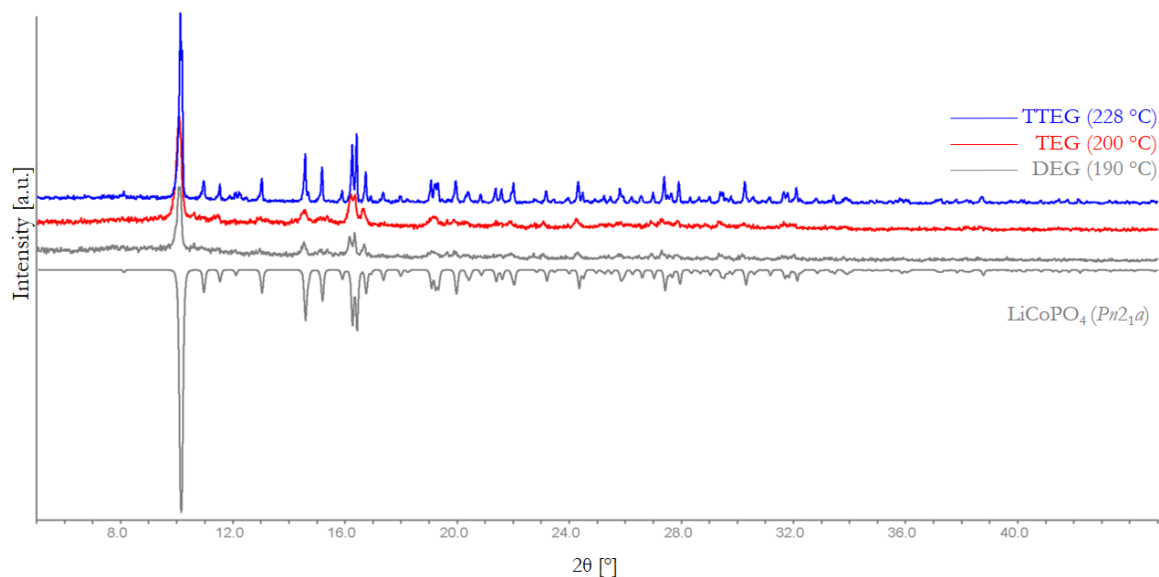


Figure 3-20: Influence of the polyalcohol media. PXRD of samples refluxed using DEG, TEG and TTEG with their respective b. p. reached. Pattern recorded after the drying process. The negative intensity corresponds to the reported phase of LCP- $Pn2_1a$ (grey). The measuring time is 20 min.

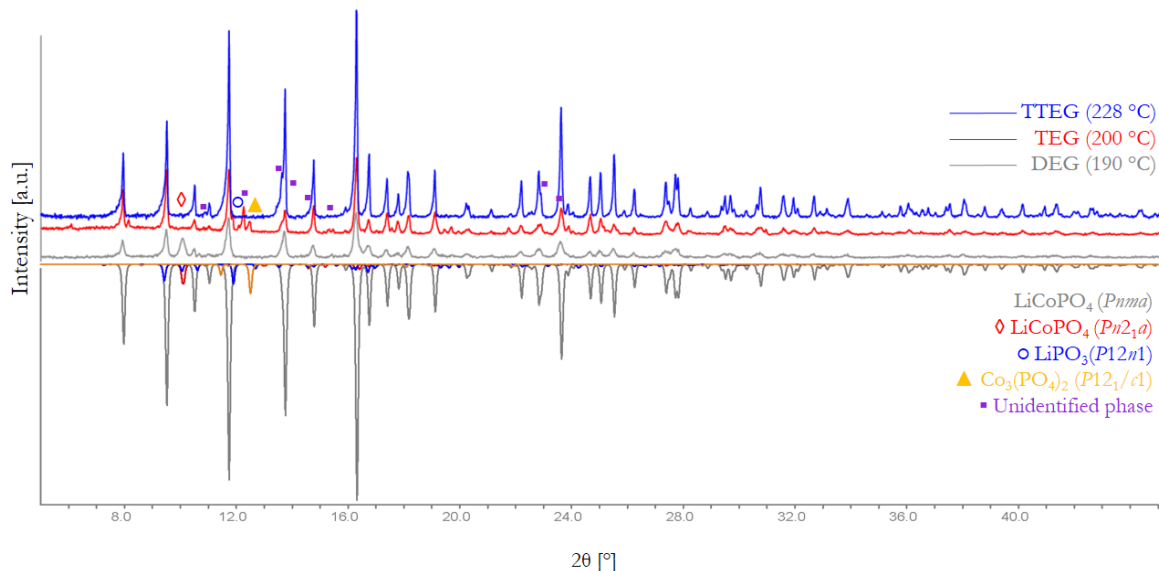


Figure 3-21: Influence of the polyalcohol media. Solvents: DEG, TEG and TTEG with their respective b. p. reached. Pattern recorded after annealing at 400 °C for 5 hours under air. The negative intensity corresponds to the reported phases of LCP-*Pnma* (grey), LCP-*Pn21a* (◊ red), LiPO_3 -*P12n1* (○ blue), $\text{Co}_3(\text{PO}_4)_2$ -*P121/c1* (▲ orange) and a unidentified phase (■ lila). The measuring time is 20 min.

The second discussion point is related with the morphology of the sample. Figure 3-22 shows the SEM pictures of the dried and annealed samples synthesized using DEG, TEG and TTEG. In general, it can be seen that using high b.p. polyols a formation of primary nm particles is strongly preferred. The pictures after drying process in figure 3-22 reveal particles under 1 μm . In contrast, the particles synthesized in EG, after drying process are bigger in size and form more complex and bigger agglomerates (see figure 3-7). It can be observed in pictures 3-18, 3-12 and 3-7. No substantial differences between in the shape of the particles after synthesis in DEG, TEG and TTEG are observed. However, it has to be noted that after annealing densification and grain growth processes has happened. Furthermore, the reduction of particle size is beneficial (as demostred with the capacity values), but still there are problems due to the strong agglomeration of the particles which can not be dispersed at the moment of the ink preparation and contributes to the decrease of the electrochemical performance.

As final remark, the main outcome using high b.p. polyols is the fact that the particle size can be strongly reduced. Nevertheless, the control of agglomeration and secondary phases should be improved by testing additional water:polyalcohol ratios and combine it with the use of surfactants.

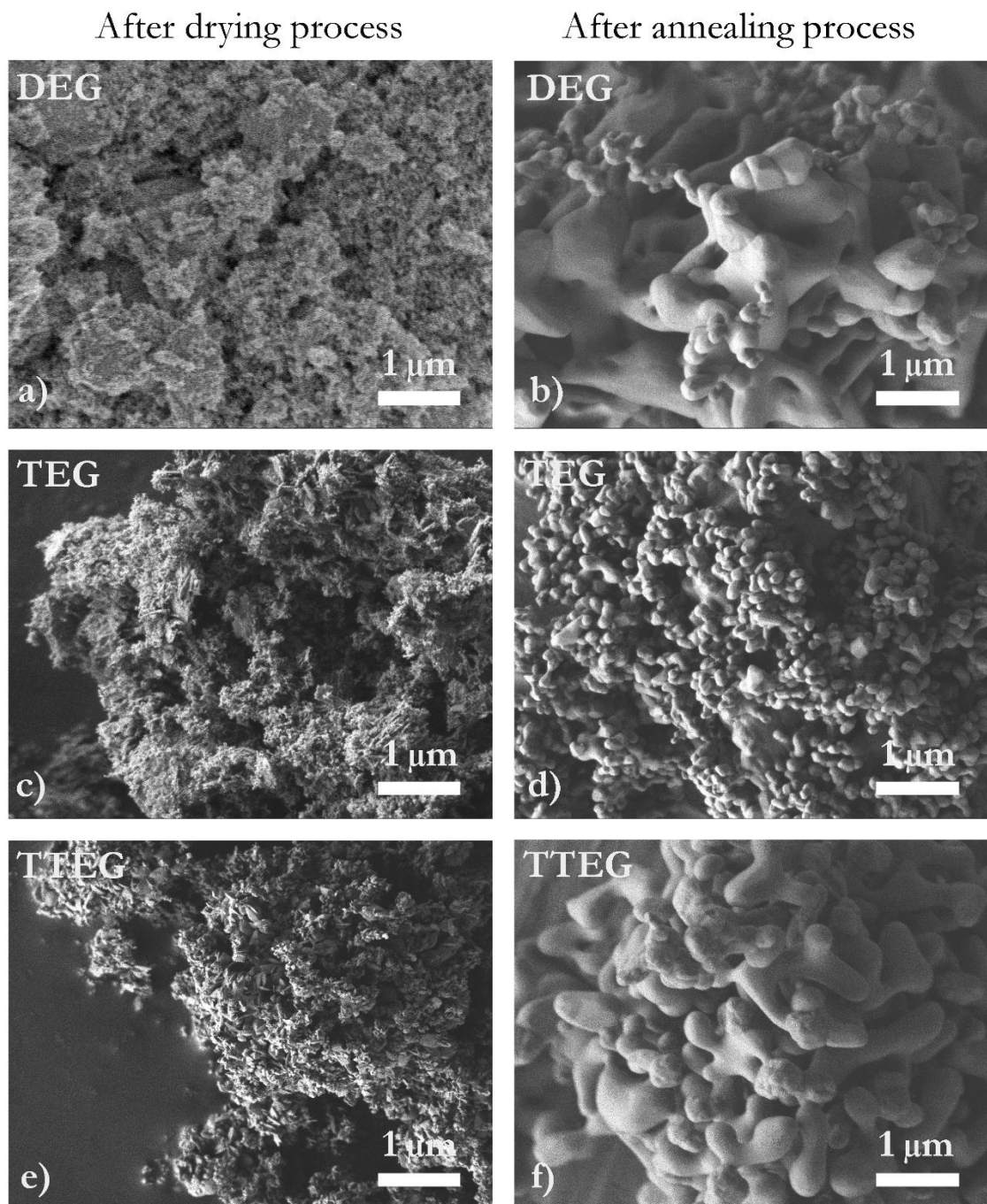


Figure 3-22: SEM images of the samples produced using the CoAc₂ and LDP system with different polyalcohols. The pictures correspond to the samples after drying/annealing process. **a)** DEG; **b)** TEG; **c)** TTEG. Microscope B. Magnification: left column 10000X, right column 20000X

3.1.2.5.2 Combination of pre-dissolution of CoAc_2 in water and high b.p. polyols

This case combines a pre-dissolution step of CoAc_2 in 30 mL of water and the use of DEG, TEG, TTEG. Figures 3-23 and 3-24 show the PXRD patterns after drying and annealing respectively. Main phases are corresponding to LCP- $Pn2_1a$ after drying and LCP- $Pnma$ after annealing. The measurement of the temperature of the solution under refluxing conditions reveals a decrease of the boiling point due to the water used in pre-dissolution step of CoAc_2 . The samples present a high signal:background ratio; however, after annealing, secondary phases are presented (see figure 3-24). An interesting point is that particles conserve their morphology after annealing process. As seen in figure 3-25, the particles does not present the same densification and agglomeration as particles obtained without CoAc_2 pre-dissolution (see figure 3-22). Morphology and average grain size is summarized in table 3-11.

Equally important, after annealing the samples do not agglomerate and do not suffer a remarkable grain growth, as happened for samples of the last section. This implies that the water content allows to conserve the size and the homogeneity along all the samples after the thermal treatment. Particles also do not agglomerate after annealing in the same way as it is seen in figure 3-22. These experiments confirm the ability of water to protect the particles of strong agglomeration; as well as, achieve a narrow size distribution.

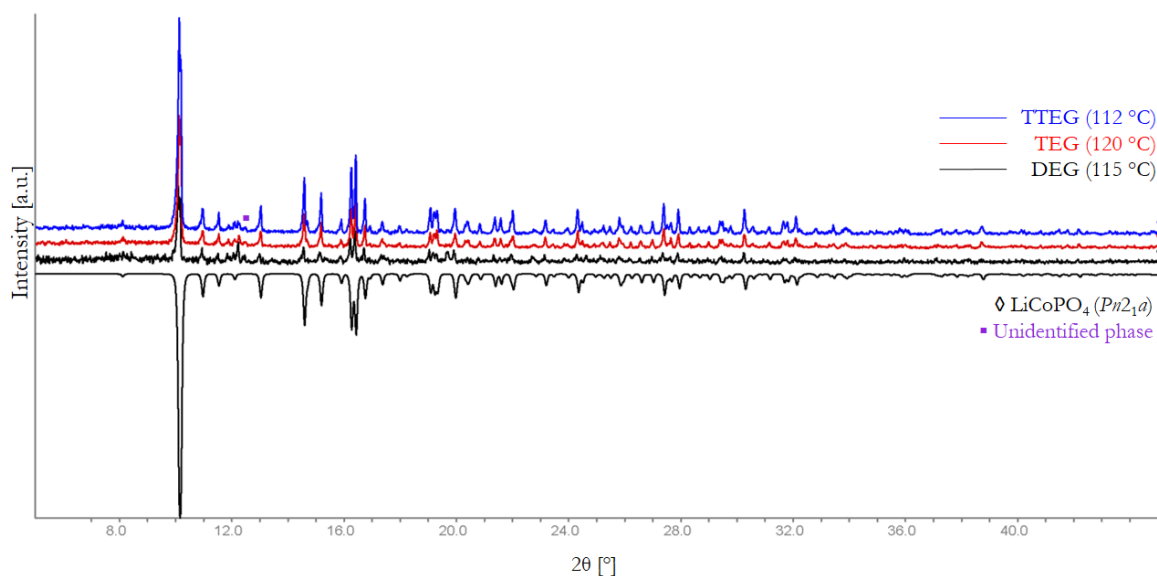


Figure 3-23: Influence of the predissolution of CoAc_2 and polyalcohol media. PXRD patter of the samples after drying. The negative intensity corresponds to the reported phases of LCP- $Pn2_1a$ (◊ black) and an unidentified phase (■ lila). The measuring time is 20 min.

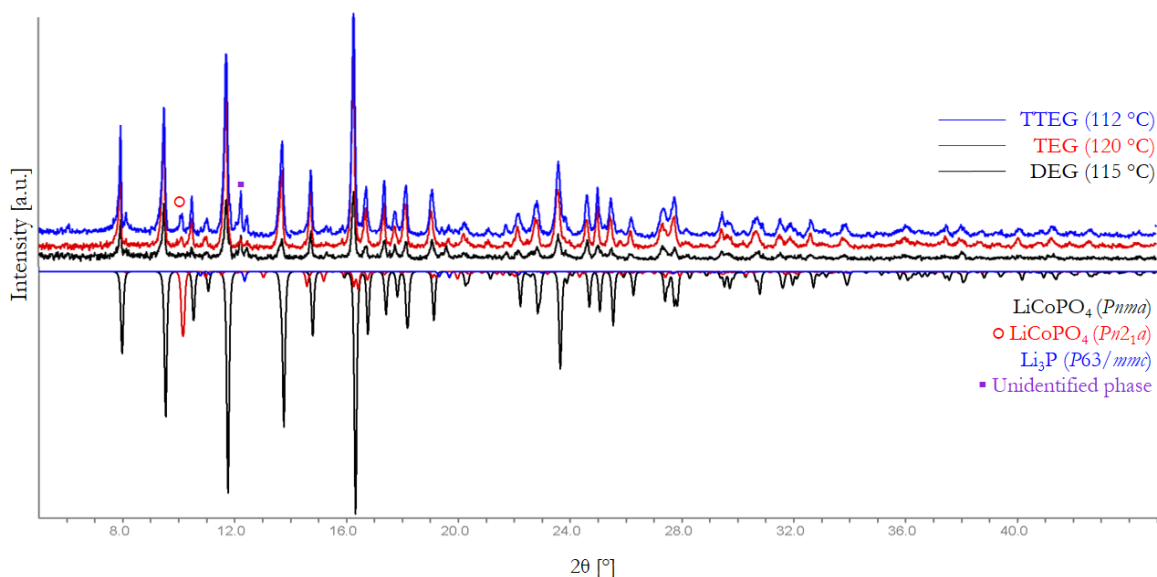


Figure 3-24: Influence of the predissolution of CoAc_2 and polyalcohol media. PXRD of the samples after drying at 400 °C for 1 hour under air. The negative intensity corresponds to the reported phases of LCP- $Pnma$ (black), LCP- $Pn2_1a$ (red), Li_3P - $P6_3/mmc$ (blue), and an unidentified phase (purple). The measuring time is 20 min.

Table 3-11: Morphology and average grain size of particles of LCP- $Pnma$ synthesized using the CoAc_2 and LDP system in various solvents.

Solvent	Morphology	Average grain size
TTEG	Bars	Length: 4.0 μm , width: 1.8 μm
TEG	Truncated bars and beams	Length: 3.0 μm , width: 678 nm
DEG	Mixture of plates, semi-spheres and bars	Length: 3.0 μm , width: 794 nm Ovals: 300 nm

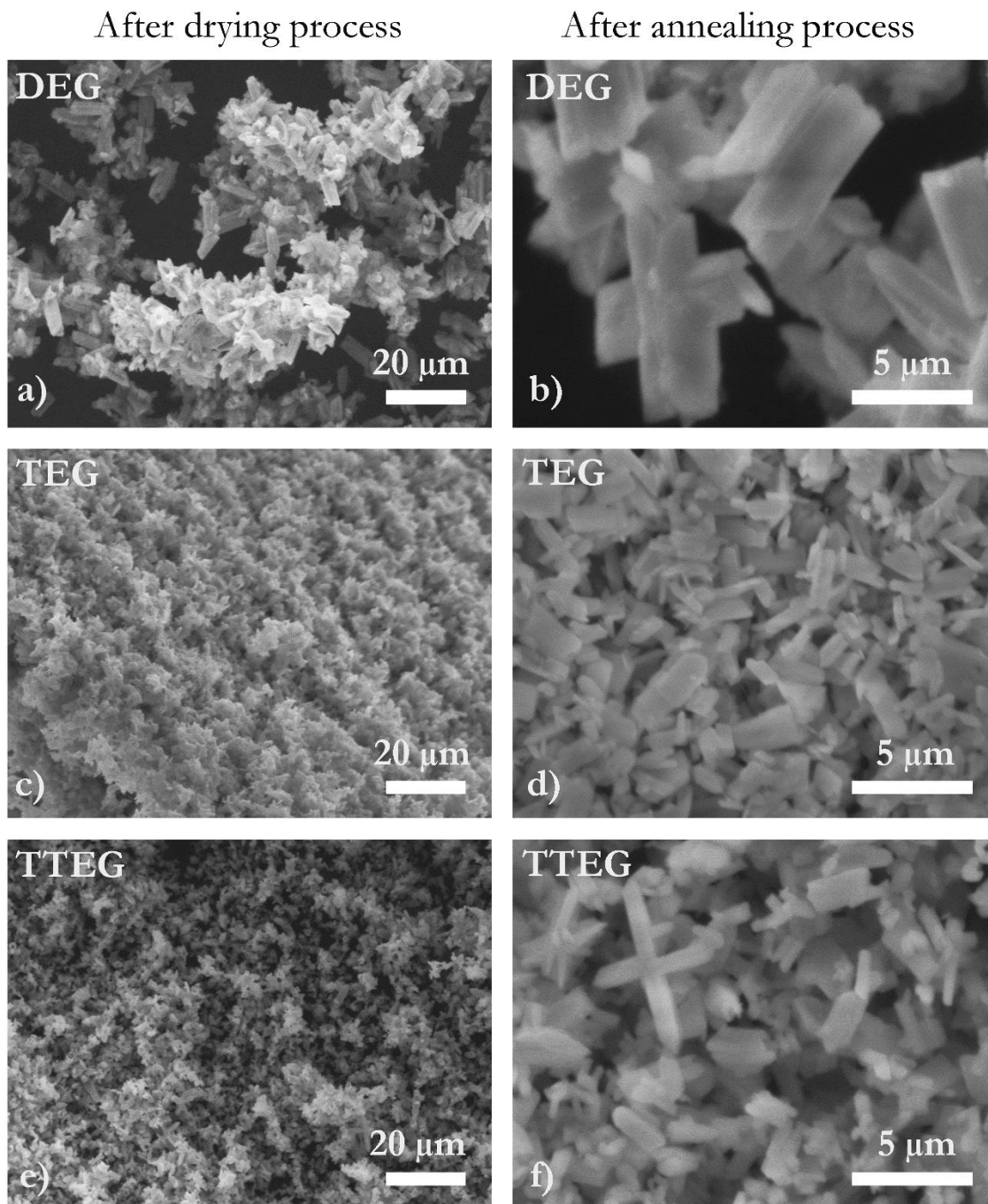


Figure 3-25: SEM images of the samples produced using the CoAc₂ and LDP system with pre-dissolution of CoAc₂ in 10 mL water. The pictures correspond to the samples after drying/annealing process. **a)** DEG; **b)** TEG; **c)** TTEG. Microscope A. Magnification: left column 1000X, right column 6000X

3.1.2.5.3 Influence of the cobalt source

As commented before, the CoAc_2 precursor is used in its tetrahydrate form and the water content induces a decrease of the boiling point of the polyalcohol under reflux conditions. In order to reach higher temperatures, two experiments using cobalt carbonate (CoCO_3) and cobalt sulfate anhydrous (CoSO_4) in TTEG were done. Figure 3-26 shows the PXRD pattern after drying process. As a result, both experiments show LCP-*Cmcm* as a main phase. After annealing of the samples at 400 °C for 1 hour (see figure 3-27), LCP-*Cmcm* is still present accompanied by a considerable proportion of CoSO_4 . No reflections corresponding to LCP-*Pnma* were found; moreover, the boiling point kept under 300 °C for both cases. This leads the discussion to three final points.

First, the use of an open reflux-system will never reach the conditions to obtain a single phase of LCP-Pnma without annealing. Assuming that the temperature under refluxing conditions could overcome 300 °C, there will be some water content that avoids reaching this value. The measure of the temperature at the beginning of the reaction shows a value over 300 °C; however this value decrease during the reaction until a value around 240 °C in both cases. On the other hand, even if the atmosphere is controlled, as reported by Wang ¹²⁶ in his reported polyol procedure under nitrogen atmosphere, a final annealing procedure at 650 °C is necessary to obtain the desire olivine phase.

Second, the use of CoCO_3 and CoSO_4 promotes the formation of LCP-Cmcm. The change in the cobalt precursor influences the chemical equilibrium between the species during the reaction. In contrast to the tendency of Co^{2+} to form tetraedrally-coordinated compounds, in this case, Co^{2+} prefer an octahedrally-coordination. The formation of the LCP-*Cmcm* is a disclosure, based on the fact that it has been synthesized only by high-pressure and high-temperature solid-state synthesis (6 GPa, 900 °C) from LCP-*Pnma* and by microwave assisted synthesis from a mixture of $\text{CoC}_2\text{O}_4 \cdot 2\text{H}_2\text{O}$, $\text{LiOH} \cdot \text{H}_2\text{O}$ and H_3PO_4 ^{155, 156}.

Third, the cobalt educts strongly influence the morphology of the samples. Figure 3-28 shows the SEM pictures before and after annealing. In the case of CoSO_4 , the formation of rounded beams or spheroid particles is noted. After annealing, the particles are bigger and another morphology is observed: μm size agglomerates that are formed by primary stacked sheets. On the other hand, the sample produced from CoCO_3 , shows a mixture of sheets and irregular nanoparticles wich tend to agglomerate after annealing, as happened with DEG, TEG and TTEG LCP-*Pnma* samples. In this case, the grain growth of the particles is smaller than in the case of particles produced from CoSO_4 precursor.

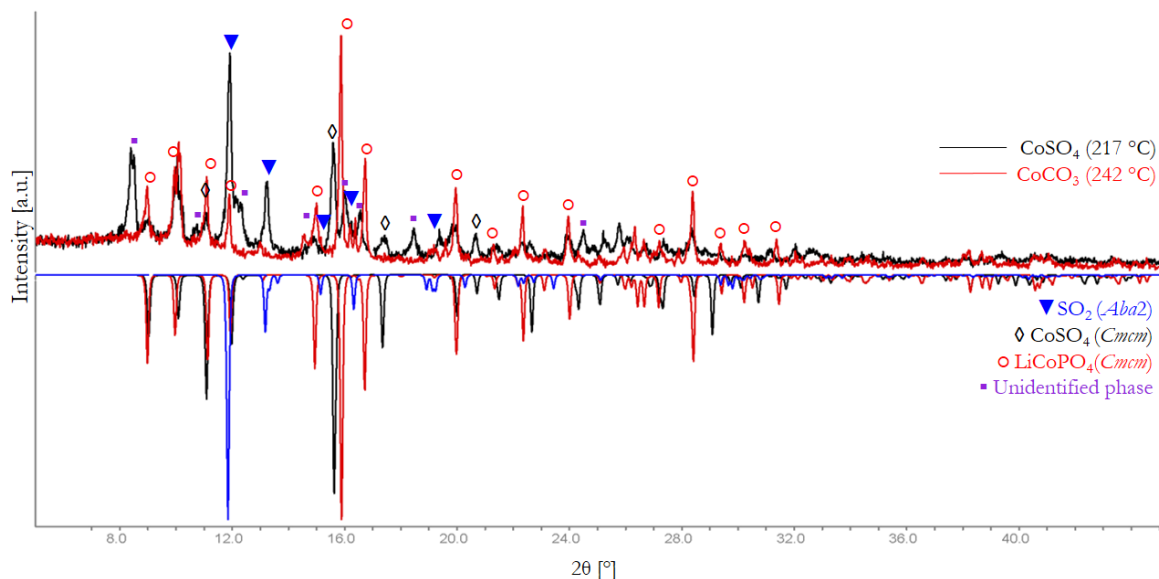


Figure 3-26 Influence of the cobalt source on the synthesis of LCP by polyol method. PXRD of the samples synthesized using CoCO_3 and CoSO_4 as cobalt precursor and their temperature under refluxing conditions. Pattern recorded after the drying process. The negative intensity corresponds to the reported phases of $\text{SO}_2\text{-Aba2}$ (\blacktriangledown blue), $\text{CoSO}_4\text{-Cmcm}$ (\blacklozenge black), LCP- Cmcm (\circ red) and an unidentified phase (\blacksquare lila). The measuring time is 20 min.

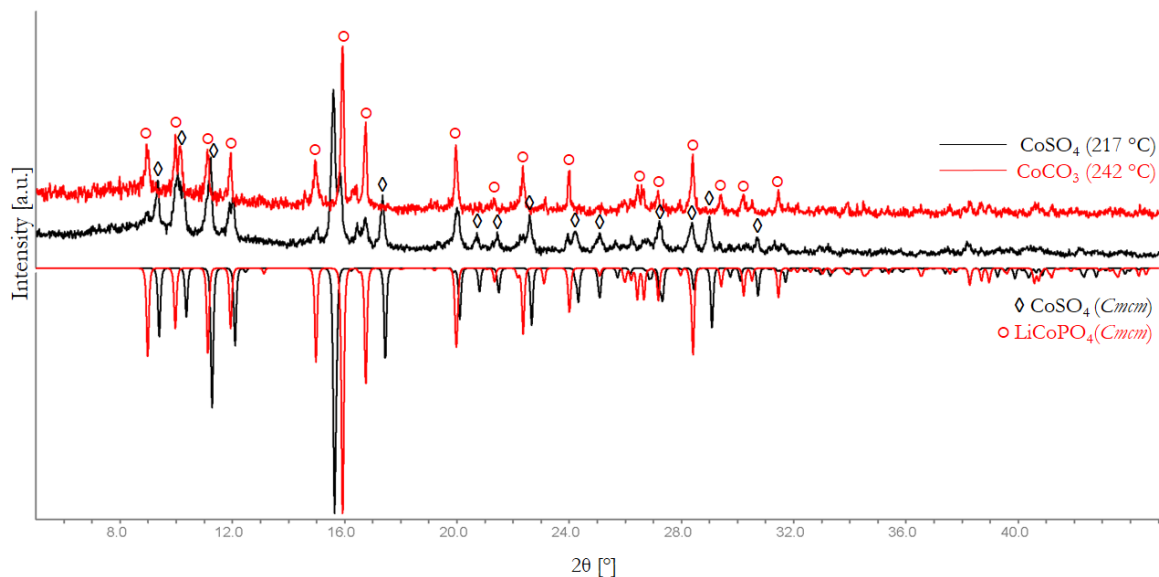


Figure 3-27 Influence of the cobalt source on the synthesis of LCP by polyol method. PXRD of the samples synthesized using CoCO_3 and CoSO_4 as cobalt precursor and their temperature under refluxing conditions after annealing at $400\text{ }^\circ\text{C}$ for 1 hour under air. The negative intensity corresponds to the reported phases of $\text{CoSO}_4\text{-Cmcm}$ (\blacklozenge black) and LCP- Cmcm (\circ red). The measure time is 20 min.

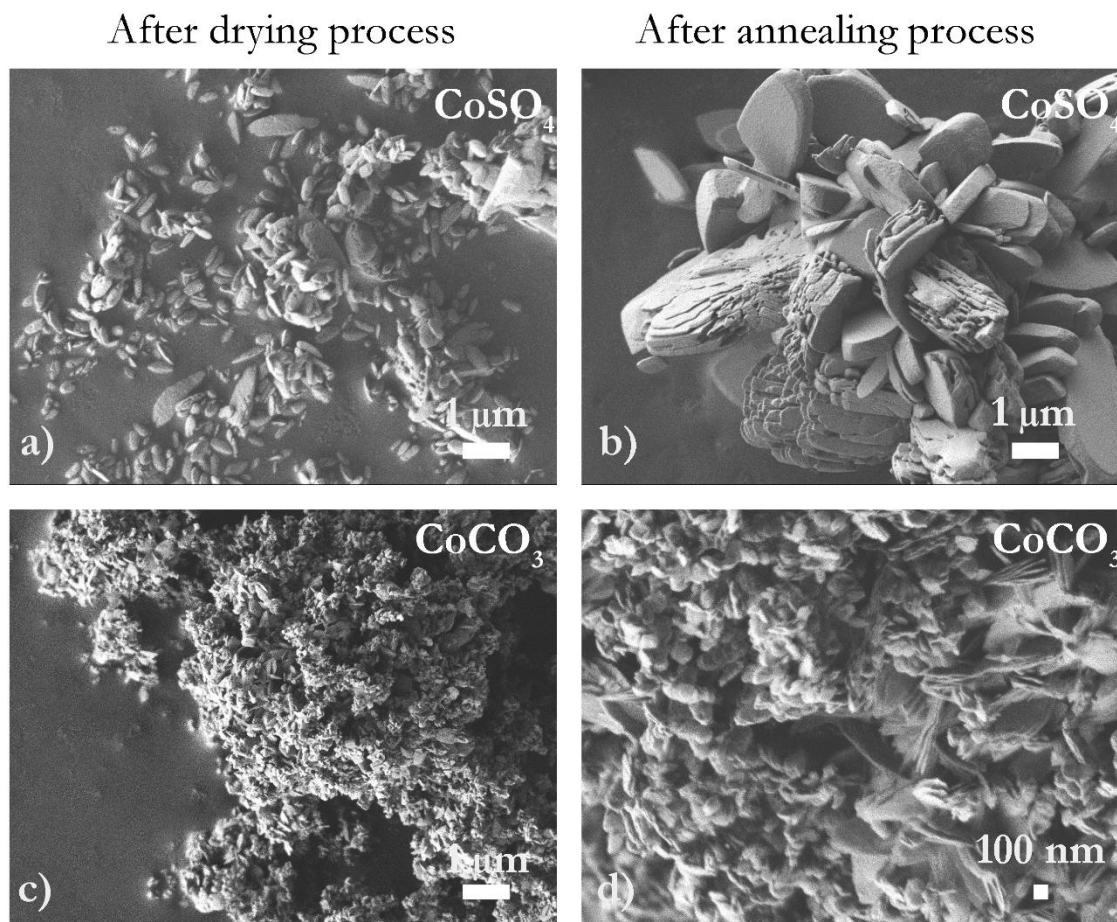


Figure 3-28: Influence of the cobalt source on the morphology of LCP produced by mean polyol synthesis. SEM pictures of the samples using CoCO_3 and CoSO_4 as cobalt precursor after drying and annealing respectively. Microscope B. Magnification: a) 10000X, b) 10000X c) 10000X and d) 30000X

This experiments confirm that specific thermodynamic conditions should be reached to synthesize single phase of LCP-*Pnma* using polyol process. To the best of our understand, the under polyol process the *Pn2₁a* and *Cmcm* are kinetically favored over the *Pnma* phase.

3.1.3 Synthesis using the CoAc_2 , H_3PO_4 , LiAc system (adapted from LiFePO_4) – standard procedure

An easy and simple polyol synthesis using the FeAc_2 , H_3PO_4 and LiAc system has been reported obtaining LFP- $Pnma$ nanoparticles without the use of annealing procedures⁹³. However, there is no reported literature using the analogous system based on the CoAc_2 , H_3PO_4 and LiAc system for the synthesis of LCP- $Pnma$. This section presents the principal results of the experiments using these precursor combination.

3.1.3.1 Standard synthesis procedure

Figure 3-29 presents the PXRD pattern after drying process. The standard procedure is a mixture of LCP- $Pn2_1a$ and LCP- $Cmcm$. Another experiment was done by using PVP as surfactant (M.W. 350000). In this case the main phase corresponds to LCP- $Cmcm$. It is important to remark that the temperature during refluxing conditions does not exceed 200 °C.

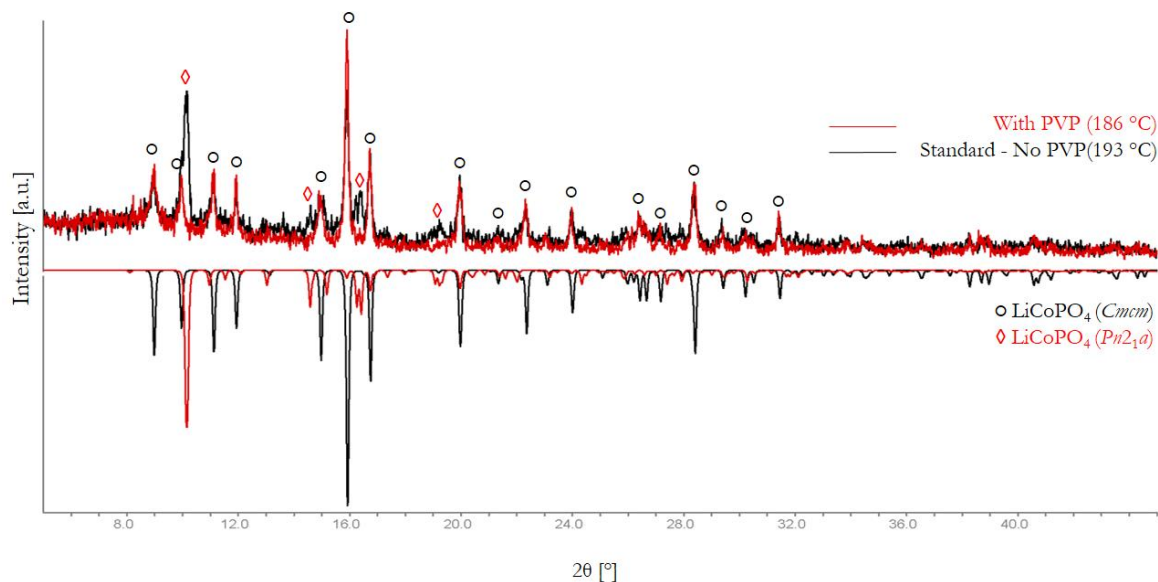


Figure 3-29: PXRD pattern of samples after drying process using CoAc_2 , H_3PO_4 and LiAc as starting precursors. The **red** pattern corresponds to the synthesis with PVP. The **black** pattern corresponds to the standard synthesis as described in experimental section. The negative intensity corresponds to LCP- $Cmcm$ (○ **black**) and LCP- $Pn2_1a$ (◊ **red**). The measuring time is 20 min.

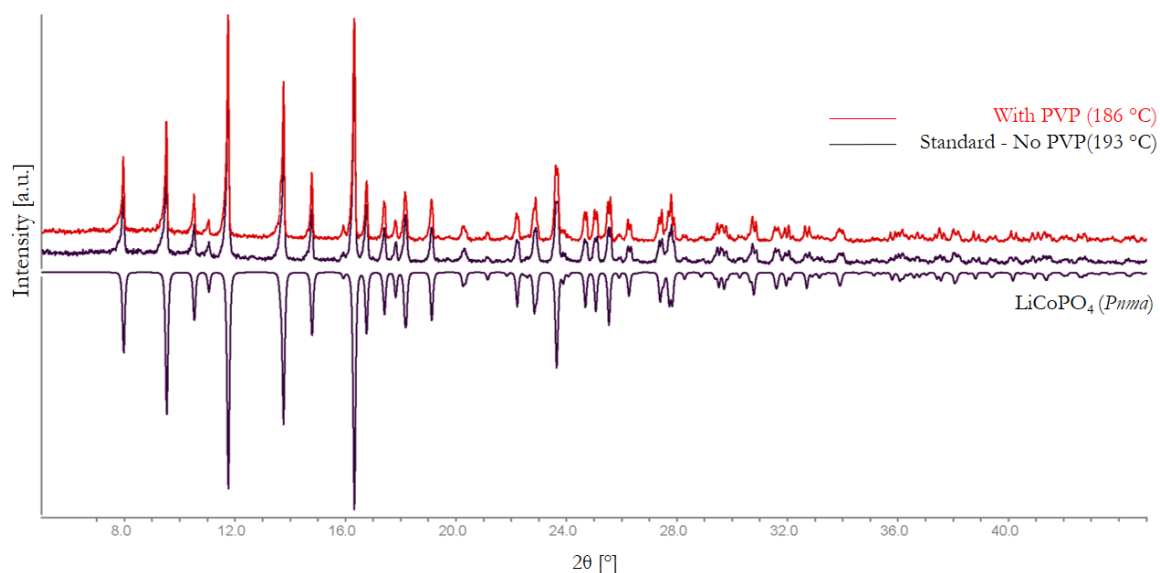


Figure 3-30: PXRD pattern of samples after annealing process using CoAc_2 , H_3PO_4 and LiAc as starting precursors. The **red** pattern corresponds to the synthesis with PVP. The **black** corresponds to the standard synthesis as described in experimental section. The negative intensity corresponds to $\text{LCP-}Pnma$. The measure time is 1 hour.

After annealing procedure, both samples show the characteristic peaks corresponding to $\text{LCP-}Pnma$ (see figure 3-30). The lattice parameter values are presented in table 3-12. On the other hand, figure 3-31 shows the morphology of the samples produced before and after annealing.

Table 3-12: Lattice parameter and crystallite size of $\text{LCP-}Pnma$ synthesized with and without PVP. Reported lattice parameters are presented at the top of the table

PVP	a (Å)	b (Å)	c (Å)	V (Å ³)	Mean domain size (nm)
No	10.203(5)	5.921(4)	4.699(5)	283.9(5)	43
Yes	10.199(7)	5.922(3)	4.688(3)	283.2(4)	36
Reported LCP - $Pnma$	-	10.2001(6)	5.9199(4)	4.6899(15)	283.2(9)

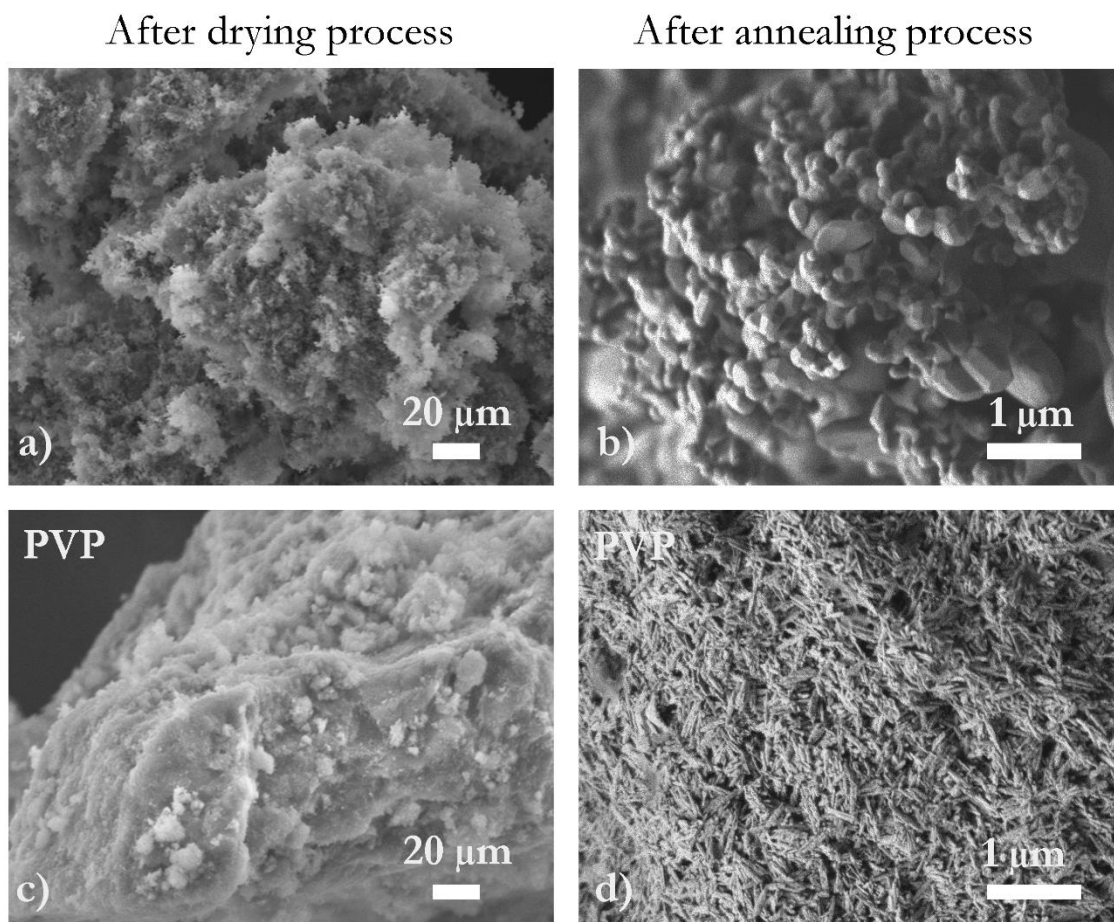


Figure 3-31: SEM images of the samples produced by using the CoAc₂ and LiAc and H₃PO₄ system with PVP and without PVP. The left side shows the samples after drying process. On the right side, the morphology of the particles after the last annealing step at 800 °C for 6 hours **a) - b):** with PVP; **c) – h)** without PVP. Microscope B. Magnification: left column 1000X, right column 20000X

Table 3-13: Capacity values and BET areas of LCP-*Pnma* using a the using the CoAc₂ and LiAc and H₃PO₄ system

Morphology	Average grain size	PVP	BET m ² g ⁻¹	C/10 3 th Cycle	C/5 3 th Cycle	C/2 3 th Cycle	C 3 th Cycle	2C 3 th Cycle
Irregular semi rounded agglomerates	Primary particles: under 500 nm	No	4.2	26	19	10	6	4
Sticks	c.a. 40 nm x c. a. 300 nm	Yes	5.8	61	42	30	21	14

After drying and annealing processes, an agglomeration of nanoparticles can be seen (see figure 3-30). The sample without PVP present a similar morphology in comparison to samples produced in TEG using the CoAc₂ and LDP system (see figure 3-22 c and 3-22 d). The particles produced with PVP form

nano-sticks or nano bars with small particle size distribution. The summary of these morphologies as well as the capacity is presented in table 3-13.

As a result, three main ideas can be discussed. *First, it is related to the type of LCP-polymorph obtained after drying process.* Along the previous sections, only an equilibrium between LCP- $Pn2_1a$ and LCP- $Pnma$ was analyzed; however, the change of the precursors to $CoAc_2$, H_3PO_4 and $LiAc$ induces the formation of other complexes between the ions in solution. Thus, the thermodynamic conditions and the kinetics associated with the formation of intermediates, as well as, nucleation and crystallization processes are totally different. In this case during the nucleation phase, the precursor solution is under thermodynamic control, allowing to obtain the most stable product. In this case the single-crystal seeds are produced due to minimize the total interfacial free energy of the system with in a given volume. After an uniaxial growth rates along one direction and cubic seeds will grow into octagonal rods ¹⁵⁷. A scheme explained the nucleation process is presented in figure 3-32.

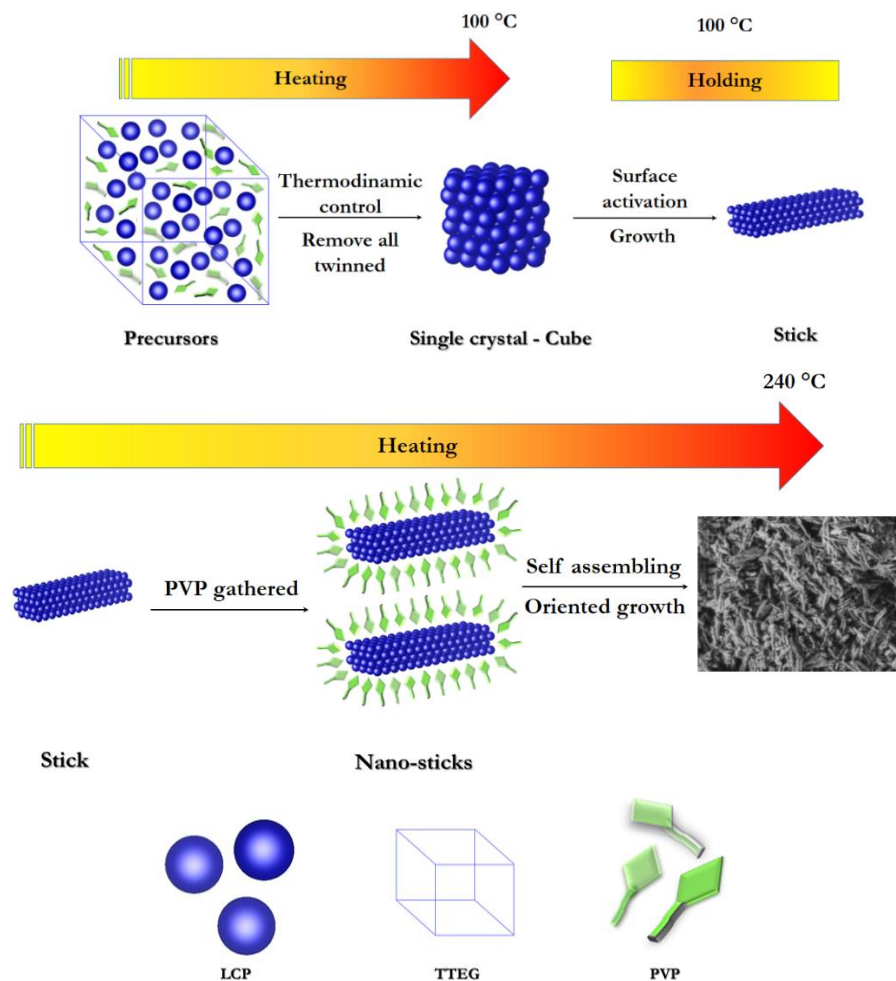


Figure 3-32: Schematic illustration of the growth mechanism of LCP sticks with PVP

Second, the metastability of the LCP-Cmcm modification. After annealing process, the samples are transformed into LCP-*Pnma*. This feature is confirmed by reports, published during this work, which claim the transition from LCP-*Cmcm* to LCP-*Pnma* at temperatures between 450 °C – 600 °C ^{155, 158}.

Third is the slightly increase of the capacity due to the use of PVP. In sections 3.1.2.2 and 3.1.2.3, a small improvement due to the decrease in particle size, as consequence of the effect of PVP was discussed. The PVP induces the growth of stick-like or bar-like shape of approximately 300 nm length and 40 nm width. This shape is beneficial because the diffusion of lithium ions is shorter in a stick-like particle compared to a rounded one. The BET values suggest a high specific surface area for the sample using PVP, but it is not large than the BET area obtained for the spheres of the section 3.1.2.2 (19 m²g⁻¹). This supports the concept regarding the importance of the shape control in the design of cathode materials. Apart of the importance to obtain nanometer particles, the plate-like, sheet, or plate morphology enhances the electrochemical performance, as reported for other materials such as LFP and LCP ^{159, 160}.

Additional experiments changing experimental parameters were done and are presented in the appendix 5.2.

3.2 Microwave assisted-polyol synthesis route of LCP-*Pnma*

This method was done in order to extend the discussion regarding the thermodynamics in polyol synthesis. The main point is the effect of the microwave (MW) radiation on the polyol solution, temperature and morphology. Additionally, a reproduction of a synthesis reported in the literature using MW-assisted polyol route is applied in order to compare it with the polyol system.

3.2.1 MW-assisted synthesis using the Co X and LDP system ($X = \text{Ac}_2, \text{SO}_4, \text{CO}_3$)

Microwave-assisted synthesis has been implemented in systems formed by CoAc₂, LiOH and H₃PO₄ ¹⁶¹; CoAc₂, LiAc and DAHP ¹⁶²; CoSO₄, LiOH, and H₃PO₄ ^{131, 163}; Co(OH)₂, LiOH and ADP ⁷⁷ and CoAc₂, LiAc and H₃PO₄ ¹⁶⁴. In all cases nanoparticles of LCP-*Pnma* have been obtained after synthesis. In order to see the influence of the microwave radiation on the polyol assisted process, a system based on LDP and different cobalt educts: CoCO₃, CoSO₄ and CoAc₂ was tested. Indeed, the precursor solution is obtained using the same molar ratio and amount of educts as used for the polyol synthesis to make them comparable.

The figure 3-33 shows the PXRD pattern after microwave reaction. For the experiments using CoCO₃ and CoSO₄ reflections can be indexed as LCP-*Pnma*; however, this samples present secondary phases corresponding to Co₃(PO₄)₂ and LCP-*Pn21a*, respectively. Based on the thermodynamic conditions of the system and nature of the educts, the discussion of these results can be divided in several points.

First, is the thermodynamic conditions that rule the system. The use of MW radiation assures a very fast and uniform heating of the total volume of reactants within a short time. Indeed, during the microwave reaction, the mixture absorbs energy (coming from dielectric microwaves) that allows to reduce the thermal gradients inside the reactor. The heating mechanism occurs by dipolar polarization and ionic conduction. During MW reaction, polar molecules try to orientate with the rapidly changing alternating electric field, this heat is generated by rotation, friction and collision of molecules. Ions will move through the solution based on the orientation of the electric field causing an increase of temperature due to collision and friction ¹⁶⁵. This allows the solvent to reach solvothermal equilibrium conditions in a few minutes.

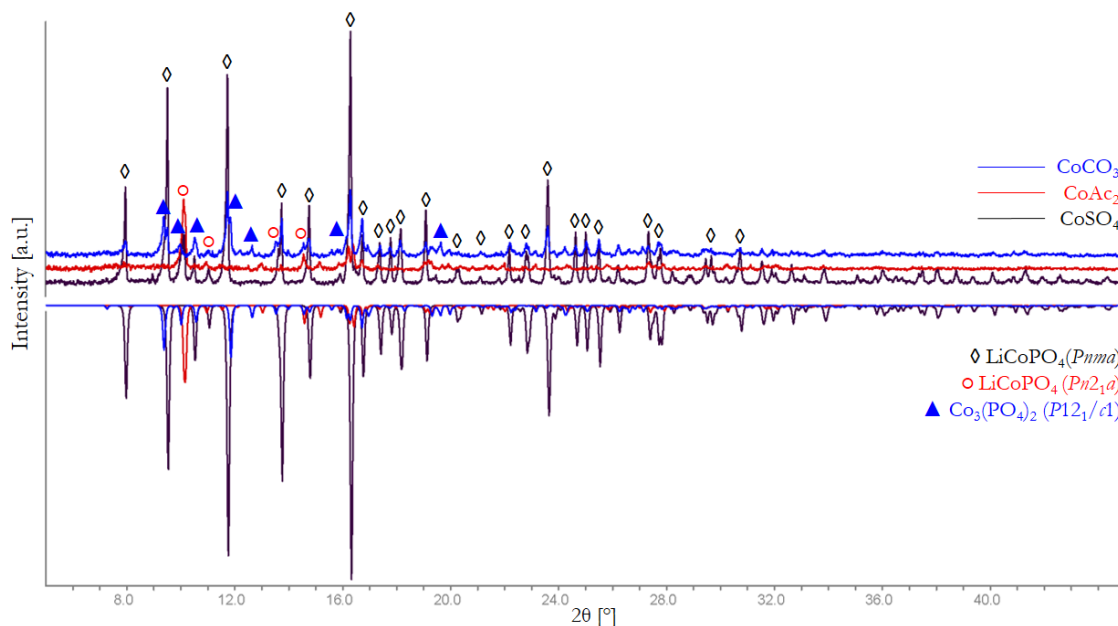


Figure 3-33: Influence of the cobalt source in the MW synthesis of LCP. PXRD pattern of the samples using CoCO_3 , CoSO_4 and CoAc_2 as cobalt precursor, after drying process. The negative intensity corresponds to the reported phases of LCP- $Pnma$ (\blacklozenge black) and LCP- $Pn2_1a$ (\circ red) and $\text{Co}_3(\text{PO}_4)_2$ - $P12_1/c1$ (\blacktriangle blue). The measuring time is 20 min.

As for the solvent, one of its most important properties is the polarity. The more polar the solvent is, the higher is its ability to couple with the microwave energy. This results in a rapid increase of the temperature and fast reaction rate ¹⁶⁶. This ability is determined by the “*loss tangent factor (δ)*” described in the equation 3.4:

$$\delta = \delta'' / \delta' \quad \text{Eq. 3-4}$$

Where δ'' is the conversion efficiency of the electromagnetic radiation into heat (dielectric loss) and δ' is the polarizability of the molecules in the electric field (dielectric constant) ¹⁶⁷⁻¹⁶⁹. EG has a very high δ value (1.350 at 2.45 GHz and 20 °C); therefore, it belongs to the family of strongly MW absorbing solvents, allowing reach its boiling point (~ 198 °C) ¹⁷⁰⁻¹⁷². This feature combined with the reductive and chelating properties of the polyalcohol, facilitates the control of the morphology and nuclei formation of LCP- $Pnma$. Those thermodynamic conditions cannot be reached in open-polyol system experiments.

Second, the influence of the educts on the formation of the different crystalline phases. In order to compare them, table 3-14 summarizes the phases obtained using polyol and MW routes.

Table 3-14: Summary of phases formed after polyol and microwave synthesis using the CoX and LDP systems (X = Ac₂, SO₄, CO₃) system

Co source	Polyol	Microwave
CoAc ₂ .4H ₂ O	Main phase: LCP- <i>Pn2_{1a}</i> Secondary phase:	Main phase: LCP- <i>Pn2_{1a}</i>
CoCO ₃	Main phase: LCP- <i>Cmcm</i> Secondary phase: LCP- <i>Pn2_{1a}</i> Unidentified	Main phase: LCP- <i>Pnma</i> Secondary phase: Co ₃ (PO ₄) ₂ , LCP- <i>Pn2_{1a}</i>
CoSO ₄ .7H ₂ O	Main phase: LCP- <i>Cmcm</i> Secondary phase: CoSO ₄ , SO ₂	Main phase: LCP- <i>Pnma</i> Secondary phase: LCP- <i>Pn2_{1a}</i> , LiSO ₄

When CoAc₂ is used, the metastable form LCP-*Pn2_{1a}* is obtained by both polyol and MW syntheses. On the contrary, when CoCO₃ and CoSO₄ are used, LCP-*Cmcm* and LCP-*Pnma* phases are obtained by polyol and microwave, respectively. Based on the nature of the educts, CoAc₂ and CoSO₄ are hydrated forms, in other words, both contain water that can be removed and forms a gas phase during the synthesis. The water gas-phase exerts extra pressure at high temperatures and it can be favorable on the formation of the LCP-*Pnma* phase. Moreover, CoSO₄ precursor can lead to the formation of a SO₂ gas-phase. Despite the internal pressure can not be measured due to experimental limitations, this behavior can be inferred due to the high energy and solvothermal conditions during the MW irradiation. However, this result is contrary to the reported for LFP. Corr *et. al.*¹⁷³ reported the synthesis of nanoparticles of LFP-*Pnma* and LFP-*Cmcm* using MW procedure. In this case the pure LFP-*Pnma* phase is obtained from iron acetylacetonate and LDP as precursors. A mixture of LFP-*Pnma* and LFP-*Cmcm* is obtained from iron oxalate dehydrate and LDP. Authors claim that the formation of the LFP-*Cmcm* phase is a consequence of the partial pressure due to water molecules released from iron oxalate precursor. In our case and as presented in the section 3.1.3, the formation of the *Cmcm* phase of LCP can be obtained in an open system. This suggest that the formation of *Pnma* phase is favored with the increase of the partial pressure in the system, in the case of cobalt but not in the case of iron. However, this must be verified by in-situ pressure measurements during the reaction in each vessel.

The third point is related to the solubility. In water the solubilities of the cobalt educts are: CoSO₄: 330 g/L¹⁷⁴; CoAc₂: 380 g/L¹⁷⁵ and CoCO₃: 12.98g/L¹⁷⁶. This is also observed by the deep purple color for sulfate and acetate solutions in comparison with the carbonate one, prior to microwave treatment. This indicates the superior reactivity of CoAc₂ and CoSO₄ over CoCO₃ precursor.

Figure 3-34 shows the SEM pictures of the samples. Larger morphological differences are palpable between polyol samples and MW samples which is based on the differences during the nucleation process, as explained before. For CoAc₂ a change from cross-bars (See figure 3-7 g) to spheres (see

figure 3-34 a, b) can be observed; for CoSO_4 from rounded beams (see figure 3-28 a) to plates (see figure 3-34 c, d) and for CoCO_3 (see figure 3-28 c) from sheets and irregular nanoparticles to needles (see figure 3-34 e, f).

After drying process

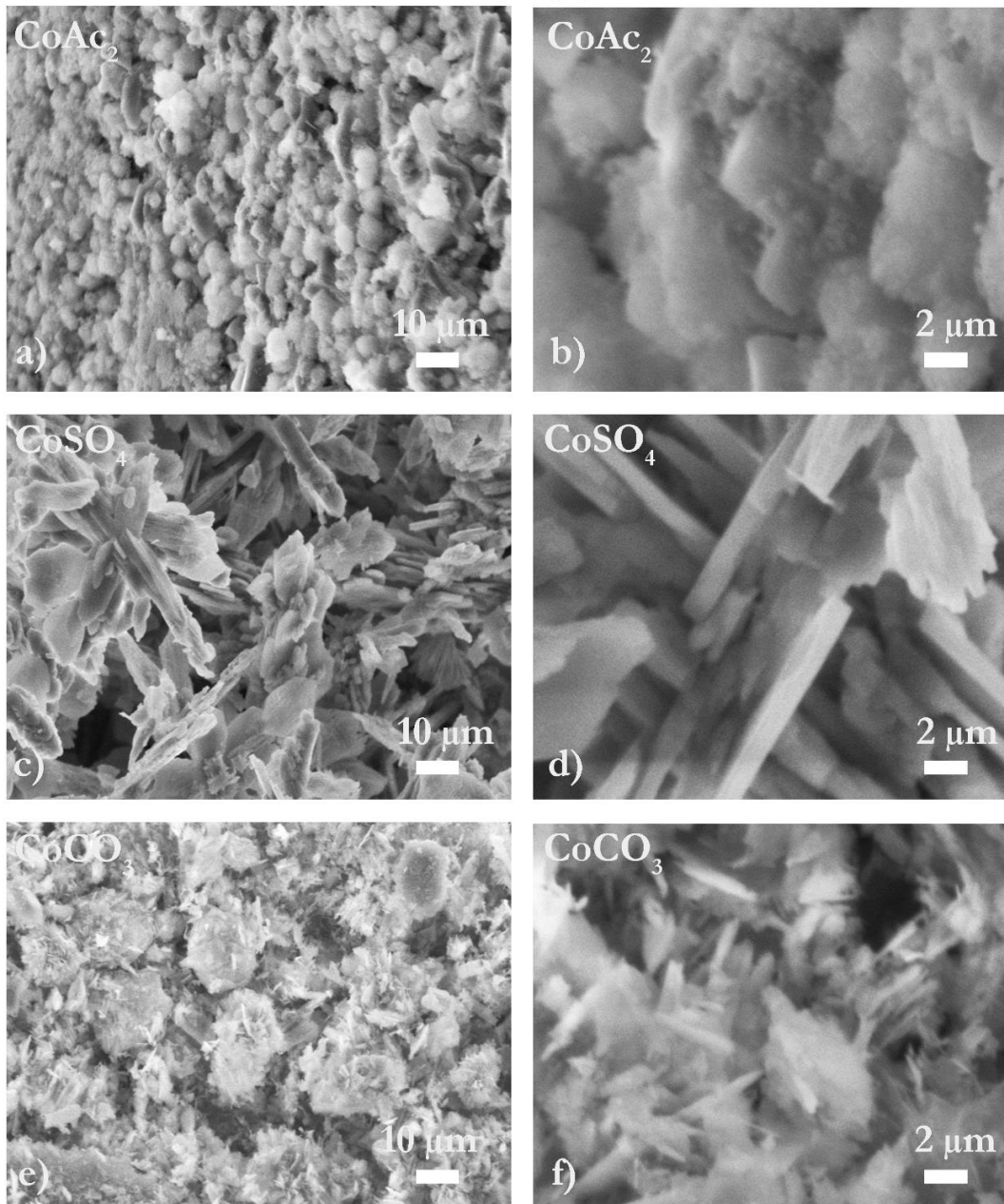


Figure 3-34: Influence of the cobalt source in MW-assisted polyol synthesis. SEM pictures of the samples using CoAc_2 (LCP- $Pn2_1a$), CoCO_3 (LCP- $Pnma$) and CoSO_4 (LCP- $Pnma$) as cobalt precursor after drying. Microscope A. Magnification: left column 2000X, right column 10000X

3.2.2 MW-assisted polyol synthesis using the CoAc_2 , H_3PO_4 and LiOH system

After the reproduction of the experimental procedure reported by Manthiram *et.al.*¹³¹, the sample present a main phase of LCP-*Pnma* with secondary phases of Co_3O_4 -*Fd-3m* and Li_3PO_4 -*Pcmm* (see figure 3-35). This confirms the superior ability of MW-assisted polyol process to obtain LCP-*Pnma* phase, based on the fact that this system was also tested by polyol synthesis giving LCP-*Pn21a* as main phase.

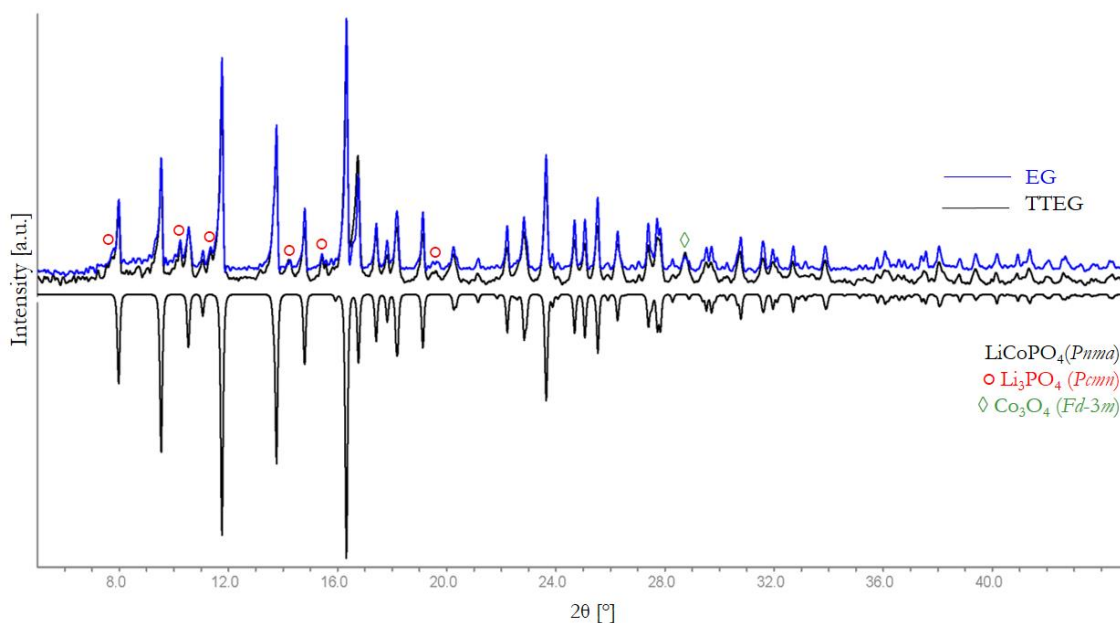


Figure 3-35: PXRD pattern of sample produced by MW-assisted polyol synthesis. The **blue** pattern sample synthesized in EG. **Black** pattern is the sample synthesized in TTEG (Manthiram *et. al.* reproduction¹³¹). The negative intensity corresponds to the reported phases of LCP-*Pnma*¹³⁴ (**black**), Li_3PO_4 -*Pcmm* (○ **red**) and Co_3O_4 -*Fd-3m* (◇ **green**). The measuring time is 1 hour

Figure 3-36 shows the morphology of the samples. Figure 3-36 a and 3-36 b illustrate the formation of round particles of 1 – 3 μm in diameter. The particles are agglomerated and small round-sphered particles below 100 nm are distributed along the surface. On the other hand, the sample synthesized in TTEG shows straight rhombohedral structures with dimensions below 500 nm. Additionally, the sample presents a narrow particle size distribution. Not only rhombohedral, but even small irregular nanoparticles are also present in this sample. Table 3-15 summarizes the capacity values showing an improvement compared with the polyol synthesis ones. As mentioned before, the combination of the educts play an important role during the formation of LCP, as well as, the control of side phases. Certainly, this system is more suitable for the production of LCP-*Pnma* with less amount of secondary phases in comparison with the systems based on LDP and different cobalt sources. Furthermore, the nature of polyol solvent plays an important role in the shape control of the particles obtained. Similar results are observed in the synthesis of GdPO_4 nanoparticles: bigger spheroidal particles with relatively

uniform sizes are obtained during MW precipitation process in EG. When EG is replaced by butylene glycol, nanocubes are obtained¹⁷⁷.

After drying process

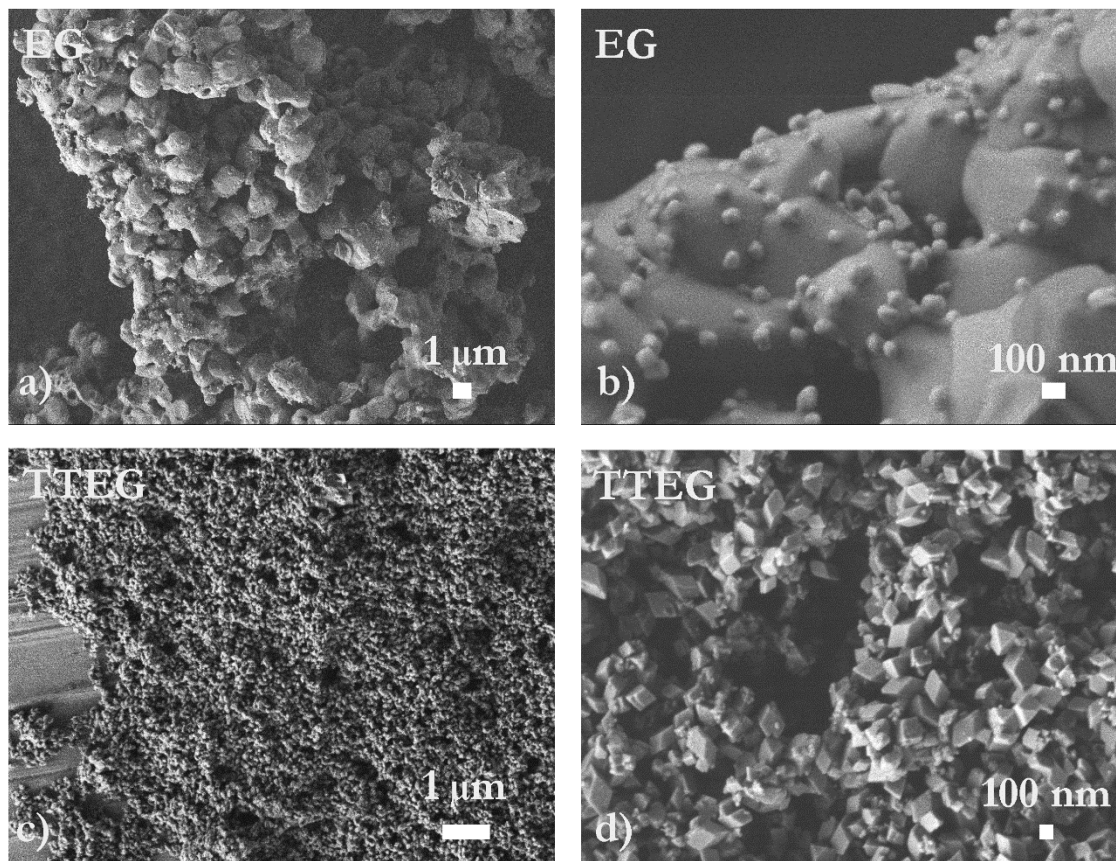


Figure 3-36: SEM images of the LCP samples produced using the MW-assisted polyol route using the CoAc_2 , H_3PO_4 and LiOH system. Samples after drying process are shown. Figures a - b: synthesis in EG. Figures c - d: Synthesis in TTEG. Microscope B. Magnification: a) X1000, b) 55000X, c) 10000X and d) 30000X.

Table 3-15: Capacity values and BET areas of LCP-*Pnma* using the using the CoAc_2 , LiOH and H_3PO_4 system

Solvent	Morphology	Mean domain size (nm)	BET m^2g^{-1}	C/10 3 th Cycle	C/5 3 th Cycle	C/2 3 th Cycle	C 3 th Cycle	2C 3 th Cycle
EG	Agglomerated spheres	53 nm	5.9	83	88	70	50	9
TTEG	Rhombohedral	36 nm	9.7	102	84	63	43	25

Other considerations such as the particle size and particle shape are fundamental to understand the increase of the capacity. First, the mean domain size of rhombohedral particles is small compared to the agglomerated spheres. Second, the LCP-*Pnma* produced by MW-polyol synthesis present a smaller

degree of agglomeration compared to LCP-*Pnma* produced by polyol route. Less agglomeration increases the probability of exposing the electrochemically active (010) surfaces. The (010) surface is considered the most facile pathway for Li⁺ migration¹⁷⁸. The Li-ion migration has been calculated using atomistic simulation techniques. For LCP-*Pnma*, it has been found that the shortest distance between Li⁺ ions lies in the [010] direction parallel to *b* axis with a jump distance between 2.9 – 3.0 Å. The migration Energy (E_{mig} , eV) is listed in the table 3-16. The results reveal that the lowest energy path for Li⁺ migration for all LMP olivines is along the [010] channel. Ideally, the thinness of the crystals in the [010] direction enhances the rate capability of the cathode material¹⁷⁹. This indicates that in rhombohedral structures a higher (010) surface area exist, compared to the spherical agglomerated ones.

Table 3-16: Mechanism and energies of Li⁺ migration in LMP-*Pnma* ($M = \text{Mn, Fe, Co and Ni}$)¹⁷⁸

Migration energy, E_{mig} (eV)				
Direction	Mn	Fe	Co	Ni
[010]	0.62	0.55	0.49	0.44
[001]	2.83	2.89	3.28	3.49
[101]	2.26	3.36	3.41	3.99

On the other hand, extremely small particles sizes are counterproductive for electrochemical performance. While one advantage of a reduced particle size is the enhancement of the rate capabilities^{100, 180, 181}, the surface area at the same time becomes large compared to the micron-sized particles. Thus the volume of the nanomaterial composite is extremely high due to the empty space between particles, resulting in a low tap density. This characteristic decreases the loading of the nanomaterial on the specific area of the current collector and limits the volumetric energy density¹⁸². Furthermore, the difference in the shape of nanoparticles directly affects the diffusion path length of lithium ions and, as a consequence, the electrochemical performance. TTEG solvent possesses more hydrophilic OH-anchors that prevent further growth into micron-sized particles and agglomeration of particles than EG solvent.

3.3 Acetate-assisted antisolvent precipitation (AAAP) synthesis of LCP-*Pnma*

This section describes the synthesis of LCP-*Pnma* by the AAAP method. This synthesis route was used for the synthesis of LMP-*Pnma*¹³² and, for the first time, is adapted for the synthesis of LCP-*Pnma*. The influence of cobalt source, dropping rate and annealing atmospheres in the formation of crystalline phases, as well as the morphology are further discussed.

3.3.1 Standard procedure

In order to understand the AAAP route, some basic principles have to be considered. In a solution, the system opposes local supersaturation by precipitating solved species as a solid. This attempt can appear in two different ways, by nucleation of the solved species directly from solution or by growth on a particle inside the solution (either of a different or the same substance). Supersaturation (defined as actual concentration over equilibrium solubility) is one of the most important parameters controlling whether new nuclei form or already existing ones grow bigger and it has been shown that higher supersaturation usually results in higher nucleation rate¹⁸³⁻¹⁸⁶. Besides, nucleation is influenced by the systems metastable zone (concentration range where no crystallization is observed in a given time). According to Guo *et. al.*¹⁸⁷ systems with a metastable zone over a wide concentration range hinders nucleation and therefore particle growth is favorable¹⁸⁷. Consequently, systems with small metastable zones have to be brought to a high level of supersaturation in order to favor nucleation over particle growth and obtain many small particles instead of few big ones. Following this idea, an antisolvent (liquid with a low solubility of the desired product) can be added to a homogeneous solution, causing high supersaturation thus rapid nucleation.

As shown in figure 3-37, as soon as nucleation begins, two processes (coagulation and condensation) are initiated, causing particle growth in order to reduce surface free energy of the nuclei. To summarize, there are many factors (i.e. supersaturation, metastable zone, reaction time, etc.) having significant influence on particle size and according to that, careful fine tuning of a given system has to be undertaken in order to produce nanometer sized particles via AAPM.

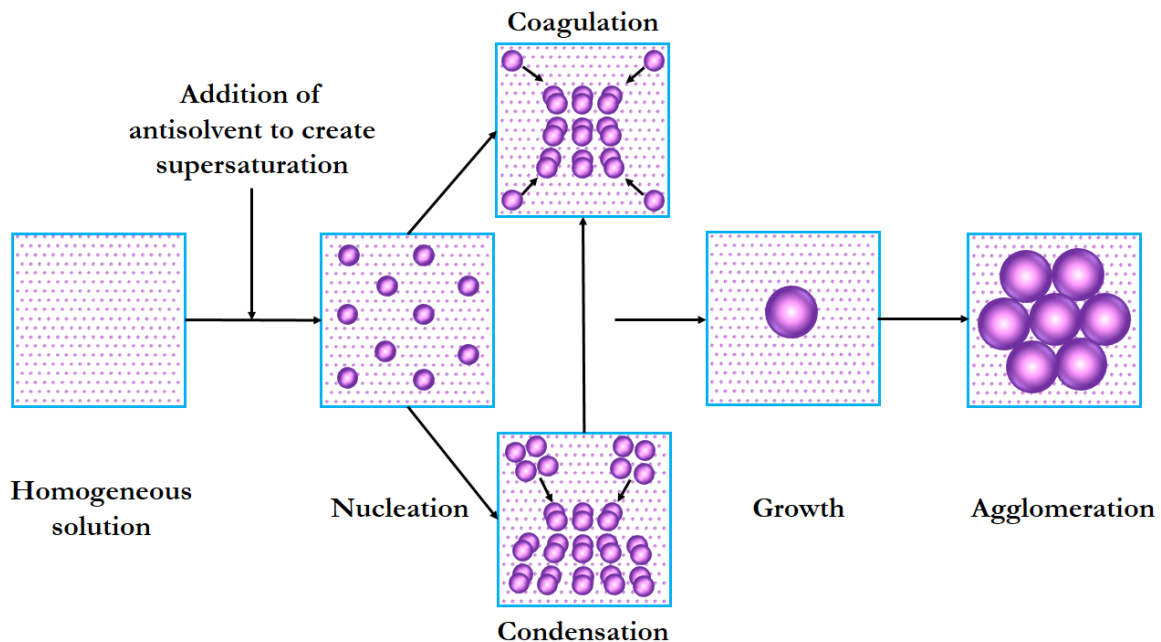


Figure 3-37: Schematic of particle precipitation process

In the particular case of LCP, H_3PO_4 , CoAc_2 and HCl are dissolved in deionized water to obtain a homogeneous aqueous solution. Then the aqueous solution is added to the LiAc solution in ethanol ethanol. Ethanol as the antisolvent induces the high supersaturation of $\text{Co}_2\text{P}_2\text{O}_7$ and $(\text{H}_3\text{O})(\text{Co}_2(\text{OH})_2(\text{HPO}_4)(\text{H}_2\text{PO}_4))$. Acetate in the ethanol as proton acceptor further increases the supersaturation. The high supersaturation created by acetate and antisolvent is supposed to lead a fast formation of nuclei and limited particle growth, yielding the precipitate with small particle size. An scheme of this process is shown in figure 3-38.

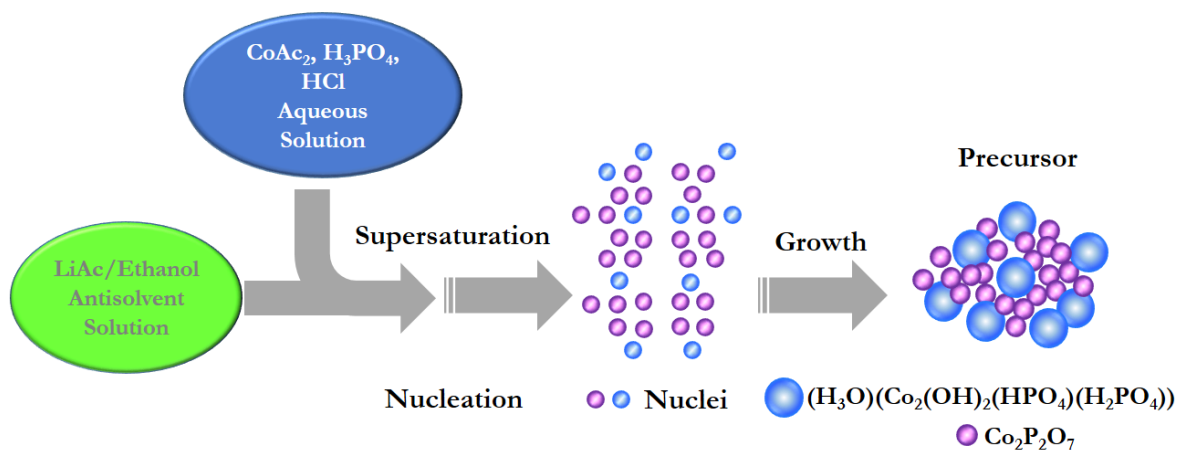


Figure 3-38: Schematic illustration of the acetate-assisted antisolvent precipitation process

The figure 3-39 shows the PXRD pattern of the sample after drying process. This material obtained after antisolvent reaction is formed by phases corresponding to cobalt phosphate and a cobalt hydrogen phosphate complex. In contrast, the reported composition of the precursor is composed by $\text{Mn}_3(\text{PO}_4)_2$ and Li_3PO_4 ¹³².

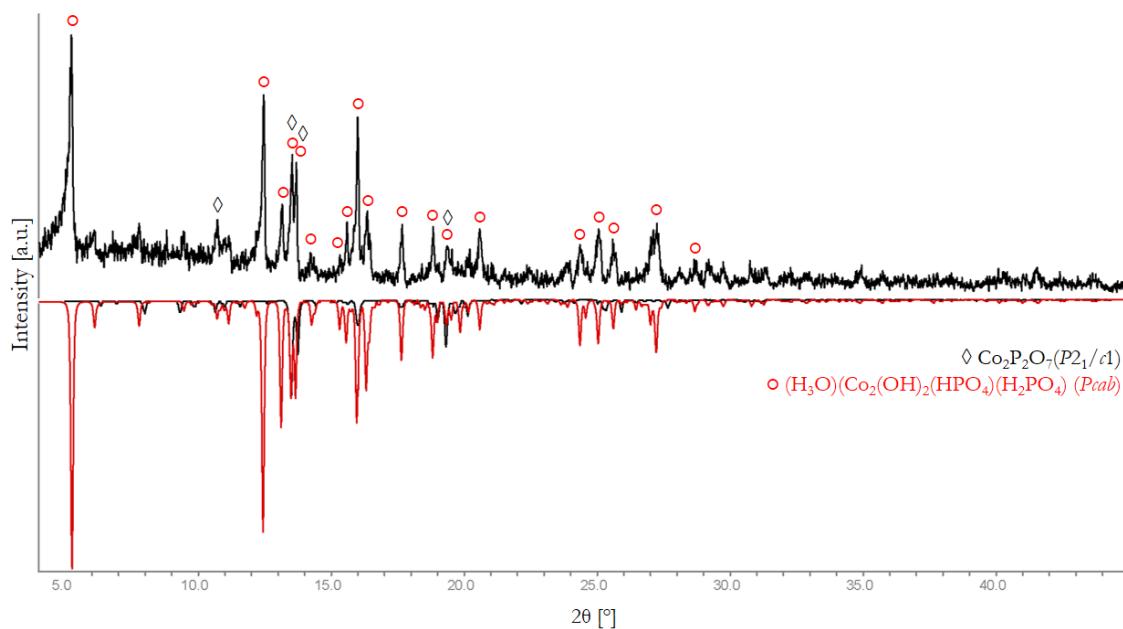


Figure 3-39: AAAP synthesis of LCP-*Pnma*. PXRD pattern of the precursor material prior carbon coating and annealing. Pattern recorded after the drying process. The negative intensity corresponds to the reported phases of $\text{Co}_2\text{P}_2\text{O}_7\text{-P}2_1/c1$ (◊ **black**) and $(\text{H}_3\text{O})(\text{Co}_2(\text{OH})_2(\text{HPO}_4)(\text{H}_2\text{PO}_4))\text{-Pcab}$ (○ **red**). The measuring time is 20 min.

The PXRD pattern after coating and annealing at 550 °C is presented in figure 3-40. A comparison is done between the samples annealed under air and under argon atmosphere. The sample obtained under air presents a main phase corresponding to LCP-*Pnma* with a small secondary phase of Co_3O_4 . In order to avoid the formation of the oxide, an argon atmosphere is used instead. However, after annealing under Ar atmosphere, the sample present a mixture of LCP-*Pnma*, LiP_7 , Li_6CoO_4 and an unidentified phase.

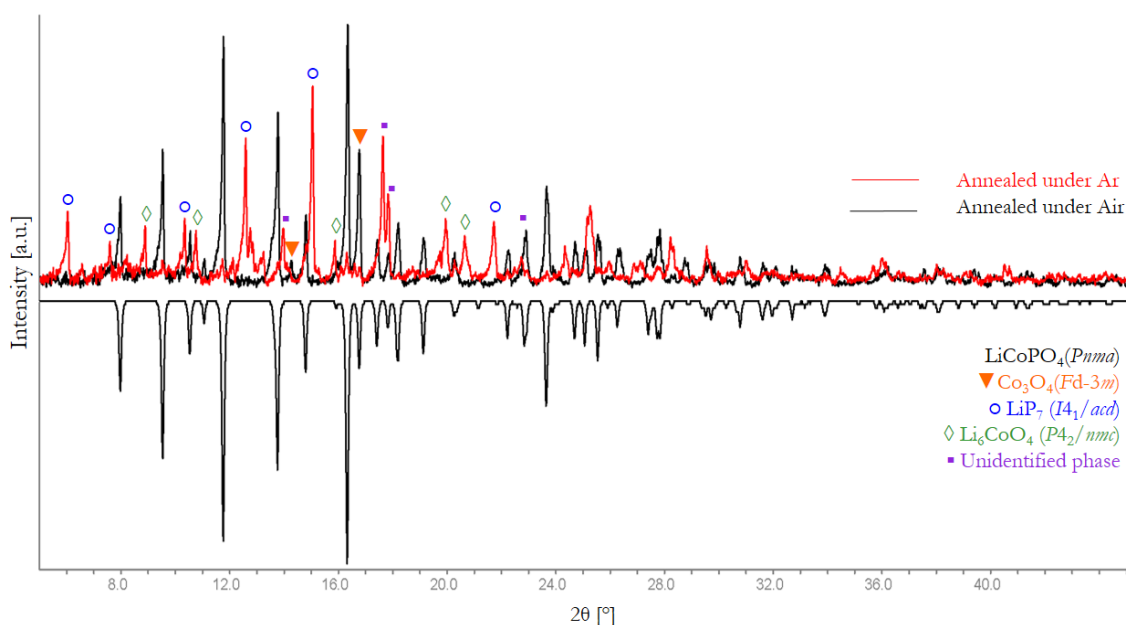


Figure 3-40: AAAP synthesis of LCP. PXRD pattern of the C-composite. The **red** pattern corresponds to the sample annealed under Ar atmosphere. The sample annealed under air atmosphere is shown in **black**. Peaks marked with symbols correspond to the secondary phases of Co_3O_4 - $Fd-3m$ (\blacktriangledown orange), LiP_7 - $I4_1/acd$ (\circ blue), Li_6CoO_4 - $P4_2/nmc$ (\diamond green) and an unidentified phase (\blacksquare lila). The measure time is 1 hour.

The usage of inert atmospheres in the synthesis of LCP-*Pnma*-carbon composites¹⁸⁸⁻¹⁹⁰ is already known; they help to avoid formation of undesirable oxides and keep the reduced form of the metal cation. However, depending on the starting materials, the composition of the precursor (material recovered after drying process) will be different; as well as possible secondary phases at the end of the C-coating procedure. For example, in the case of LCP-*Pnma* produced by sol-gel process, the starting materials are LiAc , CoAc_2 , H_3PO_4 and citric acid. Here, there is no evidence of crystalline phases after drying; indeed, after annealing at 300°C for 5 hours under nitrogen atmosphere, no reflections are found. For this case, 10 hours of thermal treatment at 730°C under nitrogen atmosphere leads to the formation of LCP-*Pnma*, $\text{Li}_4\text{P}_2\text{O}_7$ and Co_2P secondary phases¹⁹¹. Another example is reported by Wolfenstine *et. al.*, where the LCP precursor is obtained by means of solid state synthesis, from lithium carbonate, cobalt oxalate and ADP. The coating procedure is done under a mixture of Ar + 4% vol.% H_2 , reaching LCP-*Pnma* with a secondary phase of Co_2P ¹⁹². In the case of the AAAP synthesis developed, the annealing procedure under Ar conducts to a higher amount of secondary phases in comparison with the one conducted under air atmosphere. This behavior, contradicts most part of publications which use an inert gas to complete the formation of the olivine phase with less amount of secondary phases. Additionally, as no reflections of crystalline phases containing lithium are detected, the lithium remains in the LCP precursor in an amorphous form. The morphology of the LCP precursor and LCP-C composite is

presented in figure 3-41. After the drying process, formation of sticks with average size of approximately 830 nm width and 4 μm length is shown. After carbon coating and annealing, the sample forms a LCP-C composite of particles between 2 – 3 μm to approximately 600 nm (see figures 3-41 b and d).

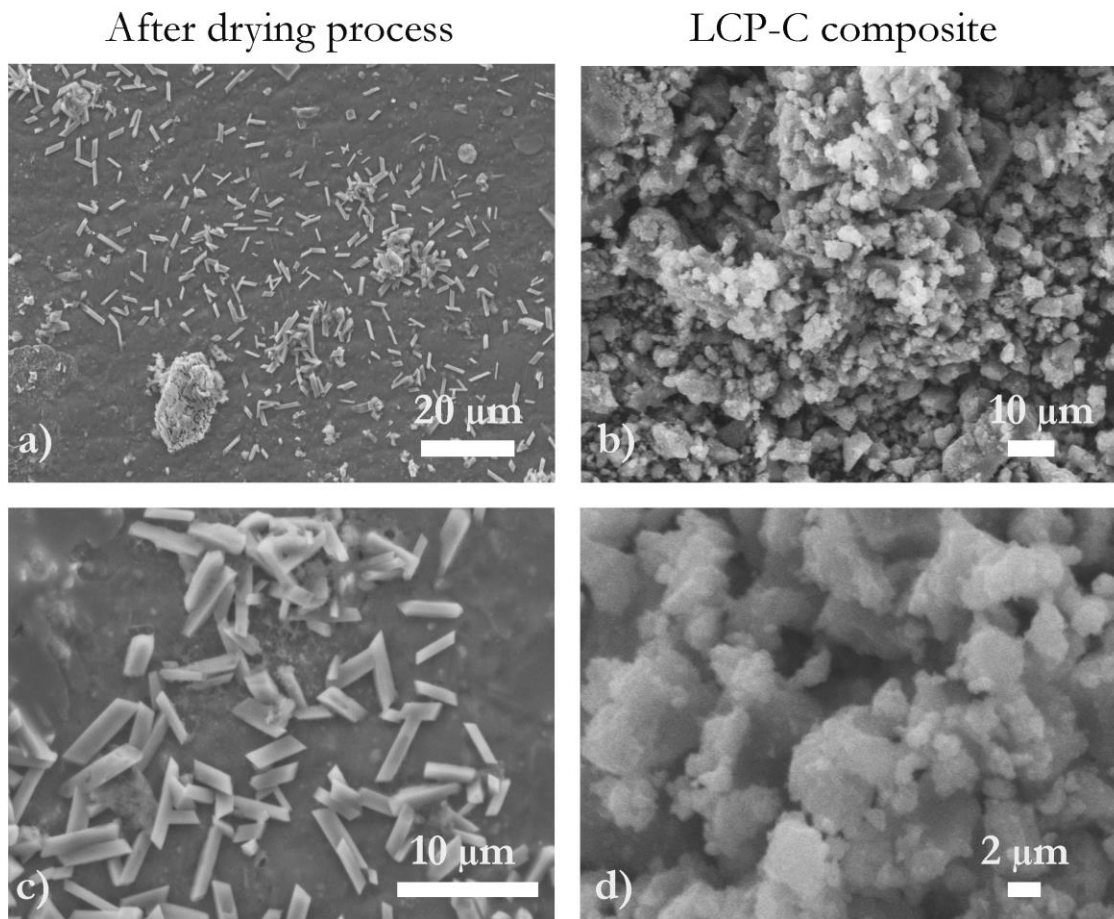


Figure 3-41: SEM images of the samples produced using the AAAP method. Samples after drying process: figures a – c, corresponding to the precursor after drying process. Figures b - d: sample after C-coating and annealing. Microscope A. Magnification: a) 1000X b) 2000X, c) 3000X and d) 7000X

Table 3-17: Capacity values and BET area of LCP-*Pnma* produced by AAAP method

C-wt% CHNS	Conductivity (S cm ⁻¹)	BET m ² g ⁻¹	Mean domain size (nm)	C/10 3 th Cycle	C/5 3 th Cycle	C/2 3 th Cycle	C 3 th Cycle	2C 3 th Cycle
5.7	7.6 x 10 ⁻³	5.6	42	79	66	53	41	29

The value of the capacity is presented in table 3-17. This value reaches the 47.3% of the theoretical value. On the other hand, the addition of 20 % glucose as carbon source increases the conductivity value of

the system by a factor of 10^7 without the use of any high-purity argon atmosphere, as reported for doped and coated samples of LCP-*Pnma*^{123, 191}.

3.3.2 Discussion about the influence of cobalt source and dropping rate

The standard synthesis is based on the use of cobalt acetate as cobalt precursor; however, in order to decrease the amount of secondary phases, additional experiments using cobalt chloride, carbonate and sulfate were done. Figure 3-42 presents the PXRD pattern of the samples after annealing process under air at 550 °C. The summary of the phase composition is presented in table 3-18.

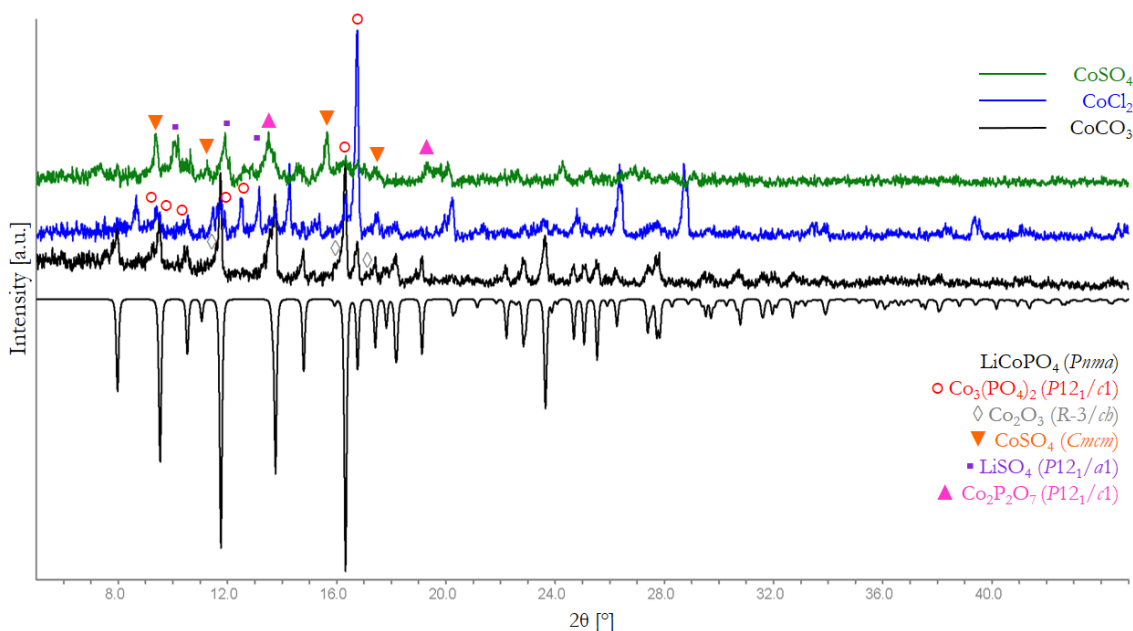


Figure 3-42: AAAP synthesis of LCP. Influence of cobalt source. XRD pattern recorded after annealing process under air. The patterns correspond to: CoSO₄ (green), CoCl₂ (blue) and CoCO₃ (black). Negative intensity corresponds to reported LCP-*Pnma* (black). Peaks marked with symbols are the main secondary phases: CoSO₄-*Cmcm* (▼ orange), Co₃(PO₄)₂-*P12₁/c1* (○ red), Co₂O₃-*R-3/cb* (◇ gray), Co₂P₂O₇-*P12₁/c1* (▲ pink) and LiSO₄-*P12₁/a1* (■ lila). The measuring time is 20 min.

In synthesis using CoCl₂ and CoSO₄ after annealing process, a mixture of different phases is obtained. Only in the case of CoCO₃, a main phase of LCP-*Pnma* is found; however, it contains secondary phases. The fact that only the use of CoAc₂ and CoCO₃ as cobalt precursors leads to olivine phase is explained by the different reactivity of each counter ion (CH₃COO⁻, CO₃²⁻, Cl⁻ and SO₄²⁻). In general, the reaction can be described by the equation below:

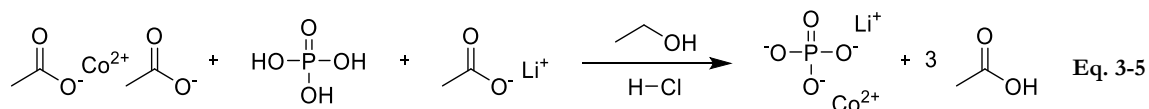
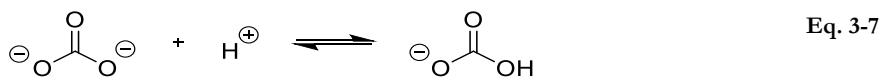
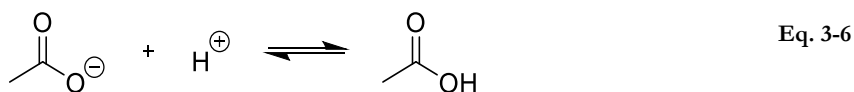


Table 3-18: Phase analysis of the product mixture after drying process and annealing process for AAAP method using different cobalt sources

Co source	Before annealing	After annealing
	Compound	Compound
CoCO ₃	LCP- <i>Pn2₁a</i>	LCP- <i>Pnma</i>
	P ₂ O ₅ - <i>Fdd2</i>	Co ₂ O ₃ - <i>R-3cb</i>
	CoO- <i>Fm-3m</i>	Co ₂ P ₂ O ₇ - <i>P12₁/c1</i>
	Li ₂ O- <i>Fm-3m</i>	Li ₂ O- <i>Fm-3m</i>
CoSO ₄		Co(PO ₃) ₂ - <i>C12/c1</i>
	Co ₃ (PO ₄) ₂ - <i>P12₁/c1</i>	Co ₃ (PO ₄) ₂ - <i>P12₁/c1</i>
	Li ₄ P ₂ O ₇ - <i>P12₁/n1</i>	Co ₂ P ₂ O ₇ - <i>P12₁/c1</i>
	CoSO ₄ - <i>Cmcm</i>	CoO- <i>Fm-3m</i>
	Li ₃ P- <i>P6₃/mmc</i>	Li ₄ P ₂ O ₇ - <i>P12₁/n1</i>
	Li ₂ SO ₄ - <i>P12₁/a1</i>	CoSO ₄ - <i>Cmcm</i>
		Li ₂ SO ₄ - <i>P12₁/a1</i>
CoCl ₂	LCP- <i>Pn2₁a</i>	
	Li ₄ P ₂ O ₇ - <i>P12₁/n1</i>	LCP- <i>Pnma</i>
	Co ₂ O ₃ - <i>R-3cb</i>	Co ₃ O ₄ - <i>Fd-3mS</i>
	CoCl ₂ (H ₂ O) ₂ - <i>C12/m1</i>	LiPO ₃ - <i>P1c1</i>
	CoCl ₂ (H ₂ O) ₆ - <i>C12/m1</i>	LiCoO ₂ - <i>R-3mH</i>
	LiOH- <i>P4/mmm</i>	PCl ₅ - <i>P4n</i>
	P ₂ O ₅ - <i>Fdd2</i>	
	Li ₂ O- <i>Fm-3m</i>	

Taking a closer look at pK_a values, it classify the ability of a substance to either accept or donate a proton. While compounds with a low pK_a value are not likely to accept a proton, those having a higher one accept it. In this case, chloride (pK_a < 1) and sulfate ions (pK_a = 1.92) can not be protonated in significant amounts, while acetate (pK_a = 4.75) and carbonate ions (pK_a = 10.32) have relatively higher pK_a values, thus they may be partially protonated¹⁹³. The associated reactions are shown in equations 3-6 and 3-7, respectively.



The formation of this equilibrium seems to facilitate reaction towards the desired product to some extent, since the counter ion is partially removed from the reaction mixture. According to this, a cobalt source comprised of a weak base as counter ion shall be used in following experiments. Since cobalt acetate as starting material lead to slightly less side phases compared to cobalt carbonate, it was used

hereafter. One possible explanation for the fact that cobalt acetate yielded slightly less side phases may be that the pKa of the acetate ion is in a more favorable range than the quite high pKa of the carbonate ion.

On the other hand, the dropping rate influences the morphology of the precursor; as well as, the final product in the AAAP method. Based on the standard procedure, different dropping rates were tested. Figure 3-43 presents the PXRD pattern after annealing process under air at 550 °C. The pattern shows secondary phases of $\text{Co}_2\text{P}_2\text{O}_7$ and Co_3O_4 . It can be noted that the dropping rate of 1.0 mL/min leads to the formation of rounded nanoparticles with an average size of approximately 700 nm. The rate of 0.6 mL/min presents a mixture between agglomerates of several irregular forms of μm size with some nano-needles. Finally, very slow rates of 0.1 mL/min, leads the formation of spikes of around approximately 300 nm width x 3-4 μm large (see figure 3-44)

Additionally, the slow dropping rate induces a low crystallinity of the final sample. This occurs because a droplet of acidic solution is formed at the tip of the syringe and it grows for a specific time until it is released into the antisolvent solution. Since a reflux cooler was used to prevent loss of solvent (see figure 2-8), the gas phase inside the reaction vessel contained significant amounts of ethanol and condenses on the surface the syringe tip. This causes partial precipitation of the educt already inside the drops and therefore it is not recommend applicable. Finally, the rate control constitutes an easy method to obtain nano-structures and control of morphology even after long annealing treatments. However, additional experiments should be conducted to control the amount of secondary phases in the final LCP-*Pnma* sample.

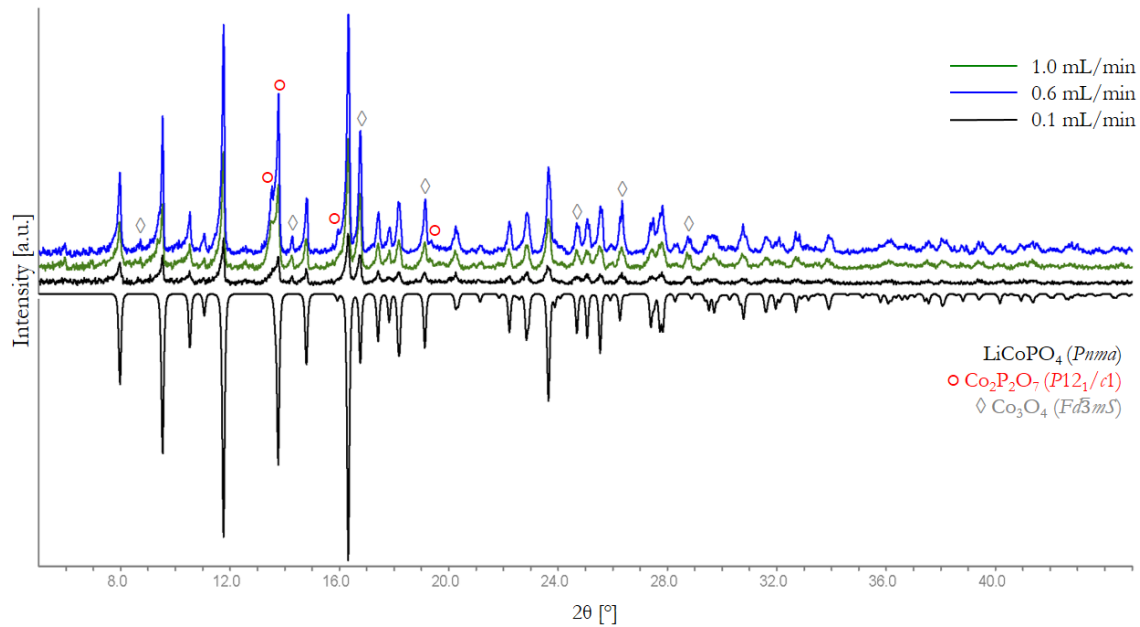


Figure 3-43: AAAP synthesis of LCP. Influence of dropping rate. XRD pattern recorded after annealing process under air. The patterns corresponds to a rate of: 1.0 mL/min (**green**), 0.6 mL/min (**blue**) and 0.1 mL/min (**black**). Negative intensity correspond to reported LCP- $Pnma$ (**black**). Peaks marked with symbols are the main secondary phases: $\text{Co}_2\text{P}_2\text{O}_7$ - $P12_1/c1$ (**red**), Co_3O_4 - $Fd\bar{3}mS$ (**gray**). The measuring time is 1 hour.

After annealing process

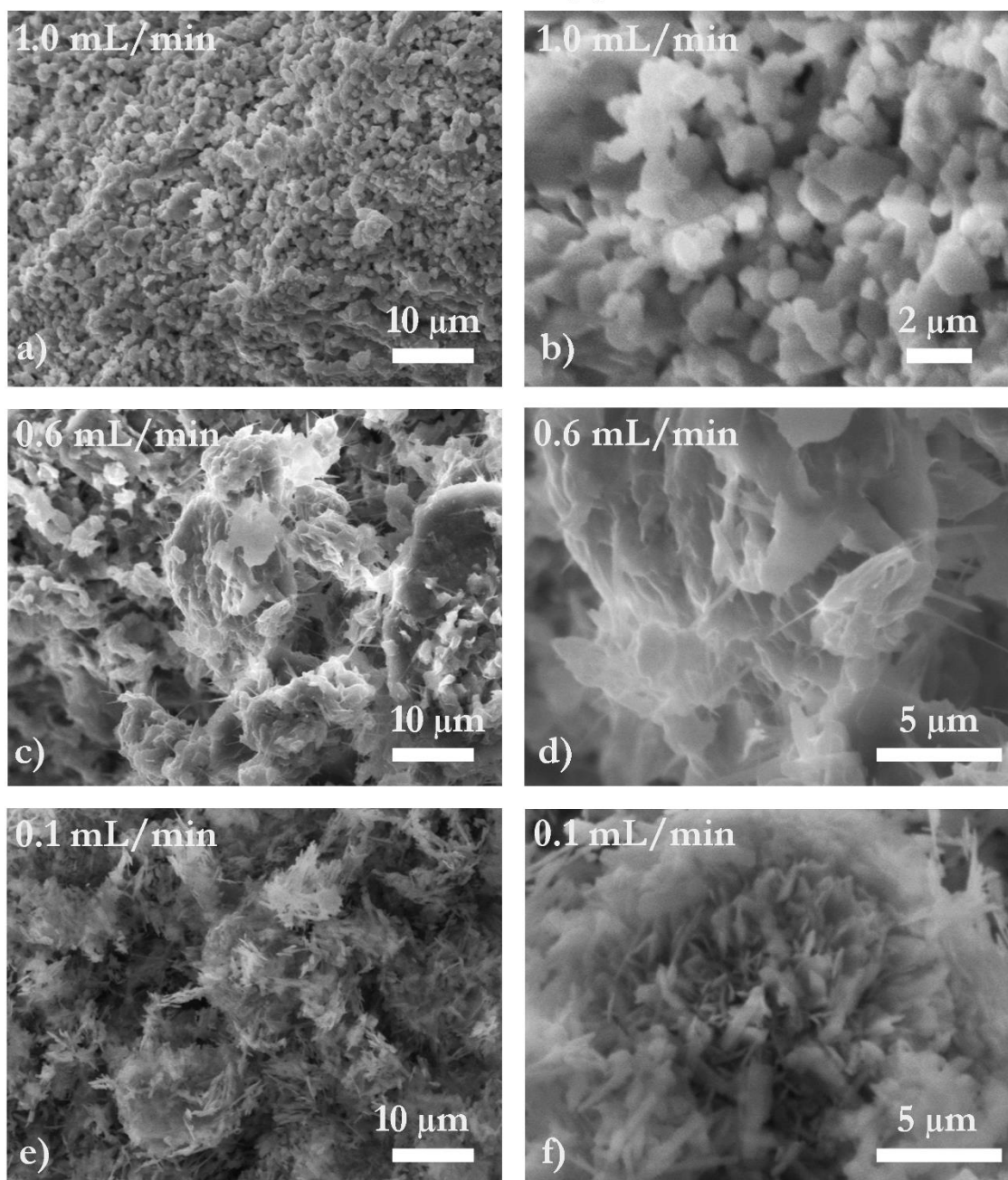


Figure 3-44: SEM images of the LCP samples produced using the AAAP method at different dropping rates. Samples after annealing at 550 °C for 10 hours. Microscope A. Magnification: left column 1000X, right column 5000X

3.4 Synthesis of LCP-*Cmcm* phase and $\text{Li}_{0.5}\text{CoPO}_4$ -*Cmcm*

This section remarks some comments about the synthesis of the LCP-*Cmcm* and a new lithium deficient $\text{Li}_{0.5}\text{CoPO}_4$ -*Cmcm* phases. The section is focus on the synthesis procedure and the control of the morphology. Further details about the crystal structure, thermal behavior, and magnetic properties are reported by Alarcón-Suesca *et.al.*¹⁹⁴ and their respective publications attached in the section 6.

In section 3.1.2.5.3 a synthesis using as starting materials LDP with CoSO_4 and CoCO_3 respectively lead to a sample with a crystalline phase of LCP-*Cmcm*, as well as, the synthesis using LiAc, CoAc₂, and H_3PO_4 presented in section 3.1.3. Those systems do not result in a phase pure LCP-*Cmcm* due to the presence of additional phases. However, through development of additional experiments (see appendix 5.3) a procedure using LiAc, CoAc₂, and H_3PO_4 with a Li:Co:P molar ratio of 3:1:10 finally results in phase pure LCP (see figure 3-45).

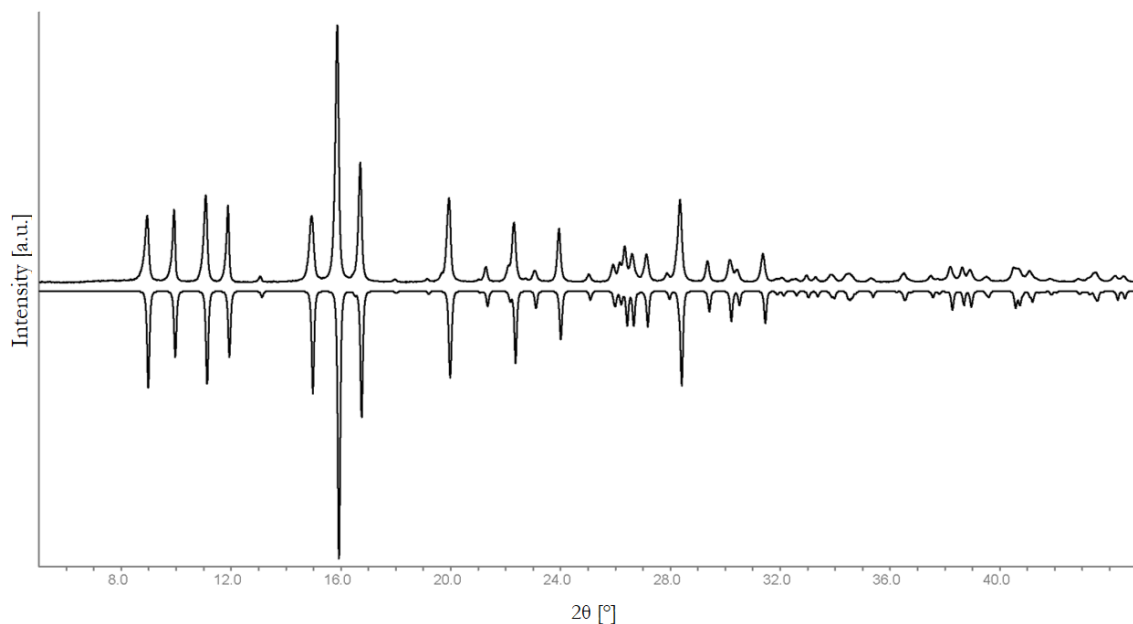


Figure 3-45: PXRD pattern of LCP-*Cmcm* synthesized using polyol synthesis. Pattern recorder after drying process. The measuring time is 1 hour.

The LCP-*Cmcm* phase has been synthesized only by the use of solid state synthesis using high pressure and high temperature parameters from LCP-*Pnma*¹⁵⁶ or applying MW-assisted synthesis, where the use of water free TTEG and cobalt acetate are fundamental to the obtaining of the LCP-*Cmcm* structure^{155, 158}. The polyol synthesis developed allows to obtain this LCP-*Cmcm* in a simple and easy way. Figure 3-46 shows the morphology of the sample. A dumbbell-like morphology with formation of hierarchical 3D structures is predominant in the along all sample. This dumb-bells are formed by agglomeration of

nano-layers. Moreover, when the order of mixing of the educts is changed (see experimental part 2.3.3) a change in the nucleation process is induced. Here, the dumb-bell morphology is conserved, but they are formed by primary nano-dots instead of layers. This kind of morphology has been beneficial in the context of cathode materials, specifically in the case of LFP-*Pnma*. In the work of Niederberger *et. al*¹⁹⁵, a synthesis of LFP-*Cmcm*/*Pnma* dumb-bells has been done using MW-assisted synthesis. The authors claimed that Li-ion diffusion and higher rate performance can be achieved due to the special 3D structure. However, in some cases this 3D structures are obtained by the use of organic templates¹⁹⁶. The advantages of the developed polyol method are the phase pure synthesis of LCP-*Cmcm* polymorph without the use of MW-radiation and access to the 3D dumb-bell structure without the use of surfactants, additive or organic templates. So far, is the first time that this kind of structure is reached in LMP compounds using such a simply synthesis method.

After drying process

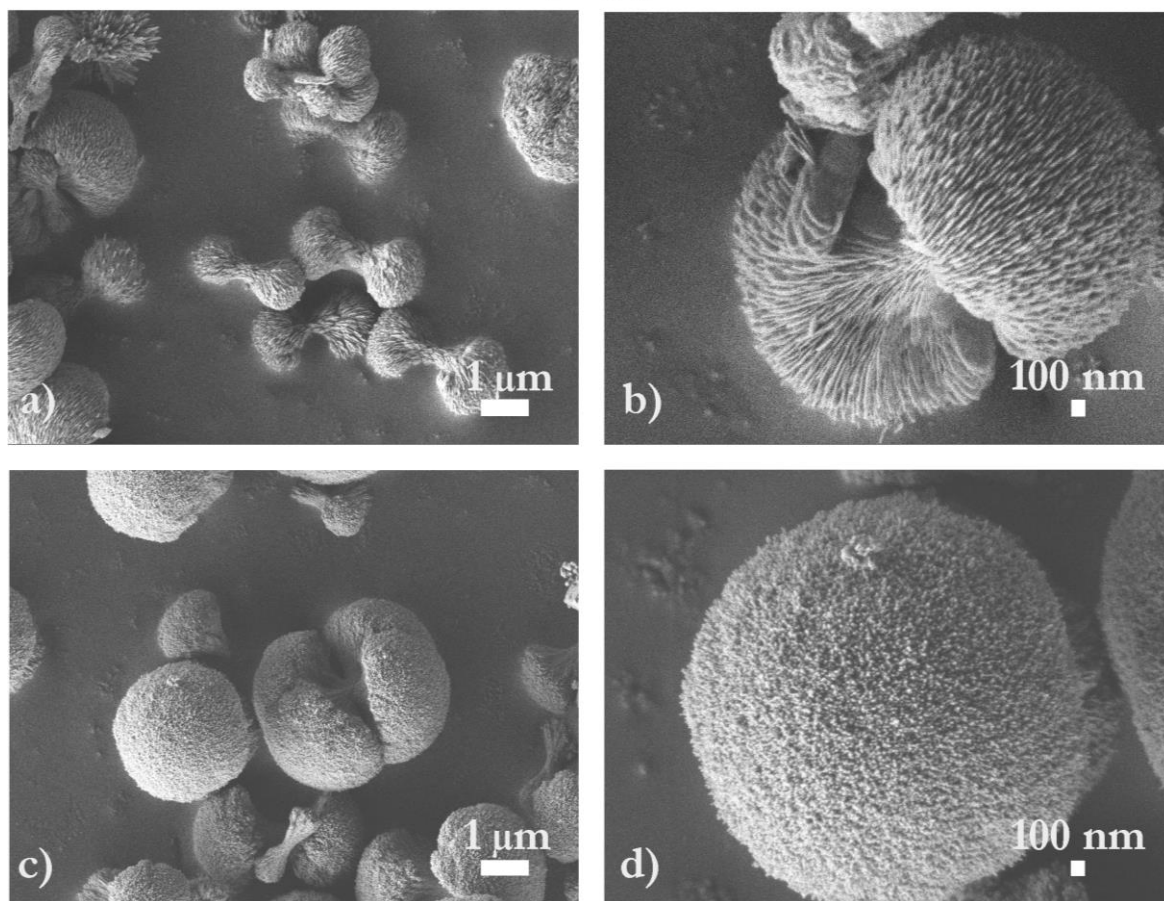


Figure 3-46: LCP-*Cmcm* samples using the standard and modified polyol route. a) and b) samples obtained using the standard method. c) and d) samples obtained using a variation in the educts mixture. Microscope B. Magnification: left column 10000X, right column 20000X

On the other hand, an interesting change in the color of the solution during the first part of the synthesis is noted. After complete the addition of CoAc_2 dissolution, the color turns from blue-violet to light-pink after 18 minutes of reaction (see figure 3-47). This behavior can be explain based on the ability of cobalt(II) to change its configuration between tetrahedral and octahedral coordination by the exchange of ligands ¹⁹⁷. The visible absorption band of tetrahedrally-coordinated cobalt(II) ion is located in the red part of the UV spectrum, giving a blue color. This band stems from d-d transition from the $^4\text{A}_2$ ground state to the $^4\text{T}_1(\text{P})$ state, and its fine structure results from spin-orbit coupling ¹⁹⁸. This happened after the addition of CoAc_2 (red solution) to the mixture of H_3PO_4 and LiAc solution. Additionally, some species can be formed in the solution. Those species are cobalt-ligand species of the type “ CoL_1L_2 ”, where L1 and L2 are ligands, for example $[\text{Co}(\text{H}_2\text{O})_4]^{2+}$ ¹⁹⁹. This effect is the so-called ***solvochromic effect*** and depends of the kind of ligands in the mixture solution. Additionally, at temperatures between 100 °C and 200 °C, aqueous solutions of cobalt(II) show a reversible color change from pink to violet, giving also a ***thermochromic effect*** ^{200, 201}. Furthermore, the occurrence of intermediate species such as, cobalt phosphates, peroxodiphosphates, lithium phosphate hydrates, phosphites can take place; however, no further literature related with the formation of LCP species at low temperature is published, therefore, this subject should be further analyze.

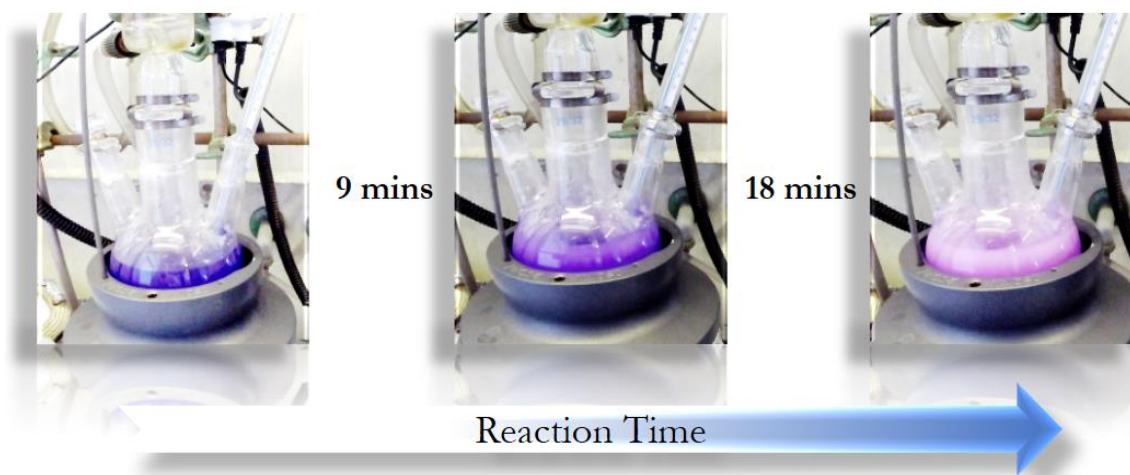


Figure 3-47: Change of the color of solution during polyol synthesis of LCP-*Cmcm*

Additionally, during the synthesis process of LCP-*Cmcm* phase the crystal structure does not change when surfactants are used. The figure 3-48 shows the PXRD patterns of the samples a reaction time of 3 hours and after use PVP and SDBS. Furthermore, the formation of the LCP-*Cmcm* phase is thermodynamically favored and the kinetic of the reaction is relatively fast. The signal:background ratio of the measurement is high and the reaction is done in a short period of time (3 hours), in comparison with the standard procedure (14 hours). Indexing and refinement of the data suggest the formation of

phase pure LCP-*Cmcm* (see table 3-19). This data confirms the ability to control the morphology without affecting the crystal structure of the *Cmcm* material obtained by the polyol route.

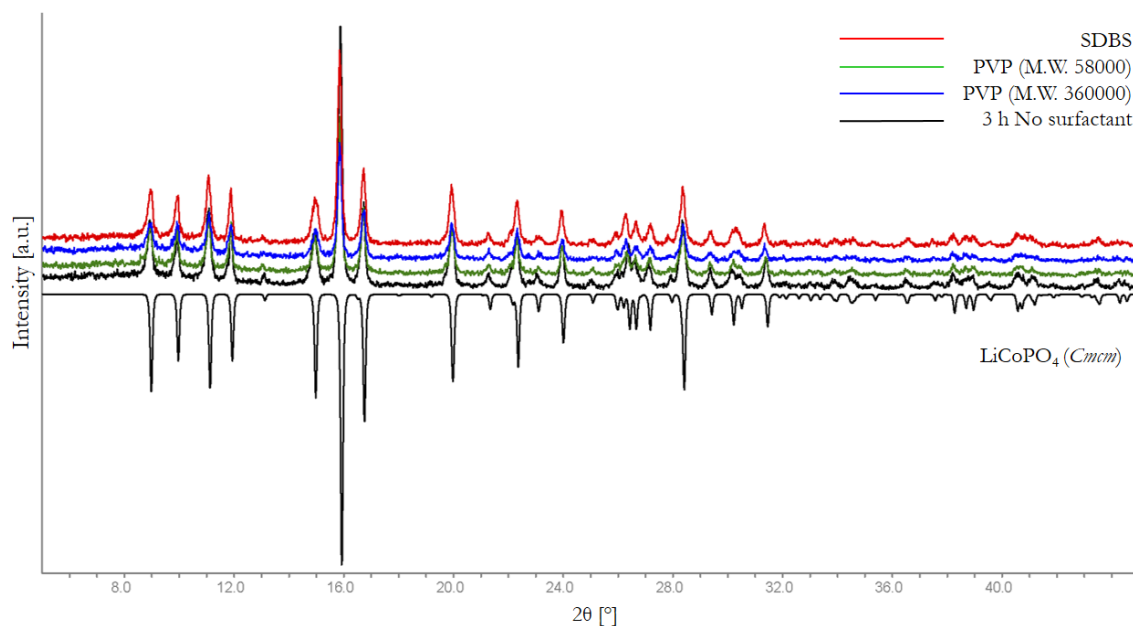


Figure 3-48: PXRD pattern of LCP-*Cmcm* synthesized using polyol synthesis. Black pattern corresponds to the synthesis using 3 hours of reflux. The red, green and blue patterns correspond to the synthesis using 3 hours of reflux and use of SDBS and PVP (M.W. 58000 and 360000) surfactants. Pattern recorder after drying process. The measuring time is 20 minutes.

Table 3-19: Lattice parameter and mean domain size of LCP-*Cmcm* synthesized with surfactants. Reported lattice parameters are presented at the bottom of the table ¹⁵⁶

Time (h)	Surfactant	<i>a</i> (Å)	<i>b</i> (Å)	<i>c</i> (Å)	<i>V</i> (Å ³)	Mean domain size (nm)	
3	No	5.439(4)	8.171(4)	6.201(6)	275.6(4)	21	
14	No	5.443(3)	8.169(4)	6.212(3)	276.2(2)	24	
14	PVP 58000	5.446(3)	8.174(6)	6.192(5)	275.6(4)	35	
14	PVP 360000	5.449(3)	8.166(6)	6.214(6)	275.5(4)	32	
14	SDBS	5.441(4)	8.162(4)	6.224(4)	275.3(4)	29	
Reported LCP - <i>Cmcm</i>		-	5.4448	8.1656	6.1938	275.18	-

After drying process

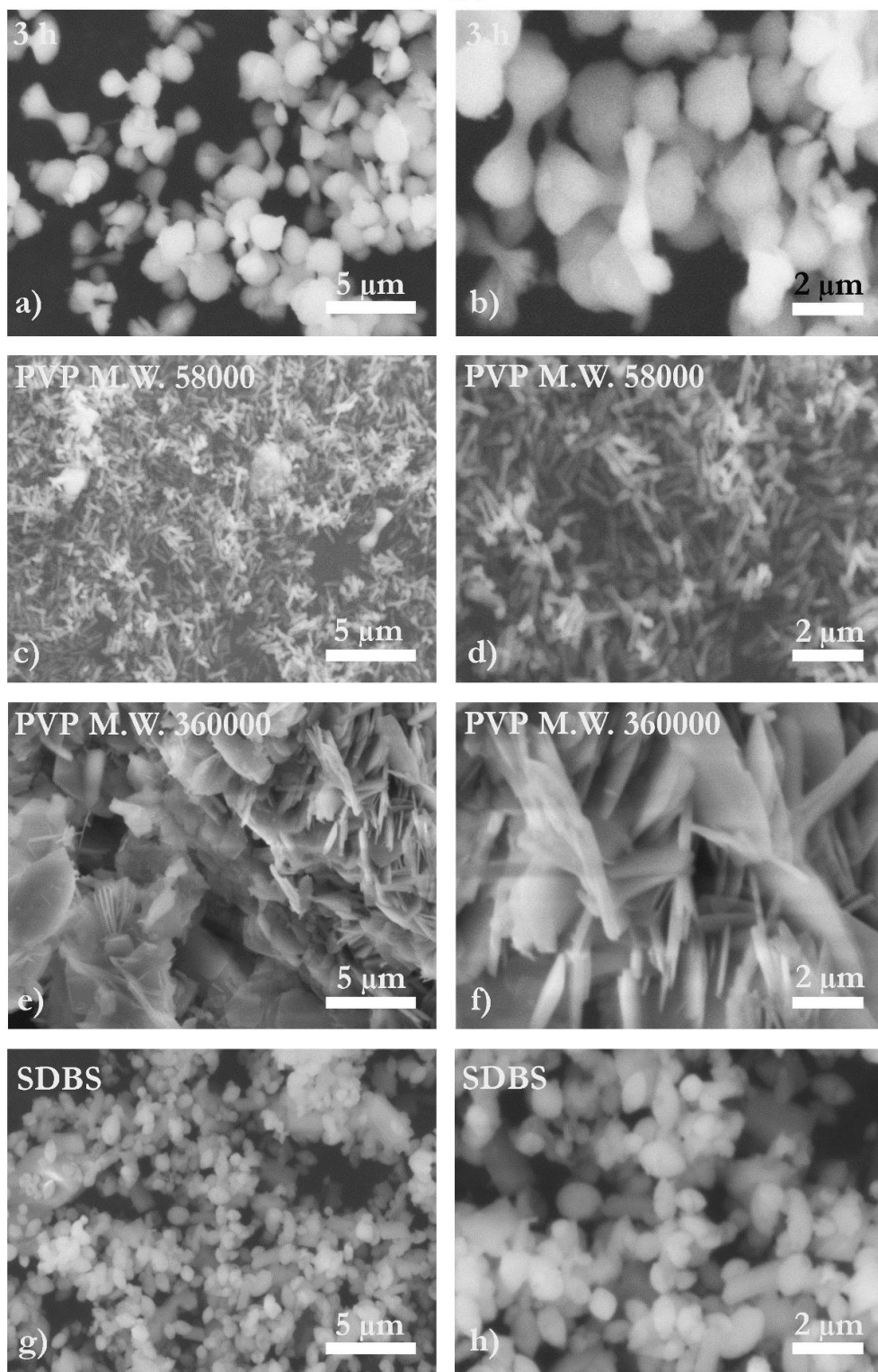


Figure 3-49: SEM pictures of LCP-Cmm. a) and b): Synthesis using 3 hours of reflux time. c) to h) synthesis using 14 hours with different surfactants. Microscope A. Magnification: left column 5000X, right column 10000X

As mentioned before, a lithium deficient compound was also synthesized using a similar methodology. In this case, based on a modification of the Li:Co:P molar ratio of 1:1:10, a new compound was identified. Previous reports of Ehrenberg *et. al.* ^{76, 79, 83} and Ju *et. al.* ²⁰² demonstrate the existence of lithium deficient phases that have been obtained after delithiation processes from LCP-*Pnma*. However, this reported phases are unstable and undergo amorphization under exposure of air. They must be studied using in-situ techniques and are thermal unstable. Figure 3-50 shows the PXRD pattern of the LCP-*Cmcm* and $\text{Li}_{0.5}\text{CoPO}_4$ -*Cmcm* samples obtained after drying process. Additionally, figure 3-51 shows the SEM images of the samples after drying. Here a similar dumbbell-like morphology is obtained, however, the primary structure is formed by nano-spheres.

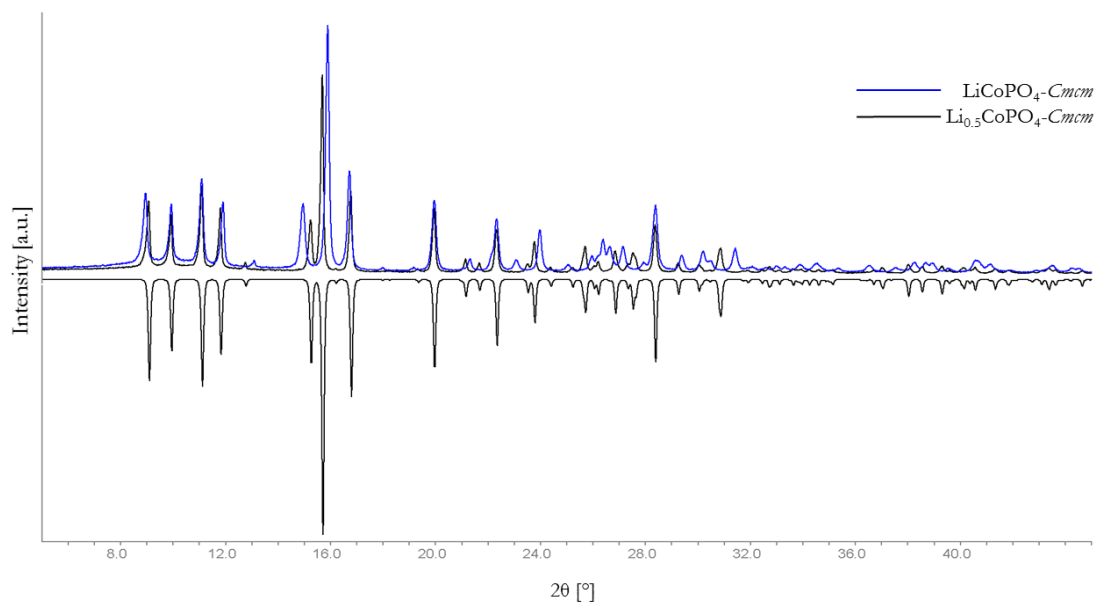


Figure 3-50: PXRD pattern of $\text{Li}_{0.5}\text{CoPO}_4$ -*Cmcm* synthesized using polyol synthesis. Blue pattern corresponds to full lithiated LCP-*Cmcm*. Negative intensity corresponds to $\text{Li}_{0.5}\text{CoPO}_4$ -*Cmcm*. Pattern recorder after drying process. The measure time is 1 hour.

After drying process

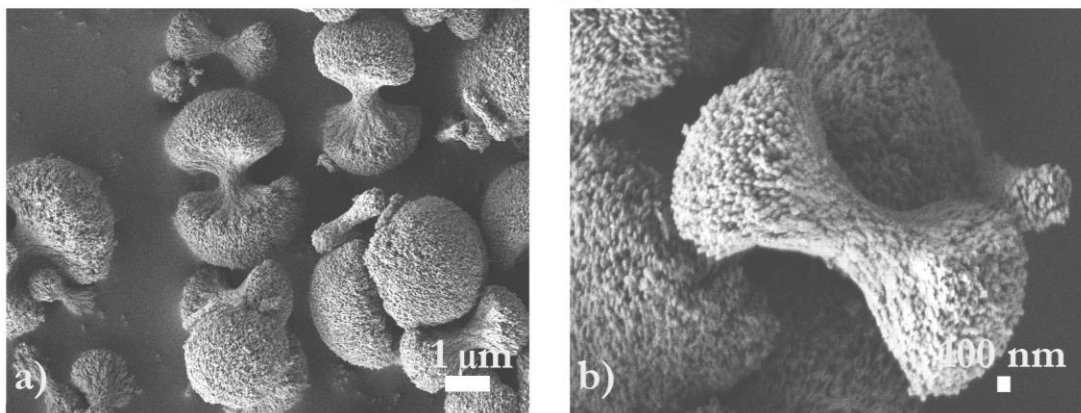


Figure 3-51: LCP-*Cmcm* samples using the standard and modified polyol route. Microscope B. Magnification: left column 10000X, right column 20000X

Regarding the electrochemical performance, this polymorphs of LCP are not attractive, as well as, in the case of the LCP- $Pn2_1a$. Based on the crystallographic considerations regarding Li^+ diffusion along the [010] direction in the case of the $Cmcm$ and $Pn2_1a$ polymorphs, the lithium path is blocked and the intercalation process can not be completely achieved. Figure 3-52, shows the comparison between the three structures. It can be observed that for LCP- $Pnma$ the detailed structural analysis of the migrating ion shows that a curved or zig-zag migration path is present between the adjacent lithium ions. There is also a certain amount of lattice distortion around the diffusing lithium ion as it passes the PO_4 and MO_6 polyhedra. On the other hand, the migration path for the $Cmcm$ and $Pn2_1a$ polymorphs are blocked by MO_6 polyhedra as well as PO_4 tetrahedra through the structure.

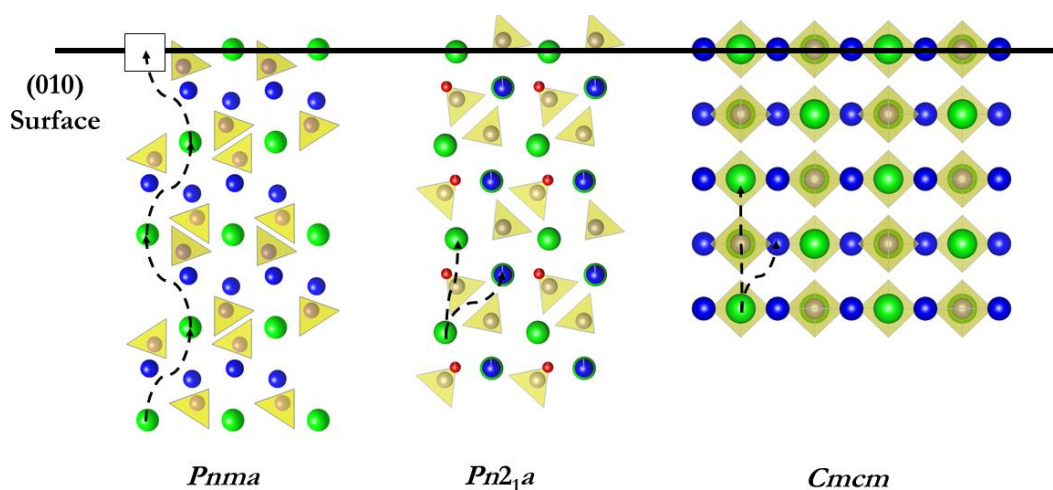


Figure 3-52: Schematic view parallel to (010) surface, showing the sinusoidal Li^+ -migration path (dotted line) to a Li^+ vacancy (open square for $Pnma$). The tilting of the PO_4 tetrahedron near the Li^+ vacancy is also shown. Li^+ : green; Co^{2+} : blue spheres; PO_4^{3-} : yellow tetrahedra.

3.5 Synthesis of LFP-*Pnma* by polyol method

This section presents an overview of the synthesis of LFP-*Pnma* by polyol method. As commented in section 1.6, the literature reports on the preparation of nanoparticles of LFP-*Pnma* by a polyol method using a simple-single step, without using any further annealing procedure. However, a common issue is that the reproduction of the synthesis does not lead to the olivine phase without secondary phases. Here a systematic approach is presented, in order to overcome the reproducibility problems of LFP-*Pnma* that are extended when the same methodology is applied to LCP-*Pnma*.

3.5.1 First step: reproduction of the synthesis reported in literature

The table 3-20 summarizes LFP-*Pnma* polyol synthesis approaches. Based on the combination of starting materials, five different systems (1 to 5) are reported. Those systems reported to obtain high crystalline LFP olivine after reflux process without annealing procedures. Systems 6 and 7 were tested for the first time. After the reproduction of the systems 1 to 5 and experiment as first “test approach” the systems 6 and 7; no olivine phase is obtained after a reflux and drying process. Despite that for each synthesis, the reported experimental steps were done as described, the materials collected did not show the characteristics mentioned in their respective publications. Indeed, the collected materials for all systems (except for systems 3, 6 and 7) are amorphous. For this reason, an annealing procedure was implemented in order to complete the formation of the olivine phase; however, only for system 4 a complete formation of LFP olivine was found. A summarize of phase analyses for each system is presented in table 3-21. After a change of synthesis parameters (see appendix 5.5) such as reflux time, order of mixing of educts, mixing at high temperatures (> 250 °C), no olivine phase was obtained.

Table 3-20: Summary of polyol synthesis published for LFP-*Pnma* (up to June 2012)

System number	Starting Materials	Reflux time (h)	Reflux temperature (°C)	Molar ratio Li:M:P	Solvent	Coating	Capacity (mAh/g)	Year	Ref.
1	Fe(CH ₃ COO) ₂	18	270	1:1:1	TEG	CNTs	129	2006	Shao <i>et. al.</i> ¹²⁶
	LiCH ₃ COO.2H ₂ O (NH ₄)H ₂ PO ₄	16	335		TTEG				
2	FeNO ₃ .9H ₂ O, (Fluka 99%) LiH ₂ PO ₄ (Aldrich 99%)	6, 18	245	1:1:1	DEG	MWCNT 250 °C, 2 h, Ar	146	2011	Porada <i>et. al.</i> ²⁰³
3	Fe(SO ₄) ₂ .7H ₂ O LiCH ₃ COO.2H ₂ O Citric Acid H ₃ PO ₄	2 – 4	105	1:1	TEG	3D-VCB 10% 600°C, 2 h	Not mentioned	2011	Jaegermann <i>et. al.</i> ⁹²
4	Fe(CH ₃ COO) ₂	16	245	1:1:1	DEG	No	124	2010	Kim <i>et. al.</i> ⁹³
	LiCH ₃ COO.2H ₂ O		278		TEG		154		
	H ₃ PO ₄		320		TTEG		167		
4	Fe(CH ₃ COO) ₂ LiCH ₃ COO.2H ₂ O H ₃ PO ₄	12	320	Not mentioned	TTEG	5, 10, 15 % of RGO	164.1	2012	Kim <i>et. al.</i> ⁹⁴
	Fe(CH ₃ COO) ₂ LiCH ₃ COO.2H ₂ O H ₃ PO ₄	4	245 285 325	Not mentioned	DEG TEG TTEG	Lactose, 700°C, 1 h	104 151	2010	Julien <i>et. al.</i> ⁹⁵
5	FePO ₄ .2H ₂ O LiOH	12	335	1:1	TTEG	No	166	2010	Munichandraiah <i>et. al.</i> ⁹⁷
6	Fe(C ₃ H ₇ O ₄) ₂ LiCH ₃ COO.2H ₂ O H ₃ PO ₄	16	206	1:1:1	TTEG	No	124	2010	Engbert, Alarcón, Nilges
7	Fe(C ₂ O ₄) ₂ .7H ₂ O LiCH ₃ COO.2H ₂ O H ₃ PO ₄	16	228	1:1:1	TTEG	No		2010	Engbert Alarcón, Nilges

Table 3-21: Phase analysis after reproduction of synthesis based on table 3-20

System number	Starting Materials ¹	Reflux time (h)	Reflux temperature (°C)	Molar ratio Li:M:P	Phases after drying	Phases after annealing ²
1	Fe(CH ₃ COO) ₂ LiCH ₃ COO.2H ₂ O (NH ₄)H ₂ PO ₄	18	210	1:1:1	Amorphous	Amorphous
2	FeNO ₃ .9H ₂ O, (Fluka 99%) LiH ₂ PO ₄ (Aldrich 99%)	18	200	1:1:1	Amorphous	Fe ₃ PO ₄ (OH) ₂ -P4 ₃ 2 ₁ 2 Unknown phase
3 ³	Fe(SO ₄) ₂ .7H ₂ O LiCH ₃ COO.2H ₂ O H ₃ PO ₄	4	185	1:1:1	Fe ₂ (SO ₄) ₃ -P-3 ₁ c Unknown phase	LFP-Pnma Fe ₂ (SO ₄) ₃ -P-3 ₁ c Fe ₃ O ₄ -Fd-3m Unknown phase
4	Fe(CH ₃ COO) ₂ LiCH ₃ COO.2H ₂ O H ₃ PO ₄	16	214	1:1:1	Amorphous	LFP-Pnma
5	FePO ₄ .2H ₂ O LiOH	12	208	1:1	Amorphous	LFP-Pnma Fe ₇ (HPO ₄)(PO ₄) ₅ -P-1 Unknown phase
6	Fe(C ₅ H ₇ O ₄) ₂ LiCH ₃ COO.2H ₂ O H ₃ PO ₄	16	206	1:1:1	Li ₃ PO ₄ -Pmm2 ₁ Unknown phase	LFP-Pnma Fe ₂ O ₃ -R3cH Fe ₃ O ₄ -Fd-3m Unknown phase
7	Fe(C ₂ O ₄) ₂ .7H ₂ O LiCH ₃ COO.2H ₂ O H ₃ PO ₄	16	228	1:1:1	Fe(C ₂ O ₄) ₂ .2H ₂ O Li ₃ PO ₄ -Pmm2 ₁ Unknown phase	LFP-Pnma Fe ₂ O ₃ -R3cH LiFeP ₂ O ₇ -P1 ₂ 1 ₁ Unknown phase

¹ All reactions conducted in TTEG

² Annealing procedure under argon for 8 hours

³ The experiment was done with and without use of citric acid

Since no olivine phase was obtained after by following the experimental setups published, there is lack of important information to obtain the olivine phase in a simple synthesis. For instance, only the systems 3, 6 and 7, shown some reflections, after the drying process. For the systems 6 and 7, corresponding to iron oxalate and iron acetylacetonate the PXRD patterns show a very low signal:background ratio.

3.5.2 Second step: variation of the synthesis parameters

The system based on iron sulfate represent the best evidence of phase formation in comparison with systems 6 and 7. Thus, this system is selected to explore additional variations of the synthesis parameters. Further experiments suggested that the change in the molar ratio of the educts induces a strong change in the phase composition. As an example, figure 3-53, present the PXRD pattern of the system 3 with a Li:Fe:P molar ratio 1:1:1 and 3:1:1. It can be observed, that the PXRD pattern of the 3:1:1 sample shows

reflections corresponding with LFP-*Pnma*. However, a considerable Li_2SO_4 phase is also present. Also, reflections with higher intensity in the PXRD pattern of the 3:1:1 sample corresponds to this phase.

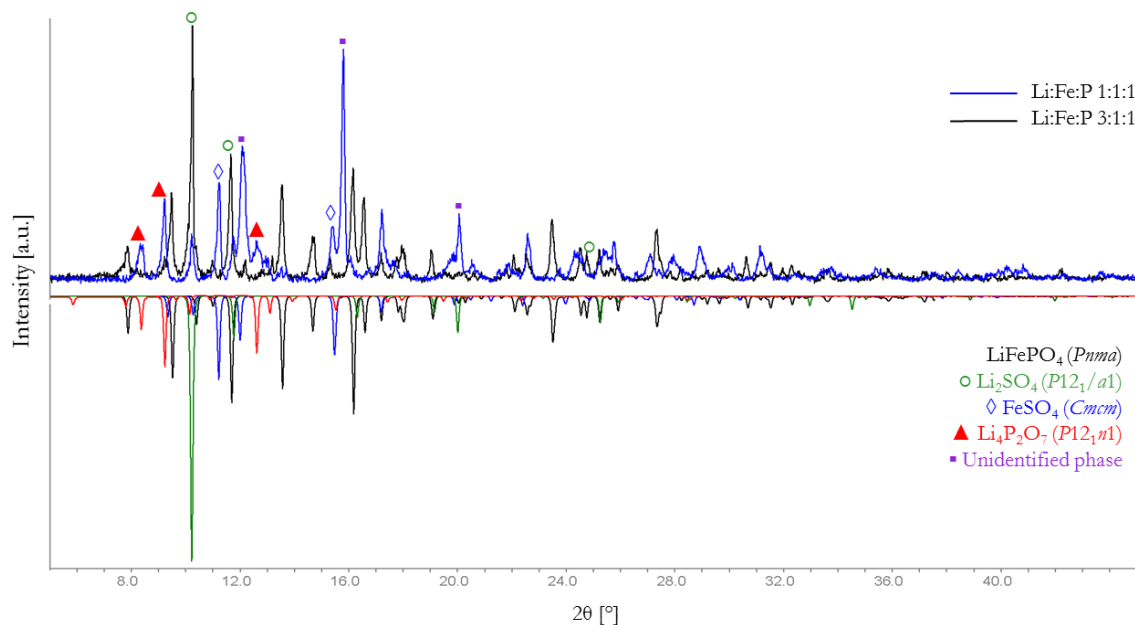


Figure 3-53: Influence of the molar ratio on the synthesis of LFP-*Pnma*. PXRD pattern of samples refluxed after the drying process. The patterns corresponds to samples with Li:Fe:P molar ratios of 3:1:1 (**black**) and 1:1:1 (**blue**) respectively. The negative intensity corresponds to the reported phases of LFP-*Pnma* (black), Li_2SO_4 -*P12₁/a1* (○ Green), FeSO_4 -*Cmcm* (◇ blue), $\text{Li}_4\text{P}_2\text{O}_7$ -*P12₁n1* (▲ red) and unidentified phase (■ lila). The measuring time is 30 min.

3.5.3 Third step: tuning the Li:Fe:P molar ratio

The last section suggested that the change in the Li:Fe:P molar ratio; more precise by an increase in the amount of lithium starting material, leads to the formation of LFP-*Pnma*. After testing a wide range of molar ratios (see appendix 5.5), the interval is restricted between 1:1:1 and 3:1:1. Figure 3-54 shows the comparison of the PXRD patterns of the experiments conducted within this interval. Among all experiments, the one with a Li:Fe:P molar ratio of 2:1:1, shows a best correspondence in comparison with the reported LFP-*Pnma*. It is observed that a small difference in the molar ratio induces the formation of several phases is observed for the 2:1:1 and 2.5:1:1 samples. In this case, the 2:1:1 ratio was fixed and in the next steps, another synthesis parameter is optimized.

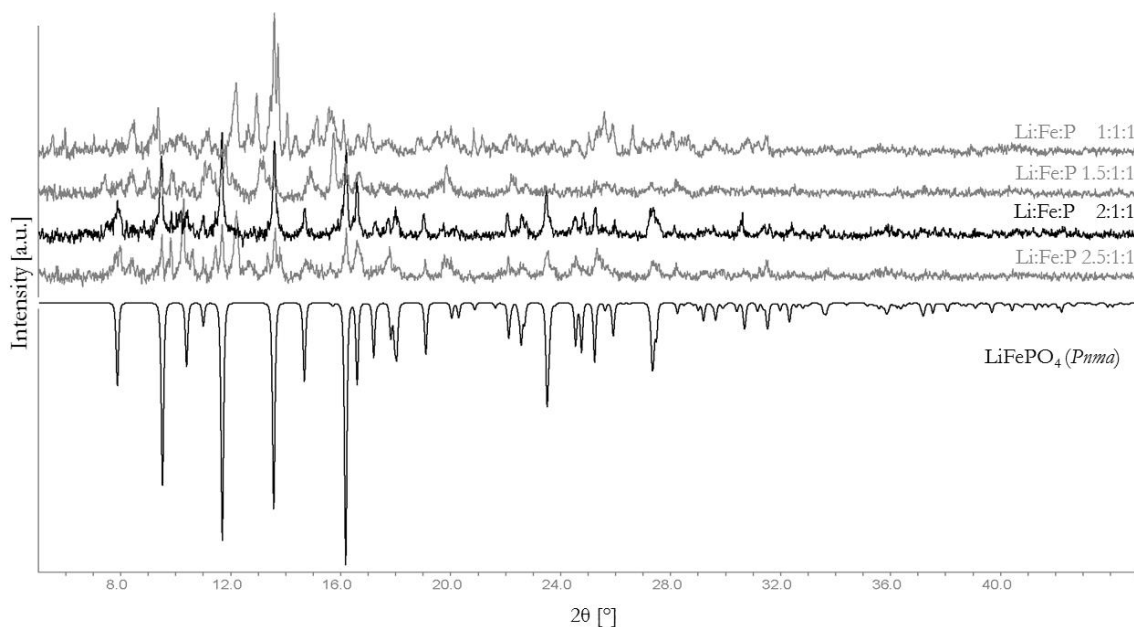


Figure 3-54: Influence of the Li:Fe:P molar ratio on the synthesis of LFP-*Pnma*. PXRD pattern of the samples after drying process. The PXRD pattern in **black** corresponds to the Li:Fe:P ratio 2:1:1. Negative intensity corresponds to LFP-*Pnma*. The measuring time is 20 minutes.

3.5.4 Fourth step: variation of the mixing method of educts

Generally, the literature related to polyol syntheses of cathode materials do not specify the mixing order of educts, the use of pre-dissolution steps in between or the way of adding starting solutions (dropwise or single shot). The importance of these details is further analyzed in this section. Figure 3-55 shows three different methods of mixing for LiAc, FeSO₄ and H₃PO₄. In addition, the figure 3-56 shows the PXRD patterns of samples corresponding to each mixing method. All mixing methods include a previous dissolution of lithium and iron sources in TTEG. When the PXRD patterns of samples prepared by the mixing methods 1 and 3 are compared, it can be noted that the signals corresponding to the secondary phases are higher in intensity for method 3. It can be a consequence of the difference of solubility between LiAc and FeSO₄ in TTEG. The solubility of LiAc is higher than the one of FeSO₄, this leads to a reaction with bigger amount of LiAc dissolved in TTEG with H₃PO₄. On the other hand, mixing method 2 includes an extra step of 30 minutes mixing of LiAc and H₃PO₄. This simple step is important to decrease considerably the amount of secondary phases present in the olivine product.

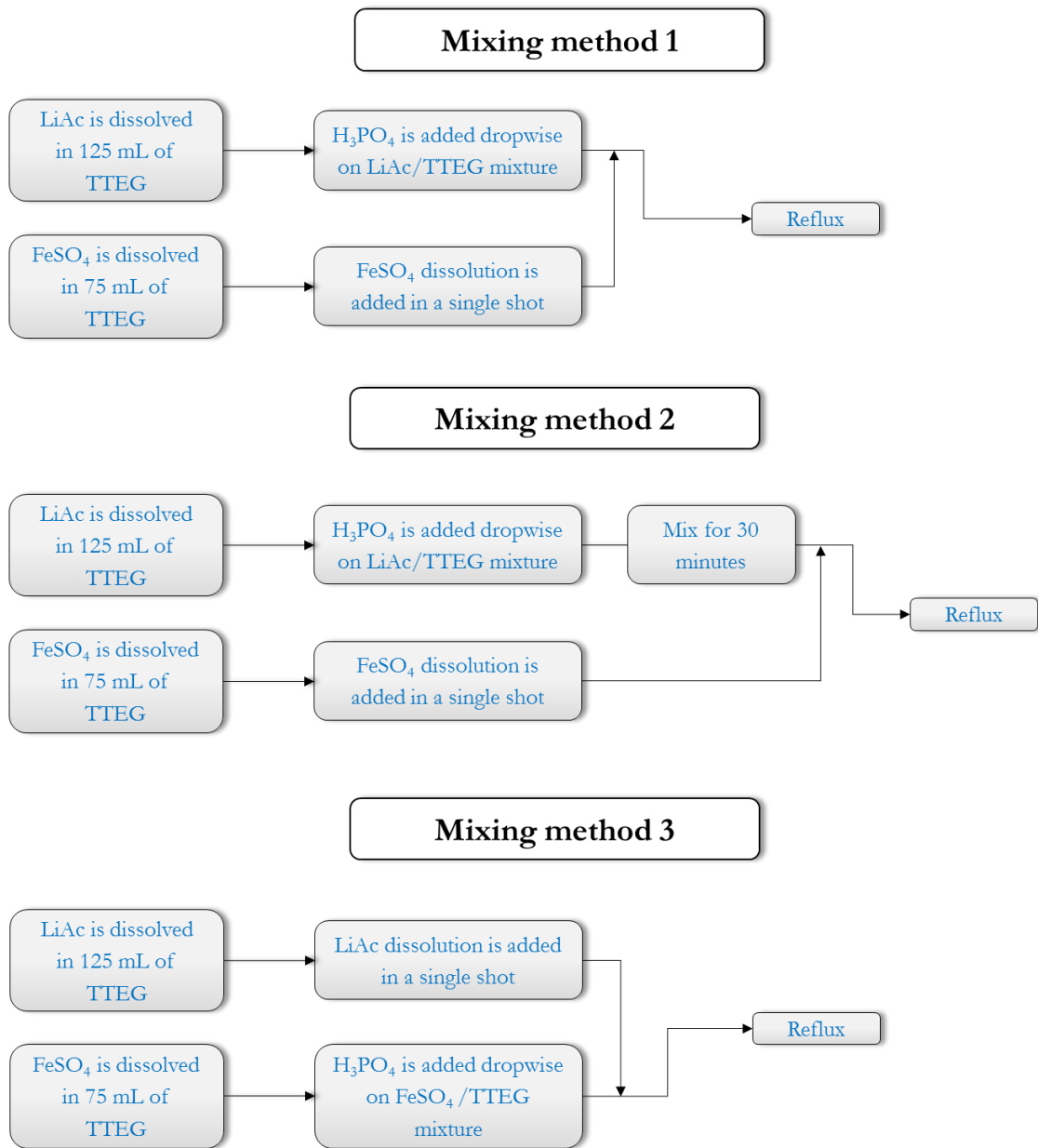


Figure 3-55: Mixing methods tested in the polyol synthesis of LFP-*Pnma*. Additional experimental details are described in experimental section 2.6.

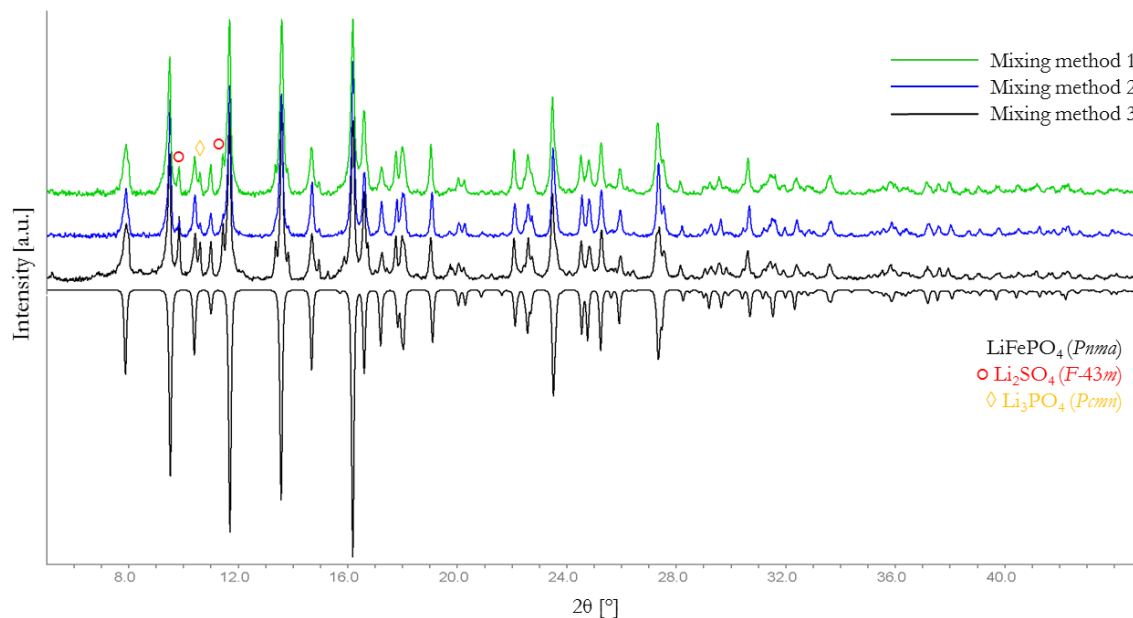


Figure 3-56: Influence of the mixing method on the synthesis of LFP-*Pnma*. PXRD pattern of the samples after drying process. The mixing details are specified in figure 3-55. Negative intensity corresponds to LFP-*Pnma*. Secondary phases corresponds to (○ red) $\text{Li}_2\text{SO}_4\text{-}F\text{-}43m$ and (◇ yellow) $\text{Li}_3\text{PO}_4\text{-}Pcmm$. The measuring time is 1 hour.

3.5.5 Fifth step: variation of the polyalcohol

The system 4 detailed in table 3-20 uses DEG, TEG and TTEG as solvents for the production of LFP-*Pnma*. It is important to remark that the data reported by Julien *et.al.*⁹⁵ suggest that pure LFP-*Pnma* can only be obtained in TEG and TTEG solvents. However, after testing EG, DEG and TEG as solvents, a complete formation of the olivine phase is achieved using DEG and TEG. In the case of EG, small differences can be observed for different reflection positions in the 2-theta range, when it is compared with the reported LFP pattern. For example, at 17.74 2-theta, the first peak has a lower intensity and it is shifted to lower 2-theta values. At 2-theta 20.13° there is only one signal instead of two. The refined lattice parameters, as well as, the size of the crystallite are presented in table 3-22.

Table 3-22: Lattice parameter and crystallite size of LFP-*Pnma* synthesized in EG, DEG and TTEG. Reported lattice parameters are presented at the top of the table

Solvent	<i>a</i> (Å)	<i>b</i> (Å)	<i>c</i> (Å)	<i>V</i> (Å ³)	Mean domain size (nm)	
EG	10.307 (7)	5.988 (4)	4.697 (4)	289.8 (4)	26.8	
DEG	10.302 (3)	5.995 (6)	4.705 (4)	283.2 (4)	30.6	
TEG	10.305 (4)	5.982 (5)	4.696 (7)	289.5 (3)	30.7	
Reported LFP - <i>Pnma</i>	-	10.304 (1)	5.982 (8)	4.695 (5)	289.4	-

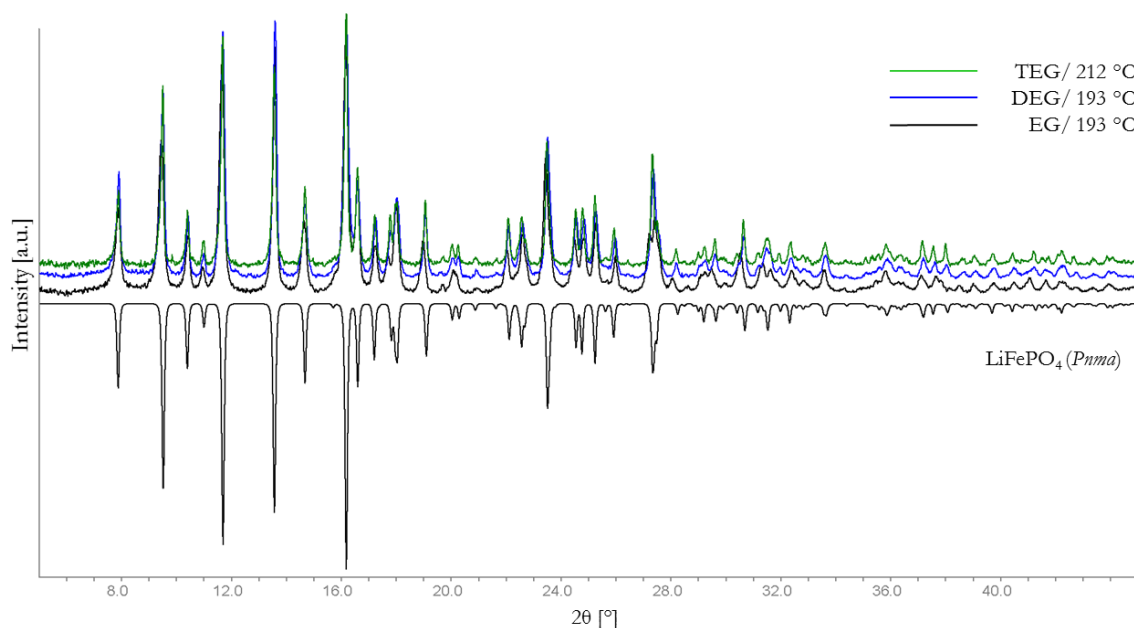


Figure 3-57: Influence of the polyalcohol on the synthesis of LFP-*Pnma*. PXRD pattern of the samples after drying process. **Black** pattern: EG; **blue**: DEG and **green**: TEG. The reflux temperature is also included. Negative intensity corresponds to LFP-*Pnma*. The measure time is 1 hour.

The morphology of the samples are presented in figure 3-58. In general, the samples show a rod-like morphology, however, in the case of DEG, some particles appears to be semi-rounded or oval. The estimated particle size calculated from HR-SEM images is: EG: 100 x 50 nm; DEG: 100 x 50 nm and TEG: 100 x 40 nm. After comparison between LCP-*Pnma* and LFP-*Pnma* particles (figures 3-19 and 3-58 respectively) it can be concluded that LFP show less agglomeration than LCP. The LFP particles can be easily identified along the sample, especially in the case of EG. Indeed, EG produces the smallest mean domain size (see table 3-22). The morphology obtained is similar to the particles synthesized by Kim *et. al.*²⁰⁴ and Heng *et. al.*²⁰⁵, with particle sizes around 100 to 200 nm in length, 60 to 100 nm in diameter.

Finally, this section shows the importance to specify the order of mixing of precursors as well as the ability of reproduction of polyol synthesis from the literature. Moreover, the role of the molar ratio is fundamental in order to achieve olivine phases without the presence of impurities. Finally, it is important to underline that, in contrast to the reports in literature, a LFP synthesis is possible without the use of ascorbic acid as reduce agent.

After drying process

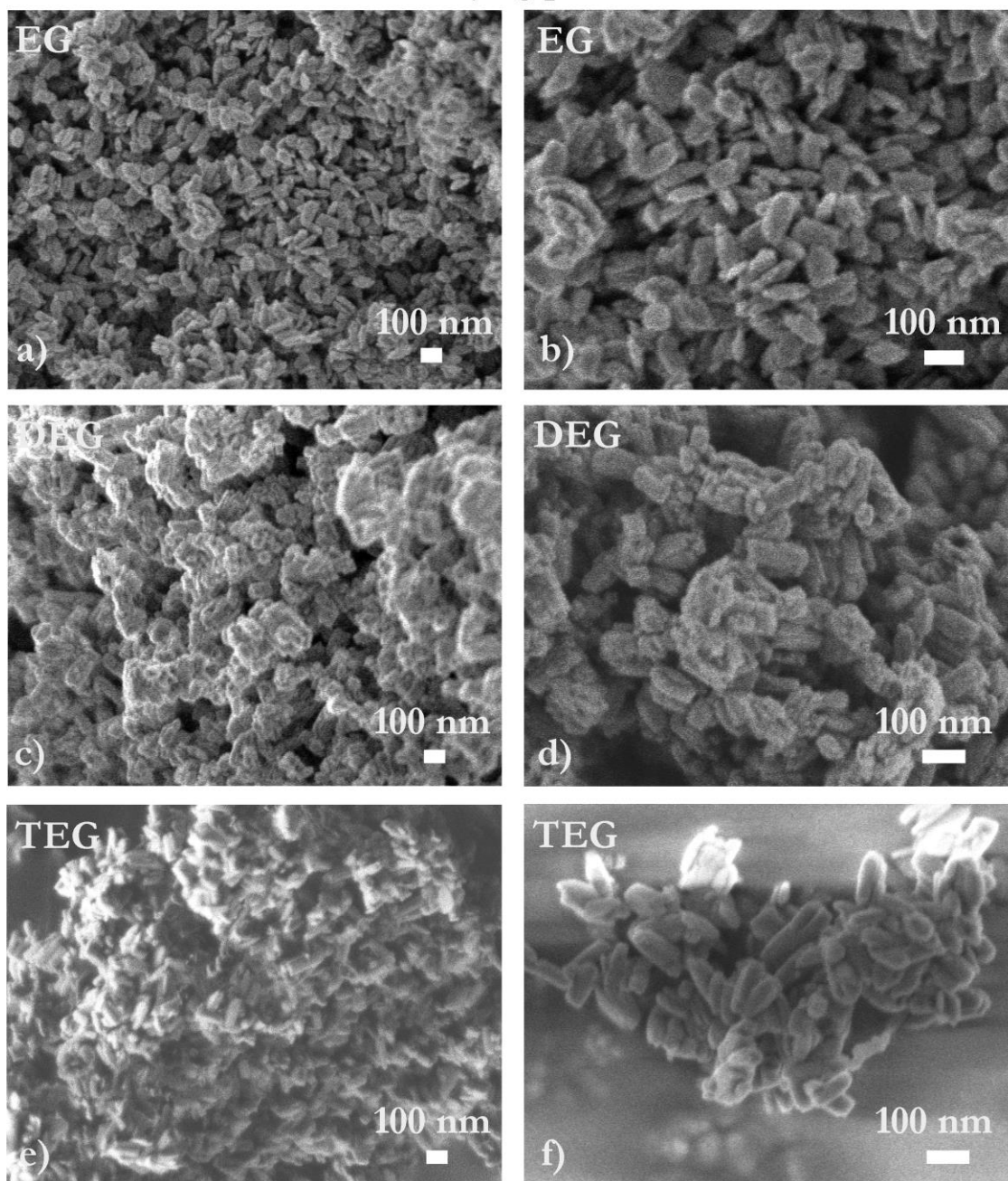


Figure 3-58: Influence of the polyalcohol. SEM images of LFP-*Pnma* produced using EG, DEG and TEG. Microscope B. Magnification: left column 50000X, right column 100000X

3.6 Synthesis of LFP-*Cmcm* phase

The first report of the *Cmcm* polymorph of LFP was reported by Amador *et. al.* ²⁰⁶. The phase was obtained in a high pressure (65 kbar) synthesis at an elevated temperature of 900 °C from LFP-*Pnma*. Years after, Haase *et. al.* ²⁰⁷, published a liquid-phase method at ambient pressure and low temperature. However, this methodology request a multi-step synthesis between FeCl₂.4H₂O, LiCl with methanol, diphenylether and tris-*n*-octylphosphine oxide with a reduction step under nitrogen atmosphere and a final reaction with H₃PO₄. The H₃PO₄ is previous prepared with dihexylether and hexylamine. Afterwards, Niederberger *et. al.* ²⁰⁷, Corr *et. al.* ¹⁷³ and Manthiram *et. al.* ¹⁵⁸ reported MW-assisted synthesis based on the control of the solvent. For example, Niederberger uses a mixture of benzyl alcohol and 2-pyrrolidinone; however the mixture with the raw materials is done inside a glovebox to avoid oxidation of Fe(II). Manthiram claims that in order to complete the *Cmcm* phase it is crucial to use oxalate as iron precursor source and dried TTEG. Finally, Corr uses 1-ethyl-3-methyl imidazolium trifluoromethanesulfonate (EMI-TFMS) in a mixture with EG; however, in this case the phase is mixed with LFP-*Pnma*.

On the other hand, in the last section, during the synthesis of LFP-*Pnma*, a sample synthesized present a mixture of LFP-*Pnma*, Li₃PO₄, an unidentified phase (see figure 3-53). After developing an analogous methodology compared with in the last section, a LFP-*Cmcm* was synthesized for the first time by a simple-single synthesis. Although the sample present a small fraction of LFP-*Pnma* (see figure 3-60), this methodology strongly simplifies the procedures reported in the literature. Table 3-23, summarizes the experimental variations employed, focused mainly on the Li:M:P molar ratio and the solvent.

Table 3-23: Summary of the variations in molar ratio and solvent in the polyol synthesis of LFP-*Cmcm*

Starting Materials	Reflux time (h)	Reflux temperature (°C)	Molar ratio Li:M:P	Solvent	pH range
Fe(C ₂ O ₄) ₂ ·7H ₂ O LiCH ₃ COO·2H ₂ O H ₃ PO ₄	16	A range cover from 102 to 260	0.5:1:1, 1:1:1, 1.5:1:1, 2:1:1, 3:1:1, 2:1:10, 3:1:10, 2:1:5	EG, DEG, TEG, TTEG, PEG, TTEG:H ₂ O 50:50, TTEG:H ₂ O 90:10	3.5 – 5.0

After screening the complete set of experiments, the best experimental conditions are identified: they are Li:Fe:P 1:1:1 molar ratio using TTEG as solvent. The temperature in the solution during reaction was 216 °C. On the other hand, the morphology of the sample is show in figure 3-61. In general, the sample presents agglomerates of rod-like and oval-like particles.

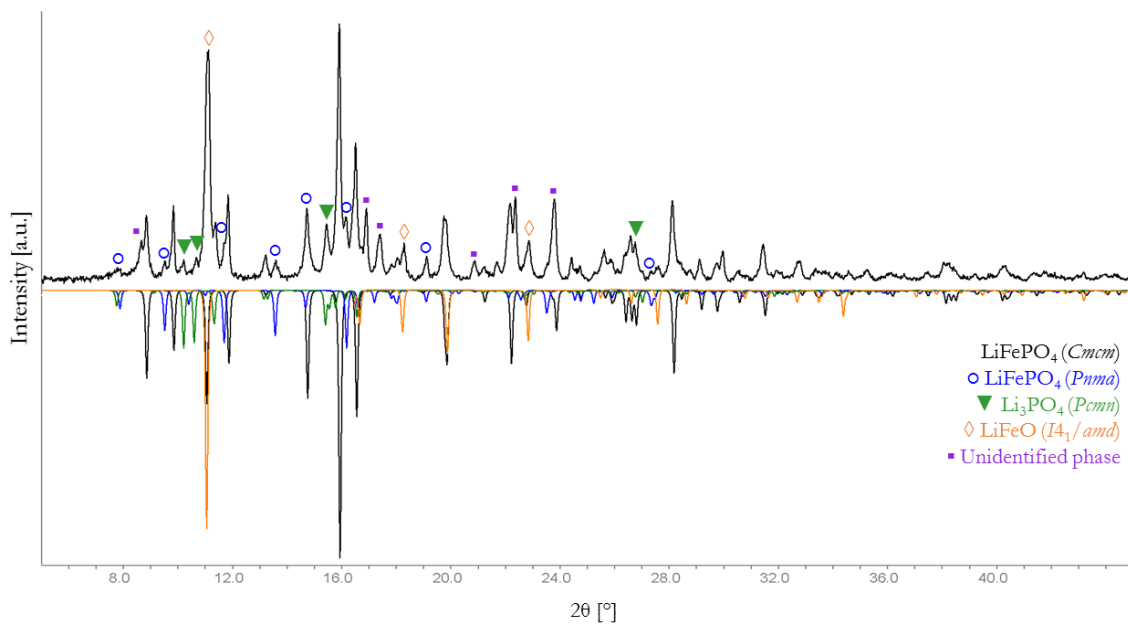


Figure 3-59: PXRD pattern of the LFP precursor sample using LiAc, iron oxalate and H_3PO_4 in molar ratio 2:1:1. Sample synthesized in TTEG. The negative intensity corresponds to the reported phases of LFP-*Cmcm* (black), LFP-*Pnma* (blue \circ), Li_3PO_4 -*Pcmm* (green ∇), LiFeO - $I4_1/amd$ (orange \diamond) and an unidentified phase (■ lila). The measuring time is 30 min.

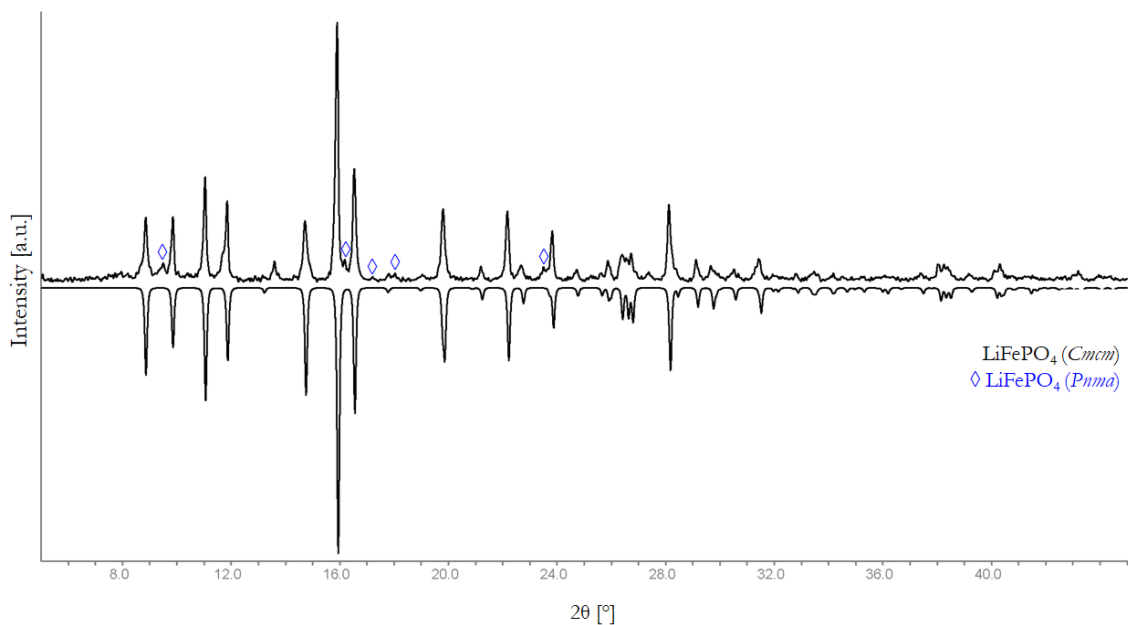


Figure 3-60: PXRD pattern of the sample using LiAc, iron oxalate and H_3PO_4 in molar ratio 1:1:1. Sample synthesized in TTEG. The negative intensity corresponds to the reported phases of LFP-*Cmcm* (black), LFP-*Pnma* (blue \diamond). The measuring time is 1 h.

Table 3-24: Lattice parameters and crystallite size of LFP-*Cmcm* synthesized in TTEG. Reported lattice parameters are presented at the top of the table.

Solvent	<i>a</i> (Å)	<i>b</i> (Å)	<i>c</i> (Å)	<i>V</i> (Å ³)	Main domain size (nm)	
TTEG	5.528 (24)	8.259 (22)	6.174 (24)	281.9 (24)	35	
Reported LFP - <i>Cmcm</i>	-	5.5230 (3)	8.2565 (5)	6.1583 (5)	280.82	-

After drying process

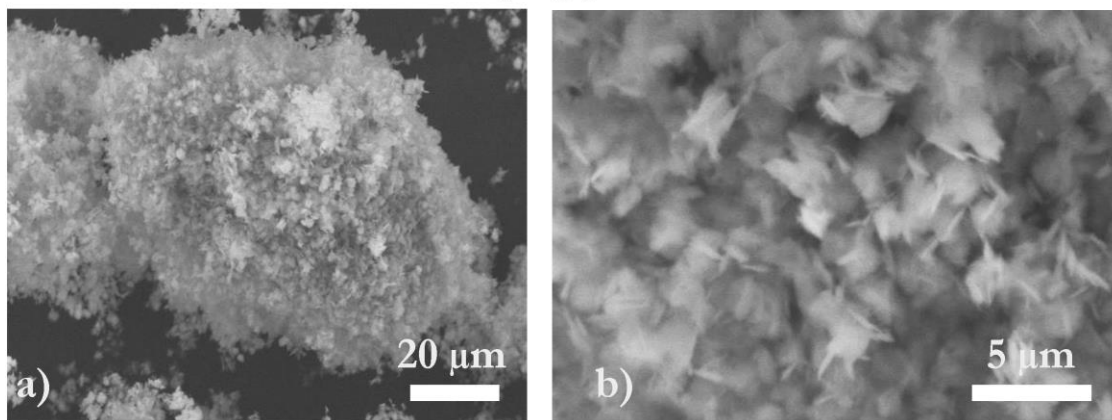


Figure 3-61: SEM images of LFP-*Cmcm* produced using TTEG. Microscope A. Magnification: left 1000X, right 5000X

Finally, the polyol synthesis represent a simple way of synthesis of LCP-*Cmcm* phase without the need of complex methodologies involving pre-treatments with organic substances or the use of expensive MW-assisted synthesis.

4. Conclusions and outlook

4.1 Conclusions

The phospho olivine-type LiCoPO_4 -*Pnma* has been subject of intensive studies due to its high thermal stability, high theoretical capacity and high energy density, allowing its application as cathode material for LIB's. Within the objectives of this work, the polyol synthesis method was used to synthesize LCP-*Pnma* using a systematic approach based on the combination of different starting materials, as well as a variation of experimental parameters. In order to achieve good electrochemical performance, the LCP-*Pnma* materials should be highly crystalline, show a small particle size (nanometer range) and also a discrete particle size distribution.

Contrary to the reports for LiFePO_4 and LiMnPO_4 and, in order to complete the formation of high crystalline LCP-*Pnma* phase, the use of annealing procedures after reflux and drying processes is necessary. Despite the inherent problems of annealing procedures represented mainly by grain growth and particle agglomeration, small and narrow particle size distributions are obtained by the use of high boiling point polyalcohols (DEG, TEG, and TTTEG) combined with water in ratios 10:1, 20:1 and 20:3, respectively. In addition, the shape of the particles, as well as the morphology can be controlled by the use of surfactants; such as PVP, without altering the crystalline structure. The best capacity mark reaches 22% of the theoretical value; to our knowledge, the best value of LCP-*Pnma* synthesized by polyol method but still low in comparison with LCP-*Pnma* produced using other synthesis routes (i.e. microwave-assisted, solid state, hydrothermal). In order to compare the influence of the synthesis procedures on the electrochemical capacity, a MW-assisted polyol route was implemented reaching 61% of the theoretical capacity. In the case of MW synthesis, the MW radiation favored to the formation of the *Pnma* phase. Furthermore, the acetate-assisted antisolvent precipitation (AAAP) method for LCP-*Pnma* was developed for the first time, reaching 42% of the theoretical capacity. This

improvement is reached by the use of C-coating procedure using glucose, leading the formation of a C-composite. An increment of the electrical conductivity by a factor of 10^7 without the use of argon atmospheres is reached.

Despite polyol process can not be considered as advantage way for the synthesis of LCP-*Pnma*, this route is beneficial for the synthesis of the LCP-*Pn2_{1a}* and LCP-*Cmcm*. These compounds can be obtained in a simple single step polyol process, avoiding the use of MW irradiation and complicated synthesis procedures reported before. The results suggest that the LCP-*Pn2_{1a}* and LCP-*Cmcm* phase formations are thermodynamically favored at temperatures below 200 °C. In addition to the reported meta-stable character of LCP-*Pn2_{1a}* and LCP-*Cmcm*, which can easily be converted to LCP-*Pnma* at temperatures above 350 °C, we found a high-temperature transition from LCP-*Pnma* to LCP-*Pn2_{1a}* at 725 °C by high-temperature in-situ XRD measurements. On the other hand, an analysis of the magnetic properties of LCP-*Cmcm* was published as the first time. The observations have shown an antiferromagnetic ordering below T_N of 11 K at 10 kOe.

The polyol route was also effective in obtaining of the first lithium deficient structure derived from LCP-*Cmcm* using a direct synthesis. In this case, phase pure $\text{Li}_{0.5}\text{CoPO}_4$ -*Cmcm* phase pure was obtained using a similar procedure than for LCP-*Cmcm*. A remarkable point is the formation of 3D microstructures based on nano-sheets that assemble to form micro dumb-bells. This kind of morphology was previously reported for LFP, however, in our synthesis, the procedure avoids the use of organic templates and expensive equipment reported by other authors. Moreover, the simple change in the order of addition of the starting materials influences strongly the nucleation process, resulting in superior control of the particle shapes. Despite the poor electrochemical performance of *Cmcm* phases, their magnetic properties were analyzed. A paramagnetic-ferrimagnetic transition is observed for $\text{Li}_{0.5}\text{CoPO}_4$ -*Cmcm* and LCP-*Cmcm* was found at T_N of 10.5 K at and 11.0 respectively, at 10 kOe.

As several publications claim the ability of the polyol procedure for the synthesis of LFP-*Pnma* in a single step synthesis, the reproduction of several published experimental procedures were done. Indeed, for the case when $\text{Fe}(\text{SO}_4)_2 \cdot 7\text{H}_2\text{O}$, $\text{LiCH}_3\text{COO} \cdot 2\text{H}_2\text{O}$ and H_3PO_4 were used as starting materials, we found that the correct Li:Fe:P molar ratio was 2:1:1 instead of the 1:1:1 as presented in the literature. Using an experimental approach after a systematic optimization, phase pure LFP-*Pnma* was obtained. The optimized synthesis avoids the use of ascorbic acid as reducing agent and decrease the requirement of energy because the temperature remains below 250 °C, in contrast to the 320 °C as reported.

4.2 Outlook

The polyol method offers a huge range of possibilities using inexpensive starting materials and simple experimental setup. However, since the reaction is controlled by parameters such as, temperature, time, molar ratio and others; the importance of the kinetics of the reaction as well as the understanding of the crystallization processes involved is vital to enhance its application.

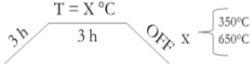
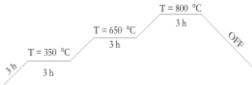
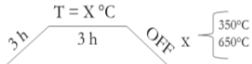
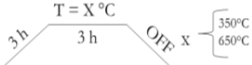
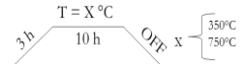
For this case, the use of a systematic approach combined with the control of the experimental parameters are relevant in order to improve the reproducibility. Certainly, the control of the heating process after the mixing of the educts is fundamental during the nucleation, crystallization and grain growth. This consideration can be extended to other active cathode materials that can be synthesized by simple one-pot synthesis.

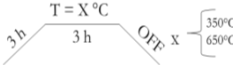
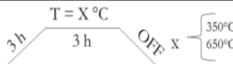
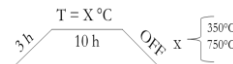
New systems can be explored by the variation of the starting materials; moreover, the use of flux controller, as in used for the AAAP method, can enhance the possibilities to find morphologies where the electrochemical active surfaces can be exposed in order to enhance the capacity. This in combination of surfactants can address new morphologies that allows to enhance the ion and electron conductivity. The modification of the reaction times and the use of additional carbon sources in the coating procedure, is necessary to increase the conductivity and formation of C-composites. A detailed control of the phase purity can be done by altering the molar ratio of the educts.

The application of polyol process to the obtain LMP polymorphs is suitable since the process is simple, safe and has been demonstrated its potential compared with MW-assisted or solid state syntheses. Finally, its use for the synthesis of potential cathode materials for Na-ion batteries is useful since the point of the scale up process and mass production.

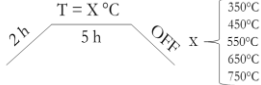
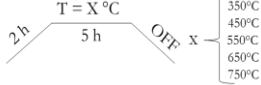
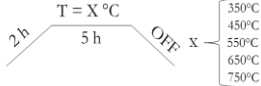
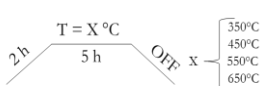
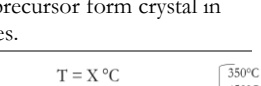
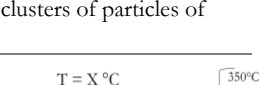
5. Appendix

5.1 Parameters tested using the CoAc₂, ADP and LiAc polyol synthesis

Synthesis Parameter	Comments	Li:M:P Ratio	Batch size (mmol)	Solvent vol. (ml)	Set T (°C)	Reflux time (h)	Annealing program
Reflux time	Test using different reflux times	1:1:1	0.876	EG 50 mL	190	3, 6, 18 and 40	
<p>Result: The temperature does not influence in the formation of a crystalline phase after drying. After calcination LCP is formed with side phases of Co₃O₄, Co₃(PO₄)₂ and Li₃PO₄. The sample of 18 hours shows less amount of side phases, however this do not represent big differences in the formation of the final sample</p>							
Annealing program	Use of a multi-step annealing program	1:1:1	0.876	EG 50 mL	190	18	
<p>Result: At the end of the drying process, the sample do not shown reflections. After annealing the sample present as mixture of LCP-<i>Pnma</i> and Li₃PO₄ phases.</p>							
Reflux temperature	Temperature over the EG boiling point	1:1:1	0.876	EG 50 mL	250	3, 6, 18 and 40	
<p>Result: After calcination LCP-<i>Pnma</i> is formed with side phases of Co₃O₄, Co₃(PO₄)₂ and Li₃PO₄.</p>							
Mixing conditions of the precursors	Mix all the precursors in solid form from the beginning into the flask for dissolution	1:1:1	0.876	EG 50 mL	190	18	
<p>Result: Mixture of phases of LCP-<i>Pnma</i> and Co₃(PO₄)₂</p>							
Long Annealing program	Use a long annealing program (over 10 h)	1:1:1	0.876	EG 50 mL	190	18	
<p>Result: The signal:background ratio is improved but still there is a mixture of phases between LCP-<i>Pnma</i> and Co₃(PO₄)₂</p>							

Synthesis Parameter	Comments	Li:M:P Ratio	Batch size (mmol)	Solvent vol. (ml)	Set T (°C)	Reflux time (h)	Annealing program
Volume of solvent	Use of the double of solvent in order to increase the solubility	1:1:1	0.876	EG 100 mL	190	18	
Result: Mixture of phases of LCP- <i>Pnma</i> and $\text{Co}_3(\text{PO}_4)_2$ and Co_3O_4							
Variation on water:EG ratio	Different H_2O amounts	1:1:1	0.876	H_2O content : 10 - 50%	190	18	
Result: Formation of LCP- <i>Pn21a</i> in the water:EG ratio of 30:70 (Or 30 % water content).							
Increase of Li and P content	Additional lithium content to avoid secondary phases	1.5:1:1 2:1:1 2.5:1:1 3:1:1 1:1:10 1.5:1:10 2:1:10 2.5:1:10 3:1:10	0.876	EG 50 mL	190	18	
Result: Mixture of phases of LCP- <i>Pnma</i> , CoO , $\text{Co}_3(\text{PO}_4)_2$							
pH Control	Use of pH 4, 7, 10 controlled using ammonia	1:1:1	0.876	EG	190	18	
Result: Formation of LCP- <i>Pn21a</i> at basic pH after drying. Secondary phases of $\text{Co}_2\text{P}_4\text{O}_{12}$ and $\text{Co}_2\text{P}_2\text{O}_7$ after annealing.							
Use of surfactants	PVP and citric acid in LCP: surfactant ratio 1:1, 4:1, 1:4, 1:10, 1:5	1:1:1	0.876	EG	190	18	
Result: Mixture of phases of LCP- <i>Pn21a</i> and $\text{Co}_3(\text{PO}_4)_2$ after drying. After calcination the sample present a mixture of LCP- <i>Pnma</i> and LiCoO_2 for both cases.							

5.2 Table of parameters tested using the CoAc₂ and LDP system (Adapted from LiMnPO₄ polyol synthesis⁹⁹)

Synthesis Parameter	Comments	Li/P:Co Ratio	Batch size (mmol)	Solvent vol. (ml)	Set T (°C)	Reflux time (h)	Annealing program
Reflux time	Test using different reflux times	1:1	0.03	EG 150	190	4, 8, 12, 40	
	<p>Result: After drying, most of the samples present a main phase corresponding to LCP-<i>Pn</i>_{21a} and sometimes with small impurities of Li₃PO₄ and Co₃(HPO₄)(OH)₂. The time does not represent a big difference on the formation of the phases.</p>						
Reflux temperature	Test using different temperatures	1:1	0.03	EG 150	100, 135, 190, 250	14	
	<p>Result: The high temperatures (above 190 °C) promotes the formation of the olivine phase; however, there is not highly crystalline.</p>						
LDP addition rate	Test to verify the influence of the addition speed on the preliminary sample	1:1	0.03	EG 150	190	4	
	<p>Result: The LDP was add in one single shot. After drying, there is only differences in the morphology: slow rates promotes formation of bigger crystals compared with fast addition.</p>						
PVP mixing form	PVP was added solid, solved with CoAc ₂ or solved in EG	1:1	0.03	EG 150	190	4	
	<p>Result: After drying process there is a formation of LCP-<i>Pn</i>_{21a} as a main phase in all the cases with secondary phases corresponding to Li₃P and after annealing Li₃PO₄. After annealing the secondary phases still remaining with the main LCP olivine phase. In some cases the precursor form crystal in the same size range without formation of agglomerates.</p>						
PVP molar weight	PVP M.W. 58000, 360000 and 630000 were used	1:1	0.03	EG 150	190	4	
	<p>Result: The formation of phases is similar to the PVP mixing form test. However, here the highest molar weights present formation of big agglomerates or formation of big clusters of particles of irregular form.</p>						
PVP molar ratio	LCP:PVP in molar ratios 1:1, 1:2 and 1:4 were tested	1:1	0.03	EG 150	190	4	
	<p>Result: The molar ratio shows formation of agglomerates or formation of big clusters of particles of irregular form. The crystal phases remain similar as previous PVP test</p>						

Synthesis Parameter	Comments	Li/P:Co Ratio	Batch size (mmol)	Solvent vol. (ml)	T (°C)	Reflux time (h)	Annealing program
LDP adding temperature	LDP was added at temperatures of 135 °C and 190 °C	1:1	0.03	EG 150	190	4	
Molar ratio	Change in the molar ratio values	1.5:1	0.03	DEG, TEG, TTTEG 150	Range from 135 °C to 220 °C	Range from 4 h to 16 h	
		2:1					
		2.5:1					
		3:1					
		1:2					
		1.5:2					
		10:1					
		1:10					
							Result: Mixture of phases of LCP- <i>Pnma</i> , CoO, Co ₃ (PO ₄), Co ₂ P ₂ O ₇ and unidentified phases.

5.3 Table of parameters tested using the CoAc_2 , H_3PO_4 , LiAc system (adapted from LiFePO_4)

Synthesis Parameter	Comments	Li:M:P Ratio	Batch size (mmol)	Solvent vol. (ml)	Set T (°C)	Reflux time (h)	Annealing program
Reflux time	Test using different reflux times	1:1:1	7.41	TTEG 200	190	4, 16	
	Result: After drying process of the precursor, short times present a main phase of LCP- <i>Cmcm</i> but for longer times is a mixture between LCP- <i>Pn21a</i> and LCP- <i>Cmcm</i> are obtained						
Solvent	Test using different solvents	1:1:1	7.41	EG DEG TEG TTEG 200	250 °C	16	
	Result: After drying process the precursor most of the times there is a formation of LCP- <i>Cmcm</i> as main phase. Every so often secondary phases, such as $\text{Co}_3(\text{PO}_4)_2$, $\text{Co}_2\text{P}_2\text{O}_7$ are also present. After annealing process, there is formation of LCP- <i>Pnma</i> with secondary phases.						
Molar ratio	Change in the molar ratio values	1.5:1:1 2:1:1 2.5:1:1 3:1:1 1:1:10 1.5:1:10 2:1:10 2.5:1:10 3:1:10	7.41	TTEG 200	From 150 °C to 250 °C	16	
		Result: After drying process, the precursor for short times is LCP- <i>Pn21a</i> but for longer times is a mixture between LCP- <i>Pn21a</i> and LCP- <i>Cmcm</i> . After annealing there is a formation of LCP- <i>Pnma</i>					
Surfactant	Use PVP (M.W. 5.8×10^{-3} , 36×10^{-3} , 1.3×10^{-6}), SBS, SDBS and citric acid	3:1:10	7.41	TTEG 200	From 150 °C to 250 °C	16	

5.4 Other systems tested in the polyol synthesis of LCP-*Pnma*

Synthesis Parameter	Educts	Li:M:P Ratio	Batch size (mmol)	Solvent and vol. (ml)	T (°C)	Reflux time (h)	Annealing program
Standard procedure		1:1:1	7.41	TTEG 200	218	4, 16	
Solvent	CoSO ₄ /CoAc ₂ H ₃ PO ₄ LiOH	1:1:1	7.41	EG TEG 200	From 150 °C to 250 °C	16	
Molar ratio		2:1:1 3:1:1 3:1:10	6.339	TTEG 200	220 °C	16	
Synthesis Parameter	Educts	Li:M:P Ratio	Batch size (mmol)	Solvent and vol. (ml)	T (°C)	Reflux time (h)	Annealing program
Standard procedure		1:1:1	7.41	TTEG 200	218	4, 16	
Solvent	Co ₃ (PO ₄) ₂ LiOH	1:1:1	7.41	EG DEG TEG 200	From 150 °C to 250 °C	16	
Molar ratio		2:1:1 3:1:1 3:1:10	6.339	TTEG 200	220 °C	16	

5.5 Tables of experimental parameters tested during the polyol synthesis of LFP-*Pnma*

Synthesis Parameter	Educts	Li:M:P Ratio	Batch size (mmol)	Solvent and vol. (ml)	T (°C)	Reflux time (h)	Annealing program
Standard procedure	H ₃ PO ₄ , LiAc, FeAc	1:1:1	6.339	TTEG 200	218	4, 16	
Solvent	H ₃ PO ₄ , LiAc, FeAc	1:1:1	6.339	EG DEG TEG TTEG_DME 200	From 150 °C to 250 °C	16	
Molar ratio	H ₃ PO ₄ , LiAc, FeAc	1.5:1:1 2:1:1 2.5:1:1 3:1:1 1:1:10 1.5:1:10 2:1:10 2.5:1:10 3:1:10	6.339	EG DEG TEG 200	From 150 °C to 250 °C	16	-

Synthesis Parameter	Educts	Li:M:P Ratio	Batch size (mmol)	Solvent and vol. (ml)	T (°C)	Reflux time (h)	Annealing program
Standard procedure	LiAc, Fe(AcAc) ₂ , (NH ₄) ₂ HPO ₄	1:1:1	6.339	TTEG 200	212	4, 16	
Solvent	LiAc, Fe(AcAc) ₂ , (NH ₄) ₂ HPO ₄	1:1:1	6.339	EG DEG TEG 200	From 150 °C to 250 °C	16	

Synthesis Parameter	Educts	Li:M:P Ratio	Batch size (mmol)	Solvent and vol. (ml)	T (°C)	Reflux time (h)	Annealing program
Standard procedure		1:1:1	6.339	TTEG 200	190	4, 16	
Solvent and molar ratio	LiAc, FeSO ₄ ·7H ₂ O, H ₃ PO ₄	1:1:1	6.339	EG DEG TEG 200	From 150 °C to 250 °C	16	-
Molar ratio		1.5:1:1 2:1:1 2.5:1:1 3:1:1 1:1:10 2:1:10 3:1:10	6.339	EG DEG TEG 200	From 150 °C to 250 °C	16	-

Synthesis Parameter	Educts	Li:M:P Ratio	Batch size (mmol)	Solvent and vol. (ml)	T (°C)	Reflux time (h)	Annealing program
Surfactant	LiAc, FeSO ₄ ·7H ₂ O H ₃ PO ₄ , PVP	1:1:1 1:1:1:4	6.339	TTEG 200	210	16	-
Reducing agent	LiAc, FeSO ₄ ·7H ₂ O H ₃ PO ₄ , AsAc	1:1:1:0.6	6.339	TTEG 200	211	16	-
Synthesis Parameter	Educts	Li:M:P Ratio	Batch size (mmol)	Solvent and vol. (ml)	T (°C)	Reflux time (h)	Annealing program
Standard procedure	LiOH, FeSO ₄ ·7H ₂ O, H ₃ PO ₄	1:1:1 2:1:1 3:1:1 1:1:10	6.339	TTEG 200	218	16	
Synthesis Parameter	Educts	Li:M:P Ratio	Batch size (mmol)	Solvent and vol. (ml)	T (°C)	Reflux time (h)	Annealing program
Standard procedure		1:1:1	6.339	TTEG 200	228	4, 16	
Solvent and molar ratio	Educts	Li:M:P Ratio	Batch size (mmol)	Solvent and vol. (ml)	T (°C)	Reflux time (h)	Annealing program
	LiAc, FeC ₂ O ₄ ·2H ₂ O H ₃ PO ₄	1:1:1	6.339	EG DEG TEG PEG 200	From 150 °C to 250 °C	16	
Molar ratio		1.5:1:1 2:1:1 2.5:1:1 3:1:1 1:1:10 1.5:1:10 2:1:10 2.5:1:10 3:1:10	6.339	EG DEG TEG PEG 200	From 150 °C to 250 °C	16	-

6. Publications and participation in conferences

No	Name	Work presented	Dates
1	DAAD Stipendiaten Treffen – Augsburg Title: Olivines for Li-ion batteries: From energy storage to green transportation <i>Alarcón-Suesca C., Stinner C., Gasteiger H. and Nilges T.</i>	Oral contribution	25-27 May 2013
2	Graduiert Akademie DAAD – Berlin Title: Olivines for Li-ion batteries: From energy storage to green transportation – Nachhaltigkeit International gestalten <i>Alarcón-Suesca C., Stinner C., Gasteiger H. and Nilges T.</i>	Oral contribution	25-29 Sep. 2013
3	XXI Latin American Symposium on Solid State Physics SLAFES – Villa de Leyva – Colombia Title: Synthesis, characterization and electrochemical properties of olivine-type structures and its application as cathode materials <i>Alarcón-Suesca C., Stinner C., Gasteiger H. and Nilges T.</i> Title: Ferroelectric, Magnetic and structural studies of $\text{Bi}_4\text{LaSmFe}_2\text{Ti}_3\text{O}_{18}$ material using solid-state method <i>Alarcón-Suesca C., Landínez-Téllez D. and Roa-Rojas J.</i>	Oral/Poster contribution	30 Sep. - 4 Oct 2013
4	226 th Joint International meeting of ECS – Cancun – Mexico Title: Stability of Carbon Coating Surrounding LiMPO_4 (M=Fe, Co) Particles in Water Free and Water Containing Electrolytes <i>Metzger M., Haering D., Kavakli C., Alarcón-Suesca C., Puravankara S., Nilges T., Stinner C. and Gasteiger H.</i>	Poster	5-9 Oct. 2014
5	Materials Research Society Fall Meeting and Exhibition- Boston Title: Synthesis of high-pressure polymorph of LiCoPO_4 using a single-step polyol route <i>Alarcón-Suesca C., Ludwig J., Stinner C., Gasteiger H. and Nilges T.</i> Title: Microwave-Assisted Solvothermal Synthesis of LiCoPO_4 Using Various Polyol Media <i>Ludwig J., Alarcón-Suesca C., Marino C., Haering D., Stinner C., Gasteiger H. and Nilges T.</i>	Poster (2)	29 Nov -4 Dec 2015

Phospho-olivines as cathode materials for lithium ion battery: trends on microwave synthesis

This content has been downloaded from IOPscience. Please scroll down to see the full text.

[View the table of contents for this issue](#), or go to the [journal homepage](#) for more

Download details:

IP Address: 138.246.2.51

This content was downloaded on 24/11/2014 at 13:21

Please note that [terms and conditions apply](#).

Phospho-olivines as cathode materials for lithium ion battery: trends on microwave synthesis

C E Alarcón-Suesca, T Nilges

Fachgebiet Synthese und Charakterisierung Innovativ Materialien, Chemistry
Department, Technische Universität München, Lichtenbergstrasse D-85748, Garching,
Germany

Email: tom.nilges@lrz.tu-muenchen.de

Abstract. In recently years, scientific research has been focused on finding new sources of efficient energy storage and lithium batteries are one of the most outstanding alternatives. Nowadays, investigation on cathode materials constitute one of the key factors of lithium rechargeable batteries studies. Recently, oxides with olivine structures has triggered the battery field, due to its excellent electrochemical properties, crystal stability, energy density, power capacity and are not expensive. However, the demand and development of more enhanced cathode materials can be achieved by the use of sophisticated synthetic methods. The purpose of this article is to provide a perspective to the materials community on the opportunities and limitations of nanostructured materials by highlighting examples in synthesis, fundamental studies and applications on microwave synthesis as novel route to obtain high voltage phospho-olivines.

1. Introduction

Since their commercialization in the early 1990's by Sony®, Li-ion batteries (LIB) are considered an important element inside the so-called "modern electricity-based society". So far, LIB constituted the most appropriate method of energy storage: they show long cycle life, wide range of operating temperatures, high energy density, low cost and safety [1]. LIB have prompted the progress of electronic devices commercialization (mobile phones, laptops, tablets), internal combustion engines (ICE), electric vehicles (EVs) and support the storage of energy produced by renewable energy sources (RES) [2]. In currently LIB technology, the electrochemical performance (cell voltage, capacity, Li^+ transportation rate) is determined mainly by the cathode material and this justifies the intense research in this field [3]. Since report of electrochemical activity of LiMPO_4 ($M=\text{Fe}, \text{Mn}$) by Goodenough [4], lithium transition metals phosphates with ordered olivine structure (Phospho-olivines) has emerged as a promising cathode material due to its excellent electrochemical properties, good thermal stability, low cost and environmentally friendly [5]. Crystalline LiMPO_4 , has an orthorhombic unit cell (D_{2h}^{16} -space group $Pmnb$), where oxygen ions form strong covalent bonds with P^{5+} to form PO_4^{3-} tetrahedral units stabilizing the entire network assuring a stable operation and high temperatures; present the so-called "inductive effect" due to the $\text{P}_{\text{tet}}\text{-O-M}_{\text{oct}}$ linkage allowing an interaction that tunes the $\text{M}^{3+}/\text{M}^{2+}$ redox energy to useful levels (3.4 to 5.0 V) and present high theoretical capacity (up to 170 mAh/g) that provides high energy density compared with other cathode materials such as spinel-oxides or layered oxides [6,7]. The insertion and extraction of Li^+ ions into



the stable crystal lattice of the electrode is the key factor inside LIB operation. One of the main causes of poor performance of the battery is the instability of electrode materials, due to the existence of secondary phases, inhomogeneity in the compound formation, stoichiometry, crystal structure and morphology of the active material [8]. These factors are closely related and the selection of an appropriate synthesis route is the key factor to enhance the battery working. Following the report of Higuchi [9], microwave-assisted route is considered a novel processing technique to obtain nanoscale cathode materials with excellent electrochemical properties. The purpose of this article is not provide a comprehensive review; rather, this paper offers a perspective to the materials community on the microwave (mw) synthesis by highlighting examples and propose some promising developmental directions on assisted-microwave route for the synthesis of phospho-olivines for LIB cathode-materials.

2. Microwave assisted-solid state synthesis

Microwave processing method is based on a self-heating process that occurs by the absorption of electromagnetic energy; due to the use of dielectric microwave (which reduce the thermal gradients inside the reactor), a very fast and uniform heating of the total volume of reactants is obtained within a short time, resulting in very homogenous reaction conditions. Moreover, it allows the possibility to synthesized cathode materials at temperatures lower than those required in solid state synthesis using an oven [10]. The first attempts of direct microwave synthesis evolved from preliminary steps of mixing precursors, pelletizing and the use of domestic microwave ovens; in the case of LiFePO_4 a capacity value of 125 mAh/g was reported [9] and then improved until 161mAh/g at C/10 mixing stoichiometric amounts of Li_3PO_4 and $\text{Fe}_3(\text{PO}_4)_2 \cdot 8\text{H}_2\text{O}$ in a ball-milling jar with 5 wt.% acetylene black, pressed in a pellet and then irradiated for several minutes (2-5) at 750 W [11]. Recently reports shows alternative procedure using $\text{FePO}_4 \cdot 4\text{H}_2\text{O}$ and Li_2CO_3 mixed with glucose and milling in ball-mill for 5 min at 400 rpm. Mixture is transferred in a crucible and alternatively heated at a procedure of 20 seconds with 10 seconds pause for 4 times at 1000W and 2.45 GHz without use of inert gas; the reported capacity reach 162 mAh/g at C/10 which is one of the highest discharge specific capacity reported so far [12]. The use of carbonaceous substance (such as acetylene and glucose) is a good strategy to include in mw synthesis. The carbon source acts as a room temperature susceptor that reaches a critical temperature to couple with the mw radiation; besides, carbon supplies thermal energy by heat transfer by surrounding and immersing the sample in both thermal and electric fields [8] and finally, carbon covers the precursor particles and create a layer around them to facilitate the transport of electrons between the current collector and the particle surface [13].

On the other hand, reports on formation of LiCoPO_4/C nanocomposites, mixing CH_3COOLi , $(\text{CH}_3\text{COO})_2\text{Co}$, $(\text{NH}_4)_2\text{HPO}_4$ with acetylene black in alcohol media, followed by decomposition under Ar atmosphere for 2 h at 350°C and mw irradiation (2.45 GHz, 700W) for 11 min; shows particle sizes of 150 nm and capacities of 144 mAh/g at C/10 [14]. Develop of nanosized electrode materials is an essential strategy to achieve short diffusion path lengths from the particle-core to the surface, faster ion diffusion and higher rate capability in LIB's [15]. Synthesis of LiMnPO_4 nanocrystallites deposited in nanopores of porous carbon was made using mw irradiation process. Here, LiH_2PO_4 and $\text{Mn}(\text{COOCH}_3)_2 \cdot 4\text{H}_2\text{O}$ were dissolved with a Li/Mn/P molar ratio of 1/1/1 in diethylene glycol and mixed with porous carbon with an average pore diameter of 110 nm (PC110) afterward, subjected to a mw irradiation (2.45 GHz, 400 W) for 5 and 8 min at 200 °C and 250 °C respectively and finally dried at 110 °C in air for 12 h. Although capacity of the samples is not high so far ($\approx 104 \text{ mAh/g}$ at C/10), the formation LiMnPO_4 nanocrystallites-embedded porous carbons exhibited a retention capacity of 87% at 0.5 C against 0.1 C, which was comparable to that reported for $\text{LiMnPO}_4\text{-C}$ coated [16].

3. Microwave assisted-solvo/hydrothermal synthesis

The requirement of uniformity conditions during the mw irradiation is fundamental to assure good electrochemical activity in the final material. The use of an adequate hydro/solvothermal settings, facilitates the synthesis of polyanionic compounds with well controlled morphology and fine crystal particles; tuned by factors such as temperature, pH, concentration of species and kinetic parameters (speed stirring) [17]. Murugan [18], present a combination of mw and solvothermal process using as starting materials LiOH and $(\text{CH}_3\text{COO})_2\text{Fe}$ solved in tetraethyleneglycol (TEG) and mixed with H_3PO_4 . The homogenous gel is placed in an Anton Paar microwave synthesis system (2.45 GHz, 400 W) machine and heated for 5 min at 300 °C. In addition, produced LiFePO_4 particles were coated with *p*-toluene sulfonic acid (*p*-TSA) doped poly(3,4-ethylenedioxythiophene) (PEDOT) in ethanol. TEM analysis reveals well-defined crystalline nanorod morphology of 25 ± 6 nm and a length of up to 100 nm. This material exhibits high discharge capacity (166 mAh/g) at C/10. PEDOT is used due to its redox behavior (over a wide range of potentials), relative high environmental and thermal stability and high electronic conductivity in its doped state compared to other commonly available conducting polymers. A key factor in hybrid mw-solvothermal synthesis is the use of an organic solvent; indeed polyalcohols (ethylene glycol, tetraethylene glycol) acts first as a solvent in the process and then as a stabilizer to allow limit the particle growth and prohibiting agglomeration [19]. Versatility of the method includes recent contributions on synthesis of doped samples. Goodenough [20] use mw-solvothermal method to produce $\text{LiFe}_{1-3x/2}\text{V}_{x/2}\text{PO}_4$ ($x \leq 0.2$) doped samples by mixing LiOH, H_2O , H_3PO_4 , $(\text{CH}_3\text{COO})_2\text{Fe}$ in TEG and adding $\text{OV}(\text{OCH}(\text{CH}_3)_2)_3$ at 300 °C for 30 mins. First charge-discharge curves of the samples shown values around 160 mAh/g in the range of 3.8-4.5 V. This synthetic approach demonstrated a maximum V doping of 10% without the formation of impurity; in fact, the method avoid to use conventional high-temperature routes. Finally, formation of vacancies on Fe site provide an additional conduction pathway for Li^+ ions to transfer between neighbouring 1D conduction channels along the crystallographic b axis.

Microwave-hydrothermal have gained reception and made remarkable progress due to increase in kinetic rates of reactions by one or two orders of magnitude, reduce reactions times, offers large scale batch reactions and saves energy [21]. Furthermore, control of the morphology shows an improvement in electrochemical performance as published by Ji [22]. In this study, LiMnPO_4 crystals were obtained using $\text{MnSO}_4 \cdot \text{H}_2\text{O}$, H_3PO_4 , LiOH as starting materials in the stoichiometric ratio 1:1:3. Sodium dodecyl benzene sulfonate (SDBS) and citric acid (H_3cit) were used to affect the morphology of the products and 5 min mw irradiation at 180 °C – 300 °C and 300 W conditions were used. SEM analysis shows the formation of nanoplatelets (150 nm) orientated in the ac plane whose thickness is controlled mainly by the concentration of precursors. The plate-like morphology could be useful for fast charge-discharge performances as it offers short lengths for Li^+ ion insertion/exertion as comment previously. Addition of organic additives to limit the size shown and improve of capacity value from 44.1 to 89.0 mAh/g. On the other hand, the mw-hydrothermal was used in synthesis of high homogeneity LiFePO_4 with elongated parallelepiped shape in the range 0.5–1.0 mm for suitable studies onto the intrinsic defectivity, chiefly the so-called lithium iron *anti-site*, considered one of the most critical issues when envisaging electrochemical applications [23].

4. Microwave assisted-sol-gel synthesis

From the point of view of yields and use of novel strategies such as carbon-nanotubes to increase the conductivity, new mw-sol-gel synthesis offer better characteristics rather than conventional sol-gel method [24]. Gyroscope-like lithium iron phosphate/multiwalled carbon nanotubes composites has been synthesized with initial discharge capacities of 153.3, 149.6, 140.7, 135.3 and 130.1 mAh/g at 0.1, 0.2, 0.5, 0.8 and 1 C rate, respectively. Multi-wall carbon nanotubes (MWCNTs) are considered ideal materials due to hollowfiber structure and ability to be inserted in the centre of LiFePO_4 , thus forming a conductive network, which not only provide pathways for electron transference but also lead to interparticle electronic connection [25]. Not only carbon compounds are suitable to use to

make coating in phospho-olivines. Zhang [26] use mw-sol-gel method to prepare $\text{LiFePO}_4\text{-Li}_4\text{SiO}_4$ cathode material. The Li_4SiO_4 coating prevent the direct contact between LiFePO_4 and the electrolyte solution. The discharge capacity of the uncoated LiFePO_4 decayed with the increase of the discharge rates, whereas Li_4SiO_4 -coated LiFePO_4 shown a very steady cycling behaviour. Moreover, from electrochemical impedance spectroscopy coated cathode exhibits a smaller charge-transfer the resistance (135.1Ω) than that of the uncoated LiFePO_4 cathode (305.6Ω).

5. Conclusion

Microwave processes constitute a powerful tool to synthesize phospho-olivines with a strong reduced power consumption. Microwave assisted process enables us to produce crystalline cathode particles with different shapes and sizes and has the advantage that the solvent used in the synthesis can often be converted into the carbon source upon heating. Finally it is a simple method for mass production at low cost and short time of synthesis.

6. Acknowledgment

One of the authors (Alarcón-Suesca) wish thanks to Colciencias and DAAD for the grant founding.

References

- [1] Tao Z F H, Liu H, Kan X and Chen P 2011 *Open Mater. Sci. J* **5** 204
- [2] Cairns E J and Albertus P 2010 *Annu. Rev. Chem. Biomol. Eng.* **1**, 299
- [3] Xu B, Qian D, Wang Z and Meng J S 2012 *Mat. Sci. Eng. R* **73** 51
- [4] Padhi A K, Nanjundaswamy K S and Goodenough J B 1997 *J. Electrochem. Soc* **144** 1188
- [5] Zaghbi K, Mauger A and Julien C M 2012 *J. Solid State Electr.* **16** 835
- [6] Yamada A, Hosoyama M, Chunga Sai-H, Kudob Y, Hinokumaa K, Liub K Y and Nishi Y 2003 *J. Power Sources* **119** 121
- [7] Braun P V, Cho J, Pikul J H, King W P and Zhang H 2012 *Curr. Opin. Solid St. M.* **16** 186
- [8] Balaji S, Mutharasu D, Sankara N S and Ramanathan K 2009 *Ionics* **15** 765
- [9] Higuchi M, Katayama K, Azuma Y, Yukawa M and Suhara M 2003 *J. Power Sources* **119** 258
- [10] Beninati S, Damen L and Mastragostino M 2008 *J. Power Sources* **180** 875
- [11] Song M S, Kang Y M, Kim J H, Kim D Y, Kwon H S and Lee J Y 2007 *J. Power Sources* **166** 260
- [12] Zou H, Zhang G and Shen P K 2010 *Mater Res Bull* **45** 149
- [13] Zaghbi K, Guefi A, Hovington P, Vijh A, Trudeau M, Mauger A, Goodenough J B, Julien C M 2013 *J. Power Sources* **232** 357
- [14] Li H H, Jin J, Wei J P, Zhou Z, Yan J 2009 *Electrochem. Commun.* **11** 95
- [15] Lim J, Kim J, Mathew V and Kim J 2010 *Phys Scripta* **2010** T139
- [16] Aono S, Urita K, Yamada H and Moriguchi I 2012 *Solid State Ionics* **225** 556
- [17] Gong Z and Yang Y 2011 *Energy Environ. Sci.* **4** 3223
- [18] Murugan V A, Muraliganth T and Manthiram A 2008 *Electrochem. Commun.* **10** 903
- [19] Dimesso L, Spanheimer C, Jacke S and Jaegermann W 2011 *Ionics* **17** 429
- [20] Harrison K L, Bridges C A, Paranthaman M P, Segre C U, Katsoudas J, Maroni V A, Idrobo J C, Goodenough J B and Manthiram A 2013 *Chem. Mater.* **25** 768
- [21] Devaraju K M and Honma I 2012 *Adv. Energy Mater.* **2** 284
- [22] Ji H, Yang G, Ni H, Roy S, Pinto J and Jiang X 2011 *Electrochim. Acta* **56** 3093
- [23] Bini M, Ferrari S, Capsoni D, Mustarelli P, Spina G, Giallo F, Lantieri M, Leonelli C, Rizzuti A and Massarotti V 2012 *RSC Advances* **2** 250
- [24] Bao S J, Liang Y Y and Li H L 2005 *Mater. Lett.* **59** 3761
- [25] Zhang Y, Dua P, Wang L, Zhang A, Song Y, Li X and Lv Y 2011 *Synthetic Met.* **161** 548
- [26] Zhang Q, Jiang W, Zhou Z, Wang S, Guo X, Zhao S and Ma G 2012 *Solid State Ionics* **218** 31



Article

In Situ Studies and Magnetic Properties of the *Cmcm* Polymorph of LiCoPO_4 with a Hierarchical Dumbbell-Like Morphology Synthesized by Easy Single-Step Polyol Synthesis

Carlos Alarcón-Suesca^{1,†}, Jennifer Ludwig^{1,†}, Viktor Hlukhyy², Christoph Stinner³ and Tom Nilges^{1,*}

¹ Synthesis and Characterization of Innovative Materials, Department of Chemistry, Technical University of Munich, Lichtenbergstraße 4, 85747 Garching, Germany; carlos.alarcon@tum.de (C.A-S.); jennifer.ludwig@tum.de (J.L.)

² Chair of Inorganic Chemistry with Focus on Novel Materials, Department of Chemistry, Technical University of Munich, Lichtenbergstraße 4, 85747 Garching, Germany; viktor.hlukhyy@tum.de

³ BMW AG, Petuelring 130, 80788 München, Germany; christoph.stinner@bmw.de

* Correspondence: tom.nilges@lrz.tum.de; Tel.: +49-89-289-13111

† These authors contributed equally to this work.

Academic Editor: Richard Dronskowski

Received: 6 October 2016; Accepted: 10 November 2016; Published: 17 November 2016

Abstract: LiCoPO_4 (LCP) exists in three different structural modifications: LCP-*Pnma* (olivine structure), LCP-*Pn2₁a* (KNiPO_4 structure type), and LCP-*Cmcm* (Na_2CrO_4 structure type). The synthesis of the LCP-*Cmcm* polymorph has been reported via high pressure/temperature solid-state methods and by microwave-assisted solvothermal synthesis. Phase transitions from both LCP-*Pn2₁a* and LCP-*Cmcm* to LCP-*Pnma* upon heating indicates a metastable behavior. However, a precise study of the structural changes during the heating process and the magnetic properties of LCP-*Cmcm* are hitherto unknown. Herein, we present the synthesis and characterization of LCP-*Cmcm* via a rapid and facile soft-chemistry approach using two different kinetically controlled pathways, solvothermal and polyol syntheses, both of which only require relatively low temperatures (~200 °C). Additionally, by polyol, method a dumbbell-like morphology is obtained without the use of any additional surfactant or template. A temperature-dependent in situ powder XRD shows a transition from LCP-*Cmcm* at room temperature to LCP-*Pnma* and finally to LCP-*Pn2₁a* at 575 and 725 °C, respectively. In addition to that, the determination of the magnetic susceptibility as a function of temperature indicates a long-range antiferromagnetic order below $T_N = 11$ K at 10 kOe and 9.1 K at 25 kOe. The magnetization curves suggests the presence of a metamagnetic transition.

Keywords: polymorph; LiCoPO_4 -*Cmcm*; metamagnetic transition; in situ XRD; polyol; solvothermal; transition phase; hierarchical morphology

1. Introduction

Since their introduction by Whittingham [1] and commercialization in the early 1990s by Sony® [2], Li-ion batteries (LIB) have become a breakthrough technology in portable electronics. So far, LIB constituted the most appropriate method of energy storage in this sector because they show high energy density, low weight, design flexibility and long lifetime [3]. In current LIB technology, the electrochemical performance (e.g., cell voltage, capacity, Li^+ transportation rate) is mainly determined by the cathode material and, thus, intense research efforts are undertaken in this field [4]. Among several cathode materials, such as spinel types and lithium-rich layered oxides, lithium transition-metal

orthophosphates with the sum formula LiMPO_4 ($M = \text{Fe, Mn, Co, Ni}$) or simply LMP (LFP, LMP, LCP, LNP) have received particular attention due to their excellent electrochemical properties, good thermal stability, low cost and environmental friendliness [5]. While LFP and LMP have been widely investigated to date, LCP is still under investigation. In LCP, the $\text{Co}^{2+}/\text{Co}^{3+}$ redox couple offers a high operating voltage of approximately 4.8 V versus Li/Li^+ [6]. Moreover, LCP shows a high theoretical energy density of 800 Wh/kg (superior compared to the 580 Wh/kg of LFP), exhibits the lowest hole polaron migration barrier of the phospho-olivine family and subsequently has the highest electronic conductivity compared to LFP, LMP and LNP [7]. Furthermore, LCP shows a reduced cobalt weight fraction per formula unit compared to commercial LiCoO_2 , making it a lower-cost option [8,9]. LCP can exist in three polymorphs with orthorhombic crystal structures, and several electrochemical and physical properties have been reported so far [10–12]. The most widely investigated one is olivine-type LCP-*Pnma*. In the structure, Li^+ and Co^{2+} ions occupy octahedral sites and P^{+5} is located in a tetrahedral environment formed by a distorted hexagonal close-packed (*hcp*) array of oxygen atoms [13]. The $[\text{CoO}_6]$ octahedra form zigzag chains that are running parallel to the crystallographic *c* axis (Figure 1a). The chains are linked by the $[\text{PO}_4]$ tetrahedra, resulting in a 3D network structure [14]. The Li^+ ions are located in channels along $[010]$ and $[001]$. However, studies for olivine structures show that Li^+ diffusion is only promoted along the *b* direction due to a lower activation energy [15–17]. The second polymorph (Figure 1b) is LCP-*Pn2₁a*. This modification was theoretically predicted by Hautier [6] based on ab initio DFT calculations and subsequently experimentally reported by Jaehne et al. [18]. Unlike the olivine structure, Co^{2+} cations are tetrahedrally coordinated in this structure. The framework features alternating corner-sharing $[\text{PO}_4]$ and $[\text{CoO}_4]$ tetrahedra along the *c* axis, the Li^+ diffusion paths are blocked by $[\text{CoO}_4]$ tetrahedra and the compound shows a poor electrochemical performance. As a result, there are no direct Li^+ channels along any direction [6,18]. The third modification is LCP-*Cmcm*, which adapts the Na_2CrO_4 -type structure (Figure 1c). This structure was first reported by Amador and co-workers [19] resulting from a high-pressure and high-temperature solid-state synthesis (6 GPa, 900 °C). In the structure, chains of edge-sharing $[\text{CoO}_6]$ octahedra, which are running along the *c* direction, are cross-linked by $[\text{PO}_4]$ tetrahedra along *a*. As a result, layers of the composition $[(\text{CoO}_6)(\text{PO}_4)]_\infty$ are generated. Moreover, the remaining tetrahedral sites are occupied by Li^+ ions and a high activation energy is required for Li^+ -ion migration [19,20]. Recently, a microwave-assisted synthesis pathway was reported for LCP-*Cmcm*. In this report, Manthiram et al. [21,22] claimed two conditions to be necessary for the formation of LCP-*Cmcm*: the use of fresh dried tetraethylene glycol (TTEG) as a solvent and the use of cobalt oxalate as a cobalt precursor. This synthesis was performed in a closed system using a temperature of 260 °C and a pressure below 30 bar. A transformation of LCP-*Cmcm* to LCP-*Pnma* revealed by thermal analysis was also reported in this study. Besides, an ex situ XRD analysis was conducted after a long annealing process (8 h) and posterior cooling of the material. However, there is no further information about the crystal structure at temperatures above 650 °C and/or further verification of any other possible transition during the cooling process. In addition, it is well known that morphology plays an important role in the electrochemical performance of cathode and anode materials for LIB [23–25]. Some reports explain the benefits of hierarchical dumbbell-shape morphologies such as larger surface area, high porosity and the formation of small-sized primary particles, leading to a reduction of the diffusion distance of lithium ions and an increase of reaction sites of Li^+ -ions as well as preventing a decrease in volumetric energy density caused by low tap-density nanostructures [26,27]. Equally important, in order to achieve morphology control, the synthesis often requires the use of hydrothermal or solvothermal methods, sometimes microwave-assisted, as well as the use of expensive organic surfactants or additives, co-solvents and temperatures above 250 °C making the process expensive and complicated [28–30]. Herein, we report two alternative, kinetically controlled synthesis pathways towards the *Cmcm*-type LCP polymorph under mild conditions using a solvothermal as well as a polyol synthesis approach. Our synthesis is conducted at temperatures as low as 200 °C in a traditional round bottom flask. This simple synthesis does not require the use of water-free TTEG and is conducted using different cobalt ion precursors. The thermal behavior of LCP-*Cmcm* is examined comprehensively, revealing a

transformation of LCP-*Cmcm* to LCP-*Pnma* and finally to LCP-*Pn2₁a* at high temperature. Finally, the magnetic properties and metamagnetic transition of LCP-*Cmcm* are presented for the first time.

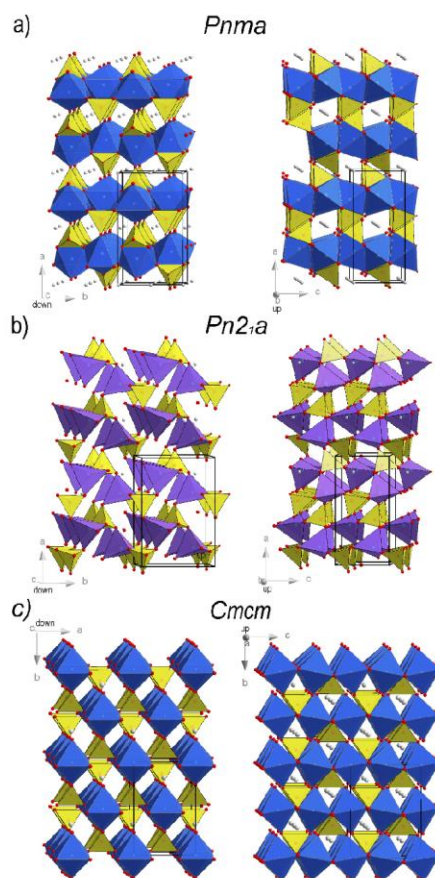


Figure 1. Projections of the crystal structures of the three orthorhombic polymorphs of LiCoPO₄ (LCP) along the crystallographic *c* and *b* axes with the space groups: (a) *Pnma*; (b) *Pn2₁a*; and (c) *Cmcm*. [CoO₆] octahedra are drawn in blue, [PO₄] tetrahedra in yellow, [CoO₄] tetrahedra in purple, Li⁺ ions in grey and O²⁻ ions in red.

2. Results and Discussion

2.1. X-ray Powder Diffraction

From solvothermal synthesis, the LCP polymorph with *Cmcm* symmetry was obtained from all solvents (see experimental section), yet varying amounts of Li₃PO₄ as well as traces of olivine-type LCP (space group *Pnma*) were observed as impurities (cf. Supplementary Materials, Figure S1, Tables S1–S3). The sample formed in diethylene glycol (DEG) solvent showed the smallest amount of impurities and was therefore selected for further characterization (designated as LCP-*Cmcm* (ST) in the following). Figure 2 shows the Rietveld refinement of the X-ray powder diffraction patterns

of the LCP-*Cmcm* samples obtained by solvothermal (ST) and polyol (PO) synthesis. The refined lattice parameters and refinement details are presented in Tables S2 and S3 of the Supplementary Materials. In the case of the solvothermal sample from the DEG solvent (Figure 2a), the refined lattice parameters are $a = 5.4347(4)$ Å, $b = 8.1638(5)$ Å, and $c = 6.2135(4)$ Å. However, very small amounts of Li_3PO_4 , which is often formed in solution-based synthesis [31,32] and olivine-type LCP (space group *Pnma*) are observed as side phases. For the polyol sample (Figure 2b), no impurities were detected. All of the identified reflections can be fully indexed using the space group *Cmcm*. The refined lattice parameters $a = 5.4433(3)$ Å, $b = 8.1694(4)$ Å, and $c = 6.2129(3)$ Å are in good agreement with the values for LCP-*Cmcm* reported in the literature [19]. Atomic coordinates, thermal displacement parameters, and selected interatomic distances can be found in the Supplementary Materials (Tables S2–S4). Furthermore, the appearance of sharp diffraction peaks strongly reflects the high crystallinity of the samples produced at comparably low pressure, temperature and in a one-step synthesis without post-annealing. It has to be pointed out that, according to reference measurements presented in our previous work [33], the background can be fully attributed to the capillary and no amorphous components are present in the sample.

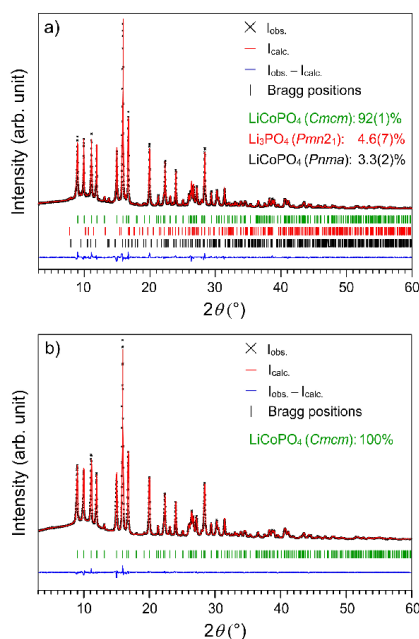


Figure 2. Rietveld fit of the X-ray powder diffraction data of LCP-*Cmcm* prepared by different synthesis pathways: (a) solvothermal; and (b) polyol synthesis.

2.2. Scanning Electron Microscopy (SEM)

High-resolution SEM images (Figure 3) of the two materials reveal that the synthesis conditions strongly affect the morphology of the particles. The solvothermal synthesis results in the formation of irregular macrostructures formed by agglomeration of primary platelets with overall dimensions of 5–10 µm (Figure 3a,b). The agglomerates consist of cross-linked, leaf-shaped platelets of about 0.5–1 µm × 5–6 µm in size, and about 80 nm in thickness. Complex morphologies like this are generally obtained by solvothermal or hydrothermal routes [34]. On the contrary, the polyol synthesis

results in the formation of agglomerates with dumbbell or bow-tie shapes in the size range of 1–4 μm , which are formed by nanosheet-like primary particles with average dimensions of 20–40 nm in length, and 3–4 nm in thickness (Figure 3c,d). Given the fact that to date the synthesis of cathode materials with dumbbell-like morphologies is only reported by the use of templates and/or under solvothermal/hydrothermal conditions, and sometimes assisted by microwave irradiation [26,27,29], it is remarkable that such a well-organized hierarchical morphology was obtained by a simple synthesis approach. Moreover, this morphology type allows for the obtainment of materials with high surface areas which offer a larger interface between the electrode and the electrolyte, a fast intercalation probability and an improved electron transport as reported for LFP [30]. In our case, the polyol synthesis is conducted without the use of special additives or under high temperature or high pressure conditions. We suggest in accordance with the literature that the tetraethylene glycol acts not only as a solvent and mild reducing agent but also as a soft template to direct the growth and self-assembly of structures with preferred orientations [35]. Furthermore, the mixing order of the precursors has an influence on the morphology of the final product. Figure 3e,f show LCP particles prepared after direct mixing of the cobalt acetate and lithium acetate solutions and the subsequent addition of phosphoric acid. In this case, no primary nanosheet-like particles were observed but even primary nano-dots with the same bow-like morphology. This implies that only by a simple variation of the mixing sequence, the morphology can be modified, thereby inducing a change from primary nano-needles to primary nano-dots without the use of any surfactant or organic template. The crystal structure remains unaltered (not shown). Results of Fourier transform infrared spectroscopy (FT-IR), including band assignment and literature comparison, are presented in Figure S2 and Table S4 in the Supplementary Materials section.

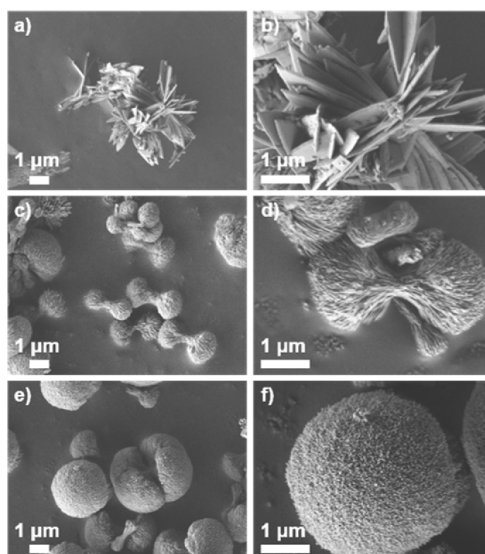


Figure 3. Scanning electron microscopy (SEM) images of LCP-Cmc prepared by different procedures. (a,b) Solvothermal synthesis; (c,d) Polyol synthesis; Addition of H_3PO_4 to LiAc solution and posterior addition of CoAc_2 to H_3PO_4 /LiAc mixture; (e,f) Polyol variation on the order of mixture: First mixture of CoAc_2 and LiAc with posterior addition of H_3PO_4 to the CoAc_2 /LiAc mixture.

2.3. Elemental Analysis

The chemical composition of the samples was determined by means of CHNS (determination of the C, H, N, and S contents by combustion analysis) and AAS (atomic absorption spectroscopy) analyses. The results are given in Table 1. The Li:Co:P wt % ratio is found to be close to the theoretical composition 4.3:36.6:19.3 of LiCoPO_4 in both cases. The results correspond to Li:Co:P molar ratios of 0.99(5):0.97(3):1.00(2) and 0.93(5):0.91(5):1.00(2), implying that both materials are stoichiometric within three standard deviations. The CHNS analyses show that no significant amounts of hydrogen as well as carbon are present in the sample, which might be arising from residual water or the decomposition of residual organic polyol solvents and precursors. However, it has to be emphasized that, whereas the solvothermal sample tends to be stoichiometric, the phase pure polyol material seems to be deficient both in Li and Co. Hence, the results indicate that the synthesis method affects the stoichiometry of the phase. A more systematic investigation of the role of the synthesis route on the chemical composition will be the focus of oncoming research.

Table 1. Elemental analysis of LCP-*Cmcm* synthesized by (a) the solvothermal (ST) and (b) the polyol process (PO) ^{1,2}.

Element	(a) LCP(ST)	(b) LCP(PO)	Theoretical
C (wt %)	0.7(3)	0.8(3)	0
H (wt %)	0.2(3)	0.4(3)	0
Li (wt %)	4.2(2)	4.1(2)	4.3
Co (wt %)	35(1)	34(1)	36.6
P (wt %)	18.9(3)	19.6(3)	19.3
<i>n</i> (Li): <i>n</i> (P)	0.99(5)	0.93(5)	1
<i>n</i> (Co): <i>n</i> (P)	0.97(3)	0.91(3)	1

¹ The composition is determined from the experimental values of the CHNS (combustion analysis to determine the C, H, N, and S contents) and AAS (atomic absorption spectroscopy) analyses (standard deviations in parentheses); ² The N and S values were below the detection limit (= 0).

2.4. Thermal Stability and Phase Transformation

As reported previously, the polymorphs LCP-*Cmcm* and LCP-*Pn2₁a* are metastable with transition temperatures to the thermodynamically stable LCP-*Pnma* of 220 and 550 °C, respectively [18,21,22]. However, all these conclusions were based on (a) TGA (thermogravimetric analysis)/DSC (differential scanning calorimetry) experiments which were only performed in a temperature range up to 700 and 500 °C, respectively, and (b) only supported by ex situ XRD analyses, which exclusively provide information about the particular phase at the end of the cooling process. Moreover, the reports were lacking additional SEM studies, which provide information about morphological changes upon heating. Taking the metastable behavior of LCP into consideration, it is important to examine the thermal behavior and respective phase transitions more thoroughly. The TGA/DSC data for the sample obtained by polyol synthesis are presented in Figure 4. In the TGA curve, a mass loss is observed between 200 and 300 °C, which can be attributed to the removal of residual water as well as to the decomposition of residues of the organic solvent. A strong signal occurs in the DSC experiment in the temperature range from 550 to 700 °C. At first glance, this effect can be attributed to the transition from LCP-*Cmcm* to LCP-*Pnma*, which represents a typical monotropic solid–solid phase transition of a metastable to a stable phase (irreversible process). Figure 5 shows the corresponding ex situ room temperature powder diffraction data of LCP-*Cmcm* produced by the polyol method, in the temperature range between 200 and 900 °C with an increment of 100 °C and posterior cooling. Herein, the transformation of LCP-*Cmcm* to LCP-*Pnma* takes place in the region between 500 and 700 °C. Moreover, the formation of an additional unidentified phase is evident. The corresponding peaks are marked with the symbol ♦.

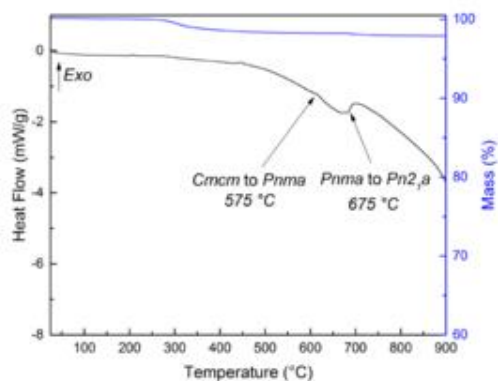


Figure 4. Thermal and gravimetric analyses for LCP-Cmcm (PO) obtained from the polyol route. TGA data are drawn in blue, and DSC data in black.

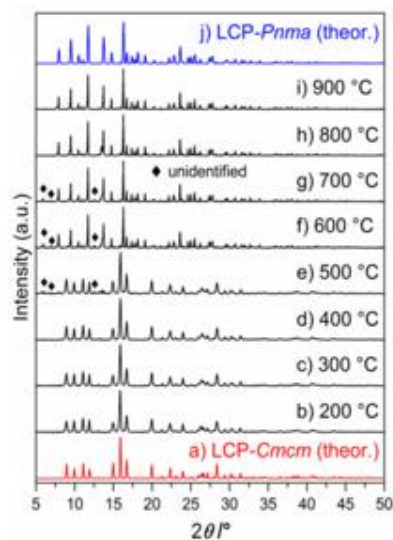


Figure 5. Ex situ X-ray powder diffraction patterns of LCP-Cmcm (PO) samples after heat treatment for 6 h in air in the temperature range from 200 to 900 °C (increment: 100 °C, **b–i**), in comparison with the theoretical patterns of LCP-Cmcm (**a**, red) and LCP-Pnma (**j**, blue). The quantitative transition from phase-pure LCP-Cmcm (**h**) to the olivine-type LCP-Pnma (**a**) can be observed upon heating. The reflections arising from an unidentified secondary phase are marked with the symbol ◆.

In order to elucidate the formation and stability of the phases at high temperatures without performing annealing and cooling steps in between, which is not suitable for the observation of metastable intermediates, we performed a temperature-dependent in situ powder XRD experiment between 21.8 and 600 °C. In Figure 6a, the section of the diffraction pattern is presented where the strongest reflections of LCP-Cmcm, (112) and (130), are observed. It can be clearly derived that the transformation to LCP-Pnma occurs at 575 °C. Hence, the data up to this temperature confirm the

metastable nature of LCP-*Cmcm*, which was reported previously [21]. To check the thermal stability, we further increased the temperature to 800 °C (Figure 6b). Surprisingly, the LCP-*Pnma* phase is only stable up to 625 °C, which is in strong contrast to any previous reports about the thermal behavior of olivine-type LCP [36,37]. The (101) and (210) peaks of LCP-*Pnma* are present from 575 to 625 °C. At 650 °C, no reflections are present in the measured range. Finally, starting from 675 °C, LCP-*Pn2₁a* is formed, which is indicated by the characteristic (210) reflection. The two-phase transition temperatures found in the in situ XRD experiments are marked by two arrows in the DSC (differential scanning calorimetry) trace of Figure 4. After cooling from 800 °C to room temperature, the LCP-*Pnma* structure reemerges in the powder XRD (PXRD) pattern of the in situ study (see Figure S3). To the best of our knowledge, the complete thermal properties and phase stabilities touching all three LCP polymorphs are reported for the first time. Combining the information derived from in situ XRD and DSC experiments, it becomes obvious that the broad signal between 500 to 700 °C is caused by the phase transitions.

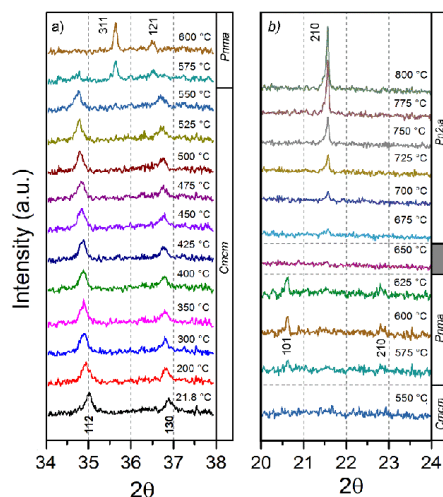


Figure 6. In situ X-ray powder diffraction patterns of LCP-*Cmcm* (PO): (a) Temperature range from 21.8 to 600 °C showing the transition from the *Cmcm* to the *Pnma* polymorph. The 2θ range is from 34° to 38° where the main reflection (112) of LCP-*Cmcm* is observed; (b) Temperature range from 550 to 800 °C in the 2θ range from 20° to 24°. The transition from the *Pnma* to the *Pn2₁a* modification is evident from the disappearance of the *Pnma* (101) and (210) reflections and the emergence of the *Pn2₁a* (210) reflection.

In addition, the morphology of the samples obtained from the ex situ annealing experiments on LCP-*Cmcm* (PO) was examined using SEM (Figure 7). The studies reveal that the nanosheet-like primary structure of the dumbbells continuously changes upon heating. After annealing at 400 °C (Figure 7c), the material starts to sinter and, finally, a denser and more compact material is formed. Simultaneously, the dumbbell-like shape is preserved (Figure 7d,e). At about 700 °C (Figure 7f), the phase transition of the material takes place and the dumbbells start to conglomerate. Further heating (Figure 7g,h) destroys the primary particle shape and results in irregular particles.

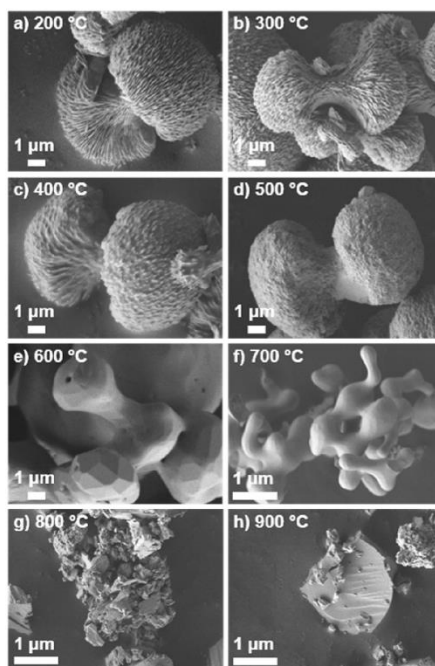


Figure 7. SEM images (a–h) of LCP-Cmcm (PO) after annealing in the temperature range from 200 to 900 °C (increment: 100 °C). The samples (f–h) are shown with higher resolution for clarity.

2.5. Magnetic Properties

The results of the static magnetic susceptibility as a function of the temperature measured on the LCP-Cmcm sample are shown in Figure 8. In the high temperature regime, the data obey the Curie-Weiss law ($\chi = \chi_0 + (N_A \mu_{eff}^2) / (3k_b(T - \theta_C))$) with χ_0 being the temperature-independent contribution, μ_{eff} the effective magnetic moment, N_A the Avogadro number, θ_C the Weiss temperature (negative value), and k_b the Boltzmann constant. Table 2 shows the results of the Curie-Weiss fitting for the measurements at 1, 10 and 25 kOe.

Table 2. Results of the Curie-Weiss fitting in the high temperature regime for LCP-Cmcm sample produced by polyol method.

Variable	1 kOe	10 kOe	25 kOe
T_N (K)	12.7	12.7	9.1
θ_C (K)	−27.6	−27.7	−26.2
χ_0 (cm ³ /mol)	1.35×10^{-1}	1.73×10^{-1}	1.48×10^{-1}
μ_{eff} (μ _B)	5.46	5.42	5.56

In Figure 8, the ZFC curves reveal a long range antiferromagnetic order below the Néel temperature T_N , as result of the antiparallel alignment of magnetic moments of cobalt atoms. As seen in Table 2, the values of the magnetic moments are slightly higher in comparison to the ones reported for high spin octahedral cobalt (II) complexes (4.7 to 5.2 μ_B) [38]. As reported for LCP-Pnma, the large value of the effective magnetic moment can be explained by the strongly coupled Co–O–Co superexchange

interactions with Co^{2+} magnetic moments or higher order interactions, such as, Co-O-P-O-Co [39,40]. On the other hand, the behavior of zero-field-cooled (ZFC) and field-cooled (FC) curves below the Néel temperature changes with the increasing magnetic field. At 1 kOe (Figure 8a) the ZFC–FC curves are overlapping, then at 10 kOe (Figure 8b), below the Néel temperature, the FC curve presents susceptibility values that are slightly higher in comparison with the ZFC data. Finally, at 25 kOe, the ZFC–FC curves present a branch point suggesting a magnetic transition depending of the temperature and magnitude of the external magnetic field. This behavior can be confirmed by the magnetization measurements. The isothermal measurements of the magnetization as a function of the applied field are shown in Figure 9. At room temperature (green line), the sample exhibits a paramagnetic behavior. However, when the temperature decreases to values near to T_N (11 K), the sample presents a slightly double hysteresis behavior (blue line) which is increased when the temperature reaches 2 K (black line). The magnetic field-induced phase transition occurs at about 10 kOe caused by the switching from an antiferromagnetic to ferro (or ferri) magnetic state upon increasing the magnetic field. In literature, a weak-ferromagnetic to an antiferromagnetic state transition in LCP-*Pnma* was reported [41], caused by a distortion of the octahedral, formed by cobalt and oxygen atoms at low temperatures ($T = 23$ K); however, in order to study the origin of these metamagnetic transitions as well as the magnetic structure in different magnetic states, neutron powder diffraction experiments are required for LCP-*Cmcm*.

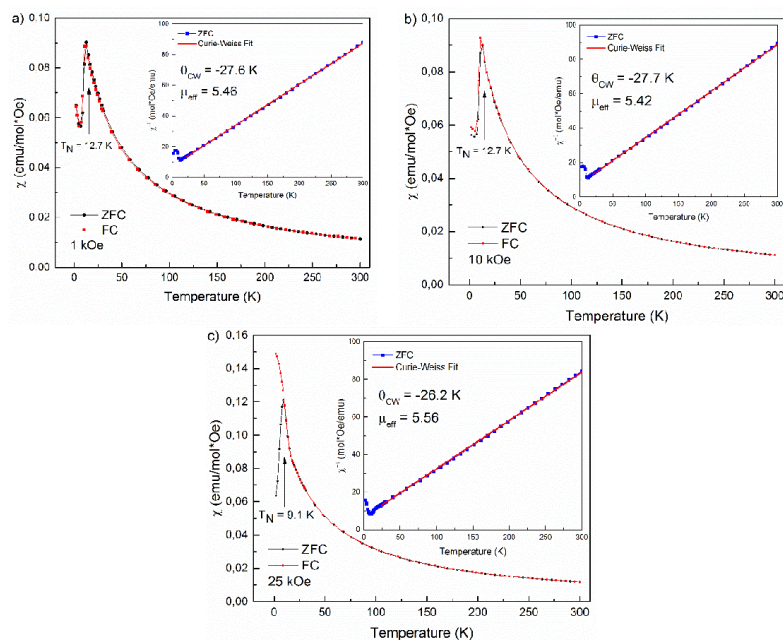


Figure 8. Magnetic susceptibility as a function of the temperature at zero-field-cooled/field-cooled (ZFC/FC) conditions under constant applied fields of: (a) 1 kOe; (b) 10 kOe; and (c) 25 kOe for LCP-*Cmcm* produced by polyol method. The inset shows the inverse magnetic susceptibility and the Curie-Weiss fitting of the high temperature data under ZFC conditions.

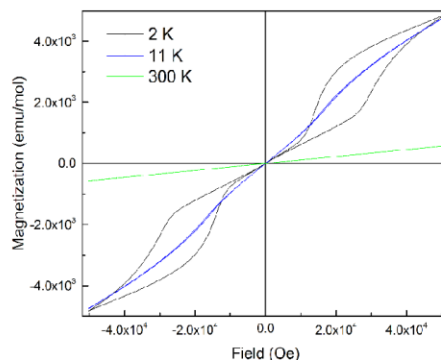


Figure 9. Magnetization as a function of the applied field between 5 and -5 T measured at 2, 11 and 300 K for the sample of LCP-Cmcm (PO).

3. Materials and Methods

3.1. Solvothermal Synthesis

For the solvothermal synthesis of LCP-Cmcm, stoichiometric amounts of $\text{CoC}_2\text{O}_4 \cdot 2\text{H}_2\text{O}$ (Alfa Aesar, Ward Hill, MA, USA, 98%) and LiH_2PO_4 (Sigma Aldrich, St. Louis, MO, USA, 99%) were introduced in 9 mL of solvent, whereas diethylene glycol (DEG; Merck, Darmstadt, Germany, $\geq 99.0\%$), triethylene glycol (TEG; Merck, $\geq 99\%$), and tetraethylene glycol (TTEG; Merck, $\geq 98\%$) were used. The resulting suspensions were homogenized for 20 min, transferred to Teflon-lined stainless steel pressure vessels (BERGHOF Products + Instruments GmbH, Eningen, Germany), and sealed. For the solvothermal treatment, the temperature was ramped to 220°C within 2 h. After a reaction period of 7 days, the mixtures were cooled to ambient temperature. The resulting bright pink precipitates were separated by suction filtration, washed several times with distilled water (Millipore water type I, $18.2\text{ M}\Omega \cdot \text{cm}$) and absolute ethanol (VWR BDH PROLABO AnalaR NORMAPUR, Radnor, PA, USA, 99.95%) followed by drying in air at 130°C overnight.

3.2. Polyol Synthesis

Powder samples were prepared via a polyol process using cobalt acetate tetrahydrate ($\text{Co}(\text{CH}_3\text{COO})_2 \cdot 4\text{H}_2\text{O}$, Merck, 99.99%), lithium acetate ($\text{Li}(\text{CH}_3\text{COO})$, ChemPUR, Karlsruhe, Germany, 99+%) and H_3PO_4 (Merck, 85%) in a stoichiometric molar ratio of 1:3:10. Tetraethylene glycol (TTEG, Merck, $\geq 99.0\%$) was used as solvent. First, lithium acetate was solved in 125 mL of TTEG and, subsequently, phosphoric acid added dropwise. Cobalt acetate was dissolved in 75 mL of TTEG and then added to the prior solution. The mixture was refluxed at 200°C for 14 h in a three-necked round bottom flask. After cooling down to room temperature, the precipitate was separated from the solvent by centrifugation (1500 rpm, 20 min) and washed several times with ethanol (VWR AnalaR NORMAPUR, 99.95%) in order to remove the solvent. The light pink powder was collected by suction filtration, washed with acetone (99% VWR, Semi grade), and dried in air at 120°C overnight. The material obtained from the polyol process is denoted as LCP-Cmcm (PO).

3.3. Structural, Physical and Chemical Properties Determination

X-ray powder diffraction data were collected at room temperature on a STADI P diffractometer (STOE & Cie. GmbH, Darmstadt, Germany) using $\text{Mo K}\alpha$ radiation (Ge(111) monochromator, $\lambda = 0.70930\text{ \AA}$) equipped with a Mythen DCS 1K silicon solid-state detector (Dectris Ltd., Baden-Daettwil, Switzerland). The ground samples were sealed in glass capillaries (Hilgenberg,

Malsfeld, Germany, borosilicate glass type no. 50, length: 80 mm, diameter: 0.5 mm, wall thickness: 0.01 mm), which were then measured in a 2θ range of 3° – 60° (PSD (position sensitive detector) step: 0.15° ; time/step: 30 s, three ranges, total measurement time: 12 h). An external calibration was performed using Si ($a = 5.43088 \text{ \AA}$, NBS standard reference material). The JANA2006 software [42] was used for Rietveld analysis of the diffraction patterns. The structure data of the LNP polymorph (ICSD database no. 97767 [20]) were taken as a starting model and refined in the space group *Cmcm*.

The temperature-dependent XRD studies were done in situ with a Stoe STADI P diffractometer using Cu K α radiation (Ge(111) monochromator, $\lambda = 1.540598 \text{ \AA}$) equipped with a Dectris Mythen 1K OEM (Dectris Ltd.) silicon solid-state detector. The data were collected between 19° and $37.93^\circ 2\theta$. The detailed temperature program is provided in Table S5 in the Supplementary Materials.

High-resolution scanning electron microscopy (HR-SEM) was performed on a JSM-7500F instrument (JEOL, Tokyo, Japan) at an accelerating voltage of 1 kV. The powders were prepared on carbon tape, which was attached to an aluminum stub.

Elemental analysis of the sample was carried out by atomic absorption spectroscopy using a Varian AA280FS sequential device for the lithium and cobalt, and by photometry using a UV-160 device (Shimadzu, Kyoto, Japan) for the P contents. CHNS analysis was performed by combustion analysis using a Euro EA CHNSO Analyzer (HEKAtech, Wegberg, Germany).

Attenuated total reflectance (ATR)-FTIR data were collected on a 670 IR FTIR spectrometer (Varian, Palo Alto, CA, USA) equipped with a PIKE GladiATR ATR stage (400 – 4000 cm^{-1} , 132 scans) (see Supplementary Materials). The Resolution Pro software (Agilent, Santa Clara, CA, USA) was used for data handling.

The thermal analysis was carried out to assess the chemical stability of the powders up to 900°C on a TGA/DSC 1 STAR system (Mettler Toledo, Columbus, OH, USA). Experiments were run at a heating rate of $10^\circ\text{C}\cdot\text{min}^{-1}$ in an argon stream flowing at $10 \text{ mL}\cdot\text{min}^{-1}$ (specimen weight of 20 mg). The effect of the thermal treatment as a function of temperature was additionally examined using ex situ powder XRD studies (Mo K α radiation (Ge(111) monochromator, $\lambda = 0.70930 \text{ \AA}$, 2θ range of 5° – 50° , PSD step: 0.49° ; time/step: 10 s, two ranges). For this purpose, approximately 50 mg of the sample were annealed for 6 h in air at temperatures ranging from 200 to 900°C with an increment of 100°C using a muffle furnace.

DC magnetization data were collected using a MPMS XL5 superconducting quantum interference device (SQUID, Quantum Design, San Diego, CA, USA). The temperature-dependent data were obtained by measurement of the magnetization from 1.8 to 300 K in an applied magnetic field of 1, 10 and 25 kOe, by using the powdered samples fixed in calibrated gelatin capsules held at the center of a drinking straw. The temperature-dependent measurements were performed in zero-field-cooled (ZFC) and field-cooled (FC) mode. Magnetization as a function of applied field measurements were done between 5 and -5 T at 2, 11 K, and room temperature.

4. Conclusions

LiCoPO_4 -*Cmcm* was synthesized by two different kinetically controlled synthesis approaches. Whereas the product of the solvothermal process showed secondary phases of Li_3PO_4 and the olivine-type *Pnma* phase, the polyol process results in the formation of a single-phase LCP-*Cmcm* material in a one-step synthesis without post-annealing. Using the polyol method, a dumbbell-like morphology could be obtained by a simple one-step synthesis without the use of additional surfactants or templates. Moreover, by a simple methodology based on the variation of the mixing order of the educts, the morphology of the samples can be controlled. The temperature-dependent in situ powder X-ray diffraction (PXRD) analysis reveals the phase transitions between the three reported LCP polymorphs. Starting from the *Cmcm* phase, a transition to the *Pnma* structure is observed at 575°C , which then converts to the *Pn2₁a* polymorph at 675°C . After cooling to ambient temperature, the thermodynamically stable *Pnma* modification is obtained. At temperatures above 675°C , the *Pn2₁a* polymorph is thermodynamically stable in contrast to that reported at room temperature. To the best

of our knowledge, this behavior is reported for the first time. Moreover, also the hitherto unknown magnetic properties of the *Cmcm* phase were investigated. The LCP-*Cmcm* polymorph shows an antiferromagnetic order below the Néel temperature at low fields (1 and 10 kOe). The measurements of the magnetic response confirm a transition from antiferromagnetic ordering to ferromagnetic (or ferrimagnetic) ordering at temperatures below T_N as a function of the applied field. This study paves the way for a novel methodology towards the synthesis and investigation of new polymorphs of transition-metal phosphates. Thus, our approach provides insights into studying potential cathode materials for lithium-ion batteries from a fundamental point of view.

Supplementary Materials: The following are available online at www.mdpi.com/2304-6740/4/4/35/s1. Rietveld refinement details, infrared spectra, PXRD pattern of the sample obtained after the temperature-dependent in situ PXRD measurement, temperature program for temperature-dependent PXRD measurements. Further details of the crystal structure investigation may be obtained from FLZ Karlsruhe, 76344 Eggenstein-Leopoldshafen, Germany (Fax: +49-7247-808-666; E-mail: crysdata@fiz-karlsruhe.de), on quoting the deposition numbers CSD 432183–432186.

Acknowledgments: The authors would like to thank the BMW AG, the DAAD, Colciencias, and the Fonds der Chemischen Industrie for financial support and the state of Bavaria and the TUM for X-Ray powder diffractometer funding. Furthermore, we thank Dr. Wilhelm Klein for the in situ XRD measurements, Katia Rodewald for SEM, Gergana Nenova for SQUID, and Pankaj Madkikar for thermogravimetric measurements. We further thank the microanalytical laboratory of the TUM for elemental analyses. Carlos Alarcón-Suesca and Jennifer Ludwig are further grateful to the DAAD, Fonds der Chemischen Industrie for their fellowships.

Author Contributions: The manuscript was written through contributions of Carlos Alarcón-Suesca, Jennifer Ludwig, Viktor Hlukhyy, Christoph Stinner and Tom Nilges. Carlos Alarcón-Suesca and Jennifer Ludwig contributed equally to this study.

Conflicts of Interest: The authors declare no conflict of interest.

References

- Whittingham, M.S. Electrical energy storage and intercalation chemistry. *Science* **1976**, *192*, 1126–1127. [[CrossRef](#)] [[PubMed](#)]
- Thackeray, M. Lithium-ion batteries: An unexpected conductor. *Nat. Mater.* **2002**, *1*, 81–82. [[CrossRef](#)] [[PubMed](#)]
- Tarascon, J.M.; Armand, M. Issues and challenges facing rechargeable lithium batteries. *Nature* **2001**, *414*, 359–367. [[CrossRef](#)] [[PubMed](#)]
- Xu, B.; Qian, D.; Wang, Z.; Meng, Y.S. Recent progress in cathode materials research for advanced lithium ion batteries. *Mater. Sci. Eng. R Rep.* **2012**, *73*, 51–65. [[CrossRef](#)]
- Padhi, A.K.; Nanjundaswamy, K.S.; Goodenough, J.B. Phospho-olivines as positive-electrode materials for rechargeable lithium batteries. *J. Electrochem. Soc.* **1997**, *144*, 1188–1194. [[CrossRef](#)]
- Hautier, G.; Jain, A.; Ong, S.P.; Kang, B.; Moore, C.; Doe, R.; Ceder, G. Phosphates as lithium-ion battery cathodes: An evaluation based on high-throughput ab initio calculations. *Chem. Mater.* **2011**, *23*, 3495–3508. [[CrossRef](#)]
- Strobridge, F.C.; Clement, R.J.; Leskes, M.; Middlemiss, D.S.; Borkiewicz, O.J.; Wiaderek, K.M.; Chapman, K.W.; Chupas, P.J.; Grey, C.P. Identifying the structure of the intermediate, $\text{Li}_{2/3}\text{CoPO}_4$, formed during electrochemical cycling of LiCoPO_4 . *Chem. Mater.* **2014**, *26*, 6193–6205. [[CrossRef](#)] [[PubMed](#)]
- Sergio, B.; Stefania, P. Recent Advances in the Development of LiCoPO_4 as High Voltage Cathode Material for Li-Ion Batteries. In *Nanotechnology for Sustainable Energy*; American Chemical Society: Washington, DC, USA, 2013; Volume 1140, pp. 67–99.
- Howard, W.F.; Spotnitz, R.M. Theoretical evaluation of high-energy lithium metal phosphate cathode materials in Li-ion batteries. *J. Power Sources* **2007**, *165*, 887–891. [[CrossRef](#)]
- Wolfenstine, J.; Allen, J.L.; Jow, T.R.; Thompson, T.; Sakamoto, J.; Jo, H.; Choe, H. LiCoPO_4 mechanical properties evaluated by nanoindentation. *Ceram. Int.* **2014**, *40*, 13673–13677. [[CrossRef](#)]
- Chen, H.; Chen, M.; Du, C.; Cui, Y.; Zuo, P.; Cheng, X.; Yin, G. Synthesis and electrochemical performance of hierarchical nanocomposite of carbon coated LiCoPO_4 crosslinked by graphene. *Mater. Chem. Phys.* **2016**, *171*, 6–10. [[CrossRef](#)]

12. Theil, S.; Fleischhammer, M.; Axmann, P.; Wohlfahrt-Mehrens, M. Experimental investigations on the electrochemical and thermal behaviour of LiCoPO₄-based cathode. *J. Power Sources* **2013**, *222*, 72–78. [[CrossRef](#)]
13. Yamada, A.; Hosoya, M.; Chung, S.-C.; Kudo, Y.; Hinokuma, K.; Liu, K.-Y.; Nishi, Y. Olivine-type cathodes: Achievements and problems. *J. Power Sources* **2003**, *119–121*, 232–238. [[CrossRef](#)]
14. Ellis, B.L.; Lee, K.T.; Nazar, L.F. Positive electrode materials for Li-ion and Li-batteries. *Chem. Mater.* **2010**, *22*, 691–714. [[CrossRef](#)]
15. Truong, Q.D.; Devaraju, M.K.; Ganbe, Y.; Tomai, T.; Honma, I. Controlling the shape of LiCoPO₄ nanocrystals by supercritical fluid process for enhanced energy storage properties. *Sci. Rep.* **2014**, *4*. [[CrossRef](#)] [[PubMed](#)]
16. Morgan, D.; van der Ven, A.; Ceder, G. Li conductivity in Li_xMPO₄ (M = Mn, Fe, Co, Ni) olivine materials. *Electrochem. Solid State Lett.* **2004**, *7*, A30–A32. [[CrossRef](#)]
17. Tealdi, C.; Spreafico, C.; Mustarelli, P. Lithium diffusion in Li_{1-x}FePO₄: The effect of cationic disorder. *J. Mater. Chem.* **2012**, *22*, 24870–24876. [[CrossRef](#)]
18. Jaehne, C.; Neef, C.; Koo, C.; Meyer, H.-P.; Klingeler, R. A new LiCoPO₄ polymorph via low temperature synthesis. *J. Mater. Chem. A* **2013**, *1*, 2856–2862. [[CrossRef](#)]
19. Amador, U.; Gallardo-Amores, J.M.; Heymann, G.; Huppertz, H.; Moran, E.; Arroyo, Y.D.D.M.E. High pressure polymorphs of LiCoPO₄ and LiCoAsO₄. *Solid State Sci.* **2009**, *11*, 343–348. [[CrossRef](#)]
20. Garcia-Moreno, O.; Alvarez-Vega, M.; Garcia-Alvarado, F.; Garcia-Jaca, J.; Gallardo-Amores, J.M.; Sanjuan, M.L.; Amador, U. Influence of the structure on the electrochemical performance of lithium transition metal phosphates as cathodic materials in rechargeable lithium batteries: A new high-pressure form of Li_xMPO₄ (M = Fe and Ni). *Chem. Mater.* **2001**, *13*, 2455. [[CrossRef](#)]
21. Kreder, K.J.; Assat, G.; Manthiram, A. Microwave-assisted solvothermal synthesis of three polymorphs of LiCoPO₄ and their electrochemical properties. *Chem. Mater.* **2015**, *27*, 5543–5549. [[CrossRef](#)]
22. Assat, G.; Manthiram, A. Rapid microwave-assisted solvothermal synthesis of non-olivine Cmcn polymorphs of LiMPO₄ (M = Mn, Fe, Co, and Ni) at low temperature and pressure. *Inorg. Chem.* **2015**, *54*, 10015–10022. [[CrossRef](#)] [[PubMed](#)]
23. Wang, F.; Zhao, M.; Song, X. Influence of the preparation conditions on the morphology and electrochemical performance of nano-sized Cu–Sn alloy anodes. *J. Alloy. Compd.* **2007**, *439*, 249–253. [[CrossRef](#)]
24. Pan, Q.; Jin, H.; Wang, H.; Yin, G. Flower-like cuo film-electrode for lithium ion batteries and the effect of surface morphology on electrochemical performance. *Electrochim. Acta* **2007**, *53*, 951–956. [[CrossRef](#)]
25. Tang, K.; Sun, J.; Yu, X.; Li, H.; Huang, X. Electrochemical performance of LiFePO₄ thin films with different morphology and crystallinity. *Electrochim. Acta* **2009**, *54*, 6565–6569. [[CrossRef](#)]
26. Dinh, H.-C.; Mho, S.-I.; Yeo, I.-H. Electrochemical analysis of conductive polymer-coated LiFePO₄ nanocrystalline cathodes with controlled morphology. *Electroanalysis* **2011**, *23*, 2079–2086. [[CrossRef](#)]
27. Ryu, W.-H.; Lim, S.-J.; Kim, W.-K.; Kwon, H. 3-D dumbbell-like LiNi_{1/3}Mn_{1/3}Co_{1/3}O₂ cathode materials assembled with nano-building blocks for lithium-ion batteries. *J. Power Sources* **2014**, *257*, 186–191. [[CrossRef](#)]
28. Zhou, N.; Uchaker, E.; Wang, H.-Y.; Zhang, M.; Liu, S.-Q.; Liu, Y.-N.; Wu, X.; Cao, G.; Li, H. Additive-free solvothermal synthesis of hierarchical flower-like LiFePO₄/C mesocrystal and its electrochemical performance. *RSC Adv.* **2013**, *3*, 19366–19374. [[CrossRef](#)]
29. Cao, J.; Zhu, Y.; Bao, K.; Shi, L.; Liu, S.; Qian, Y. Microscale Mn₂O₃ hollow structures: Sphere, cube, ellipsoid, dumbbell, and their phenol adsorption properties. *J. Phys. Chem. C* **2009**, *113*, 17755–17760. [[CrossRef](#)]
30. Zeng, G.; Caputo, R.; Carriazo, D.; Luo, L.; Niederberger, M. Tailoring two polymorphs of LiFePO₄ by efficient microwave-assisted synthesis: A combined experimental and theoretical study. *Chem. Mater.* **2013**, *25*, 3399–3407. [[CrossRef](#)]
31. Eftekhari, A. Surface modification of thin-film based LiCoPO₄ 5 V cathode with metal oxide. *J. Electrochem. Soc.* **2004**, *151*, A1456–A1460. [[CrossRef](#)]
32. Choi, D.; Li, X.; Henderson, W.A.; Huang, Q.; Nune, S.K.; Lemmon, J.P.; Sprenkle, V.L. LiCoPO₄ cathode from a CoHPO₄·xH₂O nanoplate precursor for high voltage Li-ion batteries. *Heliyon* **2016**, *2*, e00081. [[CrossRef](#)] [[PubMed](#)]
33. Ludwig, J.; Marino, C.; Haering, D.; Stinner, C.; Nordlund, D.; Doeff, M.M.; Gasteiger, H.A.; Nilges, T. Facile, ethylene glycol-promoted microwave-assisted solvothermal synthesis of high-performance LiCoPO₄ as a high-voltage cathode material for lithium-ion batteries. *RSC Adv.* **2016**, *6*, 82984–82994. [[CrossRef](#)]

34. Yang, H.; Wu, X.-L.; Cao, M.-H.; Guo, Y.-G. Solvothermal synthesis of LiFePO₄ hierarchically dumbbell-like microstructures by nanoplate self-assembly and their application as a cathode material in lithium-ion batteries. *J. Phys. Chem. C* **2009**, *113*, 3345–3351. [[CrossRef](#)]
35. Mathew, V.; Alfaruqi, M.H.; Gim, J.; Song, J.; Kim, S.; Ahn, D.; Kim, J. Morphology-controlled LiFePO₄ cathodes by a simple polyol reaction for Li-ion batteries. *Mater. Charact.* **2014**, *89*, 93–101. [[CrossRef](#)]
36. Ni, J.; Wang, H.; Gao, L.; Lu, L. A high-performance LiCoPO₄/C core/shell composite for Li-ion batteries. *Electrochim. Acta* **2012**, *70*, 349–354. [[CrossRef](#)]
37. Huang, X.; Ma, J.; Wu, P.; Hu, Y.; Dai, J.; Zhu, Z.; Chen, H.; Wang, H. Hydrothermal synthesis of LiCoPO₄ cathode materials for rechargeable lithium ion batteries. *Mater. Lett.* **2005**, *59*, 578–582. [[CrossRef](#)]
38. Nicholls, D. 41-Cobalt. In *The Chemistry of Iron, Cobalt and Nickel*; Pergamon Press: Oxford, UK, 1973; pp. 1053–1107.
39. Szewczyk, A.; Gutowska, M.U.; Wieckowski, J.; Wisniewski, A.; Puzniak, R.; Diduszko, R.; Kharchenko, Y.; Kharchenko, M.F.; Schmid, H. Phase transitions in single-crystalline magnetoelectric LiCoPO₄. *Phys. Rev. B* **2011**, *84*, 104419. [[CrossRef](#)]
40. Tian, W.; Li, J.; Lynn, J.W.; Zarestky, J.L.; Vaknin, D. Spin dynamics in the magnetoelectric effect compound LiCoPO₄. *Phys. Rev. B* **2008**, *78*, 6. [[CrossRef](#)]
41. Rhee, C.H.; Kim, S.J.; Kim, C.S. Crystallographic and magnetic properties of LiCoPO₄ at low temperature. *J. Korean Phys. Soc.* **2010**, *56*, 611–614.
42. Petricek, V.; Dusek, M.; Palatinus, L. Crystallographic computing system Jana2006: General features. *Z. Kristallogr.* **2014**, *229*, 345–352.
43. Finger, L.W.; Cox, D.E.; Jephcoat, A.P. A correction for powder diffraction peak asymmetry due to axial divergence. *J. Appl. Crystallogr.* **1994**, *27*, 892–900. [[CrossRef](#)]
44. Cromer, D.T.; Liberman, D.A. Anomalous dispersion calculations near to and on the long-wavelength side of an absorption edge. *Acta Crystallogr. Sect. A* **1981**, *A37*, 267–268. [[CrossRef](#)]
45. Berar, J.F.; Lelann, P. E.S.D.'s and estimated probable error obtained in rietveld refinements with local correlations. *J. Appl. Crystallogr.* **1991**, *24*, 1–5. [[CrossRef](#)]
46. Steger, E.; Herzog, K. Zum schwingungsspektrum der phosphorsäure. I. Infrarot- und raman-spektren von phosphatlösungen. *Z. Anorg. Allg. Chem.* **1964**, *331*, 169–182. [[CrossRef](#)]
47. Jastrzebski, W.; Sitarz, M.; Rokita, M.; Bulat, K. Infrared spectroscopy of different phosphates structures. *Spectrochim. Acta A Mol. Biomol. Spectrosc.* **2011**, *79*, 722–727. [[CrossRef](#)] [[PubMed](#)]
48. Poovizhi, P.N.; Selladurai, S. Study of pristine and carbon-coated LiCoPO₄ olivine material synthesized by modified sol-gel method. *Ionics* **2011**, *17*, 13–19. [[CrossRef](#)]
49. Burba, C.M.; Frech, R. Vibrational spectroscopic investigation of structurally-related LiFePO₄, NaFePO₄, and FePO₄ compounds. *Spectrochim. Acta A Mol. Biomol. Spectrosc.* **2006**, *65*, 44–50. [[CrossRef](#)] [[PubMed](#)]



Supplementary Materials: In Situ Studies and Magnetic Properties of the *Cmcm* Polymorph of LiCoPO_4 with a Hierarchical Dumbbell-Like Morphology Synthesized by Easy Single-Step Polyol Synthesis

Carlos Alarcón-Suesca, Jennifer Ludwig, Viktor Hlukhyy, Christoph Stinner and Tom Nilges

1. Structural, Physical and Chemical Properties

1.1. Rietveld Refinement Details

The background profile, which can rather be attributed to the capillaries used than to amorphous components of the material, was fitted with a Chebyshev polynomial function with 35 coefficients. Thereafter, the lattice parameters as well as the zero-point and scale factor were refined. A pseudo-Voigt profile function with three Gaussian and one Lorentzian coefficients was used for modeling the shape of the diffraction peaks; the profile was cut outside the 8 FWHM range. Because the FWHM of the peaks exhibited a marked anisotropy, anisotropic strain broadening implemented in JANA2006 [42] was tentatively refined. No correction for preferred orientation was applied. Peak asymmetry, which was especially observed at low scattering angles, was corrected by the axial divergence model described by Finger et al. [43]. The empirical starting values of the parameters S/L and H/L were set to -0.011 and 0.06 , according to the characteristics of the instrument. The refinement of the general atomic positions of Co, P, and O was performed unrestrictedly, the atomic site occupancies as well as the thermal parameters were fixed. As Li positions and thermal displacement parameters cannot be deduced by means of X-ray diffraction because of the low atomic scattering factor, they have been fixed as well. After applying an absorption correction (estimated packing fraction ~ 0.6) [44], the temperature factors of the Co, P and O sites were refined freely. Finally, the Berar's factor was applied to obtain more realistic standard uncertainties [45].

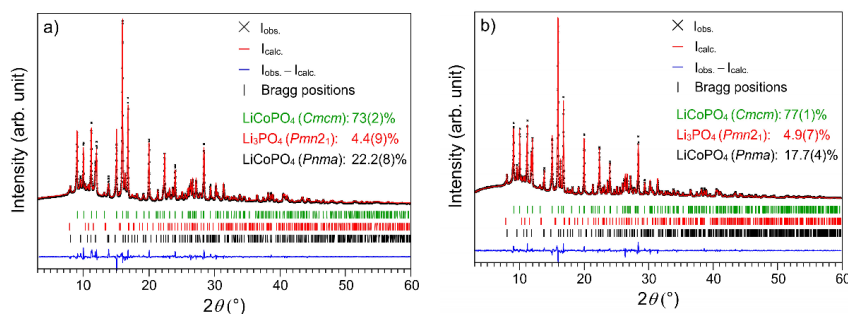


Figure S1. Rietveld fits of the X-ray powder diffraction patterns of LCP-*Cmcm* obtained from solvothermal synthesis using (a) TEG; and (b) TTEG as solvents.

Table S1. Crystallographic data, details of data collection, and structure refinement of LCP-*Cmcm* prepared by (a) solvothermal (ST) ((a) DEG, (b) TEG, and (c) TTEG solvent) and (d) polyol (PO) syntheses as refined from X-ray powder diffraction data at $T = 298\text{ K}$ ^a.

	(a) LCP (ST-DEG)	(b) LCP (ST-TEG)	(c) LCP (ST-TTEG)	(d) LCP (PO)
M_r (g·mol ⁻¹)			160.8	
Crystal system			orthorhombic	
Space group			<i>Cmcm</i> (no. 63)	
Z			4	
a (Å)	5.4347(4)	5.4354(5)	5.4341(4)	5.4433(3)
b (Å)	8.1638(5)	8.1680(7)	8.1676(5)	8.1694(4)
c (Å)	6.2135(4)	6.2159(5)	6.2176(4)	6.2129(3)
V (Å ³)	275.68(3)	275.97(4)	275.96(3)	276.28(2)
$F(000)$	112	112	112	308
ρ (calcd) (g·cm ⁻³)	3.8753(6)	3.8713(8)	3.8714(6)	3.8657(4)
R_p	0.032	0.041	0.034	0.021
R_{wp}	0.041	0.057	0.047	0.027
R_{exp}	0.026	0.026	0.030	0.025
R_f	0.018	0.024	0.027	0.013
χ^2	1.57	2.16	1.57	1.08
Data/restraints/parameter	3802/0/75	3800/0/75	3800/0/75	3835/0/55
Phase composition	93(2) wt % LiCoPO ₄ (<i>Cmcm</i>) 3.4(4) wt % LiCoPO ₄ (<i>Pnma</i>) 4(2) wt % Li ₃ PO ₄ (<i>Pmn2</i> ₁)	73(2) wt % LiCoPO ₄ (<i>Cmcm</i>) 22.2(8) wt % LiCoPO ₄ (<i>Pnma</i>) 4.4(9) wt % Li ₃ PO ₄ (<i>Pmn2</i> ₁)	77(1) wt % LiCoPO ₄ (<i>Cmcm</i>) 17.7(4) wt % LiCoPO ₄ (<i>Pnma</i>) 4.9(7) wt % Li ₃ PO ₄ (<i>Pmn2</i> ₁)	100 wt % LiCoPO ₄ (<i>Cmcm</i>)

^a The estimated standard deviations (E.S.D's) were calculated by means of the Berar's procedure and are indicated in round brackets.

Table S2. Fractional atomic coordinates and isotropic thermal displacement parameters of (a) LCP-*Cmcm* (ST; from DEG), and (b) LCP-*Cmcm* (PO) as refined from X-ray powder diffraction data at $T = 298\text{ K}$ ^a.

Sample	Atom	Wyckoff Position	x/a	y/b	z/c	U_{iso} (Å ²)
LCP- <i>Cmcm</i> (ST)	Li1	4c	0	0.675 ^b	¼	0.019 ^b
	Co1	4a	0	0	0	0.0107(9)
	P1	4c	0	0.3527(6)	¼	0.0118(13)
	O1	8f	0	0.2469(6)	0.0505(11)	0.007(2)
	O2	8g	0.2289(9)	0.4653(8)	¼	0.006(2)
LCP- <i>Cmcm</i> (PO)	Li1	4c	0	0.675 ^b	¼	0.019 ²
	Co1	4a	0	0	0	0.0107(5)
	P1	4c	0	0.3523(4)	¼	0.0064(8)
	O1	8f	0	0.2474(4)	0.0500(7)	0.0039(13)
	O2	8g	0.2255(6)	0.4653(5)	¼	0.0028(12)

^a The estimated standard deviations (E.S.D's) were calculated by means of the Berar's procedure and are indicated in round brackets; ^b Li positions and thermal factors have been fixed as they cannot be deduced by means of X-ray diffraction due to the low atomic scattering factor.

Table S3. Selected interatomic distances in (a) LCP-*Cmcm* (ST; from DEG), and (b) LCP-*Cmcm* (PO) as refined from X-ray powder diffraction data at $T = 298 \text{ K}$ ^a.

Sample	Atom Pair			d (Å)
(a) LCP- <i>Cmcm</i> (ST)	Li1	O1	×2	1.973(6)
		O2	×2	2.116(6)
	Co1	O1	×2	2.040(5)
		O2	×4	2.159(3)
	P1	O1	×2	1.511(7)
		O2	×2	1.547(6)
(b) LCP- <i>Cmcm</i> (PO)	Li1	O1	×2	1.968(4)
		O2	×2	2.107(4)
	Co1	O1	×2	2.045(3)
		O2	×4	2.174(2)
	P1	O1	×2	1.510(4)
		O2	×2	1.536(4)

^a The estimated standard deviations (E.S.D.'s) were calculated by means of the Berar's procedure and are indicated in round brackets.

1.2. Infrared Spectroscopy

Attenuated total reflectance (ATR)-Fourier transform infrared spectroscopy (FTIR) data were collected on a Varian 670 IR FTIR spectrometer equipped with a PIKE GladiATR ATR stage (400–4000 cm^{-1} , 132 scans). The Agilent Resolution Pro software was used for data handling. Figure S2 shows the FT-IR spectrum of *Cmcm*-LiCoPO₄. Generally, the spectra of LiCoPO₄ polymorphs are dominated by the fundamental vibrations of the [PO₄]³⁻ groups, which involve the displacement of oxygen atoms of the tetrahedral [PO₄]³⁻ anions. Hence, the observed frequencies are closely related to those of the free phosphate molecule [46]. In the spectrum, four fundamental vibrations are present: symmetric bending vibrations (doublet) of O–P–O (ν_2 at 466–644 cm^{-1}), antisymmetric bending vibrations of the O–P–O fragment (ν_4 around 644 cm^{-1}), asymmetric stretching vibrations (triplet) of P–O (ν_3 around 1058 cm^{-1}), and symmetric stretching vibrations of P–O bond (ν_1 967–1146 cm^{-1}). Out of these, only the vibrations ν_2 and ν_3 are infrared active. However, theoretically non-active vibrations can be observed. Hence, a band due to symmetric stretching vibration around 937–970 cm^{-1} and a band due to deformation vibrations around 358–420 cm^{-1} are expected in some cases [47,48]. Table S4 resumes the assignments of the IR vibrations. Here, two main regions can be distinguished: The first between 400 and 700 cm^{-1} is associated with the intramolecular [PO₄]³⁻ bending modes (ν_2 and ν_4); the region from 900 to 1200 cm^{-1} corresponds to the intramolecular stretching vibrations of the tetrahedral anion (ν_1 and ν_3). Furthermore, the spectrum shows a splitting in the relative intensities of the intramolecular [PO₄]³⁻ bands due to the difference of the specific interactions between the diverse ions and the unit cell, specifically between the monovalent lithium ion and the phosphate anion [48]. In addition to that, the bands below 500 cm^{-1} could be attributed to Li-ion “cage modes,” which represent translational vibrations of the Li-ions inside a potential energy environment determined by the neighbor oxygen atoms; however, due to splitting effect, this bands are overlapping with the phosphate bending vibrations [49].

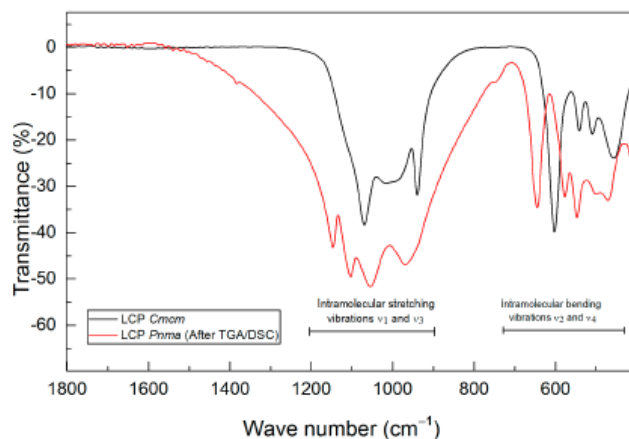


Figure S2. Comparison of the FTIR spectra of (a) the *Cmcm*-LCP (PO) obtained from the polyol route (black); and (b) *Pnma*-LCP obtained after the TGA/DSC measurement at 900 °C (red).

Table S4. Assignments of the internal and external IR vibrations for (a) LCP-*Cmcm* (PO) and (b) LCP-*Pnma* obtained after the TGA/DSC experiment.

	FT-IR Assignment Vibrational mode	Frequency (cm ⁻¹)	
		(a) LCP- <i>Cmcm</i>	(b) LCP- <i>Pnma</i>
	Li ⁺ ion "cage modes"	457	470
Intramolecular bending modes	Symmetric bending vibration O-P-O	511	501
		541	547
	Asymmetric stretching modes [CoO ₆] octahedra	603	577
	Asymmetric bending vibration O-P-O	-	646
Intramolecular stretching modes	Symmetric stretching vibrations P-O	941	970
	Asymmetric stretching vibrations P-O	1002	1050
		1071	1103
	Asymmetric stretching vibration P=O	-	1147

1.3. Temperature-Dependent In Situ X-Ray Powder Diffraction

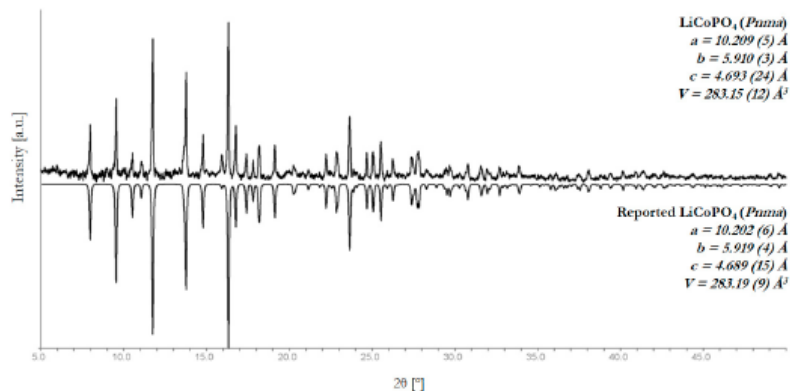


Figure S3. Room temperature PXRD of a LCP-*Cmcm* (PO) sample after the temperature-dependent in situ PXRD experiment. Heating to 800 °C and cooling to room temperature resulted in LCP-*Pnma* as the final product.

Table S5. Temperature program used for temperature-dependent PXRD measurements.

Temperature Range	Heating Rate
20 °C to 200 °C	(50 °C/min)
200 °C to 300 °C	(50 °C/min)
300 °C to 350 °C	(10 °C/min)
350 °C to 400 °C	(10 °C/min)
400 °C to 425 °C	(2° C/min)
425 °C to 450 °C	(2° C/min)
450 °C to 475 °C	(2° C/min)
475 °C to 500 °C	(2° C/min)
500 °C to 525 °C	(10 °C/min)
525 °C to 550 °C	(10 °C/min)
550 °C to 575 °C	(10 °C/min)
575 °C to 600 °C	(10 °C/min)
600 °C to 625 °C	(10 °C/min)
625 °C to 650 °C	(10 °C/min)
650 °C to 675 °C	(10 °C/min)
675 °C to 700 °C	(10 °C/min)
700 °C to 725 °C	(10 °C/min)
725 °C to 750 °C	(10 °C/min)
750 °C to 775 °C	(10 °C/min)
775 °C to 800 °C	(10 °C/min)

7. References

1. D. Lindley, *Nature*, 2010, **463**, 18-20.
2. J. B. Goodenough and Y. Kim, *Chem. Mater.*, 2010, **22**, 587-603.
3. L. Dimesso, C. Foerster, W. Jaegermann, J. P. Khanderi, H. Tempel, A. Popp, J. Engstler, J. J. Schneider, A. Sarapulova, D. Mikhailova, L. A. Schmitt, S. Oswald and H. Ehrenberg, *Chem. Soc. Rev.*, 2012, **41**, 5068-5080.
4. G. Jeong, Y.-U. Kim, H. Kim, Y.-J. Kim and H.-J. Sohn, *Energy Environ. Sci.*, 2011, **4**, 1986-2002.
5. Z. F. Haisheng Tao, Hao Liu, Xianwen Kan, P. Chen, *Open Materials Science Journal*, 2011, **5**, 204-214.
6. M. S. Whittingham, *Chem. Rev.*, 2004, **104**, 4271-4301.
7. R. R. Cacciola, M. Sarva and R. Polosa, *Allergy*, 2002, **57**, 281-286.
8. S. Couraud, G. Zalzman, B. Milleron, F. Morin and P.-J. Souquet, *Eur. J. Cancer*, 2012, **48**, 1299-1311.
9. F. Javidkia, M. Hashemi-Tilehnoee and V. Zabihi, *J. Energy Power Eng.*, 2011, **5**, 811-820.
10. A. Baccarelli and J. D. Kaufman, *Am. J. Respir. Crit. Care Med.*, 2011, **184**, 1325-1327.
11. M. R. Miller, C. A. Shaw and J. P. Langrish, *Future Cardiol.*, 2012, **8**, 577-602.
12. A. G. Russell and B. Brunekreef, *Environ. Sci. Technol.*, 2009, **43**, 4620-4625.
13. D. M. Stieb, L. Chen, M. Eshoul and S. Judek, *Environ. Res.*, 2012, **117**, 100-111.
14. X. Han and L. P. Naeher, *Environ Int*, 2006, **32**, 106-120.
15. Z. A. Needell, J. McNerney, M. T. Chang and J. E. Trancik, *Nat. Energy*, 2016, **1**, 16112-16119.
16. G. Crabtree, *Nature*, 2015, **526**, S92-S92.
17. B. Scrosati, in *Lithium Batteries*, 2013, ch. 2, pp. 21-38.
18. J. M. Tarascon and M. Armand, *Nature*, 2001, **414**, 359-367.
19. D. Deng, *Energy Sci. Eng.*, 2015, **3**, 385-418.
20. Y. Abu-Lebdeh, in *Nanotechnology for Lithium-Ion Batteries*, 2013, ch. 1, pp. 1-11.
21. L. Croguennec and M. R. Palacin, *J. Am. Chem. Soc.*, 2015, **137**, 3140-3156.

22. N. Nitta, F. Wu, J. T. Lee and G. Yushin, *Mater Today*, 2015, **18**, 252-264.
23. H. Lee, M. Yanilmaz, O. Toprakci, K. Fu and X. Zhang, *Energy & Environ. Sci.*, 2014, **7**, 3857-3886.
24. M. M. Doeff, in *Batteries for Sustainability: Selected Entries from the Encyclopedia of Sustainability Science and Technology*, 2013, ch. 1, pp. 5-49.
25. K. M. Abraham, *J. Phys. Chem. Lett.*, 2015, **6**, 830-844.
26. C. Julien, A. Mauger, A. Vijn and K. Zaghib, in *Lithium Batteries: Science and Technology*, 2016, ch. 2, pp. 29-68.
27. M. K. Aydinol and G. Ceder, *J. Electrochem. Soc.*, 1997, **144**, 3832-3835.
28. S. J. Dillon and K. Sun, *Curr. Opin. Solid State Mater. Sci.*, **16**, 153-162.
29. G. Jian, S. Si-Qi and L. Hong, *Chin. Phys. B*, 2016, **25**, 018210.
30. L. A.-W. Ellingsen, C. R. Hung, G. Majeau-Bettez, B. Singh, Z. Chen, M. S. Whittingham and A. H. Stromman, *Nat Nano*, 2016, **11**, 1039-1051.
31. J. Xu, S. Dou, H. Liu and L. Dai, *Nano Energy*, 2013, **2**, 439-442.
32. R. Chen, T. Zhao, X. Zhang, L. Li and F. Wu, *Nanoscale Horiz.*, 2016, **1**, 423-444.
33. A. Manthiram, in *Energy Harvesting Technologies*, 2009, ch. 14, pp. 365-385.
34. A. S. Hameed, *Phosphate based cathodes and reduced graphene oxide composite anodes for energy storage applications*, Springer, Singapore, 2016.
35. K. Zaghib, A. Mauger and C. M. Julien, in *Rechargeable Batteries: Materials, Technologies and New Trends*, 2015, ch. 2, pp. 25-65.
36. H. D. Yoo, E. Markevich, G. Salitra, D. Sharon and D. Aurbach, *Mater. Today*, 2014, **17**, 110-121.
37. M. T. Czyżyk, R. Potze and G. A. Sawatzky, *Phys. Rev. B*, 1992, **46**, 3729-3735.
38. A. Manthiram and T. Muraliganth, in *Handbook of Battery Materials*, 2011, ch. 12, pp. 341-375.
39. J. R. Dahn, U. von Sacken and C. A. Michal, *Solid State Ionics*, 1990, **44**, 87-97.
40. J. Morales, C. Pérez-Vicente and J. L. Tirado, *Mater. Res. Bull.*, 1990, **25**, 623-630.
41. C. Daniel, D. Mohanty, J. Li and D. L. Wood, *AIP Conf. Proc.*, 2014, **1597**, 26-43.
42. M. M. Thackeray, P. J. Johnson, L. A. de Picciotto, P. G. Bruce and J. B. Goodenough, *Mater. Res. Bull.*, 1984, **19**, 179-187.
43. J. Guan and M. Liu, *Solid State Ionics*, 1998, **110**, 21-28.
44. D. Aurbach, M. D. Levi, K. Gamulski, B. Markovsky, G. Salitra, E. Levi, U. Heider, L. Heider and R. Oesten, *J. Power Sources*, 1999, **81-82**, 472-479.
45. H. Li, Z. Wang, L. Chen and X. Huang, *Adv. Mater.*, 2009, **21**, 4593-4607.
46. P. Arora, B. N. Popov and R. E. White, *J. Electrochem. Soc.*, 1998, **145**, 807-815.

47. K. T. Lee, S. Jeong and J. Cho, *Acc. Chem. Res.*, 2013, **46**, 1161-1170.
48. C. Li, H. P. Zhang, L. J. Fu, H. Liu, Y. P. Wu, E. Rahm, R. Holze and H. Q. Wu, *Electrochim. Acta*, 2006, **51**, 3872-3883.
49. J.-S. Kim, C. S. Johnson, J. T. Vaughey, S. A. Hackney, K. A. Walz, W. A. Zeltner, M. A. Anderson and M. M. Thackeray, *J. Electrochem. Soc.*, 2004, **151**, A1755-A1761.
50. A. Yamada, S. C. Chung and K. Hinokuma *J. Electrochem. Soc.*, 2001, **148**, A224-A229.
51. A. K. Padhi, K. S. Nanjundaswamy and J. B. Goodenough, *J. Electrochem. Soc.*, 1997, **144**, 1188-1194.
52. H. Wu, Q. Liu and S. Guo, *Nano-Micro Lett.*, 2014, **6**, 316-326.
53. W.-J. Zhang, *J. Power Sources*, 2011, **196**, 2962-2970.
54. L.-X. Yuan, Z.-H. Wang, W.-X. Zhang, X.-L. Hu, J.-T. Chen, Y.-H. Huang and J. B. Goodenough, *Energy & Environ. Sci.*, 2011, **4**, 269-284.
55. *France Innovation Scientifique & Transfert SA, FIST SA, Assessment of the State of Lithium Metal Phosphate (LiMPO₄) Pat.*, 2010.
56. *J. Kim, D. Kim, Tae. Kim, Method for Synthesizing Electrode Material Using Polyol Process Pat.*, 2008.
57. *I. Exnar and T. Drezen, Synthesis of nanoparticles of lithium metal phosphate positive material for lithium secondary battery Pat.*, 2009.
58. B. L. Ellis, K. T. Lee and L. F. Nazar, *Chem. Mater.*, 2010, **22**, 691-714.
59. A. Yamada, M. Hosoya, S.-C. Chung, Y. Kudo, K. Hinokuma, K.-Y. Liu and Y. Nishi, *J. Power Sources*, 2003, **119-121**, 232-238.
60. S.-Y. Chung, J. T. Bloking and Y.-M. Chiang, *Nat Mater*, 2002, **1**, 123-128.
61. C. Delmas, M. Maccario, L. Croguennec, F. Le Cras and F. Weill, *Nat. Mater.*, 2008, **7**, 665-671.
62. J.-P. Jégou, K.-C. Kim, M. S. Kim and K.-B. Kim, *J. Mater. Chem. A*, 2014, **2**, 9594-9599.
63. T. Liu, L. Zhao, D. Wang, J. Zhu, B. Wang and C. Guo, *RSC Adv.*, 2014, **4**, 10067-10075.
64. K. Zaghib, A. Mauger, F. Gendron and C. M. Julien, *Chem. Mater.*, 2008, **20**, 462-469.
65. M. Thackeray, *Nat. Mater.*, 2002, **1**, 81-82.
66. H. Huang, S.-C. Yin and L. F. Nazar, *Electrochem. Solid St.*, 2001, **4**, A170-A172.
67. S. Brutti and S. Panero, in *Nanotechnology for Sustainable Energy*, 2013, vol. 1140, ch. 4, pp. 67-99.
68. W. F. Howard and R. M. Spotnitz, *J. Power Sources*, 2007, **165**, 887-891.
69. R. Santhanam and B. Rambabu, *J. Power Sources*, 2010, **195**, 5442-5451.
70. O. Toprakci, H. A. K. Toprakci, L. Ji and X. Zhang, *KONA Powder Part. J.*, 2010, **28**, 50-73.
71. K. Amine, H. Yasuda and M. Yamachi, *Electrochem. Solid St.*, 2000, **3**, 178-179.
72. M. E. Rabanal, M. C. Gutierrez, F. Garcia-Alvarado, E. C. Gonzalo and M. E. Arroyo-de Dompablo, *J. Power Sources*, 2006, **160**, 523-528.
73. L. Tan, Z. Luo, H. Liu and Y. Yu, *J. Alloy. Compd.*, 2010, **502**, 407-410.

-
74. S. Okada, S. Sawa, M. Egashira, J.-i. Yamaki, M. Tabuchi, H. Kageyama, T. Konishi and A. Yoshino, *J. Power Sources*, 2001, **97–98**, 430-432.
75. D.-W. Han, Y.-M. Kang, R.-Z. Yin, M.-S. Song and H.-S. Kwon, *Electrochem. Commun.*, 2009, **11**, 137-140.
76. N. N. Bramnik, K. Nikolowski, C. Baetz, K. G. Bramnik and H. Ehrenberg, *Chem. Mater.*, 2007, **19**, 908-915.
77. Q. Sun, J.-Y. Luo and Z.-W. Fu, *Electrochem. Solid St.*, 2011, **14**, A151-A153.
78. F. Wang, J. Yang, Y. NuLi and J. Wang, *J. Power Sources*, 2010, **195**, 6884-6887.
79. N. N. Bramnik, K. G. Bramnik, C. Baetz and H. Ehrenberg, *J. Power Sources*, 2005, **145**, 74-81.
80. V. Koleva, E. Zhecheva and R. Stoyanova, *Eur. J. Inorg. Chem.*, 2010, **2010**, 4091-4099.
81. D. Shanmukaraj and R. Murugan, *Ionics*, 2004, **10**, 88-92.
82. E. J. Kim, H. Y. Xu, J. S. Lim, J. W. Kang, J. H. Gim, V. Mathew and J. Kim, *J. Solid State Electr.*, 2012, **16**, 149-155.
83. H. Ehrenberg, N. N. Bramnik, A. Senyshyn and H. Fuess, *Solid State Sci.*, 2009, **11**, 18-23.
84. J. L. Allen, T. R. Jow and J. Wolfenstine, *J. Power Sources*, 2011, **196**, 8656-8661.
85. P. N. Poovizhi and S. Selladurai, *Ionics*, 2011, **17**, 13-19.
86. Gangulibabu, D. Bhuvaneshwari, N. Kalaiselvi, N. Jayaprakash and P. Periasamy, *J. Sol-Gel Sc. Techn.*, 2009, **49**, 137-144.
87. T. N. L. Doan and I. Taniguchi, *Powder Technol.*, 2012, **217**, 574-580.
88. I. Taniguchi, T. N. L. Doan and B. Shao, *Electrochim. Acta*, 2011, **56**, 7680-7685.
89. J. Liu, T. E. Conry, X. Song, L. Yang, M. M. Doeff and T. J. Richardson, *J. Mater. Chem.*, 2011, **21**, 9984-9987.
90. W. Tian, J. Li, J. W. Lynn, J. L. Zarestky and D. Vaknin, *Phys. Rev. B*, 2008, **78**, 184429.
91. D.-H. Kim and J. Kim, *Electrochem. Solid St.*, 2006, **9**, A439-A442.
92. L. Dimesso, C. Spanheimer, S. Jacke and W. Jaegermann, *Ionics*, 2011, **17**, 429-435.
93. D. Kim, J. Lim, E. Choi, J. Gim, V. Mathew, Y. Paik, H. Jung, W. Lee, D. Ahn, S. Paek and J. Kim, *Surf. Rev. Lett.*, 2010, **17**, 111-119.
94. S. W. Oh, Z.-D. Huang, B. Zhang, Y. Yu, Y.-B. He and J.-K. Kim, *J. Mater. Chem.*, 2012, **22**, 17215-17221.
95. T. Azib, S. Ammar, S. Nowak, S. Lau-Truing, H. Groult, K. Zaghbi, A. Mauger and C. M. Julien, *J. Power Sources*, 2012, **217**, 220-228.
96. G. Wu, Y. Zhou, X. Gao and Z. Shao, *Solid State Sci.*, 2013, **24**, 15-20.
97. N. N. Sinha and N. Munichandraiah, *J. Electrochem. Soc.*, 2010, **157**, A824-A829.

98. S. K. Martha, B. Markovsky, J. Grinblat, Y. Gofer, O. Haik, E. Zinigrad, D. Aurbach, T. Drezen, D. Wang, G. Deghenghi and I. Exnar, *J. Electrochem. Soc.*, 2009, **156**, A541-A552.
99. N. P. W. Pieczonka, Z. Liu, A. Huq and J.-H. Kim, *J. Power Sources*, 2013, **230**, 122-129.
100. D. Wang, H. Buqa, M. Crouzet, G. Deghenghi, T. Drezen, I. Exnar, N.-H. Kwon, J. H. Miners, L. Poletto and M. Grätzel, *J. Power Sources*, 2009, **189**, 624-628.
101. C. Delacourt, P. Poizot, M. Morcrette, J. M. Tarascon and C. Masquelier, *Chem. Mater.*, 2004, **16**, 93-99.
102. S. Karthickprabhu, G. Hirankumar, A. Maheswaran, C. Sanjeeviraja and R. S. Daries Bella, *J. Alloy. Compd.*, 2013, **548**, 65-69.
103. F. Fiévet and R. Brayner, in *Nanomaterials: A Danger or a Promise? A Chemical and Biological Perspective*, 2013, ch. 1, pp. 1-25.
104. J. Kim, D. Kim, Tae. Kim, *Method for Synthesizing Electrode Material Using Polyol Process Pat.*, 2008.
105. T. S. Sreepasad and T. Pradeep, in *Springer Handbook of Nanomaterials*, 2013, ch. 8-9, pp. 303-388.
106. J. Wang, X. Wang, Q. Peng and Y. Li, *Inorg. Chem.*, 2004, **43**, 7552-7556.
107. I. Exnar and T. Drezen, *Synthesis of nanoparticles of lithium metal phosphate positive material for lithium secondary battery Pat.*, 2007.
108. L. Poul, S. Ammar, N. Jouini, F. Fievet and F. Villain, *J. Sol-Gel Sc. Techn.*, 2003, **26**, 261-265.
109. S. Kandhasamy, A. Pandey and M. Minakshi, *Electrochim. Acta*, 2012, **60**, 170-176.
110. H. Wei, Q. Shen, Y. Zhao, Y. Zhou, D. Wang and D. Xu, *J. Cryst. Growth*, 2004, **264**, 424-429.
111. C. Luna, M. P. Morales, C. J. Serna and M. Vázquez, *Mater. Sci. Eng. C*, 2003, **23**, 1129-1132.
112. Y. Soumare, C. Garcia, T. Maurer, G. Chaboussant, F. Ott, F. Fiévet, J.-Y. Piquemal and G. Viau, *Adv. Funct. Mater.*, 2009, **19**, 1971-1977.
113. W. Zhang, Z. Shan, K. Zhu, S. Liu, X. Liu and J. Tian, *Electrochim. Acta*, 2015, **153**, 385-392.
114. D. Ung, G. Viau, C. Ricolleau, F. Warmont, P. Gredin and F. Fiévet, *Adv. Mater.*, 2005, **17**, 338-344.
115. M. Rycenga, C. M. Copley, J. Zeng, W. Li, C. H. Moran, Q. Zhang, D. Qin and Y. Xia, *Chem. Rev.*, 2011, **111**, 3669-3712.
116. F. Wu and G. Yushin, *Energy Environ. Sci.*, 2017, **10**, 435-459.
117. J. Wang and X. Sun, *Energy & Environ. Sci.*, 2012, **5**, 5163-5185.
118. Z. Tian, S. Liu, F. Ye, S. Yao, Z. Zhou and S. Wang, *Appl. Surf. Sci.*, 2014, **305**, 427-432.
119. S. Moon, P. Muralidharan and D. K. Kim, *Ceram. Int.*, 2012, **38**, **Supplement 1**, S471-S475.
120. G. Kucinskis, G. Bajars and J. Kleperis, *J. Power Sources*, 2013, **240**, 66-79.
121. L. Li, H. Yang, D. Zhou and Y. Zhou, *J. Nanomater.*, 2014, **2014**, 8.
122. M. Osiak, H. Geaney, E. Armstrong and C. O'Dwyer, *J. Mater. Chem. A*, 2014, **2**, 9433-9460.

123. J. Wolfenstine, *J. Power Sources*, 2006, **158**, 1431-1435.
124. N. Meethong, Y.-H. Kao, S. A. Speakman and Y.-M. Chiang, *Adv. Funct. Mater.*, 2009, **19**, 1060-1070.
125. P. R. Kumar, M. Venkateswarlu, M. Misra, A. K. Mohanty and N. Satyanayana, *J. Nanosci. Nanotechnol.*, 2011, **11**, 3314-3322.
126. W. H. Kan, University of Waterloo, 2009.
127. *EE.UU. Pat.*, 2009.
128. R. Vasanthi, D. Kalpana and N. Renganathan, *Journal of Solid State Electrochemistry*, 2008, **12**, 961-969.
129. S. Kandhasamy, P. Singh, S. Thurgate, M. Ionescu, D. Appadoo and M. Minakshi, *Electrochim. Acta*, 2012, **82**, 302-308.
130. B. J. Paul, S.-W. Kang, J. Gim, J. Song, S. Kim, V. Mathew and J. Kim, *J. Electrochem. Soc.*, 2014, **161**, A1468-A1473.
131. A. Vadivel Murugan, T. Muraliganth and A. Manthiram, *J. Electrochem. Soc.*, 2009, **156**, A79-A83.
132. K. Su, F. Liu and J. Chen, *J. Power Sources*, 2013, **232**, 234-239.
133. M. S. Thomas Degen, Egbert Bron, Uwe König *Powder Diffr.*, 2014, **29**, S13-S18.
134. F. Kubel, *Journal*, 1994, **209**, 755.
135. P. Scherrer, *Göttinger Nachrichten*, 1918, **2**, 98-100.
136. ME Global <http://www.meglobal.biz/product-literature> (accessed Apr. 20, 2017)).
137. The Dow Chemical Company, <http://www.dow.com/ethyleneglycol/resources/index.htm> (accessed Apr. 20, 2017)).
138. R. Vasanthi, D. Kalpana and N. Renganathan, *J. Solid State Electr.*, 2008, **12**, 961-969.
139. G. Hautier, A. Jain, S. P. Ong, B. Kang, C. Moore, R. Doe and G. Ceder, *Chem. Mater.*, 2011, **23**, 3495-3508.
140. C. Jahne, C. Neef, C. Koo, H.-P. Meyer and R. Klingeler, *J. Mater. Chem. A*, 2013, **1**, 2856-2862.
141. K. Ilona, Dissertation Doctor, Technischen Universität München, 2015.
142. M. Wagemaker, W. J. H. Borghols and F. M. Mulder, *J. Am. Chem. Soc.*, 2007, **129**, 4323-4327.
143. E. Pohjalainen, T. Rauhala, M. Valkeapää, J. Kallioinen and T. Kallio, *J. Phys. Chem. C*, 2015, **119**, 2277-2283.
144. Y. Zhang, J. Shi, Y. Hu, Z. Huang and L. Guo, *Catal. Sci. Tech.*, 2016, **6**, 8080-8088.
145. J. Liu, K. Zhou, G. Tang, B. Wang, Z. Gui, R. K. K. Yuen and Y. Hu, *Polym. Composite*, 2016, 1-9.
146. J.-M. Lee, Y.-D. Jun, D.-W. Kim, Y.-H. Lee and S.-G. Oh, *Mater. Chem. Phys.*, 2009, **114**, 549-555.

147. F. Bonet, V. Delmas, S. Grugeon, R. Herrera Urbina, P. Y. Silvert and K. Tekaiia-Elhsissen, *Nanostruct. Mater.*, 1999, **11**, 1277-1284.
148. Y. Gu, H. Wang, Y. Zhu, L. Wang, Y. Qian and Y. Chu, *Solid State Ionics*, 2015, **274**, 106-110.
149. Q. Zhang, S.-Z. Huang, J. Jin, J. Liu, Y. Li, H.-E. Wang, L.-H. Chen, B.-J. Wang and B.-L. Su, *Sci. Rep.*, 2016, **6**, 25942.
150. W. D. Callister and D. G. Rethwisch, *Journal*, 2014, 200-206.
151. F. J. Humphreys and M. Hatherly, in *Recrystallization and Related Annealing Phenomena*, 2004, ch. 1, pp. 1-10.
152. F. Teng, Z.-H. Hu, X.-H. Ma, L.-C. Zhang, C.-X. Ding, Y. Yu and C.-H. Chen, *Electrochim. Acta*, 2013, **91**, 43-49.
153. M. K. Devaraju and I. Honma, *Adv. Energy Mater.*, 2012, **2**, 284-297.
154. J. N. van Niekerk and F. R. L. Schoening, *Acta Cryst.*, 1953, **6**, 609-612.
155. K. J. Kreder, G. Assat and A. Manthiram, *Chem. Mater.*, 2015, **27**, 5543-5549.
156. U. Amador, J. M. Gallardo-Amores, G. Heymann, H. Huppertz, E. Moran and y. d. D. M. E. Arroyo, *Solid State Sci.*, 2009, **11**, 343-348.
157. Y. Xia, Y. Xiong, B. Lim and S. E. Skrabalak, *Angew. Chem. Int. Ed.*, 2009, **48**, 60-103.
158. G. Assat and A. Manthiram, *Inorg. Chem.*, 2015, **54**, 10015-10022.
159. B. Guo, H. Ruan, C. Zheng, H. Fei and M. Wei, *Sci. Rep.*, 2013, **3**, 2788.
160. Q. D. Truong, M. K. Devaraju, Y. Ganbe, T. Tomai and I. Honma, *Sci. Rep.*, 2014, **4**, 3975.
161. R. E. Rogers, G. M. Clarke, O. N. Matthew, M. J. Ganter, R. A. DiLeo, J. W. Staub, M. W. Forney and B. J. Landi, *J. Appl. Electrochem.*, 2013, **43**, 271-278.
162. H. H. Li, J. Jin, J. P. Wei, Z. Zhou and J. Yan, *Electrochem. Commun.*, 2009, **11**, 95-98.
163. J. Ludwig, C. Marino, D. Haering, C. Stinner, D. Nordlund, M. M. Doeff, H. A. Gasteiger and T. Nilges, *RSC Adv.*, 2016, **6**, 82984-82994.
164. L. Jinsub, K. Donghan, M. Vinod and K. Jaekook, *Phys. Scripta*, 2010, **2010**, 014060.
165. M. J. Collins Jr, *Future Med. Chem.*, 2010, **2**, 151-155.
166. B. L. Hayes, *Microwave synthesis : chemistry at the speed of light*, CEM Publishing, Matthews, NC, 2002.
167. M. Baghbanzadeh, L. Carbone, P. D. Cozzoli and C. O. Kappe, *Angew. Chem. Int. Ed.*, 2011, **50**, 11312-11359.
168. C. Gabriel, S. Gabriel, E. H. Grant, E. H. Grant, B. S. J. Halstead and D. Michael P. Mingos, *Chem. Soc. Rev.*, 1998, **27**, 213-224.
169. D. M. P. Mingos and D. R. Baghurst, *Chem. Soc. Rev.*, 1991, **20**, 1-47.
170. Y.-J. Zhu and F. Chen, *Chem. Rev.*, 2014, **114**, 6462-6555.
171. M. Niederberger, in *Microwaves in Nanoparticle Synthesis*, 2013, ch. 4, pp. 185-205.

172. C. O. Kappe, *Angew. Chem. Int. Ed.*, 2004, **43**, 6250-6284.
173. T. E. Ashton, J. V. Laveda, D. A. MacLaren, P. J. Baker, A. Porch, M. O. Jones and S. A. Corr, *J. Mater. Chem. A*, 2014, **2**, 6238-6245.
174. National Center for Biotechnology Information PubChem Compound Database; CID=24965, <https://pubchem.ncbi.nlm.nih.gov/compound/24965> (accessed Apr. 20, 2017)).
175. National Center for Biotechnology Information PubChem Compound Database; CID=61372, <https://pubchem.ncbi.nlm.nih.gov/compound/61372> (accessed Apr. 20, 2017)).
176. ECHA European Chemical Agency <https://echa.europa.eu/registration-dossier/-/registered-dossier/14925/4/9> (accessed Apr. 20, 2017)).
177. S. Rodriguez-Liviano, A. I. Becerro, D. Alcántara, V. Grazú, J. M. de la Fuente and M. Ocaña, *Inorg. Chem.*, 2013, **52**, 647-654.
178. C. A. J. Fisher and M. S. Islam, *J. Mater. Chem.*, 2008, **18**, 1209-1215.
179. C. A. J. Fisher, V. M. Hart Prieto and M. S. Islam, *Chemistry of Materials*, 2008, **20**, 5907-5915.
180. H. Ni, J. Liu and L.-Z. Fan, *Nanoscale*, 2013, **5**, 2164-2168.
181. B. Kang and G. Ceder, *Nature*, 2009, **458**, 190-193.
182. N. H. Kwon, H. Yin, T. Vavrova, J. H. W. Lim, U. Steiner, B. Grobéty and K. M. Fromm, *J. Power Sources*, 2017, **342**, 231-240.
183. J. A. Dirksen and T. A. Ring, *Chem. Eng. Sci.*, 1991, **46**, 2389-2427.
184. T. Sugimoto, *Chem. Eng. Technol.*, 2003, **26**, 313-321.
185. B. L. Cushing, V. L. Kolesnichenko and C. J. O'Connor, *Chem. Rev.*, 2004, **104**, 3893-3946.
186. J. W. Mullin and J. Nývlt, *Chem. Eng. Sci.*, 1971, **26**, 369-377.
187. Z. Guo, M. Zhang, H. Li, J. Wang and E. Kougoulos, *J. Cryst. Growth*, 2005, **273**, 555-563.
188. M.-S. Kim, H.-K. Kim, S.-W. Lee, D.-H. Kim, D. Ruan, K. Y. Chung, S. H. Lee, K. C. Roh and K.-B. Kim, *Sci. Rep.*, 2016, **6**, 26686.
189. C. Gong, Z. Xue, S. Wen, Y. Ye and X. Xie, *J. Power Sources*, 2016, **318**, 93-112.
190. N. Laszczynski, A. Birrozzi, K. Maranski, M. Copley, M. E. Schuster and S. Passerini, *J. Mater. Chem. A*, 2016, **4**, 17121-17128.
191. L. Dimesso, S. Jacke, C. Spanheimer and W. Jaegermann, *J. Solid State Electrochem.*, 2012, **16**, 911-919.
192. J. Wolfenstine, J. Read and J. L. Allen, *J. Power Sources*, 2007, **163**, 1070-1073.
193. A. E. Kaifer, *J. Chem. Educ.*, 1992, **69**, A305.
194. C. Alarcón-Suesca, J. Ludwig, V. Hlukhyy, C. Stinner and T. Nilges, *Inorganics*, 2016, **4**, 35.
195. G. Zeng, R. Caputo, D. Carriazo, L. Luo and M. Niederberger, *Chem. Mater.*, 2013, **25**, 3399-3407.

196. C.-H. Yim, E. A. Baranova, Y. Abu-Lebdeh and I. Davidson, *J. Power Sources*, 2012, **205**, 414-419.
197. D. Rabinovich, *J. Chem. Educ.*, 2000, **77**, 311.
198. F. A. Cotton, D. M. L. Goodgame and M. Goodgame, *J. Am. Chem. Soc.*, 1961, **83**, 4690-4699.
199. T. J. Swift and R. E. Connick, *J. Chem. Phys.*, 1962, **37**, 307-320.
200. S. Junzo and H. Tomiko, *Bull. Chem. Soc. Jpn.*, 1978, **51**, 3130-3135.
201. T. W. Swaddle and L. Fabes, *Can. J. Chem.*, 1980, **58**, 1418-1426.
202. H. Ju, J. Wu and Y. Xu, *Int. J. Energy Environ. Eng.*, 2013, **4**, 22.
203. M. Singh and M. Willert-Porada, *Adv. Powder Technol.*, 2011, **22**, 284-289.
204. V. Mathew, M. H. Alfaruqi, J. Gim, J. Song, S. Kim, D. Ahn and J. Kim, *Mater. Charact.*, 2014, **89**, 93-101.
205. Y.-K. Hu, J.-X. Ren, Q.-L. Wei, X.-D. Guo, Y. Tang, B.-H. Zhong and H. Liu, *Acta Phys-Chim Sin.*, 2014, **30**, 75-82.
206. O. Garcia-Moreno, M. Alvarez-Vega, F. Garcia-Alvarado, J. Garcia-Jaca, J. M. Gallardo-Amores, M. L. Sanjuan and U. Amador, *Chem. Mater.*, 2001, **13**, 2455.
207. B. Voß, J. Nordmann, A. Kockmann, J. Piezonka, M. Haase, D. H. Taffa and L. Walder, *Chem. Mater.*, 2012, **24**, 633-635.